

Search for $\beta\beta$ -decay of ^{48}Ca in NEMO-3 and commissioning of the tracker for the SuperNEMO experiment

Cristóvão Fernandes Vilela
University College London

Submitted to University College London in fulfilment
of the requirements for the award of the
degree of **Doctor of Philosophy**

September 30th, 2014

Declaration

I, Cristóvão Fernandes Vilela, confirm that the work presented in this thesis is my own. Where information has been derived from other sources, I confirm that this has been indicated in the thesis.

Cristóvão Vilela

Abstract

The double- β decay of ^{48}Ca was analysed with data taken by the NEMO-3 experiment with 6.99 grams of isotope and 1918.5 days of live time. The half-life of the $2\nu\beta\beta$ of ^{48}Ca was measured to be $t_{2\nu}^{1/2} = 6.4^{+0.6}_{-0.7}$ (stat.) $^{+1.2}_{-0.9}$ (syst.) $\times 10^{19}$ years, with the corresponding nuclear matrix element measured to be $|M^{2\nu}| = 0.02 \pm 0.002$. A lower limit of $t_{0\nu}^{1/2} > 2.0 \times 10^{22}$ years was placed on the half-life of the $0\nu\beta\beta$ mode, yielding an upper limit on the effective Majorana neutrino mass of $\langle m_{\beta\beta} \rangle < 6.1 - 38$ eV. Limits were also placed on the \hat{R}_p supersymmetry trilinear coupling λ'_{111} , on right-handed current couplings $\langle \lambda \rangle$ and $\langle \eta \rangle$, and on the coupling of the Majoron to the ν_e $\langle g_{\chi^0} \rangle$.

Work in preparation for the commissioning of the tracking detector for the SuperNEMO double- β decay experiment is described. The data acquisition and high voltage supply electronics were prepared to read 504 SuperNEMO tracker cells and successfully tested with a smaller 2×9 array of tracker cells. A system to supply the SuperNEMO Demonstrator with the tracking gas mixture was designed and built with stringent radon emanation requirements. The system was shown to perform well on test with a single-cell tracker prototype.

Acknowledgements

Firstly, I would like to express my gratitude to my supervisor, David Waters. His clarity of mind kept me going roughly in the right direction without drifting *off-piste* too much. From him I hope to have learned that no question is too naïve to be asked. Needless to say, without his advice and encouragement this thesis would not have been written.

I am also grateful to the SuperNEMO group at UCL in which it was a great pleasure to work. In particular, my thanks go to Stefano Torre, and Ruben Saakyan for their help in the analysis of NEMO-3 data; and Derek Attree, Michele Cascella and Rob Flack, without whom the work towards the commissioning of SuperNEMO presented here would not have been possible.

In addition, I thank my fellow SuperNEMO students, in particular James Mott, Summer Blot, Guillaume Eurin, Benjamin Soulé and Xin Ran Liu for the good times had at collaboration meetings. Working with you was also fine. I am also indebted to Inês Ochoa for her support and useful suggestions to this thesis.

Lastly, I would like to thank my parents Mi and Afonso, among many other things, for their relentless support and enthusiasm for my work; and my brother Sebastião, for his friendship and our lengthy discussions about science and other things.

Contents

List of Figures	15
List of Tables	19
1. Introduction	23
1.1. Author's contributions	24
2. Neutrino Phenomenology	27
2.1. Historical overview	27
2.1.1. Radioactive decay	27
2.1.2. Proposal and observation of the neutrino	28
2.1.3. Parity violation in weak interactions	28
2.1.4. Neutrino flavour	29
2.2. Neutrinos in the SM	30
2.3. Neutrino oscillations	31
2.3.1. The solar neutrino anomaly	33
2.3.2. Neutrino mixing	34
2.3.3. Oscillations in matter	35
2.3.4. Oscillation parameters	36
2.3.5. Mass hierarchy	37
2.4. Neutrino Mass	37
2.4.1. Dirac mass term	38
2.4.2. Majorana mass term	39
2.4.3. See-saw mechanism	40
2.5. Constraints on neutrino mass	41
2.5.1. Beta decay of tritium	41
2.5.2. Cosmology	43
2.5.3. Neutrinoless double- β decay	43

2.6. Summary and outlook	44
3. Double-β decay	47
3.1. β decay	47
3.1.1. The semi-empirical mass formula	48
3.2. Two-neutrino double- β decay	50
3.3. Neutrinoless double- β decay	52
3.3.1. Mass mechanism	53
3.3.2. \hat{R}_p supersymmetry	54
3.3.3. Right handed currents	55
3.3.4. Majoron emission	56
3.4. Nuclear matrix elements	56
3.4.1. Comparison of calculations	58
4. Double-β decay experiments and techniques	61
4.1. Detector technologies	65
4.1.1. Semiconductor experiments	65
4.1.2. Bolometer experiments	67
4.1.3. Scintillator experiments	67
4.1.4. Time projection chamber experiments	68
4.1.5. Tracker and calorimeter experiments	69
4.2. Experiments with ^{48}Ca	69
4.3. Current status of double- β decay measurements	71
I. Search for double-β decay of ^{48}Ca with the NEMO-3 detector	73
5. The NEMO-3 detector	75
5.1. Source foils	75
5.1.1. ^{48}Ca source	79
5.2. Tracker	81
5.3. Calorimeter	84
5.4. Electronics, DAQ and trigger	85
5.4.1. Calorimeter electronics	86
5.4.2. Tracker electronics	86

5.4.3. Trigger system	87
5.5. Energy and time calibration	88
5.5.1. Radioactive sources	88
5.5.2. Laser calibration system	89
5.6. Magnetic field	90
5.7. Passive shielding	90
5.8. Anti-radon facility	90
6. General analysis techniques	93
6.1. Monte Carlo simulation	93
6.2. Event reconstruction	94
6.3. Particle identification	95
6.3.1. Electrons	95
6.3.2. Photons	95
6.3.3. Alpha emission from ^{214}Bi - ^{214}Po decays	96
6.4. Time of flight	97
6.4.1. Internal hypothesis	98
6.4.2. External hypothesis	100
6.5. Statistical analysis	102
6.5.1. Fitting MC predictions to data	103
6.5.2. Limit setting	105
6.6. Half-life calculation	107
6.7. Analysis data set	108
7. Measurement of backgrounds in the ^{48}Ca source	109
7.1. Background production processes	109
7.1.1. Background classification	110
7.2. Sources of background	112
7.2.1. Decay chains	114
7.2.2. ^{222}Rn	117
7.2.3. Other natural background sources	119
7.2.4. Artificial contaminants in source foil	119
7.2.5. $2\nu\beta\beta$ as a background to $0\nu\beta\beta$	120
7.2.6. Leakage	121
7.3. NEMO-3 background model	121
7.4. HPGe measurements of internal backgrounds	123

7.5. Background fitting procedure	124
7.6. General event selection	126
7.6.1. Hot runs	126
7.6.2. Energy threshold	126
7.7. Background measurement channels	129
7.7.1. $1eN\gamma$	129
7.7.2. $1e1\gamma$ (internal)	130
7.7.3. $1e2\gamma$	131
7.7.4. $1e1\alpha$	133
7.7.5. External background measurement channels	133
7.8. Background measurement results	135
8. ^{48}Ca double-β decay results	139
8.1. $2eN\gamma$ event selection	139
8.1.1. Validation of $2eN\gamma$ selection on ^{207}Bi calibration source data	141
8.2. $2eN\gamma$ distributions	142
8.3. Systematic uncertainty on the $2\nu\beta\beta$ measurement	145
8.3.1. Optimisation of $2\nu\beta\beta$ fitting window	149
8.4. $2\nu\beta\beta$ half-life result and discussion	151
8.5. Limits on $0\nu\beta\beta$ and discussion of results	153
II. Tracker commissioning for the SuperNEMO detector	163
9. The SuperNEMO experiment	165
9.1. The Demonstrator module	166
9.2. Research and development	168
9.3. Timescale and sensitivity	171
10. The SuperNEMO tracker	173
10.1. The physics of Geiger counters	174
10.2. The SuperNEMO tracker cells	176
10.3. The tracker frame	180
10.4. Construction of the tracker	182
10.5. Tracker electronics and DAQ	183

11. Electronics for surface commissioning	187
11.1. HV supply and distribution	188
11.2. Cosmic ray trigger	191
11.3. DAQ cards	192
11.4. VME controller and read-out cycle	195
11.4.1. Read-out cycle duration and dead time	196
11.5. Testing the tracker commissioning DAQ system on the cassette test tank	198
12. Gas mixing system for the Demonstrator module	205
12.1. Principle of operation	205
12.1.1. Two-stage ethanol vapour addition	208
12.2. Materials	210
12.3. Tests	212
12.4. Flow rate and ^{222}Rn activity in the tracker	213
13. Conclusion	215
Bibliography	219

List of Figures

2.1. Measurement of the hadronic cross-section at the Z mass pole by the LEP experiments.	30
2.2. Standard Model vertices involving neutrinos.	31
2.3. Neutrino interactions with matter: charged and neutral current scattering off nucleons or atomic electrons.	32
2.4. Normal and inverted scenarios for the neutrino mass spectrum.	38
2.5. Electron energy spectrum in the β decay of tritium	42
2.6. Effective $0\nu\beta\beta$ mass against smallest neutrino mass.	45
3.1. Masses of even A nuclei, as described by the SEMF.	49
3.2. Feynman diagram for the two-neutrino double- β decay.	50
3.3. Majorana mass term due to $0\nu\beta\beta$	52
3.4. Feynman diagram for the mass mechanism $0\nu\beta\beta$	53
3.5. Summed energy spectrum of double- β decay.	54
3.6. Feynman diagram for the $\langle\lambda\rangle$ mode of $0\nu\beta\beta$ arising from left-right symmetric models.	55
3.7. Comparison between the nuclear matrix elements for 11 isotopes calculated in five different frameworks.	59
3.8. Comparison between the $0\nu\beta\beta$ half-lives of 11 isotopes assuming an effective Majorana mass of $\langle m_{\beta\beta}\rangle = 50$ meV.	59
5.1. Cutaway drawing of the NEMO-3 detector.	76
5.2. Top-view diagram of the NEMO-3 detector.	76
5.3. Arrangement of the different sources in the NEMO-3 detector.	77
5.4. Map of the ^{48}Ca and neighbouring sources as seen in NEMO-3 data.	78

5.5. Structure of the CaF_2 source discs.	80
5.6. Photograph of the ^{48}Ca source.	80
5.7. Rotated source foil strips.	81
5.8. Plan view of the tracker in one NEMO-3 sector.	82
5.9. Schematic drawing of a NEMO-3 calorimeter module.	84
6.1. Example of a two-electron event.	96
6.2. Example of an event with a delayed α track.	97
6.3. Example of events with external origin.	98
6.4. Distributions of p-values for the internal time of flight hypothesis. . .	101
6.5. Distributions of p-values for the external time of flight hypothesis. . .	103
6.6. Example of NLLR distributions.	106
7.1. Internal background production processes.	111
7.2. External background production processes.	113
7.3. Thorium decay chain.	115
7.4. Uranium decay chain.	116
7.5. Radon level in the NEMO-3 detector.	118
7.6. Exponential decay of $^{90}\text{Sr}/^{90}\text{Y}$ in the ^{48}Ca source.	121
7.7. Abnormal calorimeter activity leading to the exclusion of runs 8779 – 8786.	127
7.8. Distributions of total energy in $1eN\gamma$ and $1e1\gamma$ (internal) events for three energy thresholds.	128
7.9. Electron energy distribution in $1eN\gamma$ events.	130
7.10. Distribution of the cosine of the opening angle between the electron and the γ in $1e1\gamma$ (internal) events.	131
7.11. Distribution of the summed energy of the electron and the γ in $1e1\gamma$ (internal) events.	132
7.12. Distribution of the summed energy of the electron and the two γ 's in $1e2\gamma$ events.	132

7.13. Distribution of the length of the delayed α track in $1e1\alpha$ events.	134
7.14. Distribution of the summed energy of the electron and the γ in $1e1\gamma$ (external) events.	134
7.15. Summed calorimeter energy distribution in crossing electron events.	135
7.16. Comparison between measured internal background activities and HPGe measurements.	136
8.1. Mis-modelling of the distance between electron vertices in “same side” events and difference in efficiency of the vertex distance cuts in data and MC.	141
8.2. Distribution of events against the run number.	143
8.3. Distributions of geometrical variables in $2eN\gamma$ events.	144
8.4. Distributions of kinematic variables in $2eN\gamma$ events.	145
8.5. Distribution of the summed electron energies in $2eN\gamma$ events.	146
8.6. Optimisation of the $2\nu\beta\beta$ fitting window.	150
8.7. Comparison of the measured $ M^{2\nu} $ to theoretical calculations.	152
8.8. $2eN\gamma$ summed electron distribution with $0\nu\beta\beta$ limits.	155
8.9. $2eN\gamma$ background subtracted data with $0\nu\beta\beta$ limits.	155
8.10. Comparison of the $\langle m_{\beta\beta} \rangle$ limit measured in this analysis to the best available limits with ^{48}Ca , ^{100}Mo and ^{136}Xe	158
9.1. Exploded view drawing of the SuperNEMO Demonstrator module.	167
9.2. Construction of the SuperNEMO main wall calorimeter modules.	168
9.3. Sensitivity of the SuperNEMO experiment as a function of exposure.	172
10.1. Sketch of the signal generating process in Geiger counters.	175
10.2. Sketch of a SuperNEMO tracker cell.	177
10.3. Example set of signals from a Geiger discharge in a SuperNEMO tracker cell.	179
10.4. Sketch of a SuperNEMO tracker C-section.	181
10.5. Photograph of the wiring robot in the University of Manchester clean- room.	183

10.6. Photograph of the C0 frame at MSSL, partially populated with cells.	184
10.7. Derivative of the anode signal.	185
11.1. Schematic diagram of the tracker commissioning electronics.	189
11.2. The NEMO-3 HV distribution and decoupling system.	190
11.3. Timing diagram for the tracker commissioning DAQ system.	193
11.4. Read-out dead time and rate of the tracker commissioning DAQ system.	196
11.5. Photograph of the electronics and cosmic ray trigger at the University of Manchester	197
11.6. Sketch of a cassette in the test tank.	199
11.7. Results of the x -axis scan of the cassette.	200
11.8. Scan of the Geiger plateau.	202
11.9. Efficiency of the avalanche propagation of six cells in a cassette. . . .	203
11.10 Distribution of the propagation time to the read out cathode ring for six cells in a cassette.	204
12.1. Flow diagram for the Demonstrator's gas mixing system.	207
12.2. Diagram of a tentative gas outlet system of the Demonstrator.	208
12.3. Fractional volumes of ethanol obtained at equilibrium under controlled temperature and pressure conditions.	210
12.4. Photograph of the Demonstrator's gas mixing system.	211
12.5. Ethanol volume fraction in the gas measured by the depletion rate of liquid ethanol.	213

List of Tables

2.1. Best fit oscillation parameters assuming normal hierarchy.	37
2.2. Current limits on neutrino mass.	44
4.1. $Q_{\beta\beta}$ and natural abundances for isotopes commonly considered for double- β decay experiments.	63
4.2. Most precise direct measurements of $2\nu\beta\beta$	72
4.3. Best limits on the $0\nu\beta\beta$ half-life of the isotopes for which $2\nu\beta\beta$ has been directly observed.	72
6.1. Exposure of the NEMO-3 <i>standard</i> analysis run set.	108
7.1. NEMO-3 external background model.	122
7.2. HPGe measurement of internal backgrounds in the ^{48}Ca source.	123
7.3. Analysis channels used in the background measurement.	124
7.4. Overview of the parameters used in the global fit.	125
7.5. Results of internal background measurement.	136
7.6. Results of external background measurement.	137
7.7. Results of radon background measurement.	138
8.1. Measurement of the activity of ^{207}Bi sources with NEMO-3 and HPGe detector data.	142
8.2. Activity of the $^{90}\text{Sr}/^{90}\text{Y}$ system measured in the global fit and in the $2eN\gamma$ channel.	145
8.3. Systematic uncertainty on the $2\nu\beta\beta$ measurement due to data mis-modelling in “same side” and “opposite side” events.	149
8.4. Total systematic uncertainty on the $2\nu\beta\beta$ half-life measurement.	150

8.5. Systematic uncertainties used in $0\nu\beta\beta$ limits.	153
8.6. Limits on $0\nu\beta\beta$ modes.	154
9.1. Experimental parameters and $0\nu\beta\beta$ sensitivity for the SuperNEMO experiment and its Demonstrator module.	166

“Wonderful experiments have led to the discovery of neutrino mass. This discovery has raised some very interesting questions, and we would like very much to learn the answers to these questions.”

— Boris Kayser

Chapter 1.

Introduction

Neutrinoless double- β decay is a lepton number violating process predicted by several theories beyond the Standard Model. In particular, the existence of a massive Majorana neutrino would lead to this process. That neutrinos are massive particles is now well established, due to compelling evidence from the observations of neutrino flavour oscillation. The Standard Model requires significant modifications in order to accommodate for the small neutrino masses. In general, the description of massive neutrinos in the theory includes Majorana mass terms which lead to neutrinoless double- β decay. An overview of neutrino phenomenology is given in Chapter 2 of this thesis and double- β decay processes are discussed in Chapter 3.

The considerations outlined above have motivated a deep interest in the experimental investigation of double- β decay, which is the only known process sensitive to the nature of neutrino masses. A summary of these efforts is given Chapter 4.

NEMO-3 was an experiment which investigated double- β decay processes with a unique technique using both a tracking detector and a calorimeter. This technique allows for the full reconstruction of the topology and kinematics of rare radioactive decays. The first part of this thesis is dedicated to the investigation of the double- β decay of ^{48}Ca with the NEMO-3 detector. The experiment is described in Chapter 5 and the techniques used for the analysis of its data are detailed in Chapter 6. A significant part of the data analysis concerns the assessment of the backgrounds to double- β decay measurements. These efforts are documented in Chapter 7 and the results of the double- β decay analyses are given and discussed in Chapter 8.

The success of NEMO-3 has led to the development of a new experiment, SuperNEMO, which uses similar, but improved, experimental techniques. The first stage of this experiment, the Demonstrator module, is currently under construction. The second part of this thesis describes the efforts taken in preparation for the surface commissioning of the tracking detector for the SuperNEMO Demonstrator. The new experiment is described in Chapter 9, with focus on the research and development efforts undertaken to improve on the NEMO-3 technique. A detailed description of the tracking detector and its construction is given in Chapter 10. The data acquisition system developed for the surface commissioning of the tracking detector and its tests with SuperNEMO tracker cells are described in Chapter 11. In Chapter 12, work related to the design and construction of the gas mixing system for the SuperNEMO Demonstrator's tracker is reported.

Finally, a summary of the conclusions reached in this thesis is given in Chapter 13.

1.1. Author's contributions

NEMO-3

- Analysis of the ^{48}Ca data, including the assessment of the backgrounds, the measurement of the $2\nu\beta\beta$ half-life and setting limits on $0\nu\beta\beta$ modes;
- Participation in the development of a modular data analysis framework, in particular writing a module for managing the cut flow;
- Participation in data quality studies, namely regarding the removal of events with hits in unstable calorimeter modules;
- Production of Monte Carlo samples for the assessment of systematic uncertainties for the ^{48}Ca measurements;
- Participation in the decommissioning of the detector, in particular, the disassembly and recovery of the tracker electronics.

SuperNEMO

- Preparation of the data acquisition and high voltage supply systems for the commissioning of the tracker, including work on the high voltage cabling and connector prototyping;
- Participation in the design, construction and testing of the gas mixing system for the Demonstrator's tracker;
- Analysis of atmospheric pressure fluctuations in the underground laboratory, in relation to the point above;
- Studies with the single-cell tracker prototype, namely regarding effects due to ageing and high gas flow rates;
- Simulation studies of the electrostatic properties of the tracker cells, and investigation of their drift model.

Chapter 2.

Neutrino Phenomenology

2.1. Historical overview

Our understanding of neutrinos has been driven by experimental observations. This is true both historically and today, with unexpected observations arising from the neutrino sector which required the description of neutrino masses to be added to the otherwise well tested theoretical framework of particle physics. In this section, a brief overview of the discoveries that led to the Standard Model (SM) description of neutrinos will be given.

2.1.1. Radioactive decay

The observation of the blackening of photographic plates when exposed to uranium salts led Henri Becquerel to the discovery of radioactive phenomena. By the beginning of the 20th century it had been established that three different types of rays were responsible for radioactivity. Rutherford called them α , β and γ rays. Becquerel had also measured the charge to mass ratio of β rays and found it to be the same as J.J. Thompson's measurement of the same quantity in cathode rays. This established the nature of β rays as electrons.

While α and γ rays were emitted according to spectral lines, β rays were found by James Chadwick [1] (and later confirmed by Ellis and Wooster) to be emitted in a continuous energy spectrum. This observation seemed at the time to be inconsistent with the well established principle of conservation of energy. Niels Bohr went as far

as proposing that energy was only conserved statistically, though this too was in disagreement with the observation of an upper limit in the energy spectrum of β decay [2].

2.1.2. Proposal and observation of the neutrino

In 1930 Wolfgang Pauli proposed, as a tentative solution for the problem of the continuous spectrum of β decay, a neutral particle which interacted only weakly and so would have gone undetected in previous experiments. The emission of this particle in addition to the electron in β decays would explain the missing energy in the electron spectrum [3].

By 1934 Enrico Fermi had incorporated the neutrino in the first successful description of β decay by extending Dirac's model of the electromagnetic interaction [4]. This theory also described other weak processes such as pion decay. It was, however ultra-violet divergent and as such it was seen as a useful effective theory which predicted low energy phenomena well but was unlikely to do so at higher energy scales.

Neutrinos remained a hypothetical construct until 1956 when Reines and Cowan detected these particles by placing a 200 litre CdCl_2 -loaded water detector in the vicinity of a research reactor at the Savannah River Site [5].

2.1.3. Parity violation in weak interactions

Two other noteworthy discoveries were made in the 1950s which are important to understand the way in which neutrinos (and the weak interaction) were incorporated in the SM of particle physics.

In 1956 Chien-Shiung Wu observed parity violation in weak interaction by measuring the angular distribution of nuclear de-excitation photons and β decay electrons in ^{60}Co while changing the spin orientation of the parent nuclei [6]. A bias was found in the angular distribution of the electrons when compared to the photons. Up to then all interactions had been assumed to be invariant under parity transformations.

Lee and Yang had proposed the violation of this principle as a tentative solution to the so called θ - τ puzzle [7], where two particles were observed to be identical in every aspect except for their parity. This could be explained if the weak interaction was not invariant under the symmetry and hence parity was not a conserved quantity.

The other experiment which proved fundamental for the understanding of neutrino interactions was the measurement of the helicity of neutrinos emitted in electron capture decays of $^{152\text{m}}\text{Eu}$. In 1958 Maurice Goldhaber demonstrated that all neutrinos emitted in the $^{152\text{m}}\text{Eu}$ to $^{152}\text{Sm}^*$ were left-handed by measuring the polarisation of de-excitation photons in decays where the photon and the neutrino had been emitted back-to-back [8].

These two observations led to the SM description of neutrinos as massless particles and the weak interaction as maximally parity-violating.

2.1.4. Neutrino flavour

The experiments detailed above gave the fundamental picture of neutrinos that was incorporated into the SM. All of them relate to neutrinos produced in association to electrons (ν_e). Given the existence of other charged leptons (the μ was discovered in 1936 and the τ in 1975 [9, 10]) neutrino flavours associated with these were expected.

Indeed the existence of the ν_μ was confirmed by the observation of μ tracks produced in charged current reactions in a spark chamber placed in the first accelerator neutrino beam ever produced [11]. This work was done in 1962 by Lederman, Schwartz and Steinberger.

The discovery of the ν_τ happened only much later, in the year 2000 [12]. In the DONUT experiment, protons accelerated to 800 GeV in the Tevatron were aimed at a tungsten alloy target, producing a neutrino beam with 3% ν_τ . Neutrino interactions were registered in a nuclear emulsion target and ν_τ interactions were identified by selecting tracks with a kink after a few millimeters, a signature of τ decay.

A further constraint on the number of neutrino flavours came from precision measurements of the Z decay width at LEP [13]. Comparing the width predicted by the SM to the observed one, the number of invisible (neutrino) decay modes can be inferred (Figure 2.1). The results agree with three neutrino flavours. This

measurement applies only to neutrino flavours which interact with the Z boson and with a mass smaller than $\frac{m_Z}{2}$. Heavy neutrinos ($m_\nu > 45$ GeV) or neutrinos which do not interact weakly (sterile) are not ruled out.

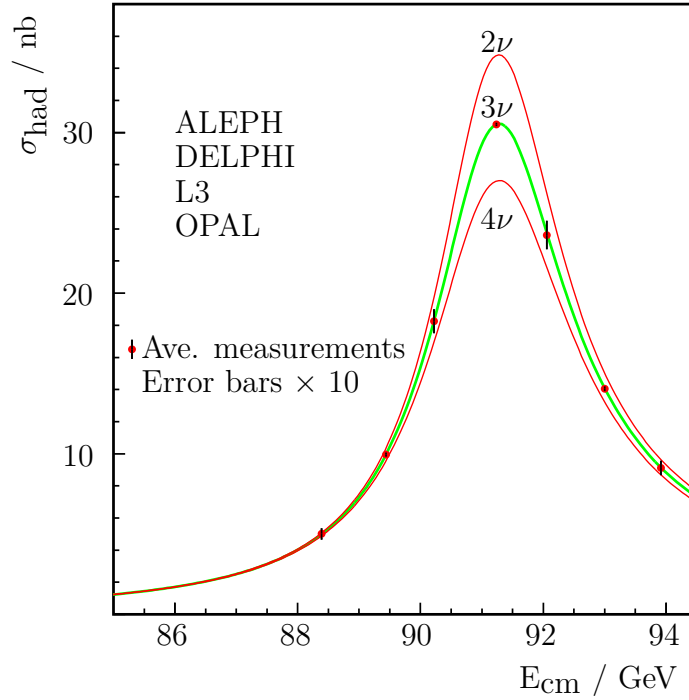
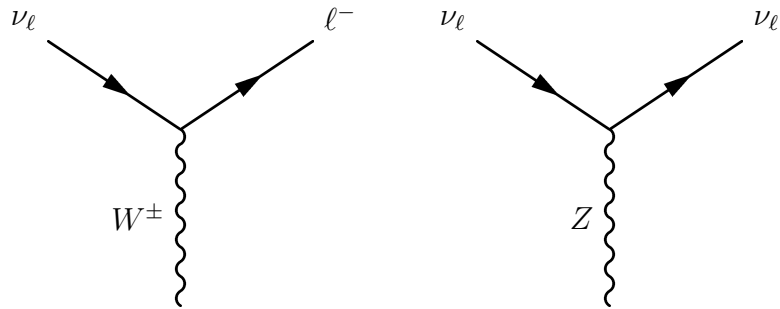


Figure 2.1.: Measurement of the hadronic cross-section at the Z mass pole by the LEP experiments [13].

The observations described above provide the setting to how neutrinos were described in the SM. More recent observations have deviated from the SM description. These will be detailed in section 2.3 of this thesis.

2.2. Neutrinos in the SM

In the SM, weak processes occur via the exchange of the massive vector bosons W^\pm and Z [14]. At low exchanges of momentum (compared to the boson masses: $m_W \approx 80$ GeV, $m_Z \approx 91$ GeV) these interactions approximate Fermi's four-fermion contact interaction. The possible reactions involving neutrinos in the SM are shown in Figure 2.2.



(a) Charged current vertex.

(b) Neutral current vertex.

Figure 2.2.: Standard Model vertices involving neutrinos.

Neutrinos can be detected by scattering reactions off quarks in nuclei or atomic electrons. Four different processes can occur, either through flavour-blind neutral currents or through flavour-changing charged currents (Fig. 2.3). Neutrino interactions with detector materials are inferred from the appearance of charged leptons with no leading tracks (charged currents) or from nuclear or electron recoil signals (neutral currents).

The parity violating character of the weak interaction is accounted for in the SM by the vector minus axial-vector (V-A) nature of the Lagrangian. This violates parity maximally in all neutrino interactions. Since only left-handed neutrinos (and right handed anti-neutrinos) are observed in nature, neutrinos are assumed to be massless in the SM.

It is now known that this description of neutrinos is partially incorrect given the observation of oscillations between neutrino flavour states. This is the first observation in particle physics that does not conform to the SM.

2.3. Neutrino oscillations

Neutrino oscillations were first proposed by Bruno Pontecorvo in 1957 [15]. In an analogy with neutral kaon mixing ($K_0 \leftrightarrow \bar{K}_0$, observed in 1956), Pontecorvo suggested that if the two-component description of neutrinos was not correct they could oscillate between the neutrino and anti-neutrino state. Although this idea proved observationally insignificant given the parity violation in weak interactions

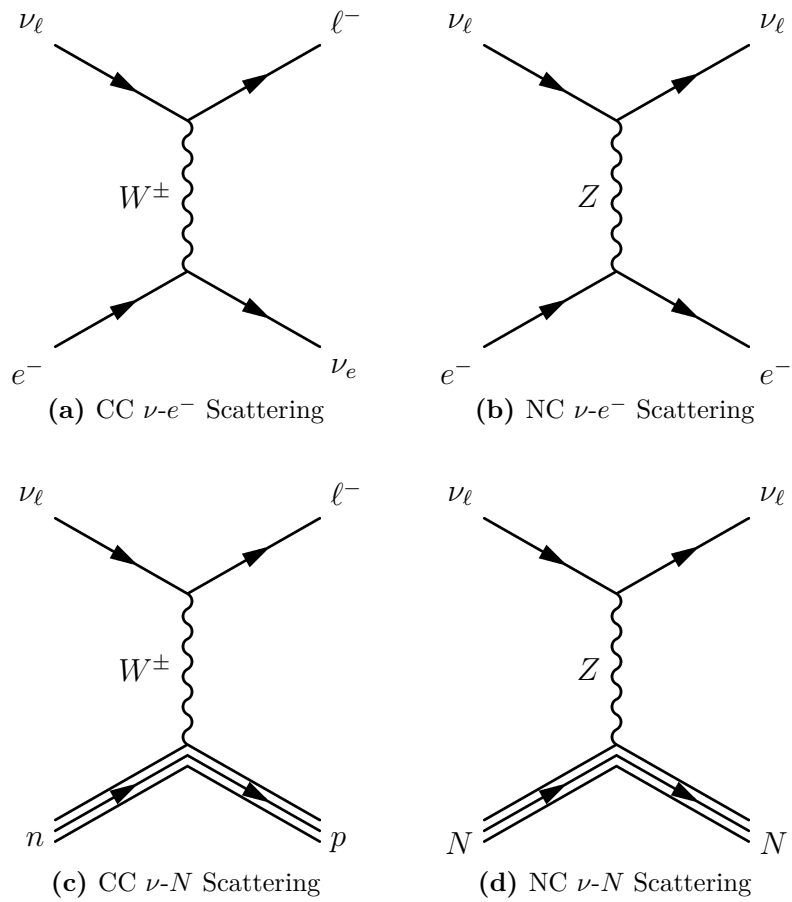


Figure 2.3.: Neutrino interactions with matter: charged and neutral current scattering off nucleons (elastic) or atomic electrons.

and the smallness of neutrino masses, it was a useful contribution to the solution of the solar neutrino puzzle.

2.3.1. The solar neutrino anomaly

In the late 1960s John Bahcall and Ray Davis set up a radiochemical experiment in the Homestake mine in South Dakota to measure the flux of ν_e produced by reactions in the Sun [16]. The experiment consisted of a large vessel filled with a chlorine-rich fluid. Neutrinos interacted with the chlorine nuclei via the reaction



The argon gas was extracted from the vessel and the amount of radioactive ${}^{37}\text{Ar}$ was measured in a proportional counter. The results revealed a significant deficit in the flux of solar ν_e predicted by the Standard Solar Model. This discrepancy was later confirmed by the GALLEX [17] and SAGE [18] experiments which used similar techniques with ${}^{71}\text{Ga}$ as a target.

Neutrino flavour oscillations were proposed as a solution to the solar neutrino anomaly [19,20]. Given that the experiments mentioned above were sensitive only to ν_e , oscillations in neutrino flavour ($\nu_e \rightarrow \nu_\alpha$, $\alpha = \nu_\mu, \nu_\tau$) could explain the observed discrepancy.

This hypothesis was confirmed in 2001 by the SNO experiment [21], which consisted of a heavy water Čerenkov detector. Both neutral and charged current reactions between neutrinos and deuterium nuclei or atomic electrons were detectable, providing a handle on neutrino flavour:

$$\nu_e + d \rightarrow p + p + e^-,$$

$$\nu_\ell + d \rightarrow p + n + \nu_\ell,$$

$$\nu_\ell + e^- \rightarrow \nu_\ell + e^-.$$

Additional evidence for neutrino oscillations had been obtained a few years earlier with atmospheric neutrino data. Neutrinos produced by cosmic ray interactions in the atmosphere have a wide energy spectrum up to 10 GeV. Unlike solar neutrinos, these have sufficient energy for muons to be produced in charged current reactions. Super-Kamiokande is a large water Čerenkov detector which measured the ν_e and ν_μ

composition of the atmospheric neutrino flux, again observing a discrepancy which could be explained by neutrino flavour oscillations [22].

Following these results, it became clear in the 2000s that neutrino oscillations occurred and so neutrinos were massive particles.

2.3.2. Neutrino mixing

The mixing between neutrino flavour and mass states that gives rise to oscillation phenomena can be incorporated into the SM in an analogous way to mixing in the quark sector. A mixing matrix relates the neutrino flavour states with the mass states:

$$|\nu_\alpha\rangle = U_{\alpha j}^* |\nu_j\rangle, \quad (2.1)$$

where α are the neutrino flavour eigenstates (e , μ and τ) and j the mass eigenstates with masses m_1 , m_2 and m_3 . This matrix is unitary and it is commonly referred to as the Pontecorvo-Maki-Nakagawa-Sakata (PMNS) matrix [19]. It is useful to parametrise it in terms of three angles and three phases:

$$U = \begin{pmatrix} 1 & 0 & 0 \\ 0 & c_{23} & s_{23} \\ 0 & -s_{23} & c_{23} \end{pmatrix} \begin{pmatrix} c_{13} & 0 & s_{13}e^{-i\delta} \\ 0 & 1 & 0 \\ -s_{13}e^{i\delta} & 0 & c_{13} \end{pmatrix} \begin{pmatrix} c_{12} & s_{12} & 0 \\ -s_{12} & c_{12} & 0 \\ 0 & 0 & 1 \end{pmatrix} D_M, \quad (2.2)$$

$$D_M = \begin{pmatrix} 1 & 0 & 0 \\ 0 & e^{i\alpha} & 0 \\ 0 & 0 & e^{i\beta} \end{pmatrix}, \quad (2.3)$$

where $c_{ij} = \cos(\theta_{ij})$, $s_{ij} = \sin(\theta_{ij})$, θ_{ij} are angles which quantify the mixing between states i and j , δ is the CP-violating Dirac phase, and α , β are two Majorana phases. The latter two parameters only have physical meaning if neutrinos are Majorana particles, while the others are accessible to oscillation experiments.

The probability of detecting a neutrino produced as flavour ν_α as flavour ν_β is measured in oscillation experiments. This probability can be obtained by solving the Schrödinger equation for the mass eigenstates in the rest frame of the neutrino¹ [23], giving:

$$P(\nu_\alpha \rightarrow \nu_\beta) = \left| \sum_i U_{\alpha i}^* e^{-im_i^2 \frac{L}{2E}} U_{\beta i} \right|^2, \quad (2.4)$$

where U_{ij} is the matrix described above, m_i the masses of the mass eigenstates, E the energy and L the distance travelled by the neutrino (L/E representing proper time for neutrinos travelling close to the speed of light).

In a simplified two-flavour scenario, the oscillation probability reduces to

$$P(\nu_\alpha \rightarrow \nu_\beta) = \sin^2(2\theta_{ij}) \sin^2\left(\Delta m_{ij}^2 \frac{1.27L}{E}\right), \quad (2.5)$$

where θ_{ij} are the neutrino mixing angles as given in the parameterisation above, $\Delta m_{ij}^2 \equiv m_i^2 - m_j^2$ in eV^2 , L is given in km and E in GeV.

It is clear from the equation above that experiments designed to measure these probabilities are sensitive to the angles in the PMNS matrix as well as to the mass differences between the mass eigenstates.

2.3.3. Oscillations in matter

While the formalism described above is valid in vacuum, interactions with matter must be taken into account when neutrinos traverse high density regions such as the interior of the Sun or the Earth's crust [24, 25]. Astrophysical matter is composed of protons, neutrons and electrons. All neutrino flavours will interact with these through neutral currents and ν_e will experience charged current reactions with electrons.

The effect of neutral current interactions with matter cancels out in oscillation phenomena, but the coherent charged current scattering has measurable consequences. An effective potential term appears in the Hamiltonian which depends on the energy

¹Even though the time evolution of neutrino flavour is derived in the rest frame, the ultra-relativistic approximation is used when converting the kinematic quantities to the laboratory frame.

of the neutrino and the density of electrons in the material it traverses. Crucially, this potential has opposite sign for ν_e and $\bar{\nu}_e$.

The same oscillation formalism given in Section 2.3.2 can be used for oscillations in matter, provided the mass-squared difference and mixing angle are replaced by effective parameters. These parameters now depend on the sign of the mass-squared difference between the vacuum mass eigenstates.

This effect is particularly relevant for neutrinos with energies of a few MeV originating in the Sun (*e.g.*, from ${}^8\text{B}$) as they traverse the very high density interior of the star on their way to detectors on Earth. At the centre of the Sun the matter effect dominates and neutrinos propagate in mass eigenstates of the effective potential. As the electron density slowly decreases towards the edge of the Sun the effective mass decreases until it coincides with the more massive vacuum eigenstate. This means that neutrinos will leave the Sun's surface in a pure ν_2 eigenstate which does not change as neutrinos traverse the distance between the Sun and the Earth. Solar neutrinos with energies of a few MeV interacting in detectors on the Earth are thus in a pure ν_2 state [23].

2.3.4. Oscillation parameters

In addition to the solar and atmospheric neutrino experiments described in Section 2.3.1, reactor and accelerator based experiments have constrained the parameters in the PMNS matrix. The three θ_{ij} angles have been measured and two distinct Δm^2 have been observed², which is consistent with the three-neutrino picture. The current best fit values for these parameters are listed in Table 2.1.

The CP-violating phase δ is yet to be constrained, but given that all mixing angles have been measured to have finite values this parameter will be accessible to oscillation experiments [29, 30].

²There are hints of a third, larger, Δm^2 which would imply the existence of a fourth, sterile neutrino [26]. These remain unconfirmed [27].

Parameter	Value ($\pm 1\sigma$)
Δm_{21}^2	$7.54_{-0.22}^{+0.26} \times 10^{-5} \text{ eV}^2$
$ \Delta m^2 $	$2.43_{-0.10}^{+0.06} \times 10^{-3} \text{ eV}^2$
$\sin^2(\theta_{12})$	$0.307_{-0.016}^{+0.018}$
$\sin^2(\theta_{23})$	$0.386_{-0.021}^{+0.024}$
$\sin^2(\theta_{13})$	0.0241 ± 0.0025

Table 2.1.: Best fit oscillation parameters assuming normal hierarchy [28].

2.3.5. Mass hierarchy

It is apparent in Equation 2.4 that, to first order, oscillation experiments are sensitive only to the magnitude of the mass-squared differences, but not their sign. This presents a potential ambiguity in the ordering of the mass states. The fact that charged current interactions with matter affect ν_e and not other neutrino flavours provides a handle on this ambiguity.

The strong matter effects felt by neutrinos originating from the Sun described in Section 2.3.3 constrain the sign of Δm_{21}^2 .

The sign of the larger Δm^2 is so far unconstrained, allowing for two possible scenarios. In the normal hierarchy, the mass eigenstate with the largest ν_e contribution (ν_1) has the lowest mass followed by ν_2 and ν_3 . This would be analogous to the charged lepton masses, where the electron has the lowest mass and the smallest mass splitting is between the two lighter particles. Alternatively, the inverted hierarchy scenario has ν_3 as the lightest state followed by ν_1 and ν_2 (Figure 2.4).

The mass hierarchy ambiguity is likely to be resolved in future oscillation experiments by exploiting the matter effect described in Section 2.3.3 [29, 30].

2.4. Neutrino Mass

Given the unambiguous evidence for neutrino mass provided by oscillation phenomena, perhaps the most interesting open question in neutrino physics is how this mass can be added to the SM formalism.

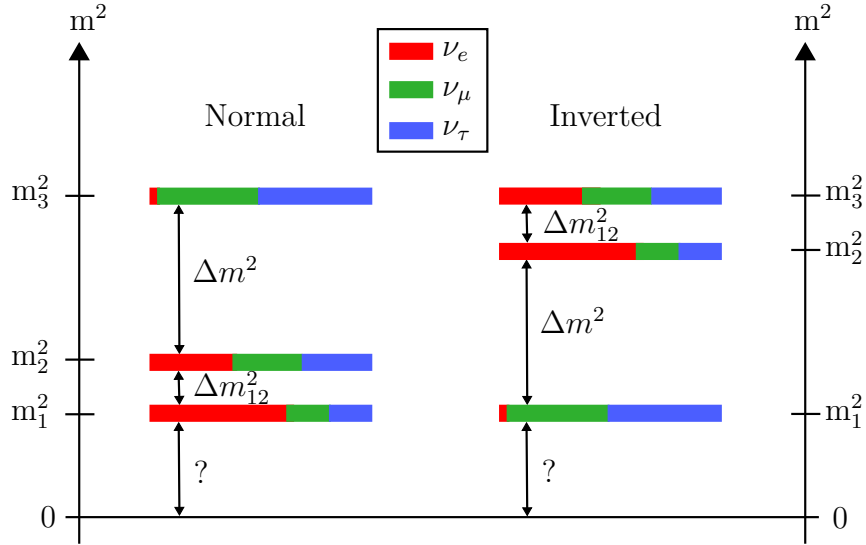


Figure 2.4.: Normal and inverted scenarios for the neutrino mass spectrum [31].

This is particularly interesting because, being electrically neutral, neutrinos are unique among the fundamental particles. The only distinguishing feature between a neutrino and an anti-neutrino in the SM is the lepton number L , defined as $L = +1$ for neutrinos and negatively charged leptons, and $L = -1$ for anti-neutrinos and positively charged leptons. This quantity is conserved in the SM; however, it is not associated to any fundamental symmetry in the theory, and as such there are no strong reasons to uphold this principle. The treatment of this subject in the next sections follows the one in [23].

2.4.1. Dirac mass term

In the SM description neutrinos are massless and so right handed neutrino fields have no physical meaning and are left out of the theory. It would seem natural to add neutrino mass terms to the Lagrangian analogous to those of the charged leptons, *i.e.*, in an L -conserving way. For this, a non-interacting right-handed neutrino field must be postulated:

$$\mathcal{L} = -m_D \bar{\nu}_L \nu_R + h.c. , \quad (2.6)$$

where m_D represents the Yukawa coupling to the Higgs field.

One problem presented by this scenario is that an unnaturally small coupling to the Higgs field would be required to generate the very small observed neutrino masses.

2.4.2. Majorana mass term

It should be noted that the right handed neutrino field postulated above has no charge or weak isospin. Apart from L conservation, there is no reason why a mass term of the form

$$\mathcal{L} = -m_M \bar{\nu}_R^c \nu_R + h.c. , \quad (2.7)$$

$$\nu_R^c = i\gamma^2 \nu_R^* , \quad (2.8)$$

should not be added to the Lagrangian, as it conforms to all of the SM fundamental symmetries.

Here we used only one field to build the mass term. This mass term violates L , mixing ν with $\bar{\nu}$ and consequently making the neutrino and anti-neutrino the same particle. Particles that obey this condition are called Majorana particles after Ettore Majorana, who proposed this treatment of neutral particles in 1936 [32].

Right handed neutrino fields are not the only way of adding neutrino mass to the SM Lagrangian. A model with a Higgs triplet with hypercharge $Y = +2$ would allow for mass terms of the form given in Equation 2.7 to be built out of left-handed fields without violating weak isospin, a well motivated conserved quantity [33]. Whichever the case, the existence of neutrino masses requires new physics beyond the SM.

2.4.3. See-saw mechanism

The most general mass term that can be written for neutrinos combines the two mass terms defined above:

$$\mathcal{L}_{\text{General}} = -\frac{m_D}{2} (\bar{\nu}_L \nu_R + \bar{\nu}_R \nu_L) - \frac{m_M}{2} \bar{\nu}_R^c \nu_R \quad (2.9)$$

$$= -\frac{1}{2} \begin{pmatrix} \bar{\nu}_L & \bar{\nu}_R^c \end{pmatrix} \mathcal{M} \begin{pmatrix} \nu_L^c \\ \nu_R \end{pmatrix}, \quad (2.10)$$

where \mathcal{M} is

$$\mathcal{M} = \begin{pmatrix} 0 & m_D \\ m_D & m_M \end{pmatrix}. \quad (2.11)$$

The neutrino states in the above expressions are weak eigenstates. To find the neutrino mass states \mathcal{M} must be diagonalised, yielding the eigenvalues:

$$m_{1,2} = \frac{1}{2} m_M \pm \frac{1}{2} \sqrt{m_M^2 + 4m_D^2}. \quad (2.12)$$

This result gives a method for generating the very small neutrino masses we observe. If we set m_M at a scale where new physics might be expected, such as somewhere below the GUT scale $m_M \leq \Lambda_{\text{GUT}}$ and m_D at the scale of the charged lepton masses we get $m_M \gg m_D$, and so:

$$m_1 \approx m_M \quad (2.13)$$

$$m_2 \approx \frac{m_D^2}{m_M}. \quad (2.14)$$

We retrieve two neutrino masses, one of which is naturally made small by the presence of an as yet unobserved very massive state. We can express these states in terms of the fields added to the theory:

$$\nu_1 \approx (\nu_L + \nu_L^c) + \frac{m_D}{m_M} (\nu_R + \nu_R^c) \quad (2.15)$$

$$\nu_2 \approx (\nu_R + \nu_R^c) + \frac{m_D}{m_M} (\nu_L + \nu_L^c). \quad (2.16)$$

We are left with a light neutrino mostly made of the fields which interact in the SM Lagrangian and a heavy neutrino mostly made of sterile fields.

While Majorana mass terms still require new physics (in the case described above sterile neutrino fields) they do provide an elegant solution to the problem of the smallness of neutrino masses.

It should be pointed out that other see-saw mechanisms exist which require new physics of the type alluded to at the end of Section 2.4.2. All these mechanisms require Majorana mass terms.

2.5. Constraints on neutrino mass

We now have a detailed knowledge of the mixing between neutrino mass and weak eigenstates, including the magnitude of the two squared-mass splittings. Even though neutrino oscillation experiments are not sensitive to the absolute mass scale of neutrinos, they provide a lower bound in the form of the largest mass splitting: at least one of the neutrino masses must be as large as the largest mass splitting ($\sqrt{\Delta m^2} = 49$ meV).

There are three independent experimental methods which give upper bounds to the neutrino masses. The only model independent constraint comes from the measurement of the electron energy spectrum in tritium β decay. Provided that neutrinos are Majorana particles, $0\nu\beta\beta$ gives one of the most stringent constraints on neutrino mass. Cosmological measurements can provide an upper limit on the neutrino mass, however it depends on assumptions of the cosmological models.

2.5.1. Beta decay of tritium

The most direct limits on neutrino masses are obtained by measuring the electron energy spectral shape in β decays. The effect of a finite neutrino mass can be observed via a change in the energy available to the emitted electron compared to the massless case (Figure 2.5). Nuclei which undergo β decays in which the difference between the masses of the parent and daughter atoms (Q-value) is small are suitable

for this type of measurement: the effect of a small neutrino mass will lead to a larger relative change in the measured electron spectrum.

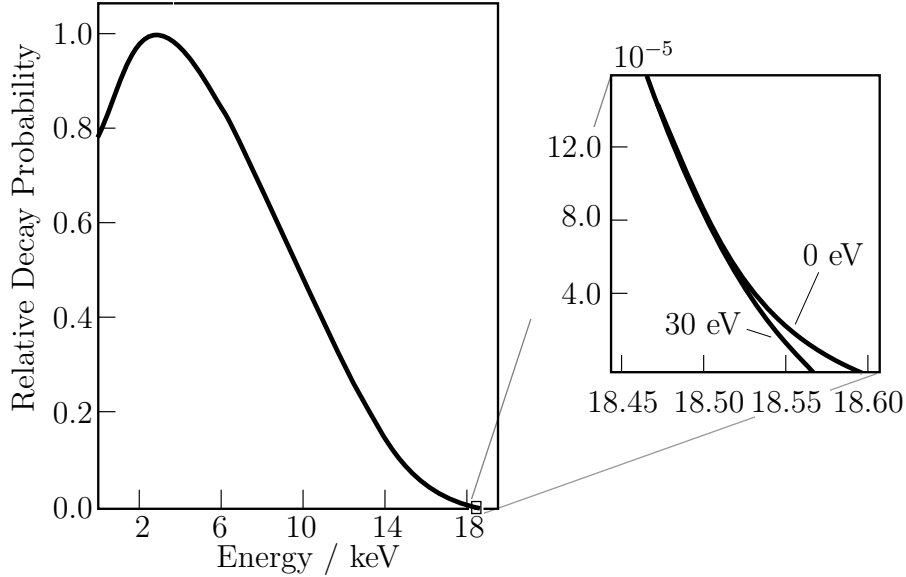


Figure 2.5.: Electron energy spectrum in the β decay of tritium, showing the effect of an exaggerated neutrino mass [34].

Two of the lowest Q-value β decaying isotopes known are ^{115}In and ^{187}Rh , with Q-values of 0.16 and 2.47 keV, respectively. However, these decays have very long half-lives that limit the sensitivity of potential experiments. There are also theoretical uncertainties in the calculation of the electron final states [35, 36].

The best limits on neutrino mass using this method come from tritium decay. Tritium is an isotope of hydrogen which undergoes β decay with a Q-value of 18.6 keV:



This decay has a short enough half-life (12.3 years) and the simple electronic structure of the intervening atoms allows for precise calculations yielding small systematic effects on the mass measurement.

Experiments of this type are sensitive to the average value of the mass states of the $\bar{\nu}_e$ produced in the decay. This is given by the sum over the PMNS matrix:

$$\langle m_\beta \rangle^2 = \sum_i |U_{ei}^2| m_i^2. \quad (2.18)$$

The current upper limit on $\langle m_\beta \rangle$ was obtained by the Troitsk [37] and Mainz [38] experiments. A combination of the results of the two experiments constrains $\langle m_\beta \rangle$ to be smaller than 2 eV (95% CL).

KATRIN is an experiment built on the same technology as the two experiments mentioned above which is expected to be sensitive to a $\langle m_\beta \rangle$ of 0.2 eV (90% CL) [39]. While an unpractically large spectrometer would make a further improvement on sensitivity unfeasible with the KATRIN technique, alternative β -decay end-point measurement techniques are currently being developed which might provide stricter constraints in the future. Two examples of this are the bolometric measurement of the β -decay of ^{187}Rh proposed by the MARE collaboration [40], and Project 8, which aims to study the β -decay of tritium by measuring the cyclotron radiation of the emitted electrons as they travel in a magnetic field [41].

2.5.2. Cosmology

Another handle on neutrino masses is provided by cosmological observations. The hot big bang model predicts a sea of relic neutrinos slightly smaller in number density than the cosmic microwave background (CMB). These cosmic neutrinos are yet to be observed. A combination of fits over a number of cosmological observables provide constraints on the sum of neutrino masses ($\sum_i m_i$).

One of these constraints comes from measurements of the power spectrum of the CMB. By combining CMB measurements with other cosmological observables it is possible to limit $\sum_i m_i$ to 0.44 eV (95% CL) [42]. Another constraint arises from probing galaxy clustering through photometric galaxy redshift surveys. These are sensitive to neutrino mass since formation of structures in the early universe is suppressed by free streaming neutrinos. A combination of galaxy clustering data and CMB measurements yields an upper limit on $\sum_i m_i$ of 0.28 eV (95% CL) or higher, depending on assumed cosmological parameters [43].

2.5.3. Neutrinoless double- β decay

If neutrinos are Majorana particles, neutrinoless double- β decay ($0\nu\beta\beta$) can occur. This decay mode will be discussed in more detail in Chapter 3 of this thesis. If

the mass mechanism dominates this decay, its rate will have a dependence on the effective neutrino mass:

$$\langle m_{\beta\beta} \rangle = \left| \sum_i U_{ei}^2 m_i \right|. \quad (2.19)$$

The current best limit on this quantity is provided by a combination of the KamLAND-Zen and EXO-200 experiments' searches for the double- β decay of ^{136}Xe . The limit is set at $\langle m_{\beta\beta} \rangle < 0.12 - 0.25$ eV (90% CL) [44], with the range reflecting the choice of Nuclear Matrix Element (NME) used.

It should be emphasised that limits on neutrino mass from $0\nu\beta\beta$ are only valid if neutrinos are Majorana particles, otherwise no relation between limits on the decay half-life to neutrino mass may be drawn.

A summary of the constraints on the mass of neutrinos from the three sources described above is given in Table 2.2.

Parameter	Value	Source
$\langle m_{\beta} \rangle$	< 2 eV (95% CL)	Tritium decay [37, 38]
$\sum_i m_i$	$< 0.28 - 0.44$ eV (95% CL)	Cosmology [42, 43]
$\langle m_{\beta\beta} \rangle$	$< 0.12 - 0.25$ eV (90% CL)	$0\nu\beta\beta$ [44]
$\max(m_i)$	> 0.05 eV (68% CL)	Oscillations [28]

Table 2.2.: Current limits on neutrino mass.

2.6. Summary and outlook

A detailed knowledge of neutrino mixing parameters has been attained and is summarised in Table 2.1. Two important parameters are yet to be constrained by experiment, namely the hierarchy of the neutrino mass spectrum, and the CP-violating phase δ . The next generation of oscillation experiments have as their main objectives the measurement of these parameters.

The mass hierarchy is of particular importance to the determination of the nature of neutrinos, and so also to the determination of their absolute mass scale from

$0\nu\beta\beta$. The relation of the effective mass constrained by $0\nu\beta\beta$ with the mass of the lightest neutrino is shown in Figure 2.6 together with the constraints from $0\nu\beta\beta$ and cosmological observations. The width of the allowed regions for each neutrino mass hierarchy hypothesis is due to the unknown CP-violating phases.

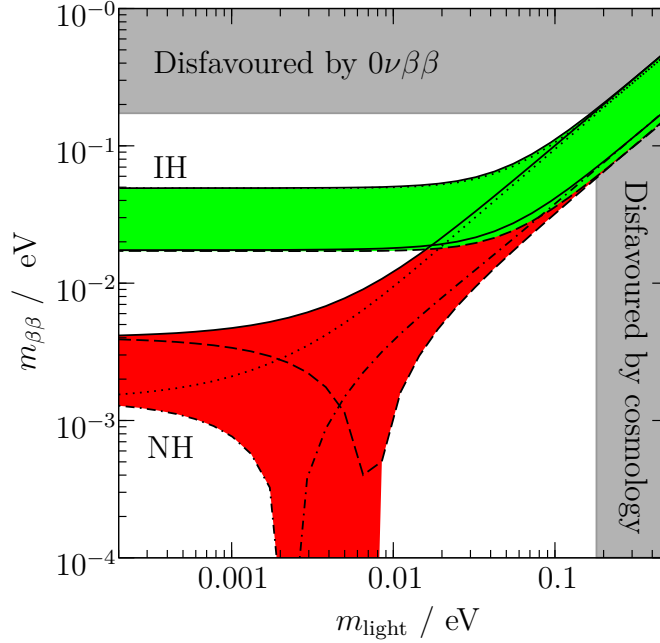


Figure 2.6.: Effective $0\nu\beta\beta$ mass against smallest neutrino mass [31] (adapted from [45]). The parameter space allowed for the normal hierarchy is shown in red and for the inverted hierarchy in green.

The next generation of $0\nu\beta\beta$ experiments is expected to be sensitive to the region allowed by the inverted hierarchy. If the neutrino mass spectrum is established to be inverted, a conclusive determination of the nature of neutrinos might be attained by next or next-to-next generation experiments.

In the case that the mass spectrum is determined to be normal the nature of neutrinos might remain elusive, though studies show that it might be possible to build a detector to probe $0\nu\beta\beta$ to the level as low as $\langle m_{\beta\beta} \rangle = 2.5$ meV at a reasonable cost in the foreseeable future [46].

Chapter 3.

Double- β decay

Double- β decay is a very rare form of radioactive decay, being a low-energy second-order weak interaction process. The process consists of two β decays (Section 3.1) occurring at once. One mode of the decay is allowed by the SM, with two neutrinos being emitted with the two electrons (Section 3.2). This process has been observed in several nuclei. Modes where the decay happens without the emission of the neutrinos are predicted by several models beyond the SM, and generally violate the lepton number by two units (Section 3.3). One major difficulty in the prediction of double- β decay rates is the calculation of the nuclear matrix elements. The different approaches used to perform these calculations are summarised in Section 3.4.

3.1. β decay

β decay is a common radioactive transition which involves the change of flavour of a quark in a nucleon such that a neutron is transformed into a proton or vice-versa resulting in the transmutation to a different element. This transformation occurs via the weak charged current and always results in the emission of a neutrino or an anti-neutrino. The three ways in which this type of decay occurs are: β^- decay, where an electron is emitted; β^+ decay, with the emission of a positron; and electron capture (EC), with no emission of charged particles.

In β^- decay, a neutron is transformed into a proton, with the emission of one electron and one $\bar{\nu}_e$:

$$n \rightarrow p^+ + e^- + \bar{\nu}_e, \quad (3.1)$$

while in β^+ decay a proton is transformed into a neutron, with a positron and a ν_e being emitted:

$$p^+ \rightarrow n + e^+ + \nu_e. \quad (3.2)$$

EC decays differ from the two decays described above, in that the charged lepton is an electron captured from the atom's inner atomic orbitals rather than being emitted in the decay:

$$p^+ + e^- \rightarrow n + \nu_e. \quad (3.3)$$

The hole in the atom's inner shells created by the capture of the electron often results in X-rays or Auger electrons accompanying the decay as electrons in its higher energy orbitals transition to the lower levels to fill the vacancy. The similarity between the nucleonic part of this decay and that of the β^+ decay shown in Equation 3.2 results in EC decay occurring in every isotope which undergoes β^+ decay and in some cases where β^+ decay is energetically forbidden it can be the only decay mode of the isotope.

3.1.1. The semi-empirical mass formula

For β decays to occur the mass of the daughter isotope must be smaller than its parent's, as energy is required for the creation and emission of the leptons. Nuclear masses are described, to a good approximation, by the semi-empirical mass formula (SEMF) [47]:

$$M(A, Z) = Zm_p + (A - Z)m_n - E_B, \quad (3.4)$$

where A and Z are the atomic and mass numbers, respectively; m_p and m_n the masses of the proton and the neutron; and E_B is the binding energy of the nucleus,

given by:

$$E_B = a_V A - a_s A^{2/3} - a_c \frac{Z^2}{A^{1/3}} - a_A \frac{(A - 2Z)^2}{A} - \delta(A, Z). \quad (3.5)$$

The terms in the expression for the binding energy written above represent corrections to the simplistic value given by the first two terms in Equation 3.4. The correction terms are, by the order they are shown in Equation 3.5: the volume term; the surface term; the Coulomb term; the asymmetry term; and the pairing term. The latter term, which takes into account the pairing between the nucleons' spins is given by:

$$\delta(A, Z) = \begin{cases} -\frac{a_P}{A^{1/2}} & \text{even } Z \text{ and } A \\ 0 & \text{odd } A \\ +\frac{a_P}{A^{1/2}} & \text{odd } Z, \text{ even } A \end{cases}. \quad (3.6)$$

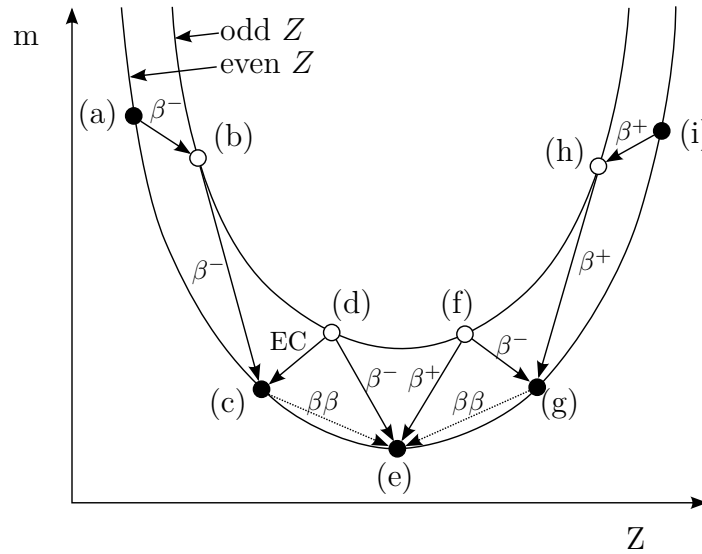


Figure 3.1.: Masses of even A nuclei, as described by the SEMF. Two parabolas are shown, one which gives the masses of odd Z nuclei (white circles) and the other for even Z nuclei (black circles). Examples of allowed decays are shown [31].

For nuclei with the same A , the masses obtained with the SEMF lie in parabolas as a function of Z , due to the Coulomb and asymmetry terms. Masses of nuclei with odd A are described by a single parabola, while in the case of even A nuclei, the

pairing term splits the masses into two parabolas, depending on whether Z is even or odd (Figure 3.1).

3.2. Two-neutrino double- β decay

In Figure 3.1 it is shown that some nuclei with even A and Z are stable against the β decays described above (*e.g.*, the nucleus labelled (c)). They can, however, undergo double- β decay: while a single β decay is forbidden by energy considerations, a process which changes Z by two units is allowed:

$$(Z, A) \rightarrow (Z, A + 2) + 2e^- + 2\bar{\nu}_e. \quad (3.7)$$

This process ($2\nu\beta\beta$), which occurs via a β^- decay to an intermediate, virtual nucleus followed by a β^- decay to the final state, was first described by Maria Goeppert-Mayer in 1935 [48]. The Feynman diagram for $2\nu\beta\beta$ is shown in Figure 3.2, where it is clear that the process is allowed by the SM, with no violation of its quantum numbers or non-standard vertices. Experiments designed to investigate double- β decay

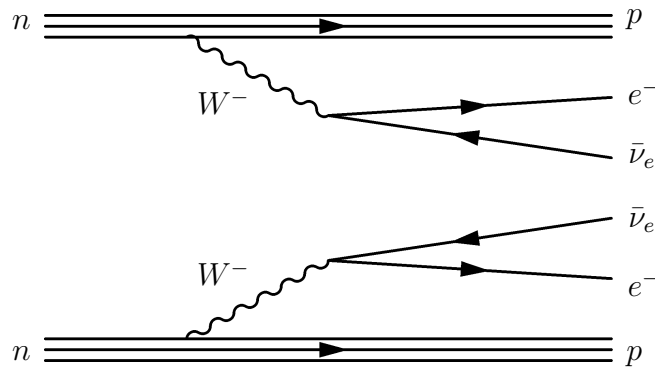


Figure 3.2.: Feynman diagram for the two-neutrino double- β decay.

measure, in general, the sum of the energies of the two electrons. Since part of the decay's energy is carried away by the undetected neutrinos, the sum of the electrons' energies is distributed over a continuous spectrum (Figure 3.5). The end-point of the spectrum is at the Q-value for the decay, defined as the energy available to the decay products:

$$Q_{\beta\beta} = M(A, Z) - M(A, Z + 2) - 2m_e. \quad (3.8)$$

The $2\nu\beta\beta$ transition rate is given by Fermi's golden rule:

$$\left(t_{2\nu}^{1/2}\right)^{-1} = G^{2\nu} g_A^4 |M^{2\nu}|^2, \quad (3.9)$$

where $t_{2\nu}^{1/2}$ is the decay's half-life, $G^{2\nu}$ is the phase-space factor, g_A^4 is the axial-vector coupling constant and $|M^{2\nu}|$ is the nuclear matrix element.

The phase space factor can be calculated exactly. These factors vary widely for different isotopes and in particular depend strongly on the transition's $Q_{\beta\beta}$, with [49]:

$$G^{2\nu} \propto Q_{\beta\beta}^{11}. \quad (3.10)$$

The nuclear matrix elements, however, present a difficult calculation problem, with different approximations giving a wide range of values. Measured half-lives of $2\nu\beta\beta$ are used to constrain effective nuclear model parameters used in the calculations. While this allows for improvements in the precision of calculations of the nuclear matrix elements for neutrinoless double- β decay, in general the relationship between the calculations for the two modes is not straightforward.

In the case of ^{48}Ca , the calculations are simpler compared to the other, heavier, double- β decay isotopes. While precise shell model descriptions of the ^{48}Ca nucleus are computationally accessible, having provided relatively accurate predictions of its energy levels [50], the choice of model for the effective interaction between nucleons results in a wide range of predictions. This is discussed in more detail in Section 8.4 of this thesis.

Other double- β decay modes exist in the SM, namely double- β^+ , double-EC and $\text{EC}\beta^+$. However, these modes have smaller Q-values and hence smaller transition amplitudes, and challenging final state topologies, making their observation difficult [49].

3.3. Neutrinoless double- β decay

In several beyond the SM theories, double- β decay can proceed without the emission of neutrinos:

$$(Z, A) \rightarrow (Z, A + 2) + 2e^- . \quad (3.11)$$

Such a process would violate lepton number (a SM accidental symmetry) by two units. While this in itself motivates $0\nu\beta\beta$ searches, the observation of neutrino masses through flavour oscillations coupled with a theoretical preference for the Majorana nature of the neutrino (Section 2.4.2) provide an ever stronger incentive for the investigation of this process: the existence of massive Majorana neutrinos would induce $0\nu\beta\beta$ via an exchange of neutrinos between the W bosons in the so called mass mechanism.

While the exchange of Majorana neutrinos is the most well motivated $0\nu\beta\beta$ mode, this decay is also predicted by R-parity violating (\hat{R}_p) supersymmetry and left-right symmetric extensions to the SM [45, 51].

Even though the Majorana nature of neutrinos does not appear to be, *a priori*, a requisite for $0\nu\beta\beta$ modes other than the mass mechanism, it has been demonstrated [33] that the existence of any $0\nu\beta\beta$ mode would imply an effective Majorana mass term, as shown in Figure 3.3. Generic estimates of the mass arising from such a mechanism result in masses too small to explain the neutrino mass splittings observed in oscillation experiments [45]. This reinforces the standard interpretation of $0\nu\beta\beta$ as being likely to be mediated by the exchange of massive Majorana neutrinos, if it occurs.

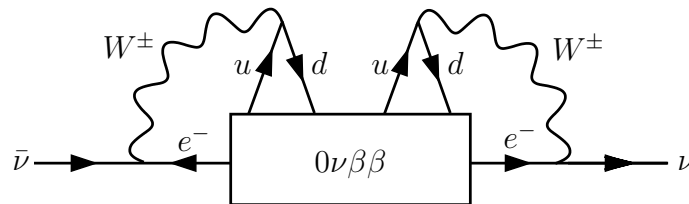


Figure 3.3.: Majorana mass term due to $0\nu\beta\beta$. A “black-box” $0\nu\beta\beta$ process is shown converting a $\bar{\nu}$ into a ν , generating a Majorana mass term [33].

Other non-standard modes of $0\nu\beta\beta$ occur in theories which predict massless (or very light) neutral particles (Majorons) that couple to neutrinos. In this case the decay involves the emission of one or more Majoron, with the kinematics of the electrons emitted in this decay being significantly different from those of the decay modes mentioned above [45, 52].

3.3.1. Mass mechanism

In the standard interpretation of $0\nu\beta\beta$, the decay proceeds through the exchange of light Majorana neutrinos, as shown in Figure 3.4. The decay rate for this process

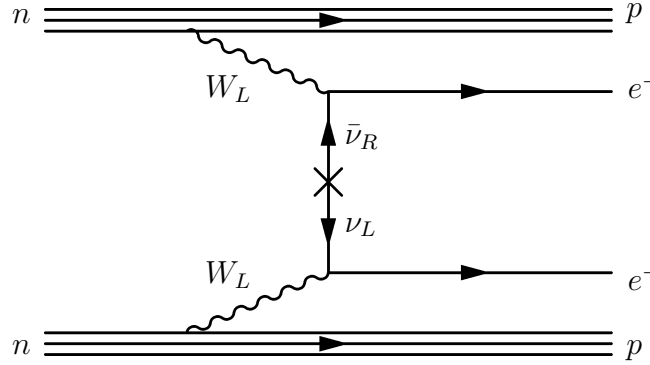


Figure 3.4.: Feynman diagram for the mass mechanism $0\nu\beta\beta$.

acquires a dependency on the effective mass of the exchanged neutrino due to the spin-flip required for coupling to the SM left-handed W :

$$\left(t_{0\nu}^{1/2}\right)^{-1} = G^{0\nu} g_A^4 \left|M^{0\nu}\right|^2 \langle m_{\beta\beta} \rangle^2, \quad (3.12)$$

where $G^{0\nu}$ and $|M^{0\nu}|$ are the phase space factor and nuclear matrix element, and the effective Majorana mass, $\langle m_{\beta\beta} \rangle$ is a sum of the neutrino masses weighted by the elements of the PMNS matrix, as given in Equation 2.19. The dependence of the phase space factor on $Q_{\beta\beta}$ is weaker for this decay mode compared to $2\nu\beta\beta$ [49]:

$$G^{0\nu} \propto Q_{\beta\beta}^5. \quad (3.13)$$

As with the case of $2\nu\beta\beta$, the phase space factor depends strongly on the isotope considered, with values spanning more than one order of magnitude, with ^{150}Nd

having the largest factor and ^{76}Ge the smallest [53]. The effect of this (and of differences in the nuclear matrix elements) on the sensitivity to $\langle m_{\beta\beta} \rangle$ is illustrated in Figure 3.8.

Due to the absence of neutrinos in the final state to carry away energy, the energies of the electrons emitted in the decay sum up to $Q_{\beta\beta}$, producing a sharp peak in the spectrum (Figure 3.5).

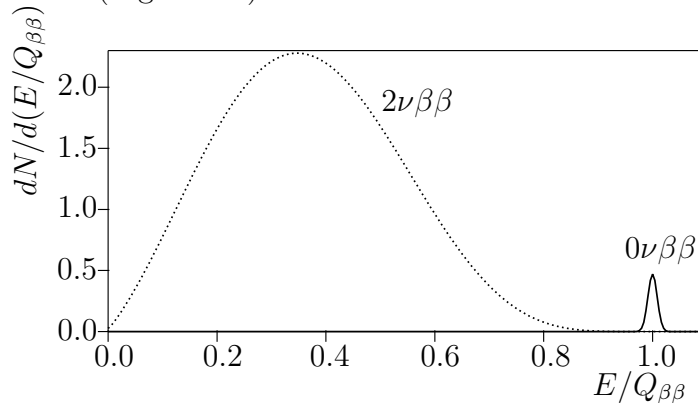


Figure 3.5.: Summed energy spectrum of double- β decay. The $0\nu\beta\beta$ mode is shown with an exaggerated rate of 1% of the $2\nu\beta\beta$ rate. Both spectra are smeared to mimic an energy resolution of 2% [54].

Extracting limits on the effective Majorana mass from experimental half-life limits requires the evaluation of the nuclear matrix elements. This is discussed in Section 3.4.

3.3.2. \mathcal{R}_p supersymmetry

To accommodate the very long experimental limits on the life-time of the proton [55], interactions in the minimal supersymmetric model conserve R-parity, defined as:

$$R_p = (-1)^{3B+L+2s}, \quad (3.14)$$

where B is the baryon number, L is the lepton number and s is the spin. This quantity takes the value 1 for SM particles and -1 for their supersymmetric partners.

The requirement that R_p is conserved in all interactions forbids lepton number violating processes. However, if R-parity is broken (\mathcal{R}_p), $0\nu\beta\beta$ can proceed, for example, via the exchange of a neutralino or a gluino, with the transition amplitude

governed by the trilinear coupling λ'_{111} [45]. The strictest limits on this coupling have been obtained in $0\nu\beta\beta$ searches [56]. This is discussed further in Section 8.5.

3.3.3. Right handed currents

In left-right symmetric models, proposed as an alternative to the maximally parity-violating $V - A$ structure of the weak interaction, $0\nu\beta\beta$ is possible without the neutrino spin-flip required in the mass mechanism. This decay mode is therefore not dependent on the neutrino mass, but on the couplings between the right- and left-handed fermions.

Two possibilities exist: the SM W might itself be a superposition of right-handed and left-handed states, governed by a mixing angle ϵ ; or a new (heavy) right-handed W' boson might exist [45].

In the first case, the rate of $0\nu\beta\beta$ depends on the $\langle\lambda\rangle$ parameter, which represents the coupling between right-handed quarks and right-handed leptons (Figure 3.6). This decay mode differs significantly from the other modes discussed here in that it produces a large asymmetry in the individual energies of the emitted electrons.

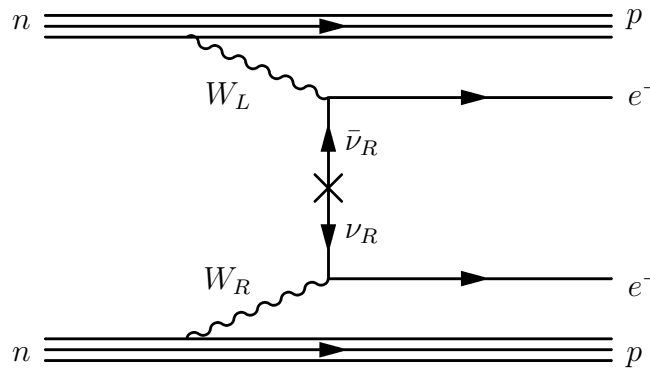


Figure 3.6.: Feynman diagram for the $\langle\lambda\rangle$ mode of $0\nu\beta\beta$ arising from left-right symmetric models.

The other $0\nu\beta\beta$ mode arising from left-right symmetric models is described by the $\langle\eta\rangle$ parameter, which is related to the coupling between left-handed quarks and right-handed leptons.

A more detailed discussion on the constraints on these models is given in Section 8.5.

3.3.4. Majoron emission

Majorons (χ^0) have been proposed as massless Goldstone bosons for theories where a $B - L$ symmetry is spontaneously broken. Most of these models predicted additional couplings to the Z boson and have thus been excluded by LEP measurements (Section 2.1.4). Due to the smallness of the neutrino masses, the surviving models require substantial fine tuning in order to have observational consequences. However, alternative models have been proposed where $0\nu\beta\beta$ occurs with the emission of one or two Majorons, where these particles are not required to be massless or Goldstone bosons and in some cases carry a non-zero L , resulting in lepton number conserving $0\nu\beta\beta$ [45, 52].

The kinematics of such decays are described in terms of a spectral index n , related to the phase-space factor by:

$$G^{0\nu\chi^0} \propto (Q_{\beta\beta} - E_{e_1} - E_{e_2})^n, \quad (3.15)$$

where E_{e_i} are the energies of the electrons.

The $0\nu\beta\beta$ mode with the emission of one Majoron with spectral index $n = 1$ is investigated in this thesis (Section 8.5):

$$(Z, A) \rightarrow (Z, A + 2) + 2e^- + \chi^0. \quad (3.16)$$

3.4. Nuclear matrix elements

To extract the physical parameters of interest from $0\nu\beta\beta$ searches, namely $\langle m_{\beta\beta} \rangle$ for the mass mechanism and the coupling strengths relevant for other mechanisms, the quantification of the nuclear matrix elements is necessary. The lack of other observables related to these amplitudes means that they must be calculated in the theoretical framework of nuclear structure. A precise knowledge of the nuclear

matrix elements is also important for the identification of the isotopes which are most suitable for constraining the parameters of interest.

Calculations of nuclear matrix elements generally consist of two parts: the calculation of the two-body transition matrix element for the two interacting nucleons; and the construction of multi-body wave functions for the initial, final and, in cases where the closure approximation is not used, intermediate (virtual) nuclei.

Given the complexity of such calculations, approximations and simplifications must be assumed, different choices of which result in a range of values for each nuclear matrix element. Five approaches have been developed to tackle these calculations [53]:

- the interacting shell model (ISM);
- the quasi-particle random phase approximation (QRPA);
- the interacting boson model (IBM);
- the projected Hartree-Fock-Bogolubov method (PHFB);
- the energy density functional method (EDF).

In the ISM a limited number of nuclear orbits are considered, but all correlations within the space are included. Calculations in the ISM framework tend to result in smaller matrix elements when compared to the other approximations. These calculations are only adequate for smaller nuclei such as ^{48}Ca as the computational power required for isotopes with larger valence spaces makes these calculations impractical and nuclear deformation is not well modelled. This approach has had success in predicting the nuclear energy levels in agreement with spectroscopy data [50].

The QRPA method is complementary to the ISM in that it is particularly suitable for larger nuclei. In this approach, calculations are performed over large valence spaces, but not all possible configurations are taken into account and the interactions between nucleons are approximated. This method depends on a number of free parameters that must be constrained elsewhere. In particular the determination of the particle-particle strength of the Hamiltonian g_{pp} from $2\nu\beta\beta$ measurements can be used to reduce the uncertainty on the $0\nu\beta\beta$ matrix element calculations.

The IBM approach is similar to the ISM. However, in this method the low-lying nuclear states are treated as bosons in states with $L = 0$ or 2 (s and d boson states, respectively). While the IBM and ISM methods are expected to produce the same results in the limit of spherical nuclei, calculations have resulted in disagreement between the two methods [53].

The PHFB method has the advantage of using few parameters for the calculation of both the $2\nu\beta\beta$ and the $0\nu\beta\beta$ matrix elements. This approach involves a simplification of the nuclear Hamiltonian in which only the quadrupole terms are taken into account and only neutron pairs with even angular momentum and positive parity are described. The EDF method is an improvement on the PHFB method in which the Gogny interaction [57] is used.

3.4.1. Comparison of calculations

A comparison between the matrix elements for 11 isotopes calculated with the methods outlined above is shown in Figure 3.7. The ISM calculations are shown to give similar results for all isotopes with the exception of ^{48}Ca , with the values being systematically smaller compared to other techniques. Even disregarding the ISM calculations for the heavier nuclei, the different methods give a wide range of results for most nuclei, with the possible exception of the Te isotopes where the calculations for the other four methods agree with each other. It should also be noted that given the dispersion of values for each isotope, it is not clear which isotopes have the most favourable nuclear matrix elements for $0\nu\beta\beta$ searches, with the transition amplitudes being heavily affected by differences in the phase space factors (Figure 3.8).

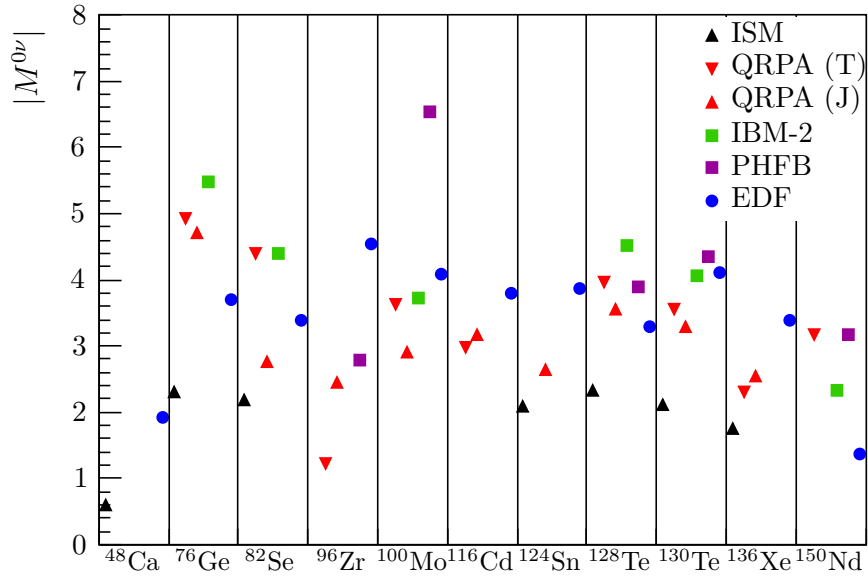


Figure 3.7.: Comparison between the nuclear matrix elements for 11 isotopes calculated in five different frameworks [31] (with nuclear matrix elements from [53]). Two QRPA sets calculations are given: one by the Tübingen group (T) and the other by the Jyväskylä group (J).

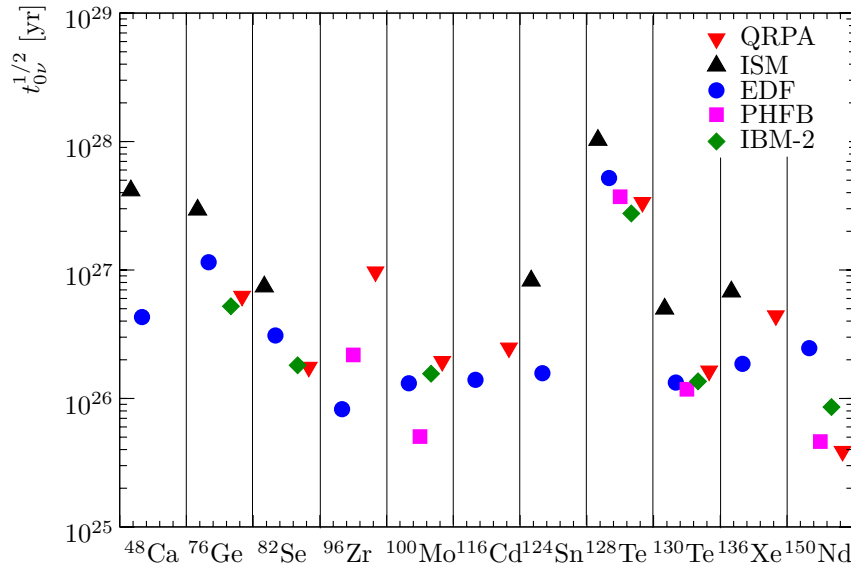


Figure 3.8.: Comparison between the $0\nu\beta\beta$ half-lives of 11 isotopes assuming an effective Majorana mass of $\langle m_{\beta\beta} \rangle = 50$ meV. The methods used for the nuclear matrix element calculations are given in the legend [53].

Chapter 4.

Double- β decay experiments and techniques

The experimental investigation of $0\nu\beta\beta$ is a rich field of research, with a wide range of complementary techniques employed to place increasingly stringent limits on the half-life of this as yet unobserved¹ process. Indirect detection experiments using radio and geochemical techniques have been performed. These experiments do not allow for discrimination between the $2\nu\beta\beta$ and $0\nu\beta\beta$ modes of the decay, being sensitive only to the combined decay rate [53]. The experimental techniques used in the direct detection of double- β decay processes are discussed in this chapter, with a brief overview of experiments using different technologies being given in Section 4.1 and experiments using ^{48}Ca as the source being described in Section 4.2. The current best double- β decay measurements are listed in Section 4.3.

The sensitivity to the $0\nu\beta\beta$ half-life can be estimated for a generic experiment [54]:

$$t_{0\nu}^{1/2} = \frac{4.16 \times 10^{26} \text{ yr}}{n_\sigma} \left(\frac{\varepsilon a M t}{W} \right) \sqrt{\frac{1}{N_b}}, \quad (4.1)$$

where:

- n_σ is the number of standard deviations corresponding to the exclusion CL ($n_\sigma = 1.64$ for 90% CL);
- ε is the signal detection efficiency;

¹The claim of observation of the $0\nu\beta\beta$ of ^{76}Ge [58] has been largely discredited [59] and is currently all but directly ruled out [44, 60, 61].

- a is the abundance of the double- β decay isotope;
- W is the molecular weight of the source material;
- $M t$ is the exposure of the source in kg yr;
- and N_b is the number of expected background events.

The equation above is derived under the assumption that the number of background events is distributed according to a Poisson distribution, with its uncertainty being given by $\sqrt{N_b}$.

For the half-life sensitivity of a double- β decay experiment to be maximised, each of the variables in Equation 4.1 must be considered.

The half-life sensitivity increases linearly with the signal detection efficiency. Double- β decay experiments can generally be categorised as having a homogeneous or heterogeneous design. The first refers to experiments in which the source is an integral part of the sensitive components of the detector, while in the latter designs the source is a separate part of the detector, independent of the sensitive components. Experiments of the homogeneous type in general have higher detection efficiency, with limiting factors on this parameter including, for example, the light attenuation in large scintillator detectors. Conversely, heterogeneous detectors tend to have lower efficiencies, due to energy losses in the non-sensitive source, or incomplete coverage of the source by the sensitive components.

The number of double- β isotope nuclei in an experiment is determined by the interplay of three factors: the source mass, the abundance of the isotope and its molar mass.

The mass of the source is the ultimate limit for the number of nuclei in an experiment, and therefore experiments aim to increase the source mass as much as possible. One negative consequence of a large source mass is that, in general, backgrounds will increase with the source mass. Experiments of the homogeneous type are more suitable for very large source masses, with proposed experiments aiming towards a tonne scale source [62–64].

Isotopes with a small molar mass allow for a large number of nuclei for a given source mass. Using such an isotope might help mitigate the problem of the increase in background counts associated to larger source masses. It should be noted, however,

that in terms of extracting the physics parameters of interest, such as $\langle m_{\beta\beta} \rangle$, the nuclear matrix elements and phase space factors must be taken into consideration when selecting the source isotope.

The last factor determining the number of nuclei in an experiment is the abundance. With the exception of ^{130}Te , the isotopes considered for double- β decay experiments occur with low natural abundances (Table 4.1). This requires the sources to be enriched in the isotope of interest. With the exception of ^{48}Ca , ^{96}Zr and ^{150}Nd , the isotopes can be enriched by means common in the nuclear industry, for example, by being synthesised into hexafluorides and processed in gas centrifuges. This allows for affordable enrichment at relatively large scales. It has been argued, however, that for possible future experiments aiming towards isotope masses of tens of tonnes (for probing the normal hierarchy parameter space) the costs related to enrichment would become prohibitive, in which case the use of ^{nat}Te stands out as a viable alternative [46]. The only method currently available to enrich the isotopes which cannot be enriched through centrifugation is electromagnetic separation. This method allows only for small amounts to be enriched at a time and is costly. Alternative means of enrichment are being investigated such as laser separation methods. The very small natural abundance of ^{48}Ca coupled with the lack of an affordable enrichment procedure makes the enrichment of this isotope particularly challenging.

Isotope	$Q_{\beta\beta}$ (keV)	Natural abundance (%)
^{48}Ca	4273.7	0.187
^{76}Ge	2039.1	7.8
^{82}Se	2995.5	9.2
^{96}Zr	3347.7	2.8
^{100}Mo	3035.5	9.6
^{116}Cd	2809.1	7.6
^{124}Sn	2287.7	5.6
^{130}Te	2530.3	34.5
^{136}Xe	2461.9	8.9
^{150}Nd	3367.3	5.6

Table 4.1.: $Q_{\beta\beta}$ and natural abundances for isotopes commonly considered for double- β decay experiments [45].

The other important parameter in Equation 4.1 is the expected number of background counts. In general, the background counts will increase linearly with the exposure ($N_b \propto M t$), making the half-life sensitivity proportional to the square root of the exposure ($t_{0\nu}^{1/2} \propto \sqrt{M t}$). If on the other hand the background expectation is too small for any events to occur due to backgrounds, or more generally, if the expected number of background events does not increase with the exposure, the relation is linear ($t_{0\nu}^{1/2} \propto M t$). It is therefore crucial to achieve the lowest possible rate of background counts in a double- β decay experiment.

The main background sources for double- β decay experiments are due to the decays of ^{214}Bi and ^{208}Tl , present in the uranium and thorium natural decay chains. A detailed discussion of these backgrounds is given in Chapter 7. Detector materials must be screened and chosen very carefully for their radiopurity to prevent these backgrounds. Contamination of the sources is particularly dangerous and source materials go through purification procedures to remove potential sources of background. Another important consideration is the use of isotopes with high $Q_{\beta\beta}$, such that the $0\nu\beta\beta$ peak occurs at energies higher than those of the naturally occurring backgrounds. In particular, sources with $Q_{\beta\beta}$ higher than the most energetic γ emission from ^{208}Tl (2.6 MeV) are preferred. Having the highest $Q_{\beta\beta}$, ^{48}Ca is a highly desirable source to this effect, as very low levels of background are expected in the region of its $0\nu\beta\beta$ peak.

Given that the $0\nu\beta\beta$ signal consists of a sharp peak at $Q_{\beta\beta}$, a good energy resolution is a powerful tool to reduce the number of background counts. By selecting a narrow energy window to measure the $0\nu\beta\beta$ peak a significant fraction of the more broadly distributed background can be rejected.

An additional contribution to the background level in double- β decay experiments has its origin in sources external to the detector. Experiments rely on passive and active forms of shielding to reduce these backgrounds. To mitigate the backgrounds due to cosmic rays, detectors are placed in underground laboratories, typically at depths of a few thousand meters of water equivalent. Dense shielding materials are placed around the detectors to absorb γ radiation, often coupled with neutron-moderating materials to prevent neutron activation of materials inside the detectors. Active shielding takes the form of detector components designed to detect crossing particles, such that events due to external backgrounds can be removed from analysis data sets.

In experiments which can identify event topologies, analysis techniques are used to greatly reduce the backgrounds, namely the selection of events with two electrons. Another technique which does not require the full reconstruction of event topologies is to use positional information to define fiducial regions in the innermost parts of the detector. Events of external origin will induce detector activity outside these regions, and therefore can be rejected. Analysis of pulse shapes in semiconductor experiments allows for discrimination between single-site and multiple-site interactions, which is used to reject γ backgrounds.

4.1. Detector technologies

A number of different detector technologies have been used to address the points made above. In general, there is a trade-off between attaining a large mass of source isotope and achieving a very low level of background. An overview of the current and future double- β decay experiments is given here. Experiments which use ^{48}Ca as the double- β decay source are discussed in Section 4.2.

4.1.1. Semiconductor experiments

Semiconductor experiments exploit the existence of suitable materials which are also double- β decay isotopes. Detectors are built by placing a semiconductor enriched in a double- β decay isotope between two electrodes. Ionising radiation creates electron-hole pairs which drift towards the electrodes, producing a current on them. The signals on the electrodes are proportional to the energy deposited in the detector. These detectors operate at cryogenic temperatures, achieving very good energy resolution, as low as $\sim 0.3\%$ FWHM.

This technique has been particularly successful when used with ^{76}Ge , having provided some of the most stringent limits on the effective Majorana mass to date. High-purity germanium detectors (HPGe) are used in nuclear spectroscopy for which there is a well established manufacturing industry. In addition, affordable enrichment methods exist for ^{76}Ge .

The Heidelberg-Moscow (H-M) experiment ran from 1990 to 2003 with five HPGe detectors enriched in ^{76}Ge to 86.6%. The detector operated in the Laboratori Nazionali del Gran Sasso (LNGS), and with a total exposure of 35.5 kg yr obtained a limit on the $0\nu\beta\beta$ of ^{76}Ge of $t_{0\nu}^{1/2} > 1.9 \times 10^{25}$ yr, corresponding to $\langle m_{\beta\beta} \rangle < 0.25 - 0.50$ eV [65]. A similar experiment, IGEX, ran concurrently with the H-M experiment, with six HPGe detectors and a plastic scintillator veto. With an exposure of 8.9 kg yr the experiment obtained a slightly weaker $0\nu\beta\beta$ half-life limit of $t_{0\nu}^{1/2} > 1.57 \times 10^{25}$ yr, giving $\langle m_{\beta\beta} \rangle < 0.28 - 0.55$ eV [66].

The current generation of ^{76}Ge experiments is being led by GERDA. In its first phase, this experiment consists of eight HPGe detectors recovered from the H-M and IGEX experiments and newly commissioned broad energy germanium detectors (BEGe) immersed in liquid argon, which provides both cooling and shielding. The liquid argon volume is in turn surrounded by a water Čerenkov active shield. After two years of operation with 21.3 kg of source mass, a limit on the half-life of the $0\nu\beta\beta$ of ^{76}Ge was obtained: $t_{0\nu}^{1/2} > 2.1 \times 10^{25}$ yr, corresponding to $\langle m_{\beta\beta} \rangle < 0.24 - 0.48$ eV [67]. This limit is an improvement on the H-M result, despite the lower exposure. The second phase of the experiment will include an additional 20 kg of source mass and is expected to be sensitive to an effective Majorana mass of 50 – 100 meV [68].

MAJORANA is a ^{76}Ge experiment which is expected to start taking data soon. It follows the strategy of the H-M experiment, but with enhanced shielding. With a source mass of 40 kg it is expected to achieve a sensitivity to $\langle m_{\beta\beta} \rangle$ of 80 – 160 meV in 2.5 years of operation [69].

A future collaboration between GERDA and MAJORANA is envisaged, with the aim of building a 1 tonne ^{76}Ge experiment, which would be sensitive to an effective Majorana mass as low as 10 meV [62].

COBRA is an experiment currently in the R&D phase which will employ a semiconductor approach with CdZnTe crystals enriched in ^{116}Cd . The experiment will consist of a segmented detector, for background reduction, operated at room temperature [70].

4.1.2. Bolometer experiments

Bolometer experiments measure small changes in the temperature of crystals due to energy deposits from ionising radiation. These detectors are operated at very low temperatures (10 mK) to achieve a very good energy resolution. CUORICINO consisted of 62 TeO₂ crystals passively shielded in a cryostat. With an exposure of 19.75 kg yr a half-life limit on the $0\nu\beta\beta$ of ¹³⁰Te was obtained: $t_{0\nu}^{1/2} > 2.8 \times 10^{24}$ yr, corresponding to $\langle m_{\beta\beta} \rangle < 0.3 - 0.7$ eV [71]. This technology has been further developed for the CUORE experiment, which is planned to consist of 1000 crystals hosting 200 kg of ¹³⁰Te. A prototype of this detector, CUORE-0, is currently running with 52 crystals, having an expected sensitivity to a $0\nu\beta\beta$ half-life of 8×10^{24} yr, corresponding to a mass of 0.18 – 0.42 eV. It is expected that the full detector will be sensitive to a half-life of 2.1×10^{26} yr, corresponding to an effective Majorana mass of 35 – 82 meV [72].

4.1.3. Scintillator experiments

Being economical and radiopure, scintillating materials are well suited for double- β decay experiments. The scintillating properties of these materials are exploited by embedding double- β decay isotopes in them and surrounding them with photomultiplier tubes (PMTs) to capture the light produced by the electrons emitted in the decay.

The most stringent limit on the effective Majorana mass has been obtained by KamLAND-Zen, a liquid scintillator ¹³⁶Xe experiment. The detector consists of a nylon balloon filled with 13 tonnes of Xe-loaded liquid scintillator placed inside another balloon, this one filled with 1 kilotonne of Xe-free liquid scintillator. The balloons are surrounded by 2000 PMTs which detect the scintillation light. This apparatus is in turn surrounded by a water Čerenkov detector which acts as a cosmic ray veto. A limit on the $0\nu\beta\beta$ half-life of ¹³⁶Xe of $t_{0\nu}^{1/2} > 1.9 \times 10^{25}$ yr, corresponding to $\langle m_{\beta\beta} \rangle < 0.16 - 0.33$, was obtained with an exposure of 89.5 kg yr [44]. The collaboration is currently involved in R&D activities to reduce the background levels and increase the mass of ¹³⁶Xe in the detector by a factor of two. There are plans for a second generation of the experiment which, with 1 tonne of ¹³⁶Xe, would be sensitive to a Majorana mass of 20 meV [63].

SNO+ is another experiment, currently under construction, which will use isotope-loaded liquid scintillator techniques to investigate double- β decay processes. An acrylic sphere will be filled with liquid scintillator loaded with 800 kg of ^{130}Te . This sphere will be immersed in water for shielding and surrounded by 9500 PMTs. A sensitivity to a mass of 50 – 100 meV is expected in the first phase of the experiment, with an increase in the mass of ^{130}Te by one order of magnitude planned which is expected to improve the sensitivity to 20 – 40 meV [73]. One challenge with this approach is the loss in efficiency due to the attenuation of scintillation light under a high ^{130}Te -loading fraction of 3%.

4.1.4. Time projection chamber experiments

In time projection chamber (TPC) experiments, the position and energy of ionising particles are measured simultaneously. A high potential difference is set across two or more electrodes in the gaseous or liquid medium. As the medium is ionised, the freed electrons drift towards the anodes. When the electrons reach the anode, a current is generated across the electrodes which is proportional to the energy initially deposited in the medium. By arranging the electrodes in sets of orthogonal wires, a two-dimensional reconstruction of the position of the ionisation is possible. The third coordinate is given by the time taken by the ionisation electrons to reach the anode. This technique is commonly coupled with scintillation methods to improve the energy resolution and provide particle identification.

EXO-200 is a ^{136}Xe experiment which uses a TPC technique. The experiment consists of a cylindrical chamber filled with liquid Xe enriched in ^{136}Xe with the cathode placed in the middle. Both charge and scintillation light are measured, the latter with arrays of avalanche photodiodes on both sides of the chamber. The fiducial volume analysed contains around 80 kg of ^{136}Xe . With an exposure of 32.5 kg yr a limit on the $0\nu\beta\beta$ half-life of ^{136}Xe was set at $t_{0\nu}^{1/2} > 1.6 \times 10^{25}$ yr which corresponds to $\langle m_{\beta\beta} \rangle < 0.17 - 0.36$ [74]. An increase of the source mass to 1 tonne is planned, as well as the deployment of a new technique in which the identification of barium ions resulting from double- β decays of ^{136}Xe will be used to greatly reduce the background levels [75].

Another experiment using TPC techniques is NEXT, currently in the R&D phase. Unlike EXO, this experiment will use gaseous Xe under pressure as the TPC

medium. The chamber will have the TPC anodes on one side and PMTs on the other. The PMTs will be used to detect two signals: prompt scintillation signals, and electroluminescence produced as the drifting electrons cross the anode plane. With 100 kg of Xe, the experiment is expected to be sensitive to a 1.9×10^{25} yr $0\nu\beta\beta$ half-life, or a Majorana mass of 70 – 150 meV [64].

4.1.5. Tracker and calorimeter experiments

While tracker and calorimeter experiments have modest energy resolution, this is overcome by the very large reduction of the backgrounds obtained by selecting events with a two-track topology. The full reconstruction of the event topology also allows for independent analysis channels to be used for the precise measurement of background activities. Additionally, in the event of the discovery of $0\nu\beta\beta$, tracker and calorimeter detectors have the unique advantage of being able to measure the decay kinematics, providing a deeper investigation of the mechanism responsible for $0\nu\beta\beta$. One advantage of having detector components which are independent from the source is that many different isotopes can be studied.

The notable tracker and calorimeter experiments are NEMO-3 and SuperNEMO. These experiments are described in detail in Chapters 5 and 9, respectively. NEMO-3 has produced the most precise measurement of the $2\nu\beta\beta$ half-life of seven of the nine isotopes for which $2\nu\beta\beta$ has been directly observed (Table 4.2). The best $0\nu\beta\beta$ limit obtained with NEMO-3 was for the ^{100}Mo isotope, with $t_{0\nu}^{1/2} > 1.1 \times 10^{24}$ yr, corresponding to a mass limit of 0.3 – 0.9 eV [76]. SuperNEMO will use the technique of NEMO-3, with an increase in the source mass by one order of magnitude and improved experimental characteristics, and is expected to be sensitive to a Majorana mass of 50 – 100 meV.

4.2. Experiments with ^{48}Ca

A number of techniques have been employed in the search for the $0\nu\beta\beta$ of ^{48}Ca . An overview of the experiments performed with this isotope is given here, in historical order.

Mateosian-Goldhaber experiment

The Mateosian-Goldhaber experiment was the first experiment to search for lepton number violating processes in ^{48}Ca . The experiment was performed in 1966, with a live time of only 28.7 days. A large CaF_2 crystal scintillator, enriched in ^{48}Ca was housed inside a steel naval gun, with additional active shielding provided by plastic scintillators surrounding the crystal. No evidence for either $2\nu\beta\beta$ or $0\nu\beta\beta$ was found, with half-life limits of $t_{2\nu}^{1/2} > 5 \times 10^{18}$ yr and $t_{0\nu}^{1/2} > 2 \times 10^{20}$ yr being obtained [77].

Beijing experiment

Another ^{48}Ca experiment was performed in a coal mine near Beijing. It employed the technique of Mateosian and Goldhaber with a final setup of four CaF_2 crystals fully surrounded by plastic scintillator active shielding and encased in lead. The volume defined by the lead shielding was ventilated with argon. With a live time of 0.87 years a limit of $t_{0\nu}^{1/2} > 9.5 \times 10^{21}$ (76% CL) on the $0\nu\beta\beta$ half-life was obtained [78].

Hoover Dam experiment

The Hoover Dam experiment achieved the first observation of the $2\nu\beta\beta$ of ^{48}Ca . The experiment consisted of thin sheets of CaCO_3 at 18 mg/cm² enriched in ^{48}Ca acting as the central cathode in a TPC. The tracking capabilities of the detector allowed for sophisticated analysis techniques to be employed: helices were fit to electron tracks and delayed α particles were used to reject background events due to ^{214}Bi . With a total mass of 42.2 g of enriched CaCO_3 the $2\nu\beta\beta$ half-life was measured to be $4.3_{-1.1}^{+2.4}$ (stat.) ± 1.4 (syst.) $\times 10^{19}$ yr [79].

TGV

The Telescope Germanium Vertical (TGV) consisted of a tower of 16 HPGe detectors of the planar type housed in a single cryostat. Thin sheets of CaCO_3 , enriched in ^{48}Ca , were placed on top of each detector, with a total ^{48}Ca mass of 1 g. The experiment was performed at the Laboratoire Souterrain de Modane (LSM), with a live time of 1 year. The $2\nu\beta\beta$ half-life was measured to be $4.2_{-1.3}^{+3.3} \times 10^{19}$ yr,

in agreement with the Hoover Dam experiment. In addition, a limit on the $0\nu\beta\beta$ half-life was obtained: $t_{0\nu}^{1/2} > 1.5 \times 10^{21}$ yr [80].

ELEGANT VI

The ELEGANT VI experiment has obtained the most stringent limit on the $0\nu\beta\beta$ of ^{48}Ca to date. The experiment consisted of 23 $\text{CaF}_2(\text{Eu})$ crystals produced with natural calcium, giving a total of 7.6 g of ^{48}Ca . Additional CaF_2 (pure) and $\text{CsI}(\text{Tl})$ crystals were used for rejecting events of external origin. With a live time of 0.6 years, a limit was obtained on the $0\nu\beta\beta$ half-life of 5.8×10^{22} yr, corresponding to an upper limit on the effective Majorana mass of $\langle m_{\beta\beta} \rangle < 3.5 - 22$ eV [81].

CANDLES

CANDLES is the successor of ELEGANT VI. The experiment, which is currently running, consists of 60 cubic CaF_2 scintillators (with natural Ca) immersed in liquid scintillator. The scintillation light is detected by 40 large PMTs which surround the scintillator. To veto external events, the different time constants of the two types of scintillator are used. While interactions in the liquid scintillator produce short light pulses, events originating in the CaF_2 produce light pulses which last longer. By integrating the PMT signals over two time windows, one short and one long, and taking their ratio, interactions in the liquid scintillator can be distinguished from those in the CaF_2 crystals. The experiment is expected to be sensitive to a half-life of 10^{26} yr.

4.3. Current status of double- β decay measurements

The best double- β decay measurements currently available are summarised here. The most precise measurements of the $2\nu\beta\beta$ half-life for the isotopes for which this process has been directly observed are listed in Table 4.2. The best limits on the $0\nu\beta\beta$ modes of the same isotopes are given in Table 4.3.

Isotope	$t_{2\nu}^{1/2}$ (10^{19} yr)	Experiment
^{48}Ca	$6.4^{+0.6}_{-0.7}$ (stat.) $^{+1.2}_{-0.9}$ (syst.)	NEMO-3 (this work)
^{48}Ca	$4.2^{+3.3}_{-1.3}$	TGV [80]
^{48}Ca	$4.3^{+2.4}_{-1.1}$ (stat.) ± 1.4 (syst.)	Hoover Dam [79]
^{76}Ge	184^{+9}_{-8} (stat.) $^{+11}_{-6}$ (syst.)	GERDA [67]
^{96}Zr	2.35 ± 0.14 (stat.) ± 0.16 (syst.)	NEMO-3 [82]
^{82}Se	9.6 ± 0.3 (stat.) ± 1.0 (syst.)	NEMO-3 [83]
^{100}Mo	0.711 ± 0.002 (stat.) ± 0.054 (syst.)	NEMO-3 [83]
^{116}Cd	2.88 ± 0.04 (stat.) ± 0.16 (syst.)	NEMO-3 [84]
^{130}Te	70 ± 9 (stat.) ± 11 (syst.)	NEMO-3 [85]
^{136}Xe	216.5 ± 1.6 (stat.) ± 5.9 (syst.)	EXO-200 [74]
^{150}Nd	$0.911^{+0.025}_{-0.022}$ (stat.) ± 0.63 (syst.)	NEMO-3 [86]

Table 4.2.: Most precise direct measurements of $2\nu\beta\beta$. Additionally, two superseded results for ^{48}Ca are shown in grey.

Isotope	$t_{0\nu}^{1/2}$ limit (yr)	$\langle m_{\beta\beta} \rangle$ limit (eV)	Exposure (kg yr)	Experiment
^{48}Ca	5.8×10^{22}	3.5 – 22	0.015	ELEGANT VI [81]
^{76}Ge	2.1×10^{25}	0.24 – 0.48	16.4	GERDA [61]
^{82}Se	2.1×10^{23}	1.0 – 2.8	4.9	NEMO-3 [31]
^{100}Mo	1.1×10^{24}	0.3 – 0.9	34.7	NEMO-3 [76]
^{96}Zr	9.2×10^{21}	7.2 – 19.5	0.031	NEMO-3 [82]
^{116}Cd	1.7×10^{21}	1.4 – 2.8	0.14	Solotvina [87]
^{130}Te	2.8×10^{24}	0.3 – 0.7	19.75	CUORICINO [71]
^{136}Xe	1.9×10^{25}	0.16 – 0.33	89.5	KamLAND-Zen [44]
^{150}Nd	1.8×10^{22}	4.0 – 6.3	0.093	NEMO-3 [86]

Table 4.3.: Best limits on the $0\nu\beta\beta$ half-life of the isotopes for which $2\nu\beta\beta$ has been directly observed. All limits are at 90% CL.

Part I.

Search for double- β decay of ^{48}Ca
with the NEMO-3 detector

Chapter 5.

The NEMO-3 detector

The general detection principle of the NEMO-3 experiment is to track the two electrons produced in double- β decays and measure their energies separately. This allows for a very pure selection of double- β decay events by rejecting backgrounds with different event topologies.

The NEMO-3 detector operated in the Laboratoire Souterrain de Modane (LSM) from February 2003 to January 2011. The experiment housed seven double- β decay isotopes in a thin foil surrounded by tracker and calorimeter modules in a cylindrical geometry (Figure 5.1).

The most stringent NEMO-3 limit on $0\nu\beta\beta$ was obtained with ^{100}Mo data [76]. The $0\nu\beta\beta$ of this isotope was excluded up to a half-life of 1.1×10^{24} years at 90% CL, corresponding to an upper limit on the effective Majorana mass of 0.33 – 0.87 eV.

An overview of the detector's components and systems is given in this chapter, written in reference to the experiment's technical design report [88].

5.1. Source foils

The NEMO-3 detector was designed to accommodate 10 kg of double- β decay sources. The sources were shaped into thin foils arranged in a cylindrical geometry inside the detector, which was itself composed of 20 sectors. The position of the source cylinder in the detector and the division into sectors are shown in Figure 5.2.

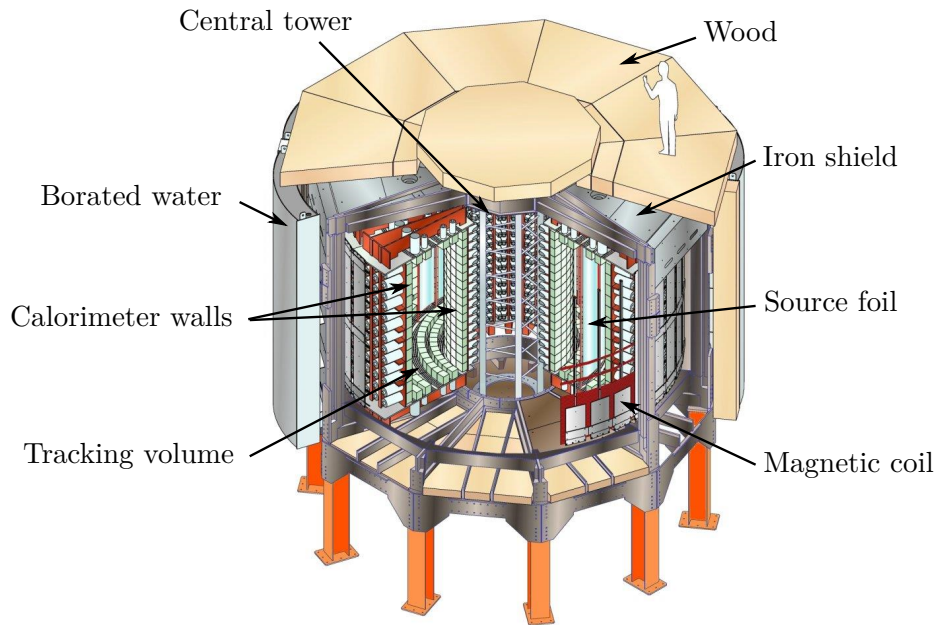


Figure 5.1.: Cutaway drawing of the NEMO-3 detector. The components described in this chapter are indicated by black arrows.

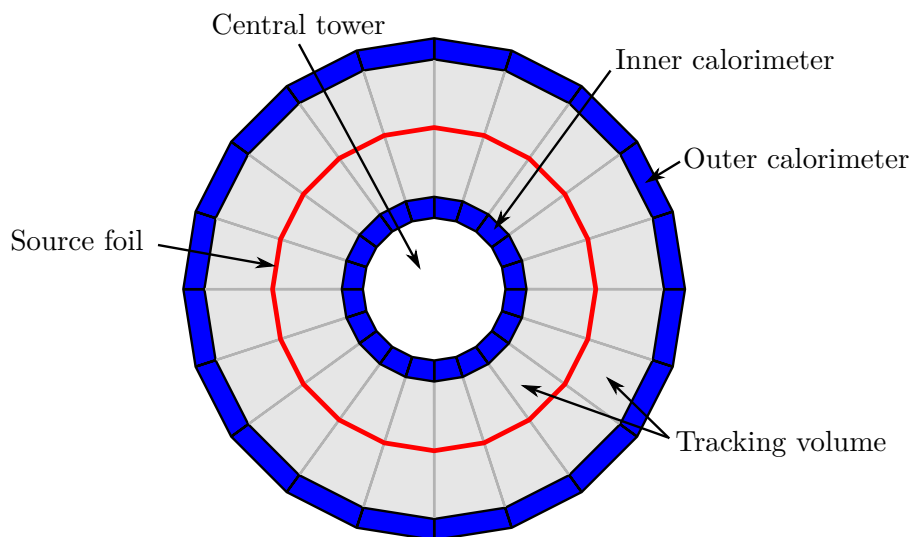


Figure 5.2.: Top-view diagram of the NEMO-3 detector. The main detector components are shown as is the arrangement into sectors.

The surface density of the foils was optimised such that the amount of source isotope would be maximised while keeping energy losses of electrons in the foil within a level which did not compromise the sensitivity of the detector to double- β decay processes. The resulting densities of most foils were between 30 and 60 mg/cm² which translates into a thickness of 60 to 300 μ m, depending on the foil construction.

Most of the detector was occupied by the ¹⁰⁰Mo (6.9 kg) and ⁸²Se (0.93 kg) sources. These isotopes were chosen to be the primary sources for $0\nu\beta\beta$ searches. In addition to these two isotopes, five other source isotopes were selected, mainly for use in $2\nu\beta\beta$ studies. The experiment included 0.61 kg of ^{nat}Te, 0.45 kg of ¹³⁰Te, 0.40 kg of ¹¹⁶Cd, 36.5 g of ¹⁵⁰Nd, 9.43 g of ⁹⁶Zr and 6.99 g of ⁴⁸Ca. Additionally, 0.62 kg of very pure Cu was included which was used (with the ^{nat}Te source) to measure the detector's backgrounds. The disposition of the different sources in the detector is shown in Figure 5.3.

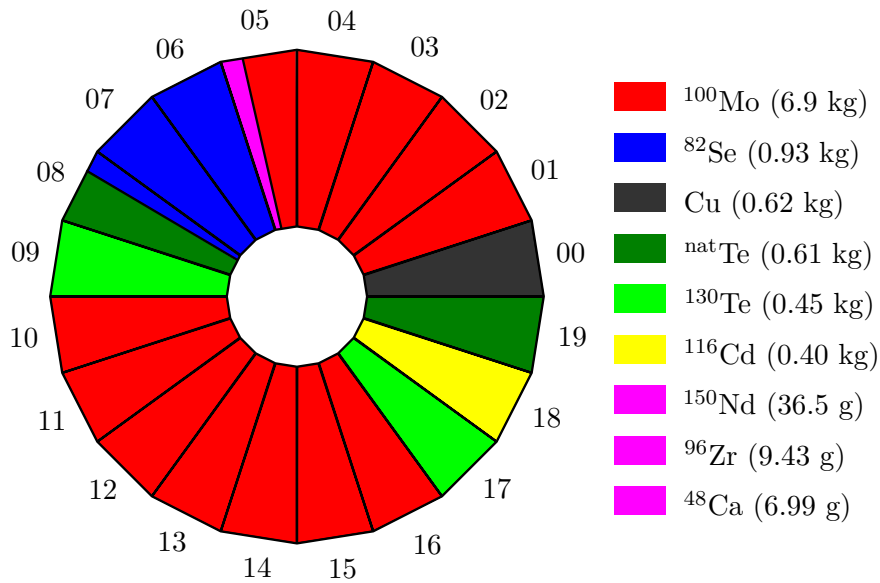


Figure 5.3.: Arrangement of the different sources in the NEMO-3 detector. The sector numbering scheme is shown.

In each sector the source foil is composed of seven 2.5 m \times 6.5 cm strips. In sector 5, strips 1 to 5 are populated with ¹⁰⁰Mo, strip 6 contains the ¹⁵⁰Nd source, and the last strip consists of the ⁹⁶Zr source on the upper half and the ⁴⁸Ca source below it (Figure 5.4).

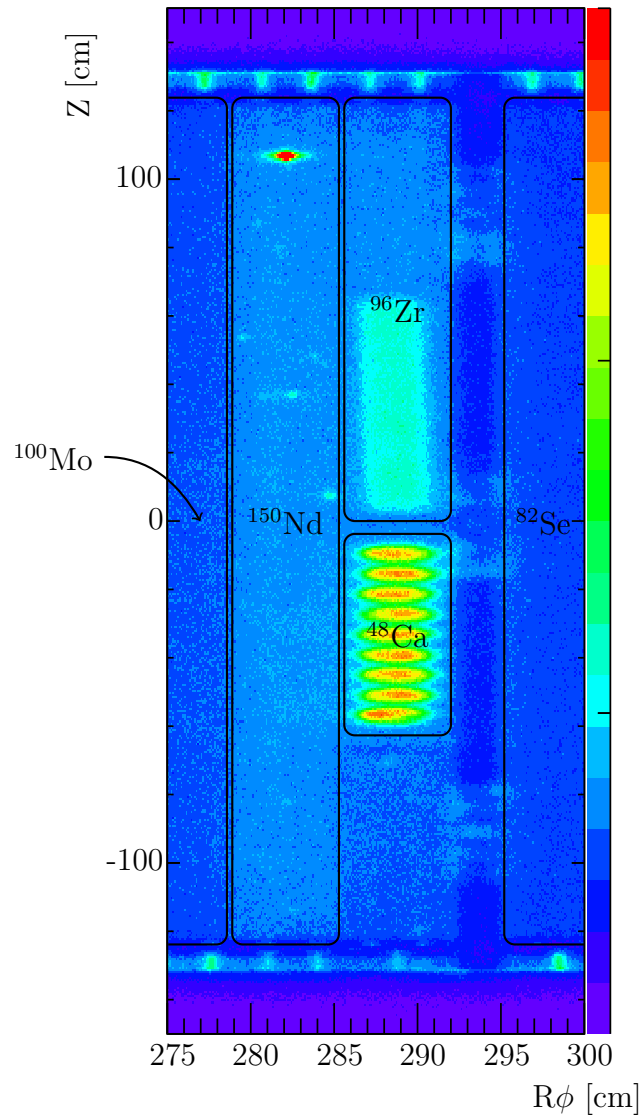


Figure 5.4.: Map of the ^{48}Ca and neighbouring sources as seen in NEMO-3 data. The linear colour scale indicates the density of electron track intersections with the source foil plane, with red being the densest and violet the least dense. The different sources are outlined in black. Above and below the source strips their support structure can be seen. The location of the calibration source tube (Section 5.5.1) is seen between the $^{48}\text{Ca}/^{96}\text{Zr}$ and the ^{82}Se sources.

5.1.1. ^{48}Ca source

The ^{48}Ca source was produced from a CaCO_3 sample which was enriched in ^{48}Ca to a fraction of $73.2 \pm 1.6 \%$ by electromagnetic isotope separation methods. The CaCO_3 was purified to remove ^{226}Ra , ^{228}Ra , ^{60}Co , ^{152}Eu and other elements from the thorium and radium decay chains. It was then processed into CaF_2 powder, 17.5 g of which were moulded into nine 4.6 cm diameter discs¹.

For the production of the source discs the CaF_2 powder was sandwiched between 10 μm thick discs of Mylar and heat resistant Teflon. It is not known if the Teflon layer was removed after pressing. The discs were then placed between two long Mylar strips, with bands of glue between them for mechanical support. The Mylar strips were 19 μm thick and were perforated by exposure to a ^{84}Kr ion beam to enhance their adhesion properties. The thickness of the pressed CaF_2 discs is not well known; it is estimated to be 0.7 mm. The mass of glue used in the production of the strip is not well known either, being estimated to be 0.7 g. A sketch of the structure of the CaF_2 discs is shown in Figure 5.5, with the materials shown adding up to a surface density of 117 mg/cm^2 . A photograph of the ^{48}Ca source taken after it was removed from the detector can be seen in Figure 5.6.

Rotation of the ^{48}Ca source from the nominal position

It was observed in NEMO-3 data that the ^{48}Ca strip was rotated off its nominal position by $10.6 \pm 0.6^\circ$. This measurement was obtained with two independent methods. The occupancy of the calorimeter modules near the ^{48}Ca source was found to be differently distributed for data and Monte Carlo for events where one electron was identified and its originating vertex reconstructed to the ^{48}Ca source. It was found that this discrepancy could be eliminated if the description of the source strip in the simulation was rotated. Another, data driven, method that returned the same result was the analysis of events where two electrons were reconstructed. The distribution of the intersection points of the two electron tracks was not in good agreement with the nominal position of the foil, favouring instead the same rotation angle as the previously described method (Figure 5.7a).

¹The diameter of the discs is erroneously given as 4.0 cm in [88]. The correct dimensions were confirmed when the source was extracted from the detector at the end of the experiment [89,90].

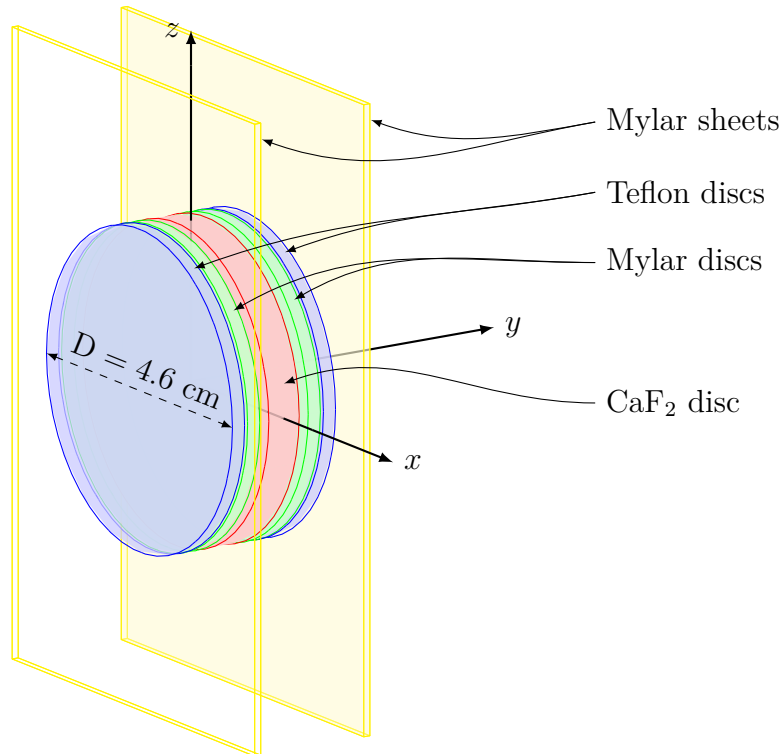


Figure 5.5.: Structure of the CaF_2 source discs. The CaF_2 is shown in red, sandwiched between two layers of Mylar (green) and two layers of Teflon (blue). The discs are supported between two long Mylar strips (yellow) by bands of glue (not shown). Dimensions are not to scale.



Figure 5.6.: Photograph of the ^{48}Ca source. Taken after the source was removed from the detector at the end of the experiment. The nine CaF_2 discs are seen as is the glue supporting them.

While the detector was being disassembled several strips were found to have moved from their nominal position. An example of a rotated pure copper strip in sector 0 is shown in Figure 5.7b.

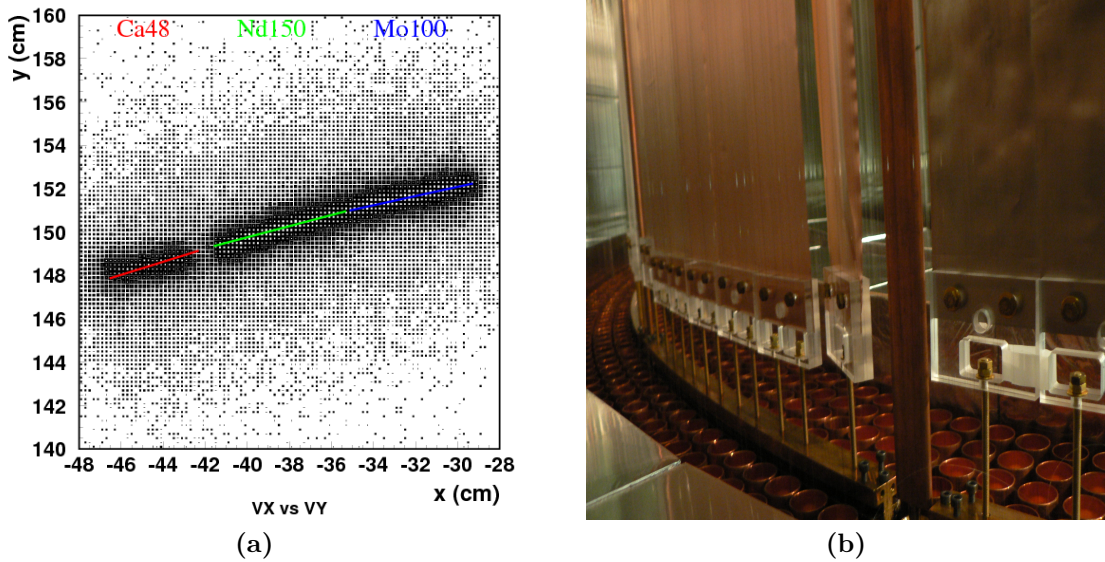


Figure 5.7.: Rotated source foil strips. A rotation of the ^{48}Ca source strip from its nominal position as seen in the analysis of the intersection points of two-track events is shown in (a) [91]. The coloured lines represent the nominal position of the strips and the size of the black squares indicates the density of two-track intersections. A photograph of a rotated Cu strip taken during the disassembly of the detector is shown in (b).

5.2. Tracker

The NEMO-3 tracking detector was a wire chamber consisting of 6180 cells strung vertically on both sides of the source foil. The cells were arranged in 18 concentric layers, nine on either side of the source foil. These layers were combined into three groups on each side of the foil with four layers immediately adjacent to the source foil, two layers in the middle and three layers next to the main calorimeter walls. Four concentric rings of PMTs were placed on the top and bottom endcaps (petals), between the groups of tracker cells (Figure 5.8).

Each cell was made of eight $50\ \mu\text{m} \times 2.7\ \text{m}$ grounded field shaping wires placed in a radius of 1.5 cm around one anode wire of the same dimensions to which a high

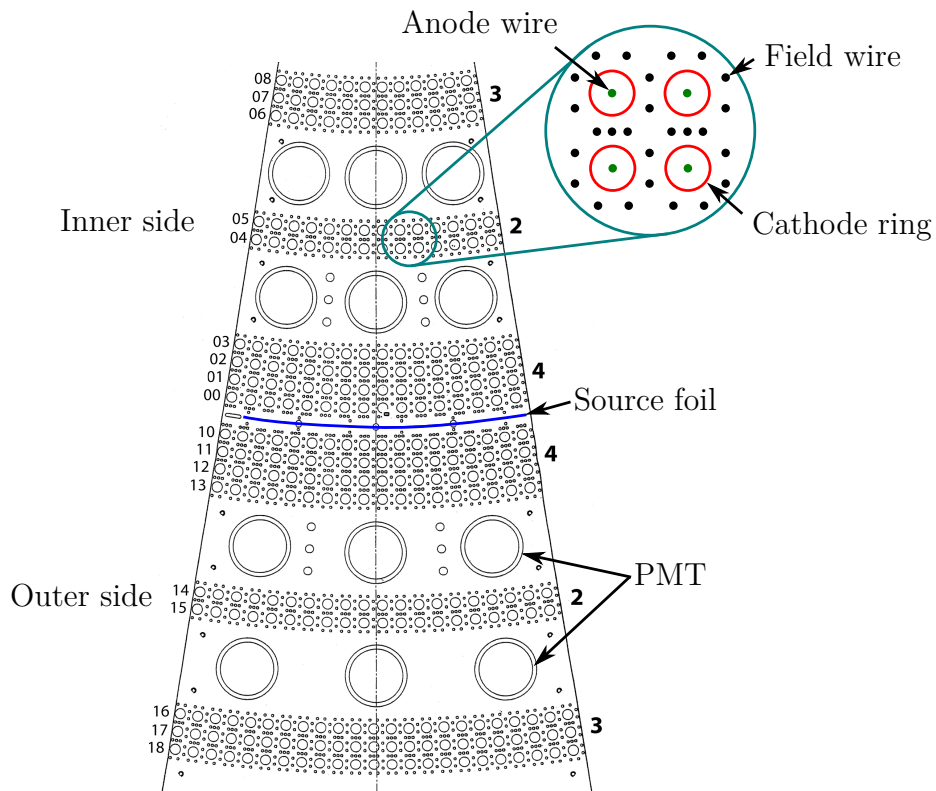


Figure 5.8.: Plan view of the tracker in one NEMO-3 sector. The position of the tracker cells and petal calorimeter blocks relative to the source foil is shown. The wiring of the tracker cells is shown in detail, where the black dots represent field wires, the anode wires are shown in green and the cathode rings in red.

voltage was applied, creating an approximately cylindrical electric field. The field wires were shared between adjacent cells and one extra wire was placed between cells on different layers to minimise the electric field bleed between cells. At the top and bottom of each cell there were grounded copper rings to pick up induced signals.

The tracker was immersed in an atmosphere consisting of 95% He, 4% ethanol vapour and 1% Ar. An electron with energy of a few MeV traversing the chamber would ionise the gas at a rate of ~ 6 electrons/cm. The freed electrons would then be accelerated through the strong electric field further ionising the gas. The voltage on the anode wire was set such that this avalanche of electrons would saturate, generating a constant amount of charge independently of the amount of initial ionisation. Ultraviolet radiation was emitted isotropically from the recombination of ionised gas atoms, spreading the avalanche stochastically along the length of the cell.

The gas mixture was optimised to provide an optimal tracking medium while keeping the energy losses in the tracker low: He is used for its low density and Ar is added to fine tune the amount of charge produced (having a lower ionisation potential than He); ethanol was added as a quencher, absorbing the recombination ultraviolet radiation through molecular dissociation. Other parameters such as the dimensions of the cells and thickness of the wires were also optimised, with the ageing effects common in gaseous detectors being taken into account.

For each cell, the voltage on the anode wire and on the cathode rings was monitored, providing three signals from which the positional information was extracted. The time of the first signal, on the anode wire, was compared to that of a hit calorimeter module. From the time difference between these two signals, typically up to 5 μs , a radial distance from the anode wire was extracted. By comparing the arrival time of the avalanche to the cathode rings at the ends of a cell to the time of the anode signal, the longitudinal position of the hit was obtained. The resolution on the measured radial and longitudinal coordinates was, respectively, 0.5 mm and 0.8 cm.

While each cell provided only two coordinates of the hit position (radial distance from the anode wire and longitudinal position along the cell), a full three-dimensional reconstruction of the particle tracks was possible by clustering tracker hits in an event and finding the track or set of tracks which better resolved the ambiguities.

5.3. Calorimeter

Besides providing the energy measurement of particles detected in the experiment, the NEMO-3 calorimeter's signals were used as the basis of time-of-flight measurements and to provide a fast trigger. As such it was required to have good timing as well as energy resolutions.

The NEMO-3 calorimeter consisted of 1940 modules placed mostly in the inner and outer walls which completely surrounded the source foil and also in the top and bottom endcaps of the detector as shown in Figure 5.8 above.

Each calorimeter module was composed of a plastic scintillator block attached to a PMT through a light guide. The scintillator blocks were inside the tracking volume, while the PMTs were outside the detector walls, to protect them from the He atmosphere (Figure 5.9).

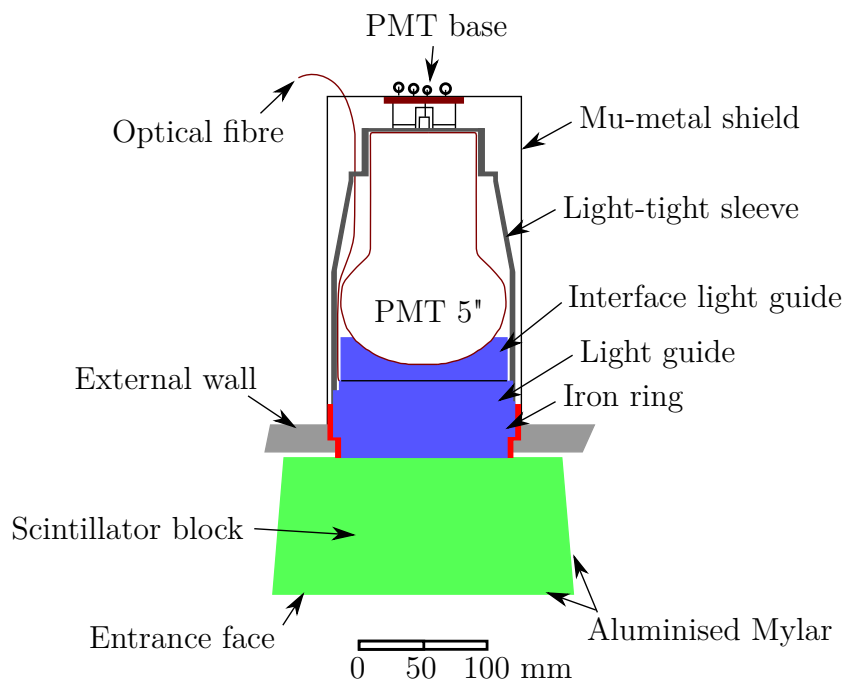


Figure 5.9.: Schematic drawing of a NEMO-3 calorimeter module. An outer wall module is shown, with its main components indicated by black arrows.

The base of the scintillators was polystyrene (PS), chosen for its radiopurity and to minimise backscattering. For modules in the main calorimeter walls this material was loaded with 1.5% p-Terphenyl and 0.01% POPOP acting as scintillating agent and wavelength shifter, respectively. The modules on the endcaps had a different

mixture with 1.2% p-Terphenyl and 0.05% POPOP. The resulting material was measured to have better radiopurity than the selected PMTs by factors of 430 and 60 for the troublesome isotopes ^{214}Bi and ^{208}Tl , respectively. The scintillator blocks were produced in seven different shapes to accommodate for the cylindrical geometry of the detector, with all the block types having a depth of 10 cm. This value was chosen to provide some sensitivity to γ 's. The efficiency of detecting a 500 keV γ was measured to be 50%. The lateral faces of the scintillator blocks were wrapped with a 350 μm thick layer of PTFE to enhance light collection by diffusively scattering the scintillation light. The whole blocks were then covered by aluminised Mylar. This final layer provided light-tightness of the block and increased the internal reflection of scintillation light.

The scintillator blocks were connected to the PMTs with a PMMA light guide which provided the interface between the tracker volume and the outside of the detector. The light guides were glued to an iron ring which provided the seal through a friction fit with the detector walls.

The PMTs used in the NEMO-3 calorimeter were developed for low radioactivity applications. Two types of PMT produced by Hamamatsu were chosen for their radiopurity and overall performance. The outer wall calorimeter and the outermost ring of endcap modules were populated with 5" PMTs while the inner wall and rest of the endcap modules were instrumented with 3" PMTs. The glass used for the production of these PMTs was 100 – 1000 times more radiopure than standard glass. All PMTs were covered by a mu-metal shield to minimise the effect of the experiment's magnetic field.

The optical modules were individually characterised and their properties were regularly monitored during the experiment's life time. At 1 MeV the calorimeter modules' energy resolutions ranged between 14% and 17% FWHM and their time resolution was 250 ps.

5.4. Electronics, DAQ and trigger

In NEMO-3, separate systems handled the distribution of high voltage (HV) and the data acquisition (DAQ) for the tracker and the calorimeter. A flexible trigger system

required both parts of the detector to pass predefined criteria before initiating the read-out.

5.4.1. Calorimeter electronics

Multi-channel power supplies manufactured by CAEN provided the HV to the PMTs. Each HV channel fed three PMTs which were grouped according to their gains. A fixed resistor divider was used to fine tune the HV supplied to each of the PMTs in the group of three. Typically, 3" PMTs required 1350 V and 5" PMTs operated at 1800 V.

Each PMT was assigned to a DAQ channel which had two preset thresholds. When the low threshold, set at 23 keV, was exceeded, a TDC counter was started and an 80 ns long charge integration window was opened. If the higher threshold energy of 150 keV was exceeded a trigger pulse was sent to the main board responsible for the channel. Each main board monitored a half-sector's worth of PMTs, *i.e.*, the PMTs on a given sector which were on the same side (inner or outer) of the source foil. The main boards would then produce an analogue Level 1 trigger pulse which was proportional to the number of PMTs in their half-sector which had exceeded the high threshold.

If the Level 1 trigger criteria were satisfied, the trigger system would send back a signal initiating the read-out of the contents of the timer and charge integrator. These counters had resolutions equivalent to 53 ps and 3 keV, respectively.

5.4.2. Tracker electronics

A detailed description of the tracker HV distribution and DAQ systems is given in Section 11.3 of this thesis. The relevant information is briefly summarised here.

The NEMO-3 tracker cells typically operated at 1620 – 1650 V. The HV was provided by CAEN power supplies, through fan-out and decoupling circuits. The decoupled signals from the anode wire and the two cathode rings were fed to DAQ boards. Each channel on the DAQ boards consisted of three TDC counters, one for each signal. When an anode signal crossed a preset threshold all TDCs were started. If the fast Level 1 trigger criteria had been satisfied, the trigger system would send a

pulse with a pre-determined delay (7.14 μs) to the tracker DAQ cards which would stop the TDC counter started by the anode signal. Given the much faster response of the calorimeter compared to the tracker, the time interval between the passage of the particle through the chamber and the arrival of the avalanche to the anode wire could be calculated with the anode TDC value and the known delay in the signal from the trigger system. The cathode TDCs were stopped by signals from the respective cathodes exceeding the threshold.

Each tracker layer in each sector was assigned a Level 2 trigger line, on which a pulse would be sent if any cell in the layer had an anode signal over the threshold. For the whole detector a total of 360 TTL signals were fed to the Level 2 trigger.

If no prompt anode signal was detected on a particular cell, the DAQ window would remain open for $\sim 700 \mu\text{s}$ during which time the arrival of an anode signal would still start the anode TDC. This feature was used to detect delayed α emissions from ^{214}Bi β -decay followed by the α -decay of ^{214}Po with a half-life of 164 μs .

The tracker DAQ electronics operated with a 50 MHz clock which gave the TDCs a resolution of 20 ns.

5.4.3. Trigger system

The NEMO-3 trigger system operated at three levels:

- at Level 1 a minimum calorimeter hit multiplicity was required over the entire detector;
- Level 2 applied a set of criteria to the tracker layer multiplicity on a sector-by-sector basis;
- Level 3 combined the information used in Level 2 with the calorimeter hit multiplicity at the half-sector level.

Special trigger criteria were defined for different types of calibration runs which used the three levels.

For regular data taking runs only levels 1 and 2 were used. At Level 1 it was required that at least one calorimeter module had a signal over the 150 keV threshold. At Level 2 it was required that there were at least three layers with tracker hits in

one half-sector. Furthermore, it was required that two of these layers were in the same group (the four nearest to the foil, the two in the middle, or the three nearest to the calorimeter wall). No correlation between the position of tracker hits and the calorimeter hits was required.

The average trigger rate during regular data acquisition runs was 7.5 Hz before the anti-radon facility was installed (Section 5.8), dropping to 5.6 Hz after the system was in operation. At these trigger rates the dead time of the DAQ system was $\sim 1\%$ of the run time.

5.5. Energy and time calibration

The NEMO-3 calorimeter was calibrated regularly so that energy and time measurements taken throughout the 8 years the detector operated remained accurate. Time consuming calibration runs where radioactive sources were introduced in the detector were performed every ~ 40 days. Between these runs, the stability of the calorimeter modules was monitored daily with a laser survey.

5.5.1. Radioactive sources

Each sector had a vertical copper tube located on the source foil plane, between source strips, into which a Delrin rod could be inserted. Each tube had three pairs of Kapton windows, with paired windows pointing inwards and outwards at the main calorimeter walls. The Delrin rods carried calibration sources which would be located at the height of the Kapton window pairs when inserted in the calibration tubes. The location of the windows at $Z = 0, \pm 90$ cm was optimised to ensure a uniform exposure of the calorimeter modules to the calibration sources.

For the regular calibration runs, alternative trigger modes were used, depending on the source isotope.

Two source isotopes were used for energy scale calibration runs:

- ^{207}Bi sources provided two calibration points through the emission of conversion electrons at 0.48 MeV and 0.98 MeV;

- a higher energy calibration point was provided by ^{90}Sr sources via the end-point of the β -decay spectrum of the daughter isotope ^{90}Y , at 2.3 MeV.

The ^{207}Bi source data was also used to evaluate the dependency of the calorimeter modules' response on the impact point of the electrons on the scintillator blocks' face.

For the time calibration, ^{60}Co sources were used. This isotope produces a cascade of two γ 's emitted coincidentally with energies of 1.2 MeV and 1.3 MeV. This allowed for measurements of the time delays in individual calorimeter modules.

In addition to the above, *special* calibration runs were performed where sources with well known activities were inserted into the calibration tubes and data was collected using the regular trigger mode. These runs provide the calibration of the overall efficiency of the detector.

5.5.2. Laser calibration system

The stability of the calorimeter modules was monitored daily with a laser calibration system. A N_2 laser beam was shifted to a wavelength of 420 nm and attenuated by an adjustable factor before being split into two beams. One of the beams was fed to all the scintillator blocks in the detector via optical fibre cables, while the other was sent to six reference calorimeter modules, external to the detector. The reference modules were exposed to ^{207}Bi sources therefore allowing for an absolute measurement of the laser light intensity in terms of an equivalent electron energy. The values read out by the experiment's calorimeter modules were then compared to the reference.

Calorimeter modules which showed energy scale instability were flagged, to be removed during data analysis. During the whole experiment no periods of instability were found for 82% of the calorimeter modules, with a further 7% having unstable behaviour in only one isolated period.

The laser calibration system was also used to test the linearity of the calorimeter modules, by scanning the attenuation factor of the laser beam through a series of steps.

5.6. Magnetic field

The NEMO-3 detector was immersed in a magnetic field produced by a coil wound around the outer calorimeter wall. This solenoid provided a 2.5 mT field in a direction parallel to the tracker wires which allowed for the discrimination of electrons from positrons. The magnetic field enabled the rejection of electron-positron pair production events from the external γ flux with an efficiency of 95%.

5.7. Passive shielding

The laboratory where NEMO-3 operated, LSM, is located under the peak of Mount Fréjus, on the French-Italian border. The cosmic muon flux is reduced by a factor of one million by the 1200 m of rock (4800 m water-equivalent) above the laboratory. This flux was measured in the laboratory to be 5.4 muons/m²/day [92].

The remaining external sources of background are the γ and neutron flux from radioactive decay in the laboratory's rock surroundings.

To shield the detector against the γ flux a 20 cm layer of pure iron was placed around the magnetic coil and also on the top and bottom endcaps. This shield also provided a return path for the magnetic field.

The effect of the neutron flux was minimised by a three-part shield. A 20 cm thick layer of paraffin was placed below the central tower, 20 cm thick layers of wood were placed above and below the detector and finally ten 35 cm thick borated water tanks were positioned around the detector's walls, with 20 cm deep wood sections separating them. Incoming neutrons would be slowed down by the wood and water and captured by the boron or iron nuclei in the outer layers of the shield. Any γ emissions resulting from neutron capture would be absorbed by the iron shield.

5.8. Anti-radon facility

About one year into the running of the experiment it was found that the radioactivity due to ²²²Rn, a radioactive noble gas, was higher than it would be expected from

the previously measured contamination in the detector components. This excess in ^{222}Rn activity was thought to be due to diffusion of radon from the laboratory air into the detector volume.

To reduce the activity of this potential background source a polyethylene tent was built around the detector through which radon-clean air was continuously flushed at a rate of $150\text{ m}^3/\text{h}$. To produce the low-radon gas, air from the laboratory was passed through two columns, each with 500 kg of activated charcoal kept at a temperature of $-50\text{ }^\circ\text{C}$. The charcoal provided a very large surface on which the radon atoms were adsorbed, containing these atoms until they decayed into non-gaseous isotopes. A reduction factor of 1000 was obtained in the activity of ^{222}Rn .

After the introduction of this system the measured activity of ^{222}Rn in the detector volume was reduced from $37.7 \pm 0.1\text{ mBq/m}^3$ to $6.46 \pm 0.05\text{ mBq/m}^3$ [93]. The smaller reduction factor inside the detector compared to the reduction in the surrounding air indicated that part of the ^{222}Rn activity inside the detector was a result of radon emanation from the internal components of the detector.

Data taken before and after this system was in operation are analysed separately, given the different activities of backgrounds due to ^{222}Rn .

Chapter 6.

General analysis techniques

The general strategy for NEMO-3 data analyses consists of the comparison of simulated data to real data obtained with the detector. The tracking capabilities and the segmented calorimeter of NEMO-3 allow for independent sets of data to be selected with different criteria. This allows for the tuning of simulation parameters as well as for obtaining a precise knowledge of the backgrounds by analysing control channel data.

6.1. Monte Carlo simulation

Monte Carlo data are produced by generating primary particles randomly positioned in specific volumes of the detector and propagating them through the detector taking into account interactions with its materials. Data are then obtained by registering the interactions of either the primary or secondary particles produced in detector interactions with sensitive components of the detector.

The package DECAY0 [94] is used for generating the primary particle information. This package generates a full kinematic description of particles originating from radioactive decays according to known nuclear data or, in the case of as yet unobserved decays, according to theoretical expectations of available models. Both signal and background processes are generated with DECAY0.

The primary particles are distributed randomly in selected detector components and propagated through a detailed geometrical description of the detector with the GEANT-3.21 package [95]. The components available for positioning decay vertices

include the source foils (for signal and internal backgrounds), the surfaces of internal components such as the source foils and the wires (for backgrounds due to ^{222}Rn) and other detector components where radioactive contaminants are expected such as the glass in PMTs.

A last step in the simulation is to identify the events which satisfy the trigger criteria (Section 5.4.3). Events which would not trigger the DAQ system (*e.g.*, with energy below threshold or without hits in the tracker) are discarded. The information on events which pass the trigger criteria is converted to the quantities that would be observed in real events (*i.e.*, ADC and TDC counts) and written to disc.

6.2. Event reconstruction

The experimentally obtained data and those resulting from the simulation described above are then converted into useful physical quantities by an event reconstruction program. This package is interfaced with a database where the running conditions of the detector and PMT calibration data are stored. This allows for data recorded by PMTs to be converted into an accurate energy measurement and for simulated data to be smeared according to measured resolutions of individual PMTs to reflect real data in the closest possible way. Running conditions data are also used to remove simulated hits in detector modules that were inactive during the time period to which events were assigned.

Also at the reconstruction stage a tracking algorithm identifies clusters of hits in the tracking chamber in a given event and finds the helix or set of helices which better describe them, producing the tracking information used in analyses. Three helices are fit to each track: a global fit which includes all the hits in the cluster and is used to measure the length of the track; a fit local to the foil in which only the tracker hits closest to the foil are used; and a calorimeter local fit which takes into account only the hits closest to the calorimeter wall. The latter two fits are used to obtain precise measurements of the intersections of the particle path with the source foils and the calorimeter modules, respectively.

6.3. Particle identification

The information produced at the reconstruction stage is used to build objects useful for analyses. The tracking capabilities of NEMO-3 are used in conjunction with data from the segmented calorimeter to identify electrons, positrons, photons and α particles emitted in ^{214}Bi - ^{214}Po decay cascades.

6.3.1. Electrons

Electrons are identified in NEMO-3 by long tracks intersecting both the source foil and a calorimeter block with a registered energy deposit. As it is expected that electrons interacting with the scintillator are fully contained within a calorimeter module, it is required that no modules neighbouring the one associated to the track are hit in the event.

In events where more than one particle produces a hit in the calorimeter, the relative timing of these hits can be used to infer the direction of travel of the tracked particles. In these cases it is possible to discriminate electrons from positrons with the sign of the curvature of the track relative to the direction of travel and orientation of the magnetic field.

An example of an event with two electrons is shown in Figure 6.1.

6.3.2. Photons

As γ 's are not charged, they do not ionise the gas in the detector leaving no tracks in the chamber. These particles are identified by localised energy deposits in the calorimeter which are not associated to tracks. As they do not ionise the tracking chamber, events in which only γ 's are present do not trigger the DAQ and therefore these particles can only be observed in events with at least one electron.

Unlike electrons, γ 's interacting with the scintillator will not, in general, be fully contained in one calorimeter module. In order to minimise the effect of partially contained γ interactions with scintillator blocks, hits recorded on neighbouring calorimeter modules are clustered to form a single γ object. The energies of all the

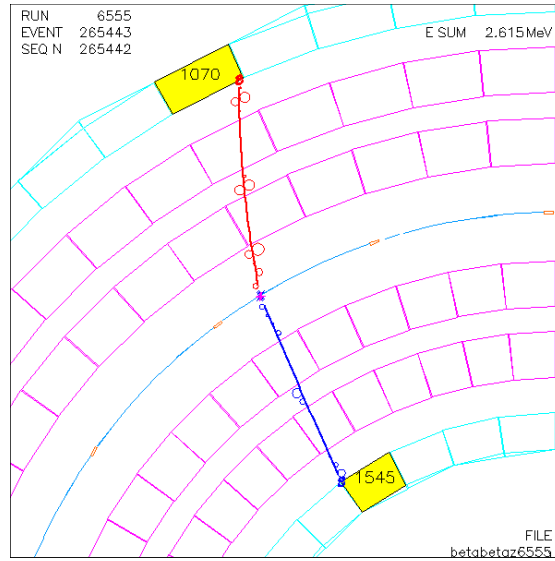


Figure 6.1.: Example of a two-electron event. Hit tracker cells are displayed as small open circles and calorimeter modules with a registered energy deposit are marked in yellow. Two tracks are seen emerging from the same point in the foil which intersect the calorimeter hits.

clustered hits are summed to give the energy of the γ while its position and timing information are given by the earliest hit in the cluster.

6.3.3. Alpha emission from ^{214}Bi - ^{214}Po decays

Being electrically charged and significantly more massive than electrons, α 's interact more strongly with the tracking gas and are less susceptible to the curving effect of the magnetic field. As a result, α 's leave straight and short tracks in the detector. As α 's emitted in radioactive decays traverse only a fraction of the width of the tracking chamber they do not leave signals in the calorimeter and therefore can only be identified in events in which electrons are present.

The only naturally occurring radioactive process where an electron and an α are emitted with a time interval which allows for their detection in NEMO-3 is the β -decay of ^{214}Bi followed by the α -decay of ^{214}Po , which is discussed in more detail in Section 7.2.2. An example of an event with a delayed α track is shown in Figure 6.2.

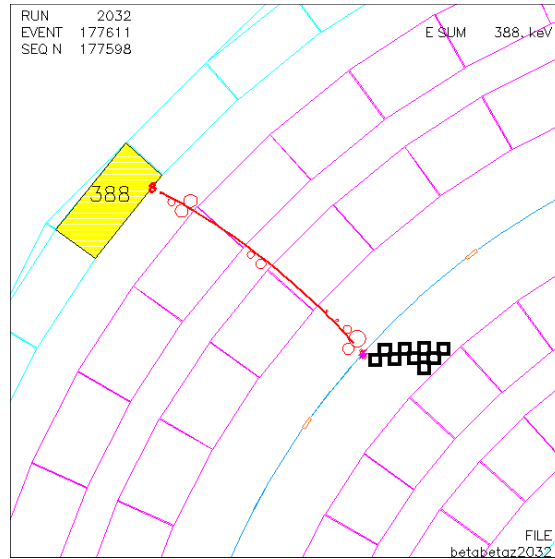


Figure 6.2.: Example of an event with a delayed α track. A short, straight track is seen emerging from the same point on the foil as the electron track (red). The delayed tracker hits are shown as black squares.

6.4. Time of flight

In NEMO-3 analyses it is important to distinguish between events where the particles originate from radioactive decays occurring in the source foils and those of external origin. This is particularly relevant in events where two electron tracks are reconstructed. As described above (Section 6.3.1), electron tracks are defined from the point of intersection with the source foil to the point of intersection with the calorimeter. In the cases where a single electron traverses the entire chamber, crossing the source foil, two tracks are reconstructed resulting in two electron objects (Figure 6.3a). A similar ambiguity exists in events with one electron and one or more γ 's. There is a possibility that the event is a result of a decay in the source foil with the emission of an electron and the γ 's and also the hypothesis where a single γ interacts first in the calorimeter, leaving an energy deposit, and then Compton scatters in the dense source foil producing an electron track (Figure 6.3b).

Discriminating between these classes of events is crucial for reducing the background in the two-electron event selection used for signal measurement and also to obtain precise measurements of the background contribution originating from sources external to the source foil. This distinction can be made using the precise timing information from the calorimeter hits in conjunction with the particle path length

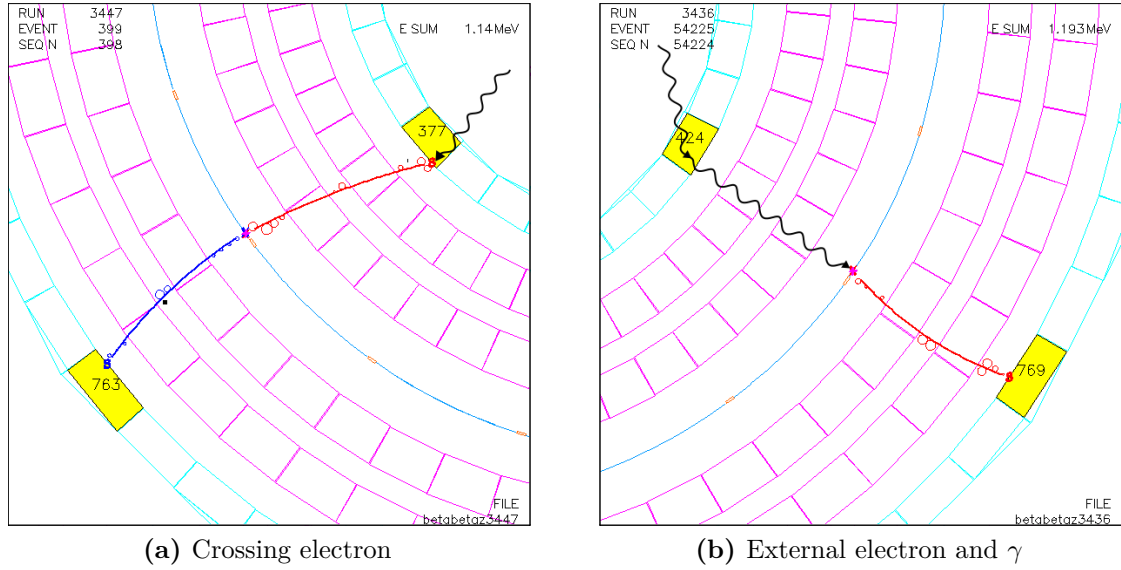


Figure 6.3.: Example of events with external origin. An event where a single electron crosses the tracking chamber is shown in (a) and an example of an event with one electron and one γ is shown in (b). The hypothetical paths of the γ 's are shown as black lines.

information provided by the tracker. The χ^2 test statistic is calculated for both hypotheses allowing internal or external events to be selected by making appropriate cuts on the resulting p-values, defined for one degree of freedom as:

$$P(\chi^2) = 1 - \frac{1}{\sqrt{2\pi}} \int_0^{\chi^2} x^{-\frac{1}{2}} e^{-\frac{x}{2}} dx. \quad (6.1)$$

6.4.1. Internal hypothesis

To calculate the χ^2 for the internal hypothesis it is assumed that the two particles are emitted from the same point in the foil and at the same time. Under this assumption, subtracting the time of flight of each particle from the relevant measurement time recorded by the calorimeter yields to hypothesised emission times which, for internal events, should be consistent with each other within experimental uncertainty. The χ^2 statistic is given by:

$$\chi_{\text{Internal}}^2 = \frac{\left((t_1^{\text{Meas}} - t_1^{\text{TOF}}) - (t_2^{\text{Meas}} - t_2^{\text{TOF}}) \right)^2}{\sigma_{t_1^{\text{Meas}}}^2 + \sigma_{t_1^{\text{TOF}}}^2 + \sigma_{t_2^{\text{Meas}}}^2 + \sigma_{t_2^{\text{TOF}}}^2}, \quad (6.2)$$

where t_i^{Meas} are the measurement times recorded by the calorimeter modules, t_i^{TOF} are times of flight of the particles, calculated from tracker and calorimeter module position data, and the σ 's are their respective uncertainties.

The uncertainty on the time measurement ($\sigma_{t_i^{\text{Meas}}}$) is estimated from calibration data, with the values being optimised separately for different types of calorimeter modules.

Electrons

In the case of electrons the time of flight is given by:

$$t_e^{\text{TOF}} = \frac{L_e}{\beta c}, \quad (6.3)$$

where L_e is the length of the electron track, c is the speed of light, and the ratio of the speed of the electron to the speed of light β is calculated with the electron energy measured in the calorimeter (E_e) and the known mass of the electron (m_e):

$$\beta = \frac{\sqrt{E_e(E_e + 2m_e)}}{E_e + m_e}. \quad (6.4)$$

Given the precision of the tracker and the fact that electrons interact very close to the face of the scintillator blocks, the uncertainty on the path length of electrons is negligible. The uncertainty on the electron time of flight is therefore dominated by the uncertainty on the speed of the particle:

$$\sigma_{t_e^{\text{TOF}}}^2 = \left| \frac{\partial t_e^{\text{TOF}}}{\partial \beta} \right|^2 \sigma_\beta^2, \quad (6.5)$$

where σ_β is obtained by propagating the energy resolution of the relevant calorimeter module through Equation 6.4.

γ 's

In the case of γ 's, the path length L_γ is given by the distance between the intersection of the electron track with the source foil and the position of the γ energy deposit in

the calorimeter. Given that γ 's are not tracked and are not guaranteed to interact close to the face of the scintillator block, their path length is not known as precisely as the electrons'. To account for this, a parameter t_{Scint} is added to the time of flight of the γ 's which depends on the type of calorimeter block and the γ energy. This parameter and its corresponding uncertainty ($\sigma_{t_{\text{Scint}}}$) are optimised in calibration source data [96]. The time of flight for γ 's is given by:

$$t_{\gamma}^{\text{TOF}} = \frac{L_{\gamma}}{c} + t_{\text{Scint}} , \quad (6.6)$$

and its corresponding uncertainty by:

$$\sigma_{t_{\gamma}^{\text{TOF}}} = \sigma_{t_{\text{Scint}}} . \quad (6.7)$$

The distribution of p-values for the internal hypothesis for two-electron events is shown in Figure 6.4a and for events with one electron and one γ in Figure 6.4b. The p-values for MC events generated in the source foil (*i.e.*, internal backgrounds and $2\nu\beta\beta$ signal) are distributed uniformly, as expected. The exception to this is the distribution $^{90}\text{Sr}/^{90}\text{Y}$ component of the internal background in the selection of events with one electron and one γ . As this isotope does not emit γ 's itself, the events included in this selection are mostly a result of bremsstrahlung interactions. In cases where these interactions do not occur in the source foil (*e.g.*, bremsstrahlung in the tracker wires) it is expected that the p-value for the internal hypothesis is lower than for events where the γ 's are produced in the foil. More details on the backgrounds and selection criteria are given in Chapters 7 and 8.

6.4.2. External hypothesis

For the external hypothesis it is assumed that one particle has interacted in a scintillator module and then traversed the tracking chamber, possibly interacting with the dense source foil before leaving an energy deposit in some other calorimeter module. The difference between the times recorded by the two calorimeter modules

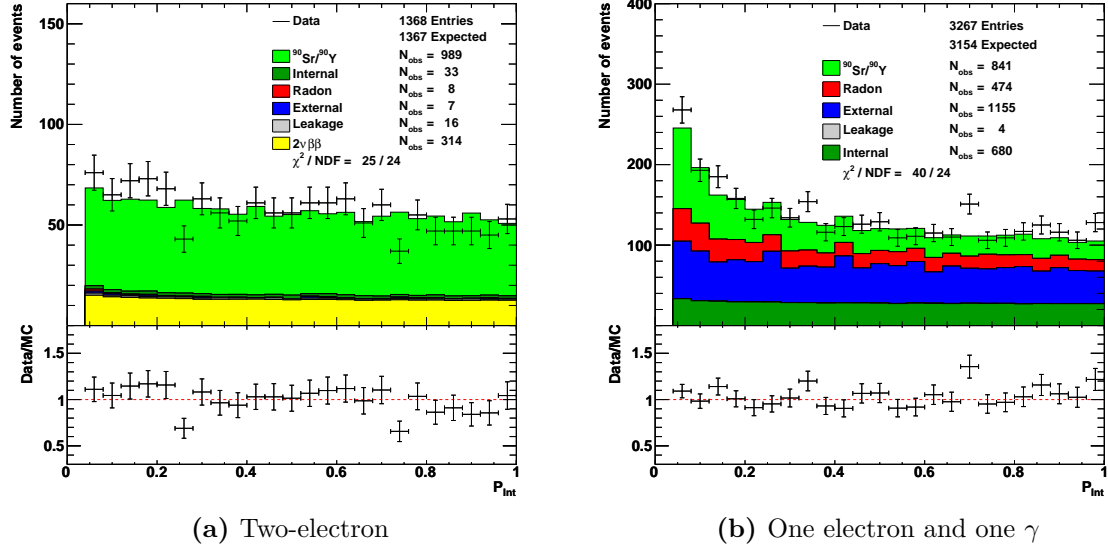


Figure 6.4.: Distributions of p-values for the internal time of flight hypothesis.

should then be consistent with the total time of flight of the particles:

$$\chi_{\text{External}}^2(1 \rightarrow 2) = \frac{\left(t_1^{\text{Meas}} - \left(t_2^{\text{Meas}} - t_2^{\text{TOF}} - t_1^{\text{TOF}}\right)\right)^2}{\sigma_{t_1^{\text{Meas}}}^2 + \sigma_{t_2^{\text{Meas}}}^2 + \sigma_{t_2^{\text{TOF}}}^2 + \sigma_{t_1^{\text{TOF}}}^2}, \quad (6.8)$$

where the direction of travel is from calorimeter hits labelled 1 to 2.

Crossing electron

In the case where two electron tracks are found in the event it is assumed in the external hypothesis that only one particle traversed the tracking chamber, where some energy is deposited in the calorimeter module where the electron originates and another calorimeter hit is found at the end of the particle trajectory. The times of flight for each leg (from the origin calorimeter module to the source foil and from the source foil to the calorimeter where the electron is absorbed) are calculated with the energy measured in the calorimeter where the electron is assumed to be absorbed:

$$t_1^{\text{TOF}}(1 \rightarrow 2) = \frac{L_1}{\beta_2 c}, \quad (6.9)$$

$$t_2^{\text{TOF}} (1 \rightarrow 2) = \frac{L_2}{\beta_2 c}. \quad (6.10)$$

The p-value is calculated for both directions of travel, $1 \rightarrow 2$ and $2 \rightarrow 1$, with the largest one taken as the p-value for the external crossing electron hypothesis.

External electron and γ

To calculate the χ_{External}^2 for events with one electron and one γ it is always assumed that the event originates from a γ interaction in the calorimeter followed by Compton scattering in the foil producing an electron (Figure 6.3b). The expression for the χ^2 is therefore given by:

$$\chi_{\text{External}}^2 (\gamma \rightarrow e) = \frac{\left(t_{\gamma}^{\text{Meas}} - \left(t_e^{\text{Meas}} - t_e^{\text{TOF}} - t_{\gamma}^{\text{TOF}} \right) \right)^2}{\sigma_{t_{\gamma}^{\text{Meas}}}^2 + \sigma_{t_e^{\text{Meas}}}^2 + \sigma_{t_e^{\text{TOF}}}^2 + \sigma_{t_{\gamma}^{\text{TOF}}}^2}, \quad (6.11)$$

where the times and uncertainties are as described for the internal hypothesis above.

Distributions of the p-values for the external crossing electron and external electron and γ hypotheses are shown in Figure 6.5, where a very pure selection of external background components is seen. More details about these backgrounds and the selection criteria used in the channels which constrain them are given in Chapter 7.

6.5. Statistical analysis

To measure the activity of backgrounds and extract the signal strength, the MC and experimental data are split into a number of independent channels with selection criteria designed to enhance sensitivity to particular contributions. The best fit of the MC samples to the real data is then obtained with a binned likelihood optimisation. In the case where no statistically significant signal contribution is observed, a limit is set on its strength.

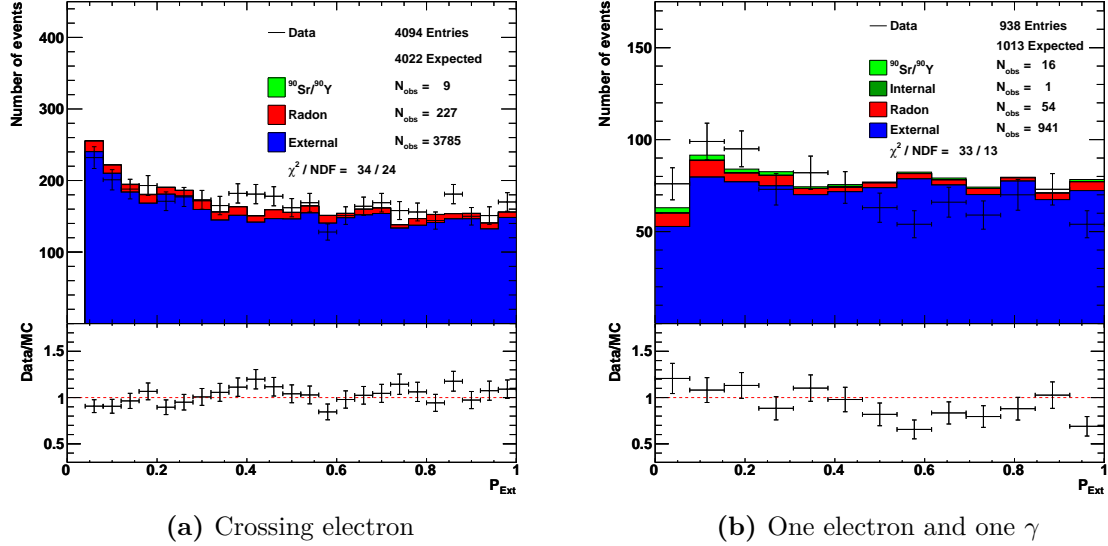


Figure 6.5.: Distributions of p-values for the external time of flight hypothesis.

6.5.1. Fitting MC predictions to data

In this analysis the fitting of MC to data is performed over several histograms originating from different analysis channels. For each bin i in each histogram j , it is assumed that the MC predicts the number of expected counts accurately and so the probability of observing $n_{i,j}$ data counts given a MC prediction $\nu_{i,j}$ is given by Poisson statistics:

$$p_{i,j} = \frac{\nu_{i,j}^{n_{i,j}}}{n_{i,j}!} e^{-\nu_{i,j}}, \quad (6.12)$$

where the MC prediction $\nu_{i,j}$ is given by the sum of the k background contributions and the signal prediction $s_{i,j}$:

$$\nu_{i,j} = s_{i,j} + \sum_k b_{i,j,k}. \quad (6.13)$$

The likelihood function is taken to be the product of the probabilities $p_{i,j}$ for all bins i and histograms j :

$$L = \prod_{i,j} \frac{\nu_{i,j}^{n_{i,j}}}{n_{i,j}!} e^{-\nu_{i,j}}. \quad (6.14)$$

The best fit of the MC prediction to data is obtained by scaling the individual background contributions and the signal strength by the set of factors which maximises L . Since the logarithmic function behaves monotonically, this is equivalent to maximising the log-likelihood function:

$$\ln L = \sum_{i,j} (-\nu_{i,j} + n_{i,j} \ln(\nu_{i,j}) - \ln(n_{i,j}!)). \quad (6.15)$$

In some cases independent constraints are available on background activities, for example, from HPGe measurements of the source foils (Section 7.4). These constraints are added to the log-likelihood function as the Gaussian probability of observing activity a_κ for background contribution κ , given the independent measurement α_κ with a standard deviation σ_{α_κ} :

$$p_\kappa = \frac{1}{\sigma_{\alpha_\kappa} \sqrt{2\pi}} e^{-\frac{(a_\kappa - \alpha_\kappa)^2}{2\sigma_{\alpha_\kappa}^2}}. \quad (6.16)$$

The log-likelihood function becomes:

$$\ln L = \sum_{i,j} (-\nu_{i,j} + n_{i,j} \ln(\nu_{i,j}) - \ln(n_{i,j}!)) - \sum_{\kappa} \frac{(a_\kappa - \alpha_\kappa)^2}{2\sigma_{\alpha_\kappa}^2}, \quad (6.17)$$

where constant terms are neglected.

To extract the background activities and the signal strength this function is maximised using the TMinuit tool [97] included in the ROOT data analysis package [98]. The statistical uncertainty of measurements is taken to be the interval around the best fit value where $\ln L$ changes by less than 1/2. This corresponds to one standard deviation [99].

6.5.2. Limit setting

Where no statistically significant signal contribution is observed in data, an upper limit is set on its strength.

The upper limits reported in this thesis are obtained with the CL_s method [100, 101], which gives the confidence level at which the signal is excluded for a given signal strength.

A negative log-likelihood ratio (NLLR) test statistic is built by taking the logarithm of the ratio of the likelihoods (as defined in Equation 6.14) for the *signal plus background* ($s + b$) to the *background only* (b) hypotheses:

$$Q(\mathbf{n}) = -2 \ln \left(\frac{L_{s+b}}{L_b} \right) = 2 \sum_i \left(s_i - n_i \ln \left(1 + \frac{s_i}{b_i} \right) \right) \quad (6.18)$$

where s_i are the predicted signal counts, b_i the predicted background counts and n_i the observed number of events. As searches in this analysis are done over one channel the index j is omitted and the index i represents the bin number, as in the formulae written above.

While for a large n_i the NLLR follows the χ^2 distribution [102], this is not the case for the analysis presented in this thesis. Instead, the distributions of the NLLR for the *background only* ($\frac{\partial P_b}{\partial Q}$) and *signal plus background* ($\frac{\partial P_{s+b}}{\partial Q}$) are obtained by generating a large number of pseudo-experiments according to both hypotheses and substituting the resulting n_i in Equation 6.18 (Figure 6.6).

Confidence levels can therefore be built for the scenarios where statistical fluctuations would yield a NLLR larger than the one observed with data \mathbf{n}_{Obs} for the *background only* hypothesis:

$$CL_b = P_b(Q > Q(\mathbf{n}_{\text{Obs}})) = \int_{Q(\mathbf{n}_{\text{Obs}})}^{\infty} \frac{\partial P_b}{\partial Q} dQ, \quad (6.19)$$

and for the *signal plus background* hypothesis:

$$CL_{s+b} = P_{s+b}(Q > Q(\mathbf{n}_{\text{Obs}})) = \int_{Q(\mathbf{n}_{\text{Obs}})}^{\infty} \frac{\partial P_{s+b}}{\partial Q} dQ. \quad (6.20)$$

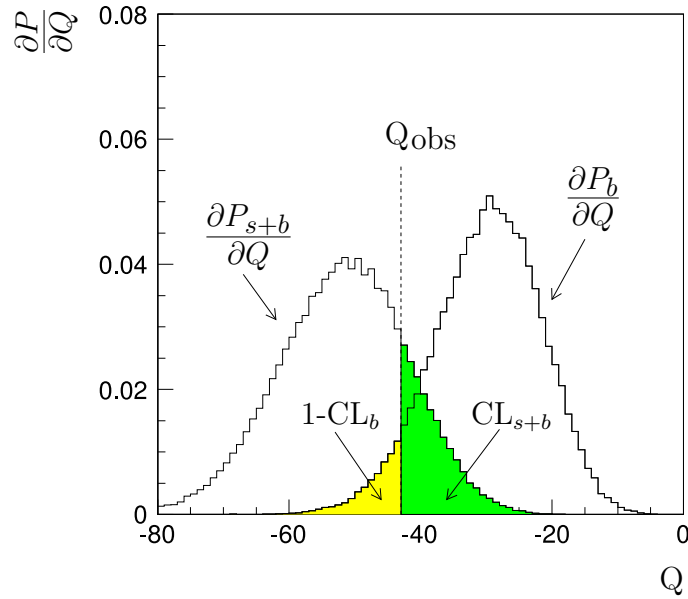


Figure 6.6.: Example of NLLR distributions for the *background only* and *signal plus background* hypothesis. The quantities $1-\text{CL}_{s+b}$ and CL_b used for calculating the confidence level on the signal are shown as shaded areas. Adapted from [103].

The confidence level on the signal is given by:

$$\text{CL}_s = \frac{\text{CL}_{s+b}}{\text{CL}_b}. \quad (6.21)$$

To extract the limit on the signal strength, the scale of the signal is optimised such that the confidence level is at the desired level. Limits reported in this thesis exclude the signal at 90% CL (*i.e.*, $\text{CL}_s = 10\%$) and are calculated with the Collie [104] package. This tool also allows for the estimation of the effects of systematic uncertainties on the signal and background distributions on the extracted limits, by producing pseudo-data with the MC predictions shifted by a Gaussian-distributed random number.

6.6. Half-life calculation

It is useful to report the observed signal strength (or limits on signal strength) as a half-life so that it can be compared to other experimental results and theoretical calculations.

Exponential decay gives the number of unstable nuclei as a function of time ($N(t)$) as:

$$N(t) = N(0)e^{-\lambda t}, \quad (6.22)$$

where $N(0)$ is the initial number of nuclei and λ is the decay constant. The half-life ($t^{1/2}$) is related to the decay constant by:

$$t^{1/2} = \frac{\ln(2)}{\lambda}. \quad (6.23)$$

Given that the half-lives of the processes investigated in NEMO-3 are much larger than the time span of the experiment, Equation 6.22 is very well described by its Taylor expansion to the first order:

$$N(t) = N(0) (1 - \lambda t). \quad (6.24)$$

The observed number of decays during run time t_{Run} is given, for a detection efficiency η , by:

$$N_{\text{Obs}} = \eta (N(0) - N(t_{\text{Run}})) = \eta N(0) \frac{\ln(2)}{t^{1/2}} t_{\text{Run}}. \quad (6.25)$$

The initial number of nuclei can be written as:

$$N(0) = \frac{N_A m}{M}, \quad (6.26)$$

where N_A is Avogadro's number, m is the mass of the isotope of interest and M its atomic mass.

The measured half-life is therefore given, as a function of the experimental quantities defined above, as:

$$t^{1/2} = \frac{\eta}{N_{\text{Obs}}} \frac{N_{Am}}{M} \ln(2) t_{\text{Run}}. \quad (6.27)$$

6.7. Analysis data set

For the analysis described in this thesis the *standard* set of NEMO-3 runs is used. In this sample runs are included in which part of the PMT DAQ system was switched off in addition to runs where the entire detector was operating nominally.

The data set is split in two subsets: phase 1 includes the runs taken before the installation of the anti-radon facility while runs taken with the facility in operation constitute phase 2.

The exposure time of the data set is listed in Table 6.1. With a ^{48}Ca mass of 6.9 g, the total exposure of the analysed data is 36.7 g yr.

Phase	Run time (days)	Dead time (days)	Exposure (days)
1	391.9	5.3	386.6
2	1548.3	16.3	1531.9
Both	1940.2	21.6	1918.5

Table 6.1.: Exposure of the NEMO-3 *standard* analysis run set. Exposures are given for each phase and for the entire run set.

Chapter 7.

Measurement of backgrounds in the ^{48}Ca source

One of the greatest strengths of NEMO-3 is its ability to discriminate events according to their topology. This allows for a very pure selection of double- β decay events by requiring that two electrons are present in the event. Nevertheless, several mechanisms allow for more prevalent decays in the detector material and surroundings to mimic a two-electron event. These constitute the backgrounds to double- β decay analyses and can be understood by analysing control channels with alternative selection criteria.

7.1. Background production processes

Several processes can lead to events with two reconstructed electrons, constituting a background to double- β decay analyses. Typically these will originate from β decaying contaminants in the detector and γ emitters in the detector or its surroundings. In addition to processes which result in final states identical to that of double- β decays (two electrons being emitted from the same point in the source) a few other topologies can be mis-reconstructed as two-electron events:

- processes with an electron-positron pair in the final state where the positron is reconstructed as an electron;
- processes with only one electron crossing the source foil plane – these will be reconstructed as two objects.

While there are no analysis methods to exclude events of the first type, the latter two classes of events are only backgrounds in the sense that analysis tools to identify them are not 100% efficient and as such can be greatly reduced. For both types of events measuring the charge of the electron-like objects via their track curvature allows for their discrimination. The timing of the calorimeter signals can be used in addition to the track curvature to exclude events of the last type.

7.1.1. Background classification

Several reactions with detector materials allow for the final states described above to be generated by very common β decays and γ transitions. In NEMO-3 analyses it is useful to classify backgrounds with respect to the location and nature of the contaminants.

Internal backgrounds

Internal backgrounds are those that originate from contaminants in the double- β decay sources. The processes that will produce backgrounds will typically be β decays, possibly accompanied by one or more γ transitions. Interactions of the emitted electron and γ 's with the high density materials of the source foils lead to final states of the types described above.

The processes via which these decays acquire two-electron-like signatures are:

- the Møller scattering of a β decay electron off an atomic electron (Figure 7.1a);
- a β decay followed by the emission of an electron via internal conversion (Figure 7.1b);
- a β decay followed by the Compton scattering of a nuclear de-excitation γ off an atomic electron (Figure 7.1c).

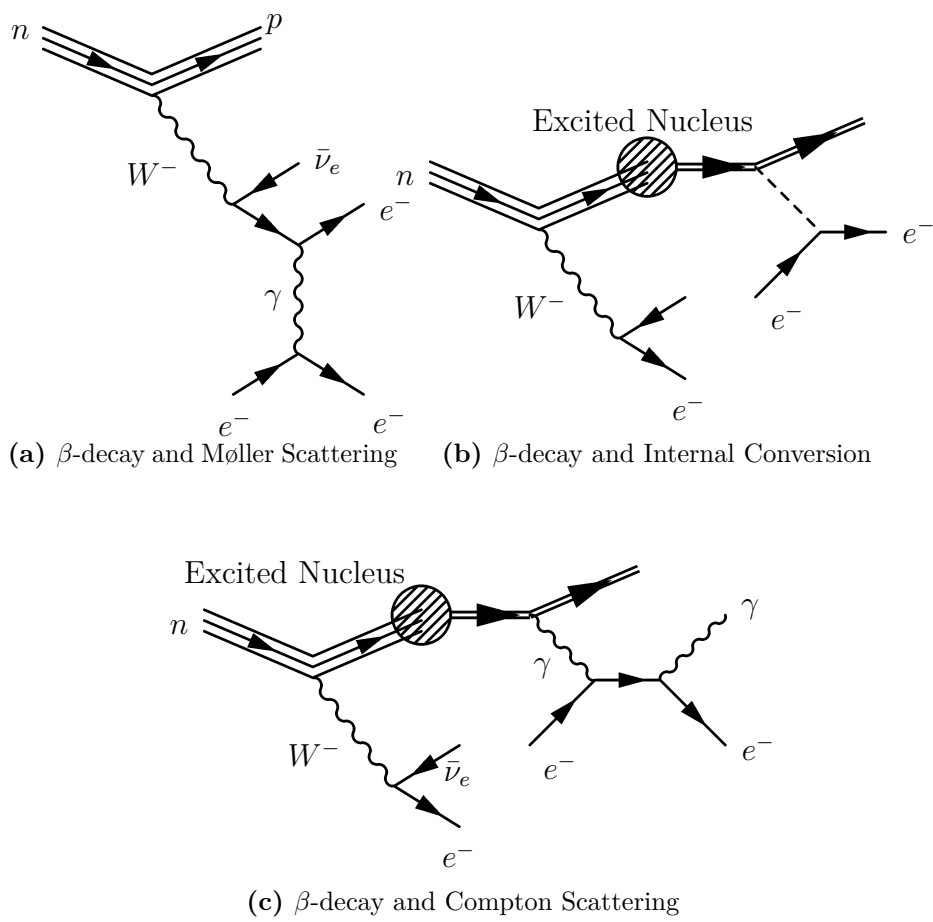


Figure 7.1.: Internal background production processes.

External backgrounds

Backgrounds produced by decays occurring outside of the source foils are classified as external backgrounds. These originate from detector components such as PMTs and shielding or from radioactivity in the laboratory environment.

In addition to the case where a single electron (*e.g.*, produced by an external γ interacting close to the surface of a scintillator block) traverses the tracking volume, crossing the source foil, external background processes can be reconstructed as two-electron events following interactions with the source foil. In general this mechanism involves γ 's which escape the material where they are produced and travel through the dense source foil where they interact producing electrons. The interactions responsible for this are:

- electron-positron pair production in the proximity of nuclei (Figure 7.2a), with the positron being mis-reconstructed;
- Compton scattering followed by Møller scattering off atomic electrons (Figure 7.2b);
- double Compton scattering off atomic electrons (Figure 7.2c).

Radon backgrounds

It is useful to classify backgrounds originating from decays of ^{222}Rn separately from other external backgrounds. Since ^{222}Rn is a gas and tends to emanate into the tracker volume, its progeny will be deposited on internal surfaces of the detector. This topic will be examined further in Section 7.2.2.

7.2. Sources of background

Even though materials used in the construction of the detector were extensively screened for potential radioactive contaminants, the main background sources for double- β decay analyses in NEMO-3 originate from naturally occurring isotopes in the detector components.

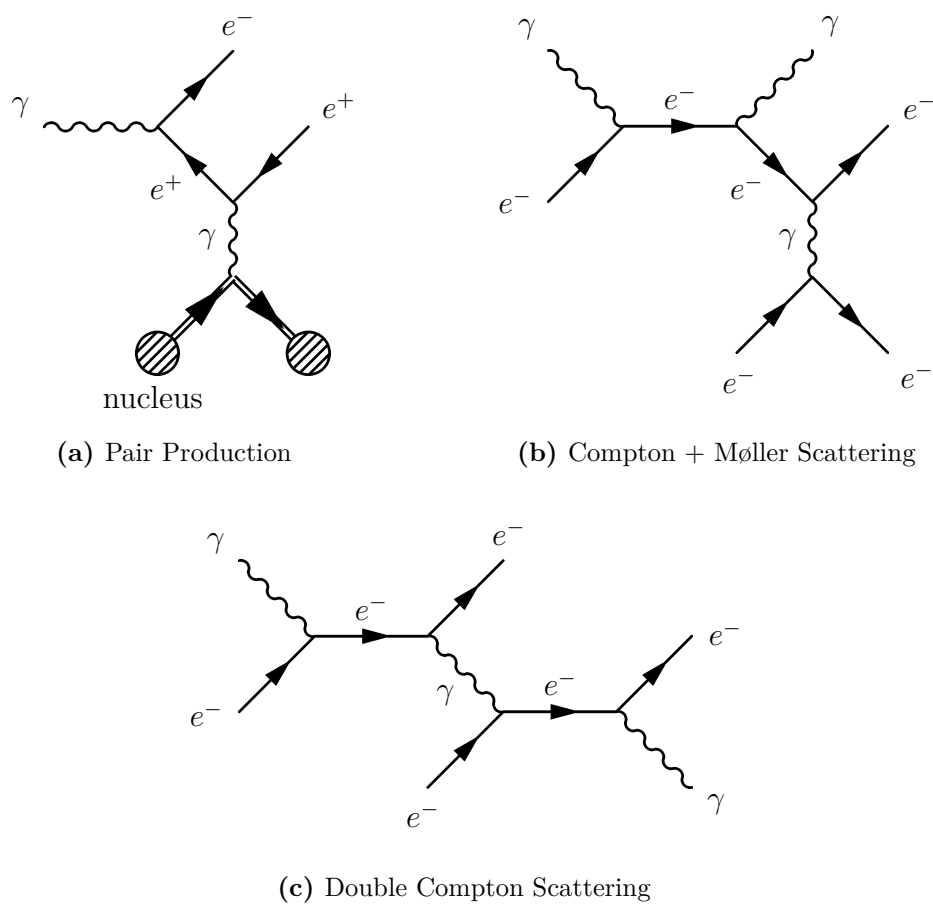


Figure 7.2.: External background production processes.

Given that all double- β decay isotopes in NEMO-3 have Q-values above 2.5 MeV, backgrounds to $0\nu\beta\beta$ analyses consist mainly of naturally occurring decays with Q-values of this order and of the tail of the $2\nu\beta\beta$ spectrum. In general, the same does not apply to $2\nu\beta\beta$ analyses, where lower energy decays also contribute to the total background.

It is important to note that given its high Q-value both $0\nu\beta\beta$ and $2\nu\beta\beta$ modes of ^{48}Ca are relatively insensitive to naturally occurring backgrounds.

7.2.1. Decay chains

Decay chains are a naturally occurring phenomenon where a primordial radioactive isotope with a half-life much longer than the age of the Earth slowly decays into more rapidly decaying isotopes forming a chain of unstable isotopes with different half-lives, decay modes and Q-values. Isotopes belonging to these chains are present in small quantities in most materials. These small quantities of naturally occurring isotopes are an important component of the NEMO-3 background. In particular two chains, one originating from ^{232}Th (thorium series) and the other originating from ^{238}U (uranium series) lead to isotopes with high energy β decays. Schemes for these chains are shown in Figures 7.3 and 7.4, respectively.

Even though it is expected that pairs of isotopes which have short half-lives between them in the decay chains are in equilibrium, this cannot be assumed when long half-lives separate two isotopes. Chemical or mechanical processing of the materials in which these isotopes are present can remove specific elements of the chain, breaking the equilibrium. Isotopes which are connected by a sequence of half-lives much shorter than the life-time of NEMO-3 are assumed to be in equilibrium. A further source of equilibrium breaking comes from the nature of ^{222}Rn , present in the uranium series (Section 7.2.2).

An isotope present in the thorium series which is of particular concern is ^{208}Tl . This isotope undergoes β decays to excited states of ^{208}Po with a Q-value of 5 MeV and is always followed by the emission of two (65% of decays) or three (35% of decays) γ 's¹. One of the de-excitation γ 's always has an energy of 2.6 MeV which can present

¹The Q-values, branching ratios and half-lives reported throughout this chapter are taken from the National Nuclear Data Center ENSDF database [105].

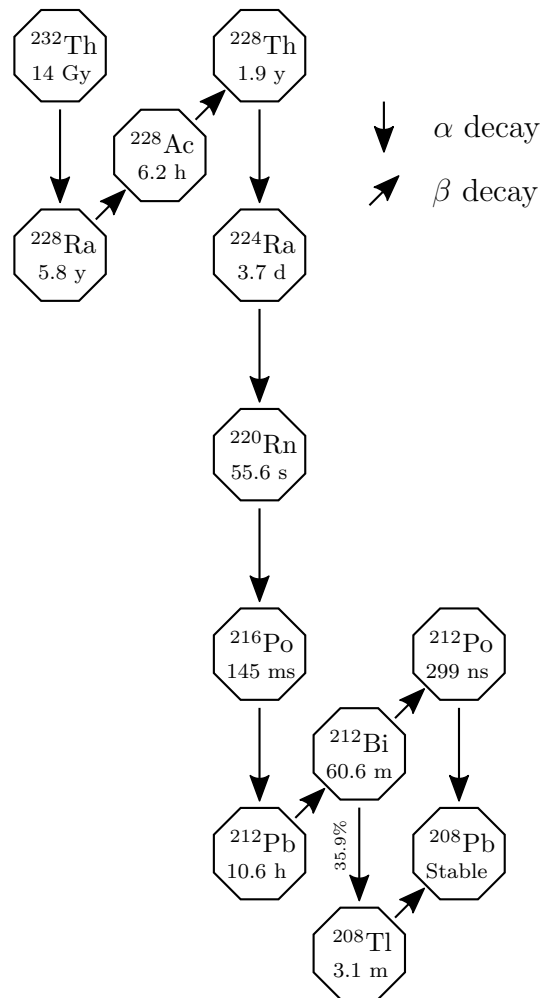


Figure 7.3.: Thorium natural decay chain. Both α and β decays are indicated, as are the half-lives of the isotopes and decay branching ratios.

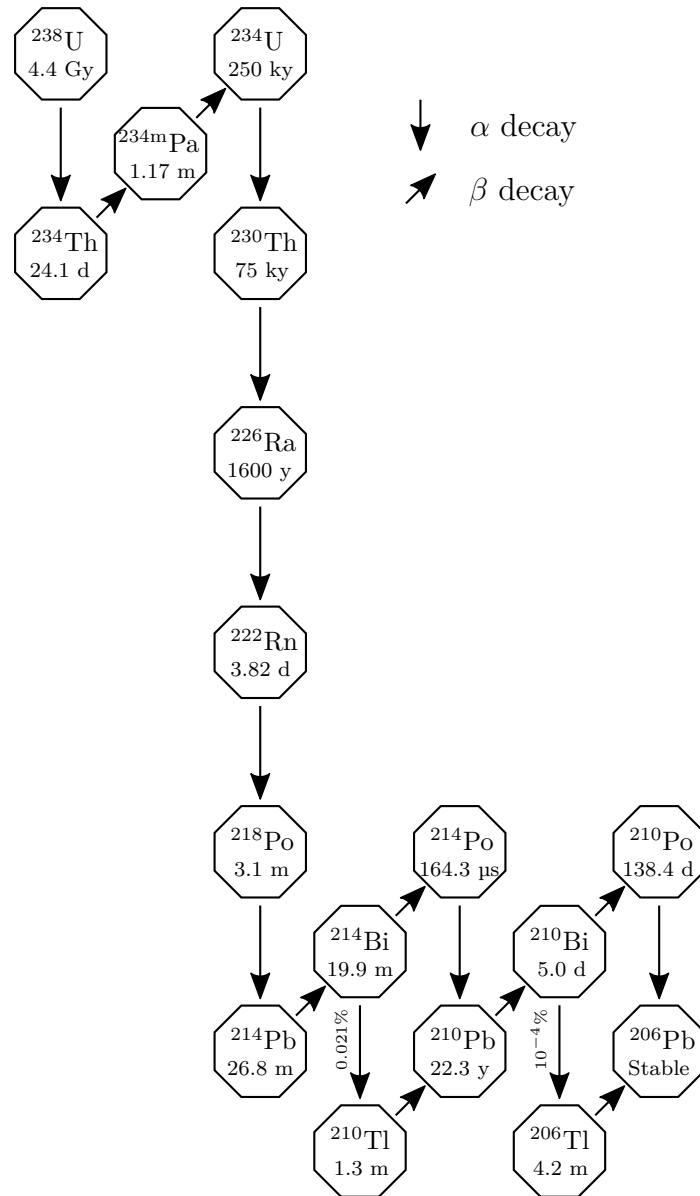


Figure 7.4.: Uranium natural decay chain. Both α and β decays are indicated, as are the half-lives of the isotopes and decay branching ratios.

a problematic background if internal conversion occurs, as such a decay could mimic double- β decay at energies close to the Q-values of the isotopes of interest. Because of the $\beta+2(3)\gamma$ topology of these decays, they can be constrained by analysing data where selected events have two or three reconstructed γ 's in addition to an electron.

Another isotope which presents a significant background to double- β decay analyses is found in the uranium series. With a Q-value of 3.2 MeV, ^{214}Bi decays to ^{214}Po with the subsequent emission of two γ 's (46% of decays), one γ (35% of decays) or directly to the ground state of ^{214}Po (19% of decays). While this background can also be constrained with the event topologies described above, the subsequent α decay of the ^{214}Po nuclei with a half-life of 164 μs provides a powerful handle on the activity of ^{214}Bi in the detector. By keeping the tracker active for a few ^{214}Po half-lives after the trigger it is possible to identify short tracks associated to an electron vertex which are delayed with respect to the electron track. These short delayed tracks are indicative of a ^{214}Bi β decay to ^{214}Po followed by the α decay of ^{214}Po to ^{210}Pb (BiPo events) and can be used to tag or veto this class of events.

7.2.2. ^{222}Rn

The BiPo process described above lies downstream of ^{222}Rn in the uranium decay chain (Figure 7.4). This isotope is unique in the natural chains in that it is a noble gas with a relatively long half-life of 3.8 days². Being a noble gas, ^{222}Rn will diffuse through most materials with relative ease. This, in combination with a half-life which can be longer than the time it takes ^{222}Rn to diffuse through materials, implies that ^{222}Rn resulting from the contamination of detector materials with isotopes upstream of ^{222}Rn in the decay chain will emanate out of these materials, possibly into the tracker volume where it can decay to ^{218}Po . The polonium atoms resulting from the α decay of ^{222}Rn will often be in an ionised state and will have a tendency to adhere to surfaces in the tracker. The result of this is that ^{222}Rn progeny such as the BiPo isotopes will contaminate the surfaces of detector components.

Besides emanating from materials inside the detector, ^{222}Rn will diffuse into the detector from the significantly more contaminated outside air through small leak paths or radon-transparent materials. A technique that drastically reduces this

²Another isotope of radon (^{220}Rn) is part of the thorium series. However it has a much shorter half-life than ^{222}Rn and as such it does not fully share the characteristics described here.

effect is the flushing of the volume of air immediately surrounding the detector with radon-free air. For the second phase of NEMO-3 this technique was implemented by constructing a tent around the detector which was flushed with air that had been passed through large charcoal traps kept at a low temperature. This reduced the activity of short-lived ^{222}Rn progeny in the detector by a factor of 6. This effect can be seen in Figure 7.5 where the activity of BiPo events measured inside the detector is shown over time.

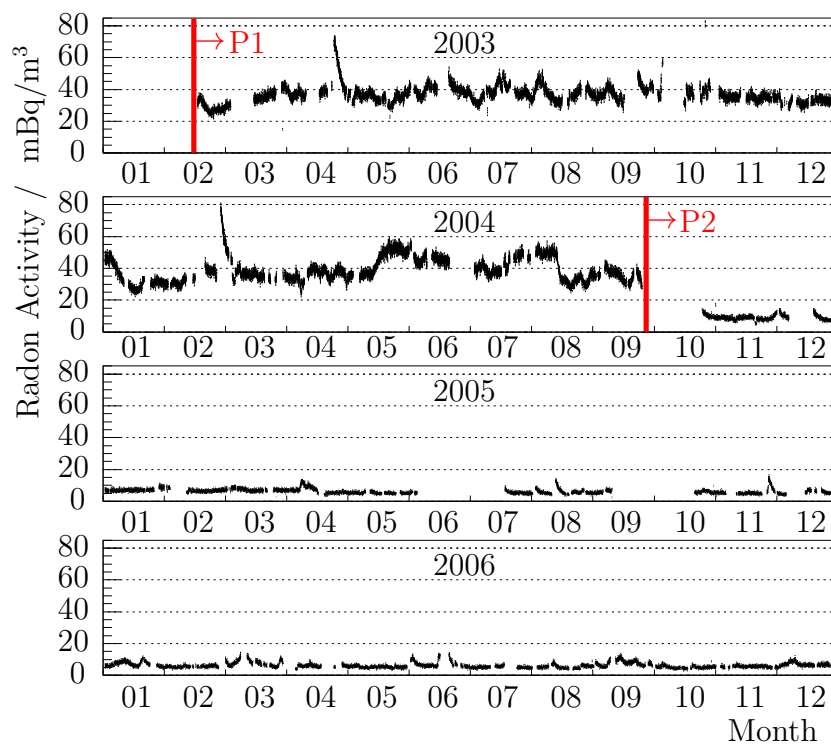


Figure 7.5.: Radon level in the NEMO-3 detector from 2003 to 2006. The radon activity was measured with BiPo events over the whole tracking volume [93]. The starting dates of phases 1 and 2 are labeled P1 and P2, respectively.

It is worth noting that such a reduction is not expected in the activity of ^{210}Pb or its progeny (^{210}Bi) as the half-life of this isotope is 22.3 years, which is longer than the life-time of the experiment. The contamination of ^{210}Pb is representative of the historical exposure to ^{222}Rn of the components. It is assumed that this exposure occurred mostly before the start of the experiment (*e.g.* during construction). However, isotopes downstream of ^{210}Pb do not present a significant background to double- β decay searches in NEMO-3 as the only decays with Q -values close to those

of double- β decays are α emissions, which do not constitute a background for the two-electron channel.

7.2.3. Other natural background sources

Two other naturally occurring contaminants are included in NEMO-3 backgrounds which do not belong to the decay chains described above.

^{40}K is a primordial isotope that decays mostly to ^{40}Ca with a Q-value of 1.3 MeV (89% of decays) and to ^{40}Ar with a Q-value of 1.5 MeV (11% of decays) via β and electron capture decays, respectively. The latter decay mode is almost always accompanied by a 1.5 MeV de-excitation γ . Given the prevalence of this isotope in nature, its decays contribute to both internal and external backgrounds.

^{60}Co has a half-life of 5.3 years, decaying to ^{60}Ni via β decay with a Q-value of 2.8 MeV. This transition occurs predominantly to an excited state of the ^{60}Ni nucleus, resulting in the emission of an electron with energy up to 0.3 MeV and two γ 's with energies of 1.2 MeV and 1.3 MeV. While, strictly speaking, this isotope does not occur naturally, it is produced by neutron capture reactions in ^{59}Co and as such trace amounts might be expected in the detector materials and surroundings, contributing to the external background.

7.2.4. Artificial contaminants in source foil

Additional background contributions arise from artificial isotope contamination of the double- β decay sources during their processing and production.

One such contaminant present in the ^{48}Ca source is ^{152}Eu . This isotope does not occur naturally but it is possible that a contamination could have been introduced in the ^{48}Ca source during enrichment or processing of the isotope. ^{152}Eu decays with a half-life of 13.5 years to ^{152}Gd via β decay (28% of decays) or to ^{152}Sm via electron capture (72% of decays) with Q-values of 1.8 MeV and 1.9 MeV, respectively. Both decay modes are always accompanied by at least one γ emission from nuclear de-excitation. Since the half-life of this isotope is comparable to the life time of the experiment it is expected that any contamination prior to the start of data taking

will persist throughout the duration of the experiment, with its activity gradually decreasing.

^{90}Sr in the ^{48}Ca source

^{90}Sr is a medium lived product of nuclear fission. It decays with a half-life of 28.8 years to ^{90}Y via low energy β decays with a Q-value of 0.5 MeV. While this decay is of too low energy to present a significant background to double- β decay analyses, its daughter isotope ^{90}Y decays to ^{90}Zr with a half-life of 64 hours and a Q-value of 2.3 MeV. To a very good approximation no γ emissions occur in either of these decays. Given the relatively short half-life of ^{90}Y it can be assumed that the activities of these two isotopes are in equilibrium.

This isotope has been identified as the main background source present in the CaF_2 discs. This can be seen in Figure 7.6 where the activity of the $^{90}\text{Sr}/^{90}\text{Y}$ system is measured over the life time of the experiment. While the measured half-life is not entirely consistent with the known half-life of ^{90}Sr , no other candidates are found in the ENSDF database which β decay with a similar Q-value and effective half-life (taking into account chains of short-lived isotopes). The discrepancy in the measured half-life could be explained by a small mis-modelling of the detector deterioration over time.

Strontium follows calcium as the next heavier element in the second group of the periodic table and so they exhibit similar chemical properties. It is therefore expected that exposure to ^{90}Sr during the processing of the CaF_2 source would easily lead to contamination.

7.2.5. $2\nu\beta\beta$ as a background to $0\nu\beta\beta$

The finite energy resolution of the detector causes the energy distributions of $2\nu\beta\beta$ and $0\nu\beta\beta$ to overlap making $2\nu\beta\beta$ an irreducible background to $0\nu\beta\beta$ searches. In the case of ^{48}Ca this effect is minimised by the improved energy resolution in the high energy region of the $0\nu\beta\beta$ distribution. However, the absence of other backgrounds in this region makes $2\nu\beta\beta$ the only significant background in the measurement of the $0\nu\beta\beta$ of ^{48}Ca .

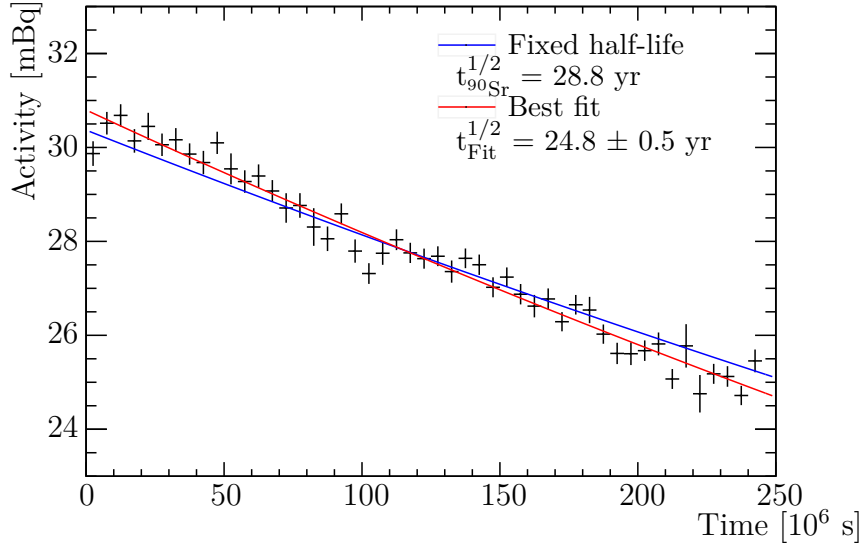


Figure 7.6.: Exponential decay of $^{90}\text{Sr}/^{90}\text{Y}$ in the ^{48}Ca source over the analysis run set. The activity was measured with one-electron events with an energy above 1 MeV. It is assumed that the data represent a pure ^{90}Y sample. Two exponential decay fits are shown: one with the half-life fixed to the known value; the other with the half-life as a free parameter.

7.2.6. Leakage

Decays originating in the neighbouring sources can make small contributions to the channels used in this analysis. The components which contribute are the most active backgrounds in the ^{150}Nd source (^{40}K , $^{234\text{m}}\text{Pa}$ and ^{214}Bi) and the $2\nu\beta\beta$ signal from the same source. All these contributions are very small and in this analysis their activities are fixed to the values measured in the ^{150}Nd double- β decay analysis [106].

7.3. NEMO-3 background model

In the present analysis, the background model detailed in [93] is used to constrain the activities of backgrounds from sources external to the CaF_2 .

Backgrounds due to ^{222}Rn were measured with BiPo events across the detector assuming that the contaminants are deposited on the surfaces. A map of the relative activities measured in different parts of the detector (foil surfaces around the source

foil cylinder and tracker wires) was created which is used in this work. A reduction factor of 6 is observed on these activities between phases 1 and 2.

An effective model of external background contributions was measured with $1e1\gamma$ events with calorimeter timing information consistent with the external hypothesis and crossing electron events where the same timing criterion is used. MC samples with decays from the radioactive sources described above being generated in several components of the detector, such as PMTs and parts of the shielding and structure were produced. The model which gave the best fit to real data over the whole detector is given in Table 7.1. As not all detector components (nor all possible radiation sources) were considered, this should be viewed as an effective model which describes the data well, not necessarily describing well the radioactivity of each component.

Detector component	Activity (Bq)			
	^{40}K	^{214}Bi	^{208}Tl	^{60}Co
PMTs	1078 ± 32	324 ± 1	27.0 ± 0.6	
Scintillator blocks	21.5 ± 0.9			
PMTs μ -metal shields				14.6 ± 2.6
Iron petals	100 ± 4	9.1 ± 1.0	3.1 ± 0.5	6.1 ± 1.8
Copper on petals				47.6 ± 7.8
Internal tower				18.4 ± 0.8
Iron shield		7360 ± 200	484 ± 24	
Air inside shielding*		660		

Table 7.1.: NEMO-3 external background model as reported in [93]. The activities are the best fit to $1e1\gamma$ (external) and crossing electron data over the entire detector.

* Phase 1 only.

The effect of this model on analysis channels was tested with data from the pure copper foils. Since these foils are intrinsically clean the external background contribution dominates over the internal and radon components, providing a good test for the model. Data obtained with one-electron, $1e1\gamma$ (internal) and two-electron selection criteria was shown to be well described by this model.

7.4. HPGe measurements of internal backgrounds

After the ^{48}Ca source was removed from NEMO-3 it was measured for internal contamination with HPGe detectors³. The source was measured in two HPGe detectors of different types: a thin planar detector, sensitive to lower energy γ 's; and a coaxial detector sensitive to higher energy γ 's.

Given the lack of γ emissions from the $^{90}\text{Sr}/^{90}\text{Y}$ system, no conclusive measurement of this contamination was achieved with HPGe detectors.

The resulting measurements are given in Table 7.2. Only positive measurements and limits relevant to this work are listed.

Isotope	Activity (mBq)
^{22}Na	0.10 ± 0.02
^{40}K	0.6 ± 0.1
^{152}Eu *	0.4 ± 0.1
^{210}Pb	4 ± 2
^{228}Th	< 0.1
^{238}U	< 0.45

Table 7.2.: HPGe measurement of internal backgrounds in the ^{48}Ca source. The data was taken between May and July of 2011 [107].

* Activity scaled to February of 2003, the reference date used in this analysis.

The positive measurement of ^{22}Na is not used in the internal background model as this is a cosmogenic isotope which decays via β^+ decay with a half-life of 2.6 years and Q-value of 2.8 MeV. The activity of such an isotope would have decreased significantly over the running of the detector and there is no evidence in data for the contamination of such a β^+ emitter.

The other measurements are used as inputs to the analysis: the measured activities of ^{40}K and ^{152}Eu are used to constrain these backgrounds directly; the limit on the activity of ^{228}Th is used to constrain the activities of ^{228}Ac and ^{208}Tl ; and the

³Prior to this there existed HPGe measurements of a CaF_2 sample from the same production batch as the one that was used in NEMO-3. These are not considered in this work as it is considered that the posterior measurement of the actual materials present in NEMO-3 provides a more accurate measurement of the source contaminants.

$^{234\text{m}}\text{Pa}$ background is constrained by the limit on the ^{238}U activity. For the indirect constraints secular equilibrium of the decay chains is assumed and branching ratios are taken into account.

As was described in Section 7.2.2, it is expected that long lived ^{222}Rn progeny such as ^{210}Pb accumulate on surfaces which may have been exposed to dirty air. This generates an ambiguity on applying the measured activity given above depending on whether a bulk or surface contamination is assumed. Given that it is not possible to resolve the ambiguity and also that the HPGe measurement is not precise, this measurement is not used as an input to the model.

7.5. Background fitting procedure

The best fit of the MC activities to data is obtained with a likelihood maximisation as described in Section 6.5.1. The fit is performed simultaneously across seven channels separated into the two phases of data taking. Six of these channels are used exclusively for the background measurement, while the other (two-electron channel) is used for both constraining the internal background and the signal (Table 7.3). Each channel is fitted on only one histogram: the summed energy of the selected particles (electrons and γ 's); or in the 1e1 α channel the length of the α track. In total, fourteen histograms with independent data sets participate in the fit.

Channel	Fitted variable	Constrains
1eN γ ($N \geq 0$)	E_e	Internal backgrounds and ^{210}Bi
1e1 γ (internal)	$E_e + E_\gamma$	Internal, external and radon backgrounds
1e2 γ	$E_e + \sum_i E_{\gamma_i}$	Internal, external and radon backgrounds
1e1 α	L_α	^{214}Bi
1e1 γ (external)	$E_e + E_\gamma$	External backgrounds
Crossing electron	$\sum_i E_{e_i}$	External backgrounds
2eN γ ($N \geq 0$)	$\sum_i E_{e_i}$	Internal backgrounds and signal

Table 7.3.: Analysis channels used in the background measurement. The variable used in the global fit and the backgrounds each channel is most sensitive to are listed.

A total of 33 parameters are used for measuring the backgrounds and one parameter is used for measuring the $2\nu\beta\beta$ signal (Table 7.4).

The external backgrounds are constrained to the central values reported in [93] being allowed to float within Gaussians with $\sigma = 10\%$. This is to account for possible local variations in the activities which would be averaged out in the full-detector measurement. Where HPGe measurements of the internal contamination are available, these are included in the fit as Gaussian constraints, using the statistical uncertainty on the HPGe values as the standard deviation for the constraint.

The activities of BiPo contributions to the radon background were first measured exclusively in the $1e1\alpha$ channel with the result of this measurement being applied as a Gaussian constraint on the global fit. These activities are measured separately for Phase 1 and Phase 2 as a reduction in the activity is expected in the latter.

Since the signal ($2eN\gamma$) channel is also sensitive to the large contribution of ^{90}Y to the internal backgrounds, the activity of the $^{90}\text{Sr}/^{90}\text{Y}$ system is measured separately in the $1eN\gamma$ and $2eN\gamma$ channels. The difference in the two results is used to estimate the systematic uncertainty on the measurement of the internal backgrounds.

Background type	Parameters	Comments
Internal	5	Parameters are constrained with a Gaussian around the activities measured in HPGe detectors.
$^{90}\text{Sr}/^{90}\text{Y}$	2	Fitted in the $2eN\gamma$ channel separately from other channels.
External	16	Parameters are constrained with a Gaussian around the activities reported in [93] with $\sigma = 10\%$.
Radon	10	^{214}Bi activities fitted separately in Phase 1 and Phase 2 data.

Table 7.4.: Overview of the parameters used in the global fit. The number of parameters assigned to each background type is listed. The detailed description of the individual parameters is given in Tables 7.5, 7.6 and 7.7.

Isotopes which are medium-lived and are expected to decay away over the running time of the experiment are weighed according to their half-lives. These isotopes are $^{90}\text{Sr}/^{90}\text{Y}$ ($t^{1/2} = 28.8$ yr), ^{152}Eu ($t^{1/2} = 13.5$ yr) and $^{210}\text{Pb}/^{210}\text{Bi}$ ($t^{1/2} = 22.2$ yr). The activities reported in this analysis are corrected to February of 2003. This

weighting is not used on ^{60}Co samples as they present a small contribution to the background model, and given that this isotope is neutron activated it is unclear whether its activity should be reduced over time according to the half-life.

7.6. General event selection

A set of quality criteria is applied to all analysed data with the aim of removing events in which unstable or dead PMTs participate. Events are removed if any calorimeter module hit in the event satisfies any of the following criteria:

- there is no calibration data (energy or time) available for the module;
- a problem was identified with the module during radioactive source calibration runs;
- laser calibration runs reported an abnormal energy scale instability for the module.

Additionally all calorimeter hits assigned to an analysis object (electron or γ) are required to be in time with the event. This eliminates uncorrelated noise.

7.6.1. Hot runs

When analysing events with one electron and one γ , a region of the outer calorimeter in sectors nine and ten was found which had a significant excess of γ hits compared to neighbouring regions (Figure 7.7a). Furthermore, it was observed that this excess of events was confined to a few runs (Figure 7.7b). While most of these events are removed by calorimeter stability requirements, runs where this abnormal behaviour was observed (8779 to 8786) are excluded from this analysis.

7.6.2. Energy threshold

For all electron and γ objects in this analysis the energy threshold is set at 400 keV. While previously published NEMO-3 analyses have used 200 keV for the energy threshold [85], in more recent analyses discrepancies were observed in the single

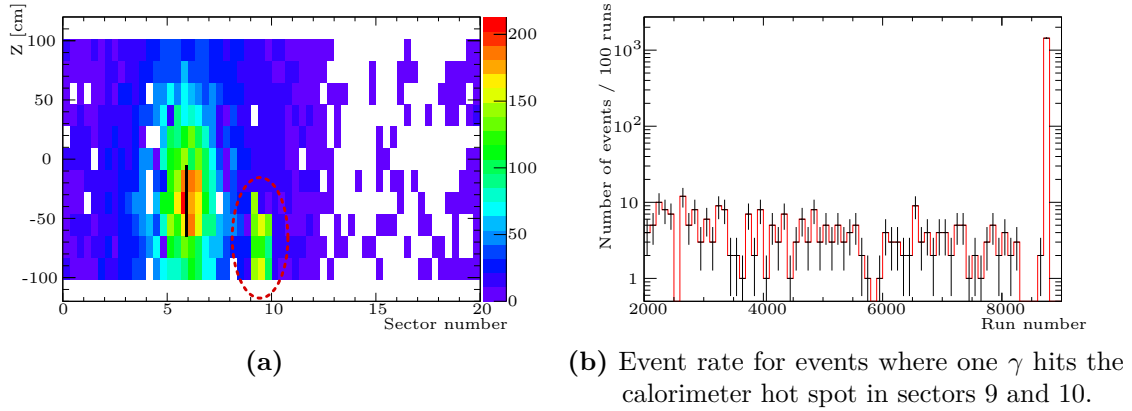


Figure 7.7.: Abnormal calorimeter activity leading to the exclusion of runs 8779 – 8786. The distributions shown were obtained with events with one electron and one γ . The calorimeter outer wall γ occupancy is shown in (a), with the position of the ^{48}Ca source shown as a black strip in sector 5, and the region of high activity circled in red. In (b), the rate of events where one γ hits the calorimeter hot spot in sectors 9 and 10 is shown as a function of the run number. The event rate is shown in red with the statistical uncertainty given black.

electron channel below 400 keV [31]. Discrepancies at the low end of the energy spectrum are also observed in the ^{48}Ca data if the threshold is set at 200 keV. In particular, a level of ^{152}Eu three times as high as was measured in HPGe detectors is required if the lower threshold is used. Being a small source which exposes just a part of the detector, it is also expected that ^{48}Ca data is particularly susceptible to spurious activity of the type reported in Section 7.6.1 above.

The agreement between data and MC for two background measurement channels (1eN γ and 1e1 γ internal) is shown in Figure 7.8 for three different thresholds: 200, 300 and 400 keV. A better description of the low end of the one-electron energy spectrum is achieved with higher thresholds and a better model of the background contribution from γ emitters is also obtained with a higher threshold.

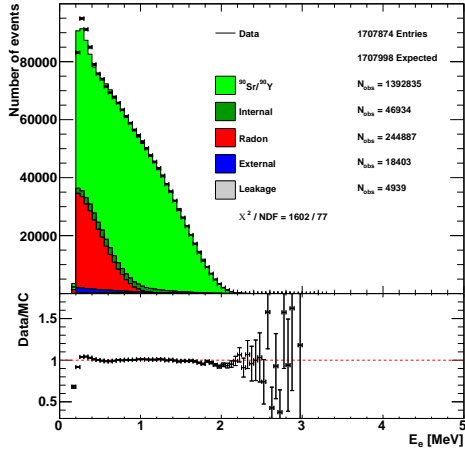
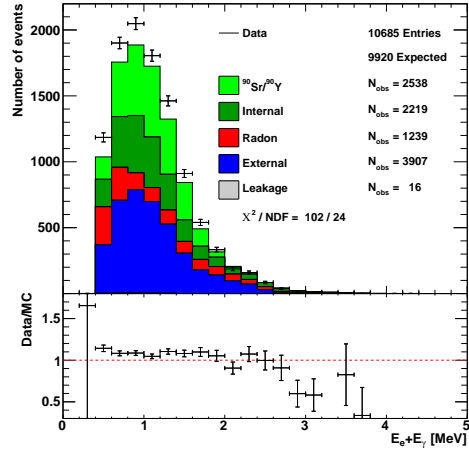
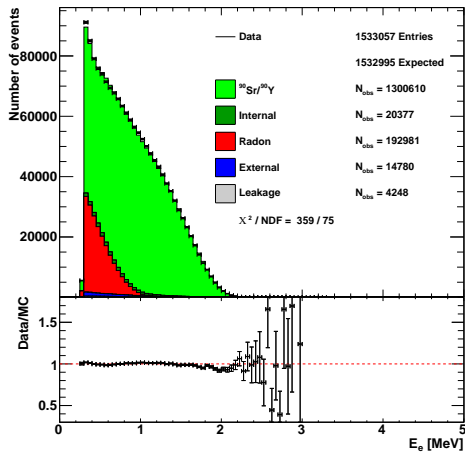
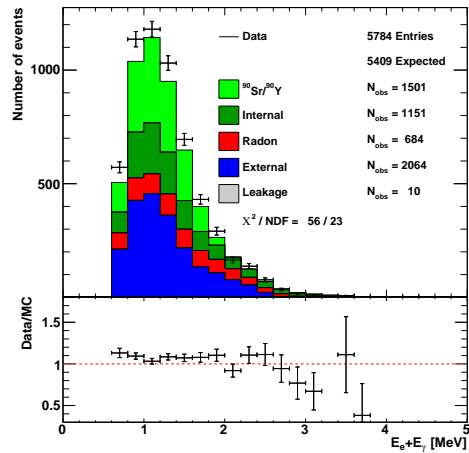
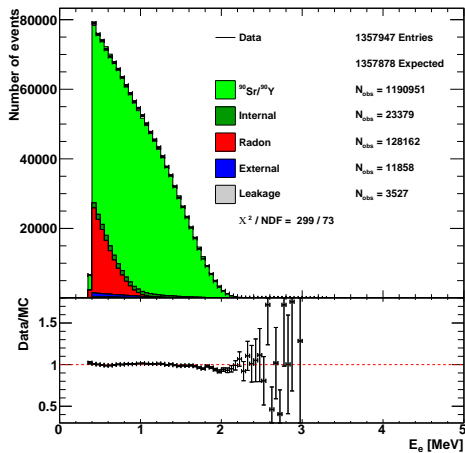
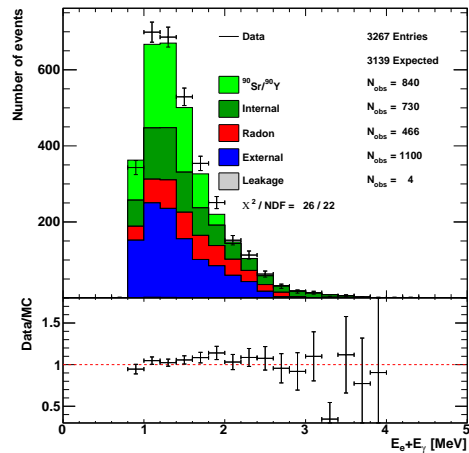
(a) $1eN\gamma$ 200 keV threshold(b) $1e1\gamma$ (internal) 200 keV threshold(c) $1eN\gamma$ 300 keV threshold(d) $1e1\gamma$ (internal) 300 keV threshold(e) $1eN\gamma$ 400 keV threshold(f) $1e1\gamma$ (internal) 400 keV threshold

Figure 7.8.: Distributions of total energy in $1eN\gamma$ and $1e1\gamma$ (internal) events for three energy thresholds. A discrepancy in the low end of the $1eN\gamma$ electron energy distribution is seen with a threshold of 200 keV. A gradual improvement is seen in the $1e1\gamma$ channel as the threshold is increased.

7.7. Background measurement channels

In this section, the selection criteria for the channels used to measure the backgrounds in the ^{48}Ca source are described. Distributions are shown with the MC scaled for the activities resulting from the background measurement.

7.7.1. $1eN\gamma$

The $1eN\gamma$ channel is mostly sensitive to internal backgrounds and in particular to pure β sources like the $^{90}\text{Sr}/^{90}\text{Y}$ system. This channel also constrains the activity of the ^{210}Bi backgrounds.

Events are selected which have one electron track originating from the ^{48}Ca source. For simplicity, no criterion is applied on the number of calorimeter hits without an associated track, so any number of γ 's (including zero) is accepted. Given the dominance of the $^{90}\text{Sr}/^{90}\text{Y}$ system, events with one or more γ 's are largely outweighed by events with no γ 's.

In addition to the general selection described in Section 7.6.2 above, the following criteria are applied to events:

- there is only one electron with energy above 400 keV in the event;
- the electron track is longer than 50 cm, intersects the ^{48}Ca strip and its curvature is consistent with a negatively charged particle emerging from the source foil;
- the electron hits the front face of a calorimeter module;
- the electron does not hit a calorimeter block in the inner (closest to the source foil) rings of the petals;
- there are no delayed α tracks in the vicinity of the electron vertex.

The electron energy distributions which are included in the background fitting procedure can be seen in Figure 7.9.

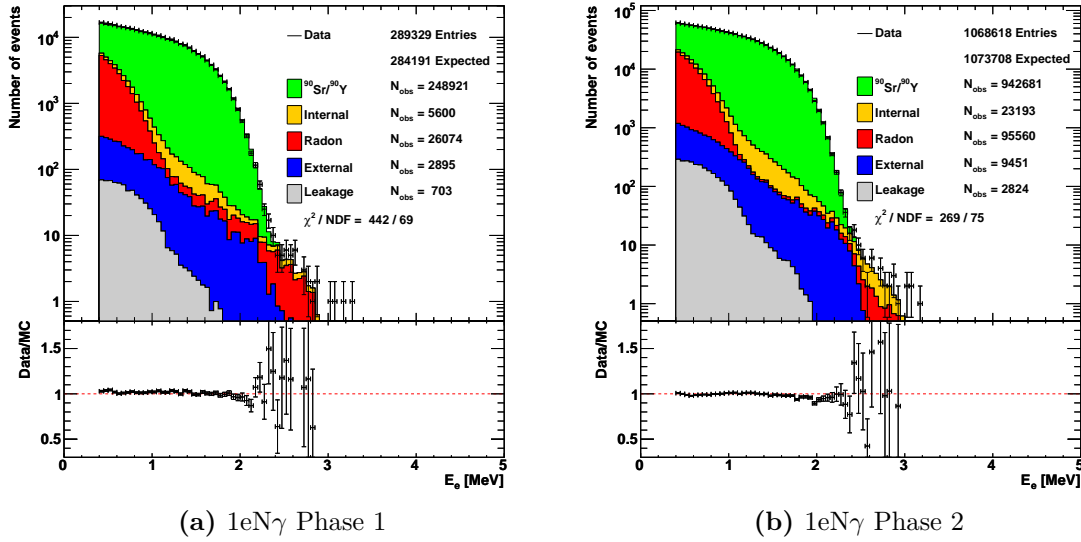


Figure 7.9.: Electron energy distribution in 1eN γ events.

7.7.2. 1e1 γ (internal)

The 1eN γ channel is particularly sensitive to γ emitting components of the internal background and external background components. There is a large contribution from the $^{90}\text{Sr}/^{90}\text{Y}$ system with the γ originating from bremsstrahlung in the source foil. This can be seen in the distribution of the opening angle between the electron and the γ (Figure 7.10), where the $^{90}\text{Sr}/^{90}\text{Y}$ component peaks in the collinear regime.

In addition to the selection criteria applied to 1eN γ events, the following cuts are applied to 1e1 γ (internal) events:

- there is only one cluster of calorimeter hits not associated to a track with an energy greater than 400 keV;
- the p-value for the internal hypothesis is greater than 4% and smaller than 1% for the external hypothesis (Section 6.4).

The distribution of the summed energies of the electron and the γ is included in the global fit (Figure 7.11). While a good agreement is obtained between data and MC in phase 2, this is not the case for phase 1. The MC model significantly underestimates the data for phase 1, indicating a possible mis-modelling of the activities of backgrounds due to ^{222}Rn . This discrepancy can be resolved if the

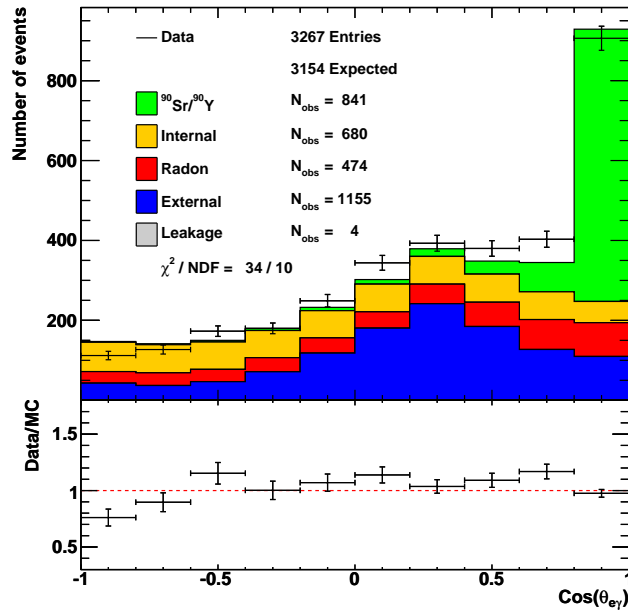


Figure 7.10.: Distribution of the cosine of the opening angle between the electron and the γ in $1e1\gamma$ (internal) events. Both data taking phases are included.

activities of such backgrounds are increased to the point where the MC description of the $1e1\alpha$ channel (Section 7.7.4) becomes poor. This suggests a systematic difference in the predicted efficiencies for the $1e1\gamma$ and $1e1\alpha$ channels. It will be shown in Section 8.3 that fluctuations in the predicted radon background have a negligible effect on double- β decay measurements.

7.7.3. $1e2\gamma$

The selection criteria for the $1e2\gamma$ channel are the same as the criteria for $1e1\gamma$ event selection, with the difference that two γ 's above 400 keV are required to pass the same cuts. The main purpose of including this channel is to constrain the activity of the internal ^{208}Tl background. This background component dominates the higher end of the spectrum of the total energy in the event (Figure 7.12).

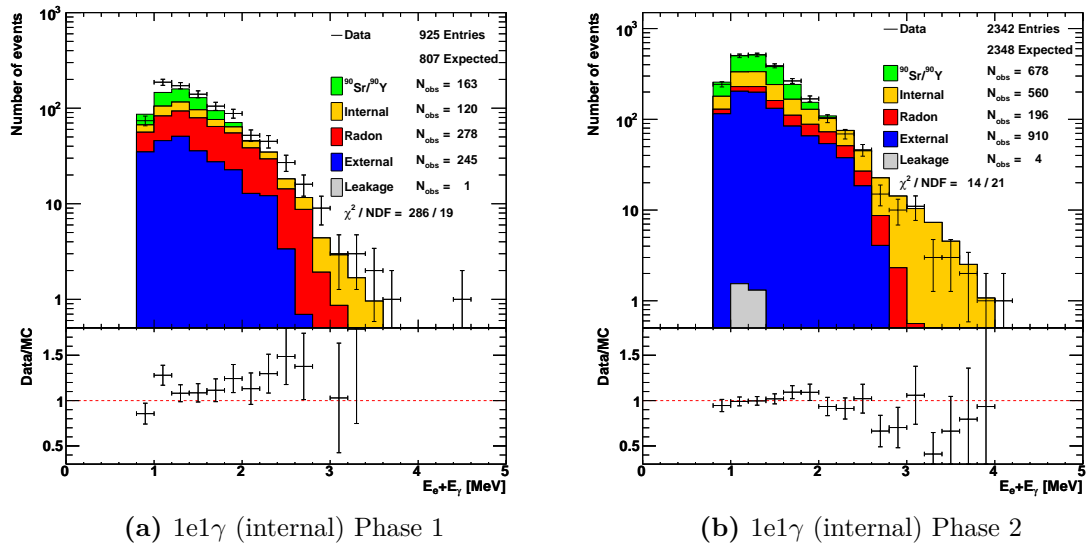


Figure 7.11.: Distribution of the summed energy of the electron and the γ in $1e1\gamma$ (internal) events.

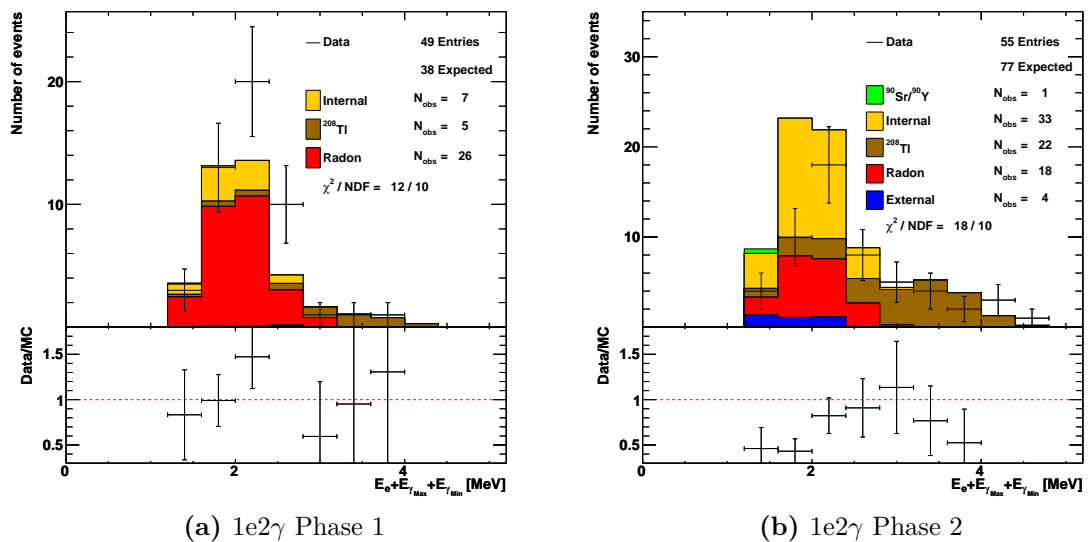


Figure 7.12.: Distribution of the summed energy of the electron and the two γ 's in $1e2\gamma$ events. The contribution of the internal ^{208}Tl background is shown separately from the other internal backgrounds.

7.7.4. 1e1 α

The 1e1 α channel is designed to detect BiPo events in the source foil. It is only sensitive to decays occurring either on or close to the surface of the foil, including the tracker layers close to the foil.

In addition to the general event selection, the criteria for the 1e1 α events are:

- only one reconstructed electron exists in the event, and its energy is at least 200 keV;
- the electron track is at least 50 cm long and it intersects the ^{48}Ca source;
- one delayed α track is reconstructed in the vicinity of the electron vertex which contains more than one tracker hit;

Given that the fitted distribution for this channel is the length of the α track and not the electron energy, the energy threshold is relaxed in this selection. The α track length allows for the discrimination of the location of the BiPo contamination by effectively measuring the energy lost in the tracker volume by the α particles. While α 's originating deep in the bulk of the source are not expected to reach the tracker volume, α 's from decays on the surface of the source are expected to travel the furthest into the tracker (Figure 7.13).

7.7.5. External background measurement channels

1e1 γ (external)

The external 1e1 γ channel provides, in conjunction with the crossing electron channel, constraints on the activities of external background samples (Figure 7.14). The selection criteria for this channel follow those of the equivalent internal channel with two differences:

- the requirement on the timing hypotheses is reversed with the p-value for the internal hypothesis being smaller than 1% and larger than 4% for the external hypothesis;
- events where the electron hits the inner rings of petal calorimeter modules are included in the selection.

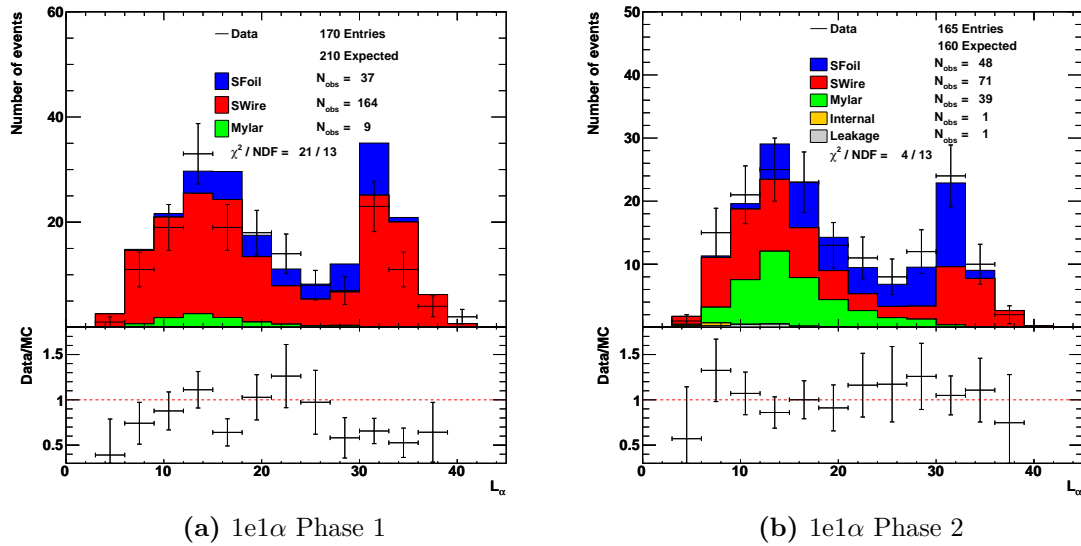


Figure 7.13.: Distribution of the length of the delayed α track in $1e1\alpha$ events. Distributions arising from ^{214}Bi contamination in the bulk of the Mylar sheets (green), the surface of the tracker wires (red) and the surface of the source foil (blue) are shown.

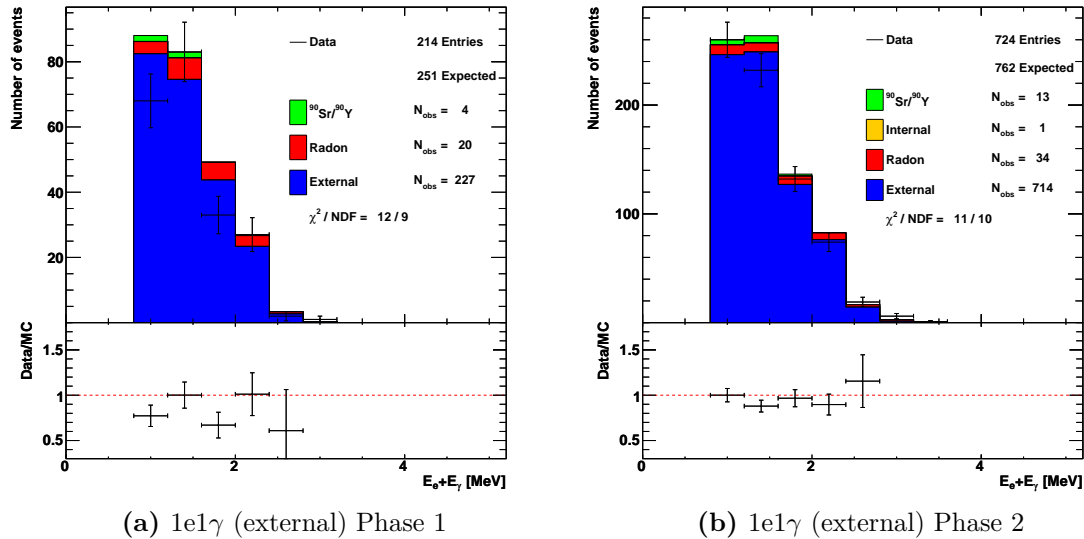


Figure 7.14.: Distribution of the summed energy of the electron and the γ in $1e1\gamma$ (external) events.

Crossing electron

Like the external $1e1\gamma$ channel described above, the crossing electron channel selection criteria are closely related to those of the $2eN\gamma$ channel. This channel will be described in more detail in Section 8.1. In general terms, two electron tracks are required to intersect the ^{48}Ca source. Their timing and track curvatures are required to be consistent with that of a single particle traversing the tracking volume. The distribution of the summed energy of the two calorimeter hits associated to the crossing electron is used in the global fit to constrain the external background activities (Figure 7.15).

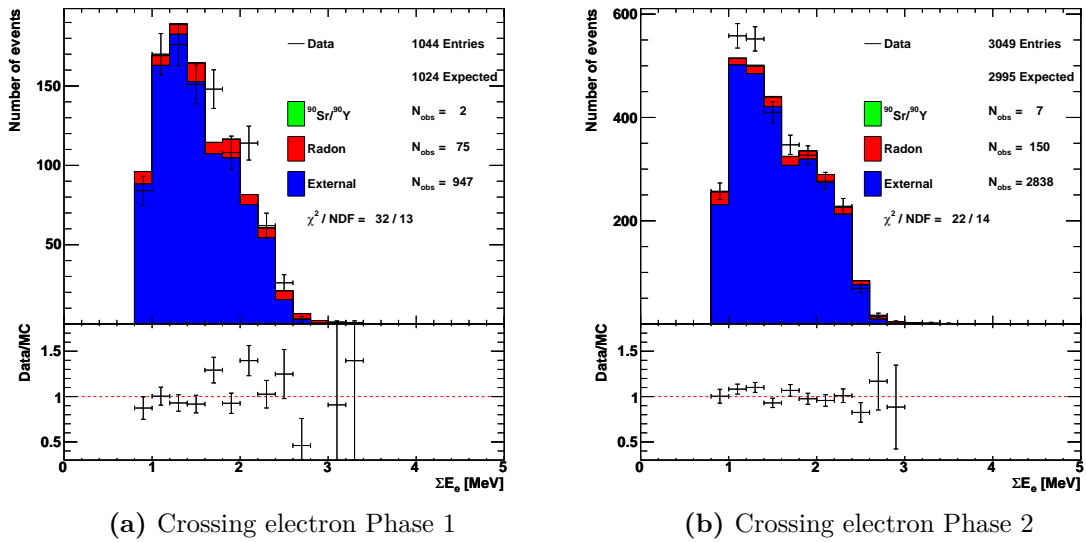


Figure 7.15.: Summed calorimeter energy distribution in crossing electron events.

7.8. Background measurement results

The activities resulting from the global fit to data described in Section 7.5 are summarised in this section.

Internal backgrounds

The activities of the internal background components are given in Table 7.5. A comparison to available HPGe measurements is shown in Figure 7.16. The dominant contribution results from the ^{90}Sr contamination of the source, with the activity of this isotope being three orders of magnitude higher than that of other contaminants. In general the fitted results are in good agreement with the HPGe measurements.

Isotope	Measured activity (mBq)
$^{90}\text{Sr}/^{90}\text{Y}$	29.6 ± 0.1
$^{228}\text{Ac}/^{208}\text{Tl}$ *	0.067 ± 0.009
$^{214}\text{Pb}/^{214}\text{Bi}$	0.08 ± 0.01
^{152}Eu	0.5 ± 0.1
^{40}K	0.49 ± 0.08
$^{234\text{m}}\text{Pa}$	0.3 ± 0.1

Table 7.5.: Results of internal background measurement.

* The activity of ^{228}Ac is reported here, the ^{212}Bi branching ratio of 35.9% should be applied to obtain the ^{208}Tl activity.

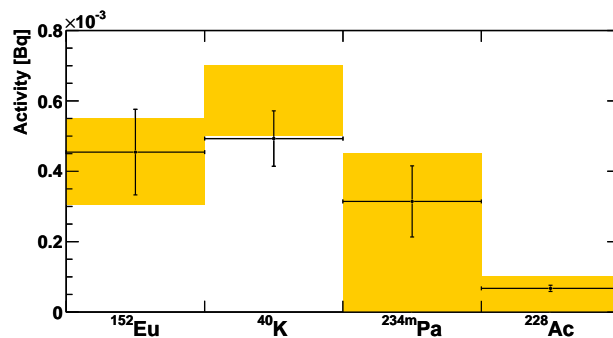


Figure 7.16.: Comparison between measured internal background activities and HPGe measurements [107].

External backgrounds

The resulting activities for the external background model are given in Table 7.6. In general, the measured activities are in good agreement with those of the external background model described in Section 7.3, with differences up to 10%.

Only one background component is measured to be significantly different from the background model measurement. The activity of $^{228}\text{Ac}/^{208}\text{Tl}$ contamination in the iron shield is required by the data to be 40% higher than the value measured across the whole detector. It should again be emphasised that the external background model is an effective one, with the aim of reproducing the γ flux through the detector. It is reasonable to expect that local variations occur and good agreement with data is shown in Figures 7.14 and 7.15.

Isotope	Detector component	Measured activity (Bq)	Ratio to model
$^{228}\text{Ac}/^{208}\text{Tl}$ *	Iron petals	8.7 ± 0.9	1.01
	Iron shield	$(1.9 \pm 0.3) \times 10^3$	1.39
	PMTs	75 ± 7	1.0
^{214}Bi	Iron petals	9 ± 1	1.0
	Iron shield	$(8.0 \pm 0.7) \times 10^3$	1.08
	PMTs	35 ± 2	1.08
	Laboratory air (P1)	726 ± 56	1.1
^{60}Co	Iron petals	6.0 ± 0.6	0.98
	PMTs μ -metal shields	15 ± 1	0.99
	Internal tower	18 ± 1	1.0
	Copper on petals	47 ± 5	0.98
^{40}K	Iron petals	100 ± 10	1.0
	PMTs	$(1.18 \pm 0.09) \times 10^3$	1.09
	Scintillator block **	18 ± 1	0.86

Table 7.6.: Results of external background measurement. The ratio to the activities reported in [93] is given.

* The activity of ^{228}Ac is reported here, the ^{212}Bi branching ratio of 35.9% should be applied to obtain the ^{208}Tl activity.

** Three parameters are used in the fit for this contribution, depending on the position of the scintillator blocks. The combined result is reported here.

Radon backgrounds

The activities of radon backgrounds measured in the ^{48}Ca data are reported in Table 7.7. Reduction factors of 3.5 and 6.9 are measured between the activities of the surface of the foil and surface of the wires components between Phase 1 and Phase 2. This values are close to the expected factor of 6.

The activity of ^{214}Bi on the surface of the scintillator is measured to be roughly the same in the two phases. This component is mostly constrained in the external channels where it represents a very small fraction of the total number of events.

Isotope	Location	Measured activity (Bq)
^{210}Bi	Surface of the foil	0.20 ± 0.06
	Surface of the scintillators	44 ± 4
	Surface of the wires	13 ± 1
^{214}Bi (both phases)	Mylar	$(2.1 \pm 0.6) \times 10^{-3}$
^{214}Bi (Phase 1)	Surface of the foil	$(2.1 \pm 0.2) \times 10^{-3}$
	Surface of the scintillators	1.1 ± 0.5
	Surface of the wires	0.96 ± 0.5
^{214}Bi (Phase 2)	Surface of the foil	$(0.60 \pm 0.06) \times 10^{-3}$
	Surface of the scintillators	0.5 ± 0.2
	Surface of the wires	0.14 ± 0.1

Table 7.7.: Results of radon background measurement.

Chapter 8.

^{48}Ca double- β decay results

In this chapter, the measurement of the $2\nu\beta\beta$ of ^{48}Ca and the search for its neutrinoless mode are described. The event selection criteria for double- β decay analysis is given in Section 8.1, with the resulting distributions shown in Section 8.2. The assessment of the systematic uncertainty on the measurements is given in Section 8.3 and the $2\nu\beta\beta$ and $0\nu\beta\beta$ results are given and discussed in Sections 8.4 and 8.5, respectively.

8.1. $2eN\gamma$ event selection

For the measurement of double- β decay signals, events are selected with two electrons emerging from the same region of the source foil, with calorimeter timing information consistent with the internal hypothesis. In addition to the general criteria described in Section 7.6, the following requirements are applied to $2eN\gamma$ events:

- there are only two reconstructed electrons in the event;
- the p-value for the internal hypothesis is greater than 4% and smaller than 1% for the external hypothesis;
- there are no hits in the calorimeter modules neighbouring those associated to the electrons;
- the electrons do not hit calorimeter modules in the petal rings closest to the source foil;

- the electron tracks point towards the front face of the calorimeter blocks;
- the electron tracks intersect the nominal source foil position at a distance smaller than 10 cm in the XY plane and 15 cm in the Z plane from each other;
- there are no delayed α tracks in the vicinity of the electron vertices.

The requirement on the distance between the intersection points of the tracks with the source foil plane is made deliberately loose compared to other NEMO-3 analyses [31,85]. There are two reasons for this. Firstly the vertices are reconstructed on an idealised source foil cylinder. Given that the ^{48}Ca source strip is known to be rotated from its nominal position (Section 5.1.1), the distance between the electron vertices is measured on a plane which does not correspond to the real source plane, therefore yielding results which are dependent on the position of the double- β decay vertex on the source strip and on the rotation angle. The second, and more important, reason is that a mis-modelling of this parameter is observed in events where the two electrons emerge from the same side of the source (Figure 8.1a), with the distribution of the distance between the two vertices in the Z direction being broader in data compared to MC.

Tracker cells traversed by two electrons simultaneously will yield information on only one of them. As this is a likely scenario for tracks sharing a vertex and with a small opening angle between them, it is expected that events where the two tracks are on the same side of the tracking volume are particularly susceptible to this effect. Such an effect is strongly dependent on low-level characteristics of individual Geiger cells (*e.g.*, the drift model) which might not be exactly reproduced in MC.

The values for the cut are chosen such that the difference between the cut efficiency on data and MC is smaller than 1% (Figure 8.1b). The cut efficiency is defined both in data and MC as the fraction of events which survive the cut. In general, pile-up of events due to uncorrelated decays (*e.g.*, two coincident β -decays) is not expected in NEMO-3, and a simple estimation yields a negligible fraction of pile-up events for the cuts chosen¹. We can therefore assume that the difference between the cut efficiency in data and MC reflects predominantly mis-modelling effects and the chosen cut values ensure that these effects are smaller than 1% while still providing

¹With an overall trigger rate of 5 Hz and a trigger window of 700 μs , it is estimated that the probability of pile-up in any given trigger is 0.3%. Assuming an even distribution of triggered events over the detector the probability of pile-up in a 10 cm \times 15 cm area of the foil is $3 \times 10^{-4}\%$.

a safeguard against very badly reconstructed events and pile-up events occurring in distant regions of the detector.

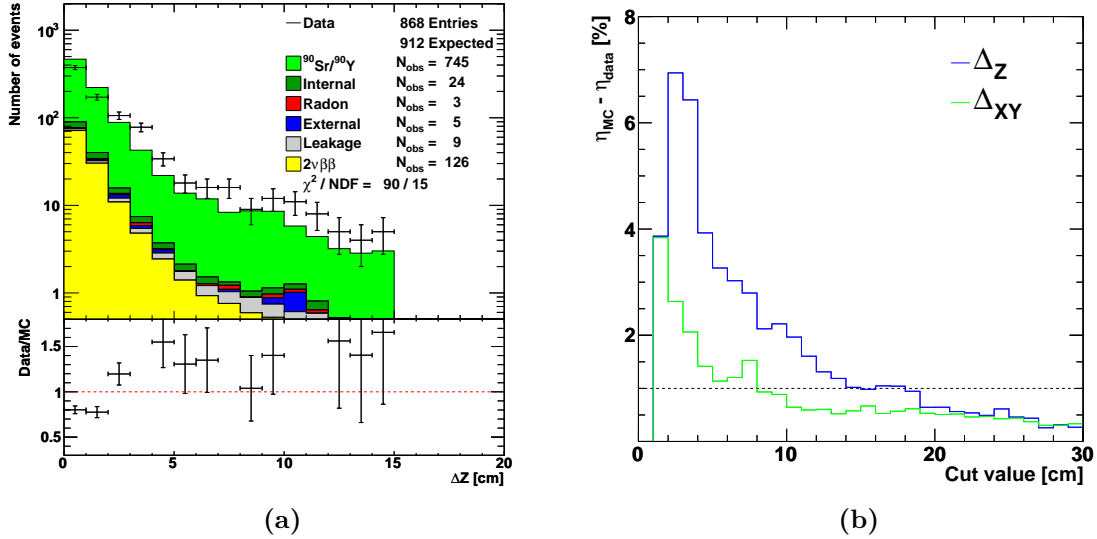


Figure 8.1.: Mis-modelling of the distance between electron vertices in “same side” events and difference in efficiency of the vertex distance cuts in data and MC. Mis-modelling of the distance between electron vertices in the Z plane, where the two electrons emerge from the same side of the source is shown in (a). The difference between data and MC of the efficiency of the cut on the distance between the electron vertices is shown in (b) for the cut applied in the XY and Z planes.

The other selection criteria have been used in double- β decay analyses previously published by NEMO-3. It has been shown in [31] that further optimisation of these cuts yields negligible effects on the precision of double β -decay analyses.

8.1.1. Validation of $2eN\gamma$ selection on ^{207}Bi calibration source data

The $2eN\gamma$ selection criteria listed above were validated with data from runs where calibrated ^{207}Bi sources were placed in the detector. Data were taken with the trigger used in double- β decay search runs. ^{207}Bi has a half-life of 31.6 years and decays predominantly via electron capture with the emission of two de-excitation γ 's with energies of 0.6 MeV and 1 MeV. The activity of the sources was measured in HPGe detectors with a systematic error estimated to be 5%.

Data from four run sets where two ^{207}Bi sources were introduced in the detector are analysed. The data were taken in March and June of 2004, and April of 2006. The selection criteria described above are applied to this data with the exception that more than two tracks are allowed in the event, as long as the additional tracks point at positions away from the source position. This change is made because the activity in the detector is much higher when the sources are introduced. The fitting procedure is identical to that used in the double- β decay analysis.

The results of this measurement are shown in Table 8.1, where the activities measured in the HPGe detectors are also given. The activities measured with NEMO-3 data are within 7% of the values obtained from HPGe data. While these values are consistent if the systematic uncertainty in the HPGe results is taken into account, a conservative approach is taken and the difference in measured activities is used as an estimate of the uncertainty on the signal efficiency in the double- β decay analysis.

Source number	HPGe measurements			This analysis (Bq)
	<i>Geranium</i> (Bq)	<i>Jasmin</i> (Bq)	Mean (Bq)	
72	180 ± 3	177 ± 3	178.5 ± 2.1	184 ± 2
76	179 ± 3	176 ± 2	177.5 ± 1.8	165 ± 2

Table 8.1.: Measurement of the activity of ^{207}Bi sources with NEMO-3 and HPGe detector data. Data from two HPGe detectors, *Geranium* and *Jasmin*, are available. The results from this analysis are compared to the mean of the HPGe results. Only statistical errors are shown.

8.2. $2eN\gamma$ distributions

In general a good agreement between the MC prediction and the observed data is seen in the $2eN\gamma$ channel. Control distributions, as well as the distributions from which the signal measurement is obtained, are shown in this section. The MC distributions are scaled to the results of the global fit from which the background activities described in Chapter 7 are obtained. The signal strength will be measured on a subset of this data, chosen to minimise the expected total uncertainty (statistical and systematic).

The distribution of events over the data taking runs is shown in Figure 8.2. A good MC prediction of the data is seen, where the activity of the ⁹⁰Sr/⁹⁰Y system is scaled over time to reflect the half-life of ⁹⁰Sr. This reflects a good modelling of the detector running conditions.

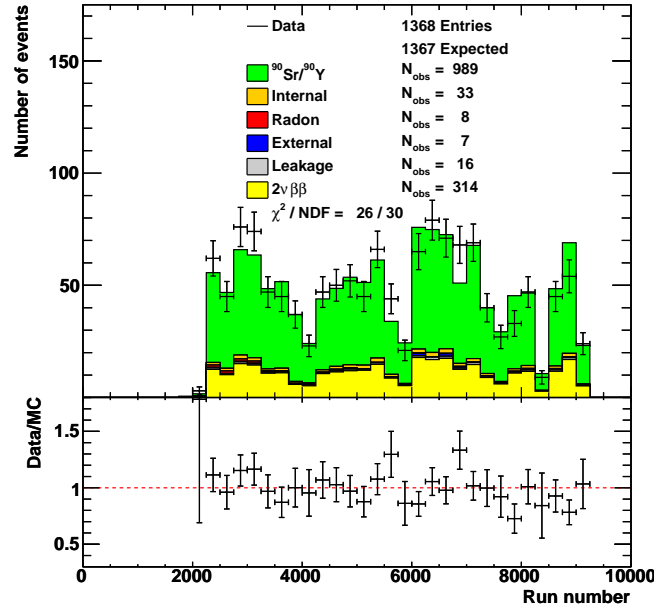


Figure 8.2.: Distribution of events against the run number. The MC prediction is shown to be in good agreement with data.

The distribution of the average Z co-ordinate of the intersection of the electron tracks with the source foil is shown in Figure 8.3a. The nine CaF₂ discs are seen and a generally good agreement between data and MC is observed.

In Figure 8.3b the distribution of the electron track lengths is shown. This variable plays an important role in discriminating internal from external events. A good prediction of the data is obtained, which provides a qualitative handle on the performance of the tracking algorithm.

The distribution of the individual electron energies in 2eN γ events is shown in Figure 8.4a. This variable is closely related to the sum of the electron energies which is the variable included in the global fit from which the signal strength is extracted.

A variable of particular interest is the opening angle between the two electron tracks, shown in Figure 8.4b. This variable is only accessible to experiments such as

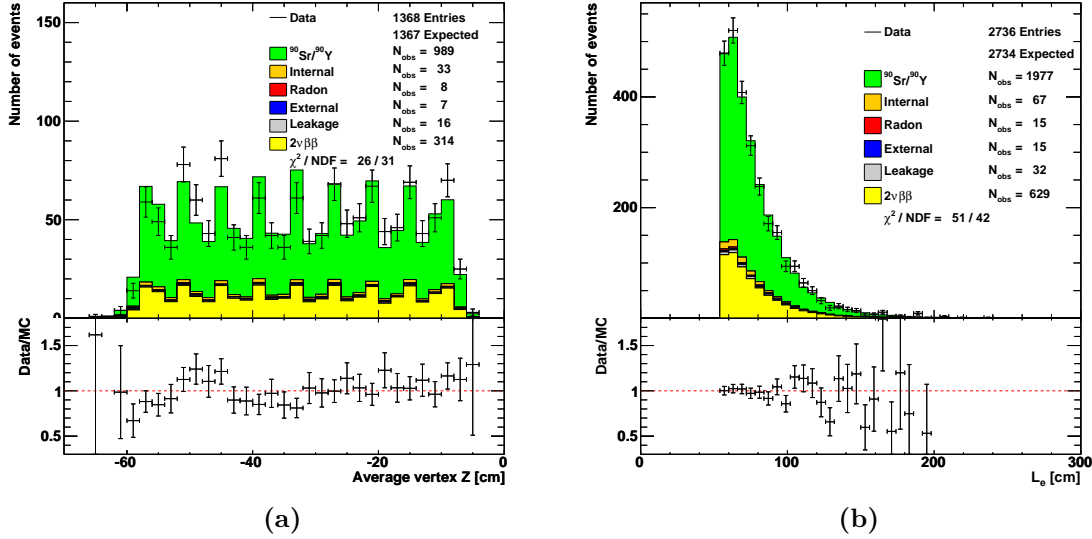


Figure 8.3.: Distributions of geometrical variables in $2eN\gamma$ events. The Z co-ordinate of the average of the two electron vertices is shown in (a). The nine CaF_2 discs are visible and a good MC prediction is observed. The distribution of the length of the electron tracks is shown in (b).

NEMO-3, where individual electrons are tracked, and it can provide discriminating power on the underlying mechanism of $0\nu\beta\beta$, should it be observed. A discrepancy is seen in this distribution where the MC prediction overestimates the data in the collinear regime (positive $\cos(\theta_{ee})$) and underestimates it in the back-to-back regime (negative $\cos(\theta_{ee})$). This effect is seen across all NEMO-3 analyses, including those of ^{207}Bi calibration source data [108]. The systematic effect of this discrepancy on the $2\nu\beta\beta$ signal measurement is discussed in Section 8.3.

The distributions of the sum of the electron energies in $2eN\gamma$ events are shown in Figure 8.5, separately for data taking phases 1 and 2. The activity of the $^{90}\text{Sr}/^{90}\text{Y}$ system is measured in these distributions with a parameter independent from the other distributions used in the global fit, where it is constrained primarily in the $1eN\gamma$ channel. The resulting activity is shown in Table 8.2 where it is compared to the activity obtained with data from the background measurement channels listed in Chapter 7. The observed difference of $(9 \pm 4)\%$ is used as an estimate for the systematic difference in the detection efficiency for internal backgrounds in the global fit (dominated by the $1eN\gamma$ channel) compared to the $2eN\gamma$ channel. This uncertainty

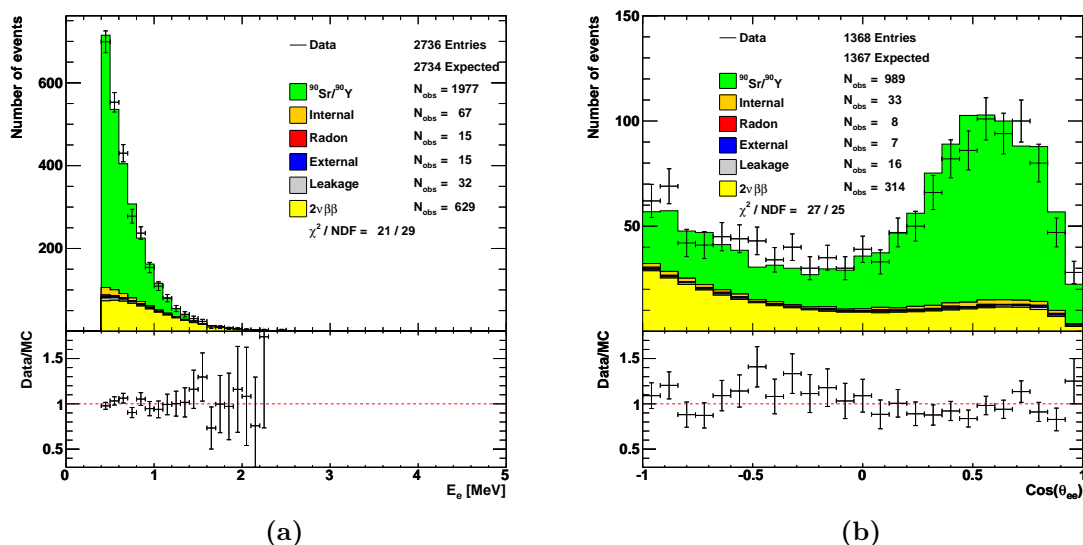


Figure 8.4.: Distributions of kinematic variables in $2eN\gamma$ events. The energy distribution of individual electrons is shown in (a), and the distribution of the cosine of the opening angle between the two electron tracks is shown in (b). MC yields a good prediction for the first variable, while a mis-modelling is observed in the latter.

is propagated through the measurement of all internal backgrounds to obtain the contribution to the systematic uncertainty on the $2\nu\beta\beta$ and $0\nu\beta\beta$ measurements.

Distributions	$^{90}\text{Sr}/^{90}\text{Y}$ activity (mBq)
All except $2eN\gamma$	29.6 ± 0.1
$2eN\gamma$	32.3 ± 1.2

Table 8.2.: Activity of the $^{90}\text{Sr}/^{90}\text{Y}$ system measured in the global fit and in the $2eN\gamma$ channel.

8.3. Systematic uncertainty on the $2\nu\beta\beta$ measurement

The sources of systematic uncertainty on the $2\nu\beta\beta$ measurement can be grouped into three types, which are treated differently:

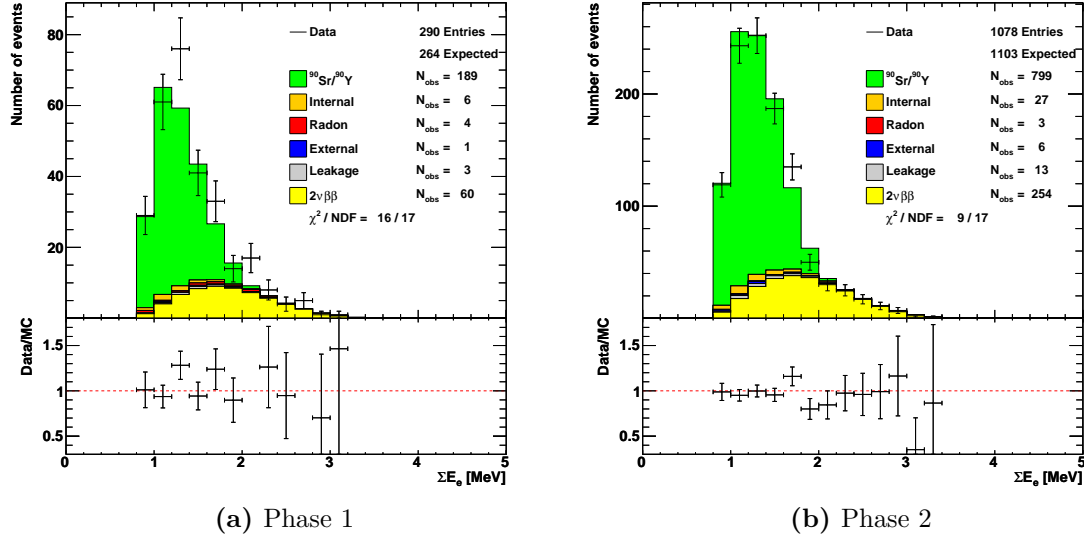


Figure 8.5.: Distribution of the summed electron energies in $2eN\gamma$ events.

- externally determined systematic uncertainties, *i.e.*, those which are measured in separate, independent, data sets from the measurement;
- uncertainties which can be modelled with MC;
- mis-modelling of data for which there are no MC hypotheses.

There are two sources of uncertainty belonging to the first group. One is the uncertainty on the enrichment fraction of ^{48}Ca in the CaF_2 source. This value is known with a precision of 2.1%. The second externally determined error is the uncertainty on the overall two-electron detection efficiency of the detector. This uncertainty is estimated to be 7% from the analysis of calibration source data described above in Section 8.1.1. Both these uncertainties are applied directly to the measured $2\nu\beta\beta$ activity.

Uncertainties for which there are known hypotheses according to which MC samples can be produced are treated differently. These uncertainties on the measurement can be estimated independently of the statistical fluctuations of observed data by running the fit on pseudo-data generated according to the best fit of MC to data.

The energy scale of the NEMO-3 calorimeter is calibrated with a precision of 1%. The effect of this on the measured $2\nu\beta\beta$ half-life is estimated by generating

pseudo-data with all measured energies shifted by $\pm 1\%$ and running the fit on the shifted pseudo-data.

The measurement of the activities of background components is performed in channels independent of the signal channel. It is expected that there are systematic uncertainties in the relative efficiencies of the channels. To estimate the effect of such uncertainties, the internal backgrounds are fixed to activities 9% above and below their measured value. The fit is then performed on pseudo-data allowing the other backgrounds and the signal to float. The range of the measured signal strength is taken as the systematic uncertainty. The same procedure is performed for the external and radon components of the background model, with these being fluctuated by $\pm 10\%$. For the radon backgrounds, this value arises from differences in the measurement of the background components' activities in the $1e1\alpha$ channel compared to the $1e1\gamma$ channel, while for the external background the systematic uncertainty is estimated by comparing the measurements made in the ^{48}Ca data to the measurements spanning the entire detector [93].

A further source of systematic error which is estimated with MC modelling is the uncertainty on the source construction and geometry, discussed in Section 5.1.1. To estimate the magnitude of this effect, MC samples were generated for the signal and the main background component, ^{90}Y , with alternative descriptions of the ^{48}Ca source:

- the rotation of the ^{48}Ca source strip is changed by $\pm 1^\circ$, to account for the uncertainty in the measurement of the rotation angle;
- the diameter of the ^{48}Ca source discs is changed by ± 1 mm, while keeping the CaF_2 mass constant;
- the thickness of the CaF_2 discs is changed by factor of 2 and 1/2 while keeping the mass constant;
- the Teflon discs surrounding the CaF_2 are removed from the source description;
- and additional 0.7 g is added to the source description by an increase in the thickness of the Teflon discs to account for the uncertainty in the total mass of the source strip.

The main contributions to the systematic error from the source construction uncertainties are the removal of Teflon, the addition of 0.7 g of material and the change in the source diameter. The effect of the last contribution occurs mostly through the change of surface density required to keep the total mass of the CaF_2 discs constant. The uncertainty on the signal measurement from source construction considerations is estimated by substituting the nominal signal and ^{90}Y MC samples with the alternative ones and fitting them to pseudo-data generated according to the nominal source construction hypothesis.

An additional check was made on the systematic effect of a possible non-uniformity of the CaF_2 discs' surface density. An alternative geometry of the ^{48}Ca source was set up in the simulation where the thickness of each disc was given by a random number generated according to a Gaussian distribution around the nominal thickness with a standard deviation of 15%. A sample of the $2\nu\beta\beta$ signal was generated. After all analysis cuts, the detection efficiency of the alternative signal sample was within 0.5% of the nominal and no significant spectral distortion was observed. Due to the smallness of this effect and its similarity to others discussed above it is not included in the total systematic uncertainty of the double- β decay measurements.

In addition to the uncertainties described above, a major contribution to the systematic error on the $2\nu\beta\beta$ measurement arises from a mis-modelling of data observed in the distribution of the opening angles between the two electrons (Figure 8.4b). The same effect was also investigated by measuring the $2\nu\beta\beta$ signal strength with events where both electrons hit calorimeter modules on the same side of the source foil ("same side" events) and comparing the result to the one obtained if events are selected where the electrons hit calorimeter blocks on the opposite sides of the source foil ("opposite side" events). It is thought that this effect arises from a mis-modelling of the tracking efficiency, particularly for events with electrons on the same side. The effect of this uncertainty on the $2\nu\beta\beta$ measurement is estimated with experimental data by measuring the signal strength independently with the two topologies. The results of the activity of the signal measured in two pairs of orthogonal data sets reflecting this mis-modelling are shown in Table 8.3.

A conservative approach is taken and the difference between the central values of the measurements with "same side" and "opposite side" events and the activity found with the inclusive data set (31.5 μBq) is used to yield a systematic uncertainty

	Signal activity (μBq)	Ratio
“Opposite side” events	34.8 ± 3.1	1.28 ± 0.24
“Same side” events	27.1 ± 4.4	
$\cos(\theta_{ee}) < -0.32$	35.0 ± 3.4	1.26 ± 0.22
$\cos(\theta_{ee}) > -0.32$	27.7 ± 3.9	

Table 8.3.: Systematic uncertainty on the $2\nu\beta\beta$ measurement due to data mis-modelling in “same side” and “opposite side” events. The signal activities measured in two pairs of orthogonal data sets are given.

of ${}_{-14}^{+11}$ % on the signal activity. Similar analyses of the very pure, high-statistics, NEMO-3 ¹⁰⁰Mo data set yielded a smaller systematic uncertainty of $\sim 4\%$, but with much higher statistical significance [109, 110].

8.3.1. Optimisation of $2\nu\beta\beta$ fitting window

It is expected that some of the uncertainties described above can be minimised by choosing an appropriate energy window to fit the signal. For example, it is clearly seen in Figure 8.5 that the effect of an uncertainty on the internal background activities could be minimised by performing the fit on energies above ~ 2 MeV.

The magnitude of the systematic uncertainties which can be measured in MC to pseudo-data fits is estimated for signal measurements performed on a range of energies. Only the lower bound of the window is optimised with the data at the high energy end of the spectrum always being included. The result of the scan is shown in Figure 8.6.

It is found that the total expected uncertainty is minimised if the signal is fitted above 1.8 MeV in the summed electron energy spectrum.

The total systematic uncertainty on the $2\nu\beta\beta$ measurement is given in Table 8.4, broken down into the components described above. The uncertainties are assumed to be uncorrelated, with positive and negative errors being added in quadrature separately.

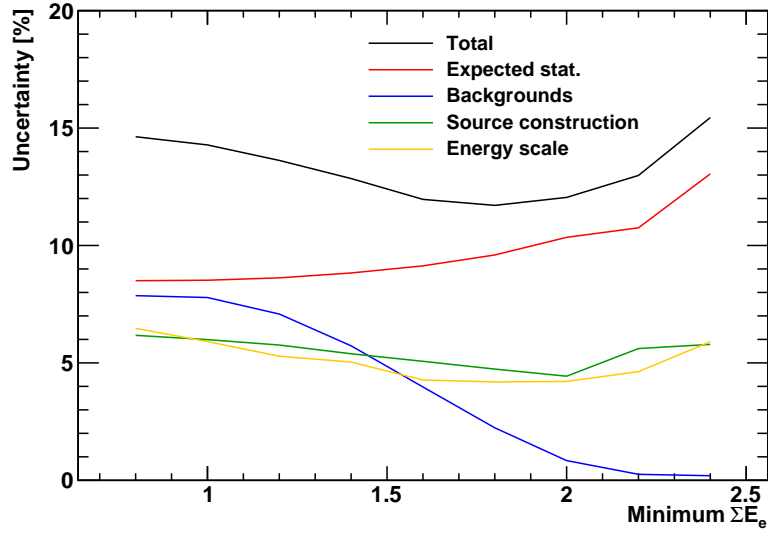


Figure 8.6.: Optimisation of $2\nu\beta\beta$ fitting window. Systematic error on the $2\nu\beta\beta$ signal measurement from uncertainties on the background model, source construction and energy scale are shown with the expected statistical error as a function of the lower bound of the window used for the fit.

Origin	Uncertainty (%)	Uncertainty on signal activity (%)	Uncertainty on signal half-life (%)
Enrichment fraction	± 2.1	± 2.1	± 2.1
Efficiency	± 7	± 7	+7.5 -6.5
Energy scale	± 1	± 4.2	+4.4 -4.0
Internal background	± 9	+2.4 -2.0	+2.0 -2.4
External background	± 10	+0.3 -0.2	± 0.3
Radon background	± 10	± 0.05	± 0.05
Source construction	–	+5.7 -3.6	+3.7 -5.5
Data mis-modelling*	–	+11 -14	+16 -10
Total	–	+15 -17	+19 -14

Table 8.4.: Total systematic uncertainty on the $2\nu\beta\beta$ half-life measurement.

* Mis-modelling of “same side” and “opposite sides” events, as described above.

8.4. $2\nu\beta\beta$ half-life result and discussion

A total of 301 ± 29 $2\nu\beta\beta$ events are observed in data, with a detection efficiency of 6.01 ± 0.01 (*stat.*)%. For a ⁴⁸Ca mass of 6.99 g and a total run time of 1918.5 days, the resulting half-life is obtained as described in Section 6.6:

$$t_{2\nu}^{1/2} = 6.37_{-0.69}^{+0.56} (\textit{stat.})_{-0.89}^{+1.21} (\textit{syst.}) \times 10^{19} \text{ yr} \quad (8.1)$$

The result given above is in agreement with the two previously published experimental results $4.2_{-1.3}^{+3.3} \times 10^{19}$ yr and $4.3_{-1.1}^{+2.4} (\textit{stat.}) \pm 1.4 (\textit{syst.}) \times 10^{19}$ yr by the TGV [80] and Hoover Dam [79] experiments, respectively, while being significantly more precise than either of them.

The $2\nu\beta\beta$ decay of ⁴⁸Ca is of particular interest as the isotope's relatively low A allows for precise calculations of nuclear matrix elements within the nuclear shell model. To compare the result given above to theoretical predictions, it is useful to factorise it as:

$$\left(t_{2\nu}^{1/2}\right)^{-1} = G^{2\nu} g_A^4 \left|M^{2\nu}\right|^2, \quad (8.2)$$

where $G^{2\nu}$ is the phase-space factor, g_A is the axial-vector coupling constant and $|M^{2\nu}|$ is the nuclear matrix element. With the phase-space factor 1.56×10^{-17} yr [111] the nuclear matrix element is measured to be (calculated with $g_A = 1.254$ [112]):

$$\left|M^{2\nu}\right| = 0.020 \pm 0.002, \quad (8.3)$$

where the statistical and systematic uncertainties on the half-life measurement were added in quadrature and propagated through².

The notorious difficulty of nuclear matrix element calculations is reflected in the range of theoretical predictions. Review articles on the subject list shell model calculations of $|M^{2\nu}|$ in the range 0.025 – 0.044 [112–114]³. More recent calculations

²The convention used here is to report the matrix element in its dimensionless form and not scaled by the mass of the electron [112, 113]. Where matrix elements are cited they have been scaled appropriately.

³A value of 0.020 is listed in [112], where it was taken from [115]. The authors of the latter article have published an erratum with a correction to this calculation resulting in 0.025 [50, 114]. Only the corrected value is shown here.

predict values in the range 0.024 – 0.033 [116, 117]. The measured nuclear matrix element presented here is smaller than any of the calculated values, being two standard deviations away from the closest theoretical prediction. The individual calculations are compared to the measured value in Figure 8.7, where calculations performed over the full p–f shell phase-space of the intermediate nucleus are distinguished from those where a closure approximation is used and the interaction models used in the predictions are given.

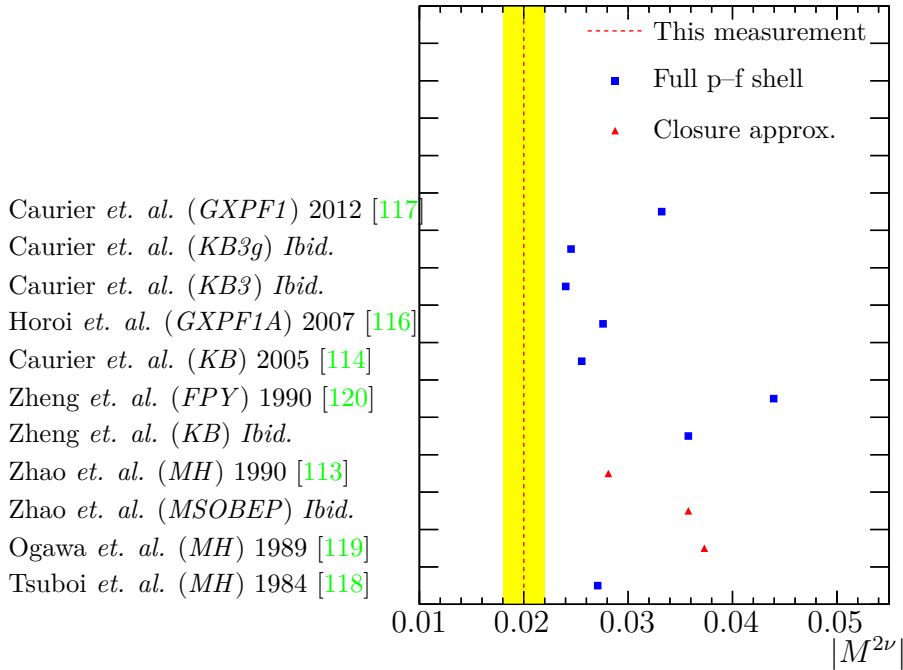


Figure 8.7.: Comparison of the measured $|M^{2\nu}|$ to theoretical calculations. The measured value is indicated by the red dotted line with the yellow band spanning one standard deviation from the mean on either side. Theoretical results are obtained from the references given in the y -axis. Results of [118, 119] are given as reported in [113]. Calculations using the full p–f shell phase-space are shown as blue squares and values obtained using closure approximations are shown as red triangles. The interaction models used in the calculations are given, for reference, in brackets. These read as follows:

MH – the approach by Muto and Horie [121];
MSOBEP – modified surface one-boson exchange potential [122];
KB – the approach by Kuo and Brown [123] and derivatives thereof;
FPY – as described in [124];
GXPF1 – as described in [125].

8.5. Limits on $0\nu\beta\beta$ and discussion of results

As no evidence is found for $0\nu\beta\beta$ modes in the $2eN\gamma$ data, limits on the half-lives for these decays are set using the CL_s method, as described in Section 6.5.2. The full spectrum of the $2eN\gamma$ summed electron energies is used for setting these limits (Figure 8.8). As the dominant backgrounds to the $0\nu\beta\beta$ search in ⁴⁸Ca are the $2\nu\beta\beta$ signal and internal backgrounds (and not the backgrounds due to ²²²Rn), the two data taking phases are combined for these measurements.

The Collie package is used to perform the CL_s calculations [104]. Systematic uncertainties are included by fluctuating the background and signal distributions by a random scale factor generated according to a Gaussian distribution. For the background components measured primarily in other channels (*i.e.*, internal, external and radon backgrounds) the systematic uncertainties are as estimated for the $2\nu\beta\beta$ measurement. Given the data-driven nature of the assessment of the $2\nu\beta\beta$ signal efficiency, the systematic uncertainty on the $0\nu\beta\beta$ signal efficiency is taken to be of the same magnitude as that of the $2\nu\beta\beta$ signal. The statistical uncertainty on the strength of the $2\nu\beta\beta$ signal is included in the limit calculation. The values of the systematic uncertainties used in the limit calculation are summarised in Table 8.5.

Component	Systematic uncertainty on activity (σ)
$2\nu\beta\beta$ background	$\pm 9 \%$
Internal background	$\pm 9 \%$
External background	$\pm 10 \%$
Radon background	$\pm 10 \%$
	Systematic uncertainty on efficiency (σ)
$0\nu\beta\beta$ signal	$^{+15}_{-17} \%$

Table 8.5.: Systematic uncertainties used in $0\nu\beta\beta$ limits.

The following $0\nu\beta\beta$ modes are investigated:

- the neutrino mass mechanism ($\langle m_{\beta\beta} \rangle$), due to the exchange of light neutrinos, or \mathcal{R}_p supersymmetry processes;
- right handed currents $\langle \eta \rangle$ and $\langle \lambda \rangle$;

- emission of a single Majoron with spectral index 1 ($\chi^0 n = 1$).

While $0\nu\beta\beta$ might result from the interference of several of these mechanisms, here they are investigated separately, with interference effects ignored.

The results of the limit setting procedure are shown in Table 8.6, with the range of expected limits corresponding to one standard deviation fluctuations of the uncertainties listed in Table 8.5 given for each decay mode. The resulting upper limits on the number of observed events are combined with the shown detection efficiencies and experimental parameters to give lower limits on the decay half-lives. The observed limits are consistently within the expected range, indicating an adequate modelling of the backgrounds.

Mechanism	Efficiency (%)	Number of events 90% CL		$t_{0\nu}^{1/2}$ 90% CL (10^{22} yr)	
		Expected	Observed	Expected	Observed
$\langle m_{\beta\beta} \rangle$	16.9	< 2.67 – 3.15	< 2.68	> 1.71 – 2.02	> 2.02
RHC $\langle \eta \rangle$	15.8	< 2.69 – 3.21	< 2.70	> 1.57 – 1.88	> 1.87
RHC $\langle \lambda \rangle$	9.91	< 2.65 – 3.07	< 2.65	> 1.03 – 1.20	> 1.19
$\chi_{n=1}^0$	13.4	< 8.54 – 17.3	< 9.35	> 0.247 – 0.499	> 0.456

Table 8.6.: Limits on $0\nu\beta\beta$ modes. The signal efficiencies and 90% CL limits are shown for the four investigated decay modes. The ranges of expected limits represent one standard deviation fluctuations of the background model.

The summed electron energy distribution from which the limits are obtained is shown in Figure 8.8. The $0\nu\beta\beta$ distributions are shown added to the total background and scaled to the respective 90% CL limits. The distribution of the data with the background subtracted can be seen in Figure 8.9 with the $0\nu\beta\beta$ signal distributions superimposed.

Mass mechanism

The summed electron distribution of the mass mechanism $0\nu\beta\beta$ is peaked near the Q-value of the decay and well separated from the background contributions, including that of $2\nu\beta\beta$. Furthermore, no events are observed in the region of highest sensitivity to this decay mode, above 3.4 MeV. The resulting 90% CL limit using the full

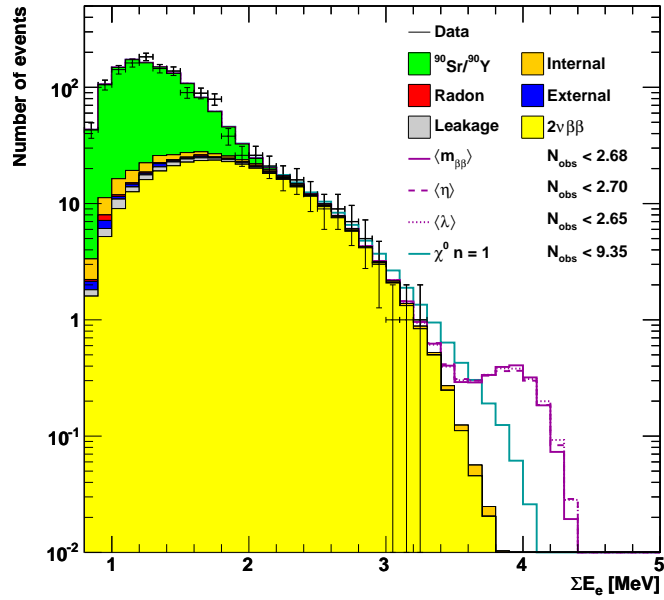


Figure 8.8.: $2eN\gamma$ summed electron distribution with $0\nu\beta\beta$ limits. Data taking phases 1 and 2 are shown combined. The $0\nu\beta\beta$ distributions are shown scaled to the respective 90% CL limits and added to the total background.

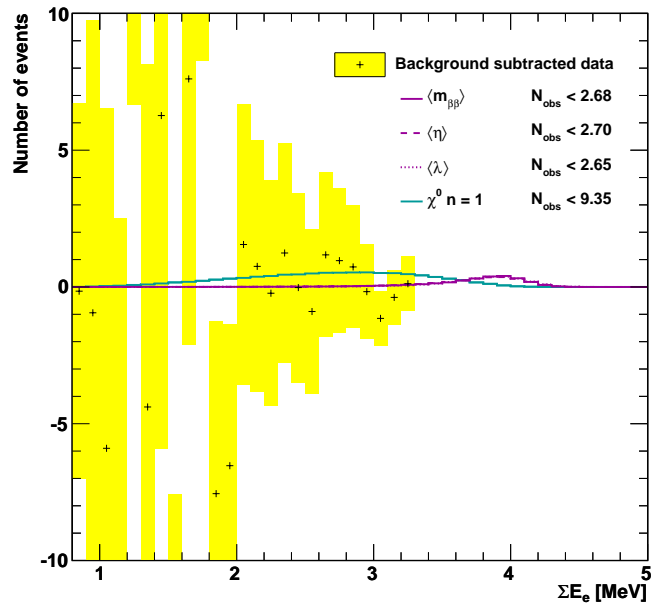


Figure 8.9.: $2eN\gamma$ background subtracted data with $0\nu\beta\beta$ limits. The statistical uncertainties on the data points are shown as yellow bars.

spectrum information with the CL_s method is:

$$t_{0\nu}^{1/2} > 2.0 \times 10^{22} \text{ yr} \quad (8.4)$$

A simpler optimised-window counting method [126] gives a limit of 1.9×10^{22} years. While this method does not include systematic effects, and is less precise than the CL_s method since it does not use the full spectral information, it is useful as a cross-check to the more complex CL_s procedure.

This result does not improve the current best limit of 5.8×10^{22} obtained with the ELEGANT IV experiment [81]. It should be noted that the ELEGANT IV result was obtained with roughly half the exposure of the NEMO-3 ^{48}Ca source. This illustrates the advantages of the higher efficiency of homogeneous experiments in terms of discovery potential.

The result from Equation 8.4 can be used to extract an upper limit on the effective Majorana mass via the expression:

$$\left(t_{0\nu}^{1/2}\right)^{-1} = G^{0\nu} g_A^4 |M^{0\nu}|^2 \langle m_{\beta\beta} \rangle^2 . \quad (8.5)$$

Using the phase-space factor $2.48 \times 10^{-14} \text{ yr}$ [111], the limit on $\langle m_{\beta\beta} \rangle$ is found to be in the range

$$\langle m_{\beta\beta} \rangle < 16 - 24 \text{ eV} \quad (8.6)$$

for nuclear matrix elements calculated within the shell model [127, 128] and

$$\langle m_{\beta\beta} \rangle < 6.1 - 38 \text{ eV} \quad (8.7)$$

for calculations in the QRPA [129, 130], IBM-2 [131] and EDF [132] frameworks.

This limit is two orders of magnitude weaker than the best published value of $0.12 - 0.25 \text{ eV}$ set by the combination of the results of the ^{136}Xe experiments KamLAND-Zen [44] and EXO-200 [60]. It is also far from the best limit obtained with the NEMO-3 experiment: $0.33 - 0.87 \text{ eV}$ with the ^{100}Mo data [76]. It should be noted, however, that the limit from the ^{136}Xe experiments was obtained with

a combined exposure of 122 kg yr and the NEMO-3 ¹⁰⁰Mo limit was set with an exposure of 36.3 kg yr, compared to 36.7 g yr of ⁴⁸Ca in NEMO-3.

To assess the potential of ⁴⁸Ca as a source for $0\nu\beta\beta$ searches, the limits obtained with ⁴⁸Ca, ¹³⁶Xe and ¹⁰⁰Mo are shown in Figure 8.10, where the measurement described here is shown extrapolated to a wide range of exposures. Two scenarios are probed: the case where the number of background events is directly proportional to the exposure, giving $t^{1/2} \propto \sqrt{\text{exposure}}$; and, given the very low level of background expected in the region of interest of ⁴⁸Ca (Figure 8.8), the idealistic scenario where the number of background counts does not change with exposure, in which case $t^{1/2} \propto \text{exposure}$. It is clear from the extrapolation of the $\langle m_{\beta\beta} \rangle$ limit that a large-scale ⁴⁸Ca experiment can only be competitive with current cutting-edge techniques if a very low background level is achieved. The expected number of background events above 3.6 MeV in the ⁴⁸Ca dataset analysed here is 0.01 and 0.03 from internal backgrounds and the tail of $2\nu\beta\beta$, respectively. This indicates that, for a NEMO-3 like experiment, the constant background scenario might be valid for an increase in exposure of at most two orders of magnitude. For exposures larger than this, the background due to $2\nu\beta\beta$ will become significant. While the reduction in sensitivity resulting from this can be mitigated by improving the experimental characteristics such as the signal efficiency and energy resolution, defeating the low natural abundance of ⁴⁸Ca remains the biggest experimental obstacle to $0\nu\beta\beta$ searches with ⁴⁸Ca.

\mathcal{R}_p supersymmetry

In the context of \mathcal{R}_p supersymmetry, the decay examined above can proceed without the involvement of intermediate neutrinos, for example through an exchange of gluinos or neutralinos. To a very good approximation the decay kinematics and hence the signal efficiency are the same as in the case of the exchange of light neutrinos described above. Assuming the dominance of gluino exchange [53] then an upper limit on the R-parity violating coupling constant λ'_{111} can be extracted as a function of the squark and gluino masses, $m_{\tilde{q}}$ and $m_{\tilde{g}}$:

$$\lambda'_{111} < 0.11 - 0.14 \times f, \tag{8.8}$$

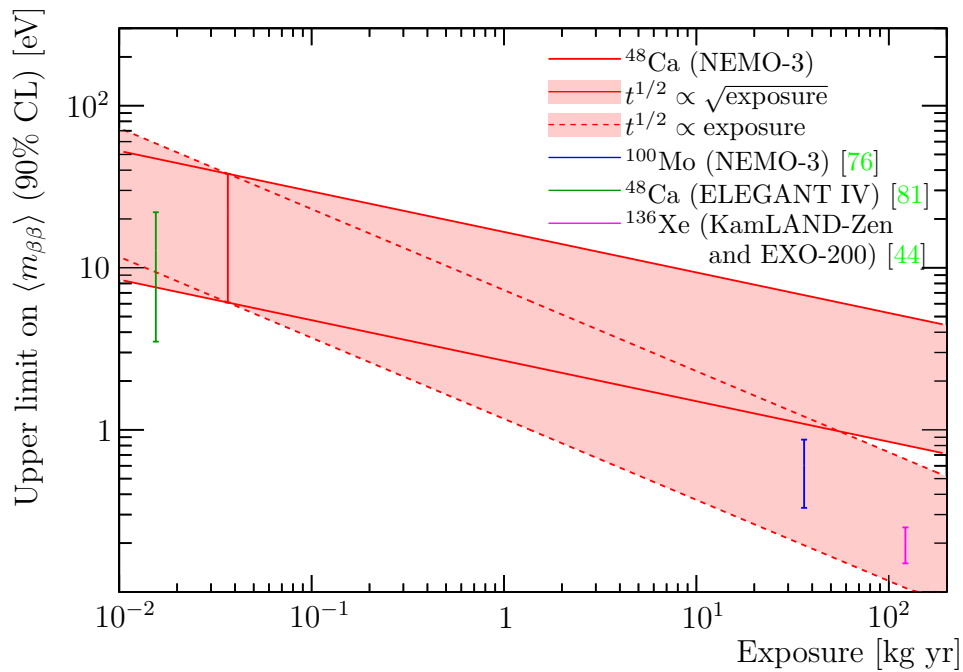


Figure 8.10.: Comparison of the $\langle m_{\beta\beta} \rangle$ limit measured in this analysis with the best available limits with ^{48}Ca (ELEGANT IV), ^{100}Mo (NEMO-3) and ^{136}Xe (KamLAND-Zen and EXO-200). Given the large disparity in exposures, the limit obtained in this analysis is shown extrapolated over the range of exposures under two background hypotheses.

where f is given by

$$f = \left(\frac{m_{\tilde{q}}}{1 \text{ TeV}} \right)^2 \left(\frac{m_{\tilde{g}}}{1 \text{ TeV}} \right)^{1/2}, \quad (8.9)$$

and the matrix elements from [127, 133] were used. Previously published limits on this coupling constant have been obtained from ⁷⁶Ge data taken by the Heidelberg-Moscow experiment [134] ($\lambda'_{111}/f < 0.10$) and more recently from ¹⁰⁰Mo data by the NEMO-3 experiment [76] ($\lambda'_{111}/f < 4.4 - 6.6 \times 10^{-2}$). This coupling is also constrained in collider experiments, for example via constraints on left-right symmetric models [135]. While the comparison between constraints from $0\nu\beta\beta$ searches and collider searches is highly dependent on the choice of model, the results from $0\nu\beta\beta$ provide the strictest limits for a significant portion of the available parameter space [135].

Right-handed currents

In left-right symmetric models, $0\nu\beta\beta$ can occur without the helicity flip of the exchanged neutrino required in the mass mechanism [51]. As such the amplitude for these decays do not depend directly on the neutrino mass but more generally on the coupling between right-handed quarks and right-handed leptons $\langle\lambda\rangle$ and on the coupling between left-handed quarks and right-handed leptons $\langle\eta\rangle$. Although these decay modes produce two electrons with energies summing up to the Q-value, their individual kinematics differ from those of electrons emitted in the neutrino mass mode. The $\langle\lambda\rangle$ mode, in particular, results in a significant asymmetry between the energies of the individual electrons which degrades the signal efficiency, compared to other modes. Limits at 90% CL on these two contributions are set separately:

$$t_{0\nu\lambda}^{1/2} > 1.2 \times 10^{22} \text{ yr}, \quad (8.10)$$

$$t_{0\nu\eta}^{1/2} > 1.9 \times 10^{22} \text{ yr}. \quad (8.11)$$

The matrix elements and phase-space factors for these decays are not easily factorised, therefore limits on the couplings are extracted via constants C_i calculated for each

nucleus:

$$\left(t_{0\nu i}^{1/2}\right)^{-1} = C_i \langle i \rangle^2, \quad (8.12)$$

where $i = \lambda, \eta$. With the C_i coefficients listed in [112], the upper bounds on the coupling constants are:

$$\langle \lambda \rangle < 7.7 - 48 \times 10^{-6}, \quad (8.13)$$

$$\langle \eta \rangle < 0.76 - 55 \times 10^{-7}. \quad (8.14)$$

Stricter limits have been placed on these couplings by searches with ^{100}Mo in NEMO-3 [76] ($\langle \lambda \rangle < 0.9 - 1.3 \times 10^{-6}$ and $\langle \eta \rangle < 0.5 - 0.8 \times 10^{-8}$) and also with ^{76}Ge by the Heidelberg-Moscow collaboration [136] ($\langle \lambda \rangle < 1.1 \times 10^{-6}$ and $\langle \eta \rangle < 0.64 \times 10^{-8}$).

Limits on the $\langle \lambda \rangle$ and $\langle \eta \rangle$ couplings can be independently estimated from the current status of searches for particles predicted by left-right symmetric models at the LHC [127, 137]. The coupling parameters can be written as

$$\langle \lambda \rangle = \epsilon \sum_k U_{ek} V_{ek}, \quad (8.15)$$

$$\langle \eta \rangle = \left(\frac{M_{W_L}}{M_{W_R}}\right)^2 \sum_k U_{ek} V_{ek}, \quad (8.16)$$

where ϵ is the parameter mixing the right-handed heavy W_R and the SM W_L , U is the PMNS matrix and V is the equivalent matrix mixing neutrino flavour states and the right-handed heavy mass states [51, 127]. W_R and heavy right-handed neutrinos have been excluded by LHC searches up to $\mathcal{O}(\text{TeV})$ [137] and the mixing parameter ϵ has been constrained to be smaller than $\mathcal{O}(10^{-2})$ [28]. In standard seesaw models the elements of U are $\mathcal{O}(1)$ and those of V $\mathcal{O}\left(\sqrt{\frac{m_\nu}{M_R}}\right)$, where m_ν is the mass of light neutrinos and M_R the mass of the right-handed heavy neutrinos [51], the couplings $\langle \lambda \rangle$ and $\langle \eta \rangle$ are expected to be smaller than $\mathcal{O}(10^{-8})$ and $\mathcal{O}(10^{-9})$, respectively. There are, however, models where the elements of V are larger [138], in which case the constraints from $0\nu\beta\beta$ searches are enhanced. Whichever the case, it is clear

that near-future double- β decay experiments will be in a position to constrain this type of model in parallel with collider experiments.

Majoron emission

In models where Majorons are predicted, $0\nu\beta\beta$ can occur with the emission of one or more Majorons in addition to the two electrons. As a result, the spectrum of the summed energies of the emitted electrons is broad, spanning a continuum of energies up to the Q-value, as shown in Figure 8.9. This makes the investigation of these decay modes more challenging given the higher level of background at lower energies. Here only the mode with the emission of a single Majoron with spectral index $n = 1$ is examined, in which case the decay's half-life is given by:

$$\left(t_{0\nu\chi^0}^{1/2}\right)^{-1} = G^{0\nu\chi^0} g_A^4 \left|M^{0\nu\chi^0}\right|^2 \langle g_{\chi^0} \rangle^2, \quad (8.17)$$

with $G^{0\nu\chi^0}$ and $M^{0\nu\chi^0}$ being the phase-space factor and nuclear matrix element; and $\langle g_{\chi^0} \rangle$ the coupling constant between electron neutrinos and the Majoron. The ⁴⁸Ca data analysed here allows for the limit on the half-life of this process to be set at $t_{0\nu\chi^0}^{1/2} > 4.6 \times 10^{20}$ yr (90% CL). With the phase-space factor and matrix elements from [112], the upper limit on the coupling constant is extracted:

$$\langle g_{\chi^0} \rangle < 0.44 - 3.1 \times 10^{-3}. \quad (8.18)$$

The most stringent limit on this decay mode was obtained by the KamLAND-Zen experiment [139] ($\langle g_{\chi^0} \rangle < 0.8 - 1.5 \times 10^{-5}$), while the best NEMO-3 result was obtained with ¹⁰⁰Mo data [76] ($\langle g_{\chi^0} \rangle < 1.6 - 4.1 \times 10^{-5}$). These results can be combined with observations of SN 1987 which exclude $\langle g_{\chi^0} \rangle$ between 10^{-7} and 10^{-5} [140] to set an upper limit on this coupling of the order of 10^{-7} .

Part II.

Tracker commissioning for the SuperNEMO detector

Chapter 9.

The SuperNEMO experiment

SuperNEMO is a next-generation double- β decay experiment based on the proven technique of NEMO-3. While the basic detection strategy is kept the same, a number of improvements were attained for each of the detector's main components in an extensive R&D programme. Materials selected for the construction of the experiment were screened for radioactive contaminants, including ^{222}Rn emanation measurements. The resulting design is modular in nature, allowing for straightforward (but costly) scalability, and foresees an increase in the source mass by one order of magnitude. This, combined with the improved experimental characteristics, will allow for a two order of magnitude gain in sensitivity to $0\nu\beta\beta$ processes.

In its baseline configuration, SuperNEMO will consist of 20 modules, each hosting 5 – 7 kg of source isotope. Each module consists of a thin source foil with a surface density of 40 mg/cm^2 in a tracking volume surrounded by a calorimeter. The isotope ^{82}Se was chosen as the primary source for SuperNEMO for its relatively low rate of $2\nu\beta\beta$, the irreducible background for $0\nu\beta\beta$ searches. Other sources considered for use in SuperNEMO include ^{150}Nd and ^{48}Ca , both of which are currently difficult to enrich in substantial quantities. The tracker and calorimeter closely follow the NEMO-3 design, with major improvements, particularly in terms of energy resolution and radiopurity.

Unlike the NEMO-3 detector, SuperNEMO modules have a planar geometry and a more complete coverage of the source by the calorimeter, resulting in an enhanced $0\nu\beta\beta$ signal efficiency. The modular design allows for gradual deployment of the detector as modules are completed and also for the distribution of modules across several underground laboratories, if required.

The first SuperNEMO module has as its main goal demonstrating the improved experimental parameters achieved through R&D, in particular the very low background level. A summary of the characteristics of the full-scale SuperNEMO and of the Demonstrator module is given in Table 9.1. A detailed description of the Demonstrator module is given in Section 9.1 and the main steps of the SuperNEMO R&D programme are outlined in Section 9.2. A brief overview of the timescale of the experiment is given in Section 9.3.

	SuperNEMO	Demonstrator
Source	^{82}Se (^{150}Nd , ^{48}Ca)	^{82}Se
Source mass	100 kg	7 kg
Energy resolution	4 % @ 3 MeV (FWHM)	
^{222}Rn in tracker volume	< 0.15 mBq/m ³	
^{208}Tl in source foil	< 2 $\mu\text{Bq/kg}$	
^{214}Bi in source foil	< 10 $\mu\text{Bq/kg}$	
Sensitivity to $0\nu\beta\beta$ (90 % CL)	$t_{0\nu}^{1/2} > 10^{26}$ yr	$t_{0\nu}^{1/2} > 6.6 \times 10^{24}$ yr
	$\langle m_{\beta\beta} \rangle < 40 - 100$ meV	$\langle m_{\beta\beta} \rangle < 200 - 400$ meV

Table 9.1.: Experimental parameters and $0\nu\beta\beta$ sensitivity for the SuperNEMO experiment and its Demonstrator module.

9.1. The Demonstrator module

The Demonstrator module is currently under construction and will take NEMO-3's place in LSM. Besides the main objective of demonstrating the very low background level required for the full-scale experiment, the Demonstrator is expected to produce competitive double- β decay results on its own, as shown in Table 9.1. To this end, the Demonstrator's source will have a higher surface density than what is planned for the full-scale detector, at 50 mg/cm², yielding 7 kg of ^{82}Se .

The detector consists of a source frame placed between two tracking chambers which in turn are surrounded by calorimeter modules (Figure 9.1). This structure occupies a volume of $6 \times 2 \times 4$ m³ which is surrounded by a magnetic field coil and shielding. The coil and parts of the shielding are reused from NEMO-3.

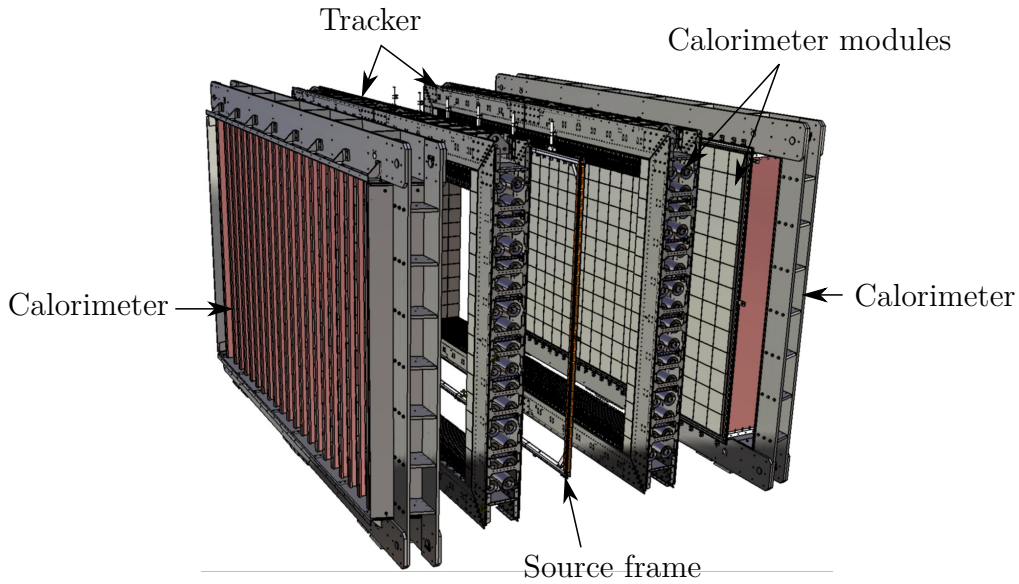


Figure 9.1.: Exploded view drawing of the SuperNEMO Demonstrator module.

The main calorimeter walls consist of 520 calorimeter modules, similar in design to their NEMO-3 counterparts but with much improved energy resolution. The scintillators comprise a mixed set of PS based and polyvinyl-toluene (PVT) based blocks. The scintillator blocks are directly coupled to a mixture of newly developed 8" high quantum efficiency Hamamatsu PMTs and 5" PMTs recovered from NEMO-3 (Figure 9.2). Eight-module *bricks* form the basic structure of the calorimeter walls, with modules in each group of eight sharing their structural support, magnetic shielding and gas seal.

The tracking chambers contain a total of 2034 cells operating in Geiger mode, with the tracking volume being enclosed on the sides, top and bottom by calorimeter blocks. These blocks are of a lower specification than those on the main walls, being instrumented with PMTs recovered from NEMO-3. In particular, the blocks on the top and bottom frames of the tracker are intended to be used primarily to veto γ 's.

As in the case of NEMO-3, the thin strips of source isotope are strung vertically in the middle of the tracking chamber. The frame designed to accommodate the source foil also includes a system for deploying radioactive calibration sources.



Figure 9.2.: Construction of the SuperNEMO main wall calorimeter modules. Scintillator blocks are shown directly coupled to NEMO-3 5'' PMTs. The module in the centre of the photograph is being wrapped in PTFE tape.

9.2. Research and development

Given the experience obtained with the NEMO-3 experiment, an extensive R&D programme was designed to improve several aspects of the technique for SuperNEMO. A brief overview of these efforts is given in this section.

Source

The main R&D activities regarding the source foils were related to the reduction of the internal backgrounds. The target ^{214}Bi and ^{208}Tl activities in the SuperNEMO source foils are one order of magnitude lower than the level attained in NEMO-3.

One of the main efforts was the development of a standalone detector able to measure the activity of ^{214}Bi and ^{208}Tl in thin strips of material down to the required limit for SuperNEMO [141]. This is achieved by the detection of BiPo delayed coincidence events, which allows the activities of contaminants present in both the thorium and uranium series downstream of the Rn isotopes to be constrained.

In addition, new isotope purification techniques were developed, as well as alternative support structures in which the amount of extraneous material in the foils is minimised. These efforts are ongoing.

Calibration systems

As part of the development of the source foil supporting frame, a system was designed to deploy radioactive calibration sources in the detector volume, as was done in NEMO-3. The new system has greatly reduced the amount of material inside the tracking volume by substituting the copper tubes of NEMO-3 with guide wires. The calibration sources are suspended from a wire on a pulley system with a plumb on the end. The weight slides on the guide wires, keeping it in a well defined position as it descends into the detector volume, carrying with it the calibration sources.

A new light injection system was developed, similar to that of NEMO-3. LED's are used as a light source for the new system, which has been shown to measure the energy scale fluctuations of calorimeter modules with a precision of 1% over the period of one month.

Calorimeter

A substantial effort was put into the optimisation of the calorimeter modules in order to improve the energy resolution by a factor of two compared to NEMO-3. The main contributions to the enhanced energy resolution of the SuperNEMO calorimeter blocks are the use of PVT instead of PS as the scintillator base and the direct coupling of the PMTs to the scintillator. The latter requires one face of the scintillator blocks to be moulded into the hemispherical shape of the PMT photocathode.

As a compromise between cost and performance part of the calorimeter is instrumented with lower specification blocks, with PS-based scintillator blocks and 5" PMTs from NEMO-3. These blocks are located in the regions of the walls with lower expected occupancy (*e.g.*, around the edges of the walls), while the areas of high occupancy are populated with the SuperNEMO specification modules.

Radon emanation

The emanation of ^{222}Rn into the tracking volume proved to be an important source of background in NEMO-3, particularly for isotopes which have their Q-value below that of the β -decay of ^{214}Bi (3.3 MeV), such as ^{82}Se . To minimise this background, detector materials in contact with the tracking gas have been screened for their radon emanation in addition to the bulk radiopurity measurements with HPGe detectors.

A specialised detector was developed which is able to measure activities of ^{222}Rn down to a few $\mu\text{Bq}/\text{m}^3$. This is achieved by passing large volumes of gas through an activated charcoal trap, and transferring the adsorbed ^{222}Rn into an electrostatic detector. This apparatus is being used to measure the ^{222}Rn emanation in the tracker at various stages of construction and also the ^{222}Rn emanating from the gas mixing system's materials into the tracking gas.

Another concern is the diffusion of ^{222}Rn from more contaminated parts (such as PMT glass) into the tracking volume. A ^{222}Rn sealing strategy was identified, where a combination of RTV silicone and styrene-butadiene rubber (SBR) are used. While the first produces a good tracking-gas seal, it performs poorly as a ^{222}Rn barrier, which is achieved by the latter. An experimental setup was developed to measure the diffusion of radon through thin sheets of material [142]. This apparatus has been used to identify ^{222}Rn sealing materials, in particular regarding the possibility of installing an anti- ^{222}Rn screen separating the tracker volume from the calorimeter walls.

As a result of this R&D work the activity of ^{222}Rn inside the tracking volume is expected to be reduced by a factor of 30 compared to NEMO-3.

Tracker

The geometry of the tracker cells was optimised, resulting in cells with a larger radius, minimising the amount of material in the tracker. To reduce the contamination of the tracker wires, which present a very large surface to the detector volume, an automated system was developed to string the tracker cells largely without human manipulation of the wires. A new technique for the read-out of tracker signals

has been developed and will be trialled in the Demonstrator module. A detailed description of the Demonstrator tracker is given in Chapter 10.

9.3. Timescale and sensitivity

The experiment is currently in an advanced stage of construction.

The first quarter of the tracker frame has been assembled and fully populated with wires and calorimeter modules. Measurements of the ^{222}Rn level in the fully populated frame will be made and the tracker will be commissioned at the surface, under cosmic rays. The preparations for surface commissioning are described in detail in Chapter 11.

The modules for the main calorimeter walls are currently in production. Modules will be assembled into 2×4 *bricks* and transported to the underground laboratory, where the *bricks* will be put together to form the main calorimeter walls.

The first prototypes of the source foil are currently being measured for ^{214}Bi and ^{208}Tl contamination in the dedicated BiPo detector mentioned above.

Integration of the different Demonstrator components at LSM will occur in 2015. The target sensitivity of the Demonstrator is expected to be achieved within 2.5 years of operation. Upon successful deployment of the Demonstrator, further modules will be built and installed in an extension of LSM currently under construction. The sensitivity achieved by SuperNEMO as a function of exposure is shown in Figure 9.3. The full-scale experiment is expected to be sensitive to a half-life of 10^{26} years within five years of operation.

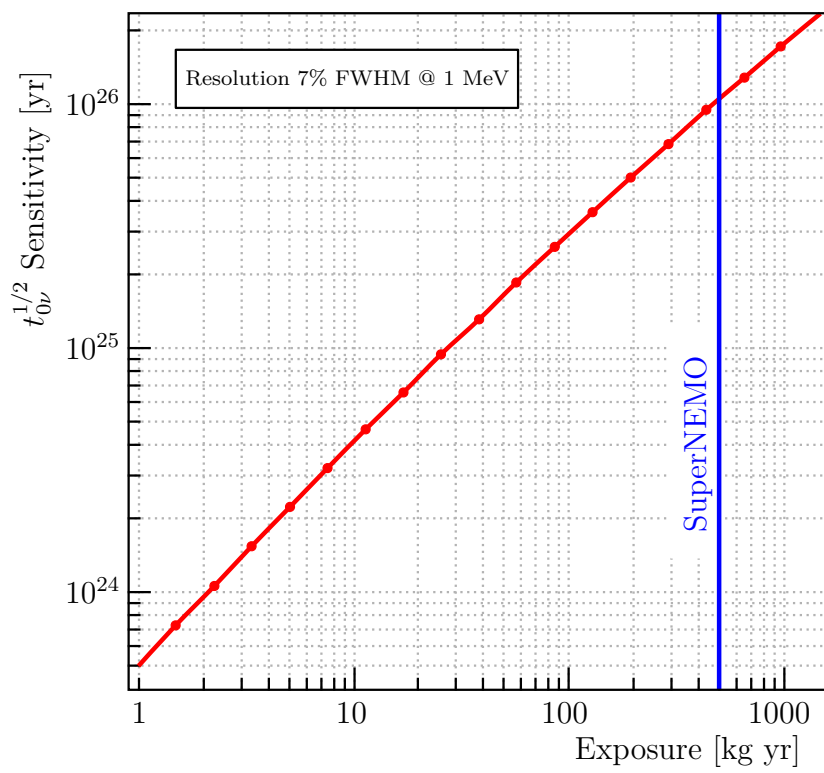


Figure 9.3.: Sensitivity of the SuperNEMO experiment as a function of exposure [31]. The exposure attained by the full scale experiment within five years is shown in blue.

Chapter 10.

The SuperNEMO tracker

As evidenced in the first part of this thesis, the strength of NEMO-3 relied in identifying electrons emerging from the source foil and tracking them to an energy deposition in the calorimeter. This method allows for the unique identification of electrons, distinguishing them from other types of naturally occurring radiation which would otherwise be a very significant background to double- β decay. Furthermore, individually tracking the electrons emitted in processes of interest allows for the measurement of their individual energies as well as the opening angle between them. The time-of-flight criteria that are essential in removing the significant backgrounds originating from sources external to the detector also rely fundamentally on measuring the position of the electron vertices in the source foil and the length of their tracks.

The considerations above make clear the necessity for a large-scale detector which is capable of tracking electrons over distances which allow for time-of-flight discrimination.

At energies of a few MeV multiple scattering has a significant impact on electron trajectories. Given that the energy measurement in SuperNEMO is performed with a dedicated calorimeter, energy losses through ionisation in the tracking chamber should be as low as possible, while still allowing for efficient tracking. These considerations motivate a tracking detector based on a low- Z medium with a minimal amount of material.

As with all other detector components, it is essential that the tracker is made as radiopure as possible. In particular, contamination on the tracker layers closest

to the source foil are indistinguishable from source foil contamination, from a data analysis perspective.

Finally, it is important that the tracker has a good vertex resolution: the identification of vertices common to pairs of electrons plays a crucial role in the selection of double- β decay events and fiducial cuts are essential to remove contaminated areas of the detector from the analysed data. An accurate measurement of the entry point of electrons in the scintillator blocks is also desired as it allows for corrections to be applied to the energy measurement.

The SuperNEMO tracker uses the same detection principle as NEMO-3, meeting the requirements outlined above by having an array of cells operating in the Geiger regime immersed in a He based gas mixture. This chapter describes the SuperNEMO tracking detector: the fundamental principles of Geiger counters are discussed in Section 10.1; a detailed description of the SuperNEMO tracker cells is given in Section 10.2; and of the tracker frame in Section 10.3. Overviews of the tracker assembly process and of its associated electronics and DAQ are given in Sections 10.4 and 10.5.

10.1. The physics of Geiger counters

Geiger counters rely on the ionisation of atoms in a gas to detect passing charged particles. A strong electric field is maintained across a volume of gas by electrodes. Typically the anode is a thin wire in the centre of a cylinder or collection of wires which form the cathode. Ionisation of the gas results in the freed electrons drifting towards the anode and the heavier ions moving slowly in the opposite direction. The ionised electrons acquire enough energy that they too will ionise the gas, resulting in an avalanche of electron-ion pairs drifting in opposite directions. The movement of these charges in the electric field induces a current on the electrodes in a phenomenon known as the Townsend avalanche.

In the Geiger regime, the electric field and gas composition are tuned such that avalanches become saturated. As the avalanche reaches the anode wire, the number of ion pairs produced is so large that the charge of relatively motionless ions clustered around the anode reduces the electric field strength substantially. At this point, newly ionised electrons will not acquire sufficient energy to further ionise the gas.

The region of the anode wire where this condition is met is said to be burned out [143]. The result of this effect is that regardless of the number of atoms ionised by the traversing particle, the integrated current induced on the electrodes will be, on average, the same. This makes for very efficient detectors, given that even the creation of a single electron-ion pair will induce a relatively large current across the electrodes, and allows for the large signals to be transmitted to the electronics racks without pre-amplification. This is advantageous both in terms of the cost of the electronics systems and in terms of radiopurity, as all tracker electronics can be placed outside the detector shielding.

Another feature of avalanches in the Geiger regime is their propagation along the very strong electric field region close to the anode wire. As sections of the wire become burned out, the avalanche spreads stochastically along the wire to regions where avalanche breeding is still possible. This occurs through the isotropic emission of de-excitation and recombination photons in an avalanche which ionise the gas in different points in the detector, seeding new avalanches [144,145]. Once the entire wire is burned out, the avalanche breeding stops and the detector is left in a non reactive state. The dead time resulting from the burn out and subsequent recovery of Geiger detectors is typically of the order of $\mu\text{s} - \text{ms}$, making these detectors unsuitable for high-rate applications.

A sketch of the Geiger counter phenomena described above is shown in Figure 10.1.

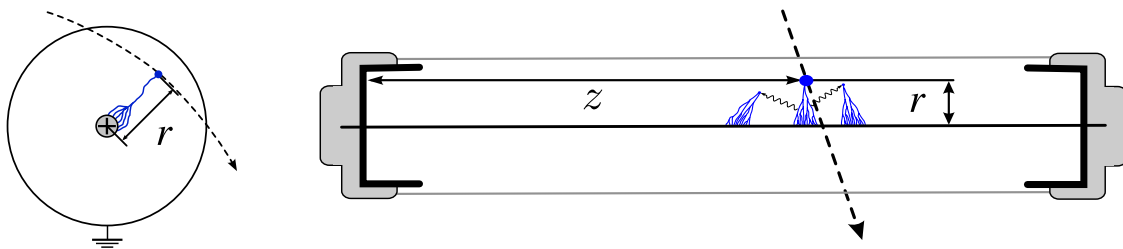


Figure 10.1.: Sketch of the signal generating process in Geiger counters. A generic Geiger counter is shown, formed of a cylindrical grounded cathode with a thin anode wire in the middle which is set at a high potential. The diagram on the left shows a view looking into the anode wire and on the right the length of the cell is seen. A passing charged particle is shown as a black dotted line and the avalanches in blue. On the right, wavy lines indicate the photons which seed secondary avalanches. The radial and longitudinal coordinates of the point of closest ionisation are indicated as r and z , respectively [146].

In general, Geiger detectors require quenching to prevent the avalanches becoming self-sustained: if regions of the detector recover to a state where new avalanches can be formed before avalanche breeding has died down elsewhere in the detector, the seeding of avalanches can continue indefinitely producing a continuous current across the electrodes, rendering the device useless as a particle detector. Quenching can be achieved by reducing the voltage applied to the anode as a signal is detected or, more commonly, by using a self-quenching gas mixture. In the latter mode of operation, a quencher (usually an organic vapour) is added to the gas which absorbs photons produced in avalanches. This process occurs primarily through the dissociation of the quencher molecules [145,147].

A common challenge encountered in the operation of Geiger detectors is the degradation of the detector's operating characteristics over time. One of the causes of this is the contamination of the detector's surfaces with quencher residues. The dissociation of the organic molecules produces polymers which can drift to the wires. Over time polymer chains are formed which disrupt the electric field close to the wire [147]. This can result in the blockage of avalanche propagation or in spurious signals caused by the ejection of electrons from the conductor's surface into the gas volume in what is known as the Malter effect [148]. Ageing can be mitigated by including additives in the gas mix which prevent polymerisation by reacting with the quencher residues to form stable and volatile molecules which are simply flushed away with the gas flow. Common additives include simple oxygen rich molecules such as CO₂ and water vapour [149].

10.2. The SuperNEMO tracker cells

The SuperNEMO tracker consists of an array of cells each of which functions as a Geiger detector, as described above. Each cell is formed of 13 wires: one anode wire in the middle of the cell to which a high voltage is applied; and 12 field-shaping wires which are grounded. The cells are 3 m long with a nominal diameter of 4.4 cm. The anode wire has a diameter of 40 μm while the field shaping wires have a diameter of 50 μm . The larger diameter for the anodic wires was chosen to minimise ageing effects due to polymer deposition on the cathode. Two copper rings, 4.2 cm in diameter and 4 cm long, are placed on the ends of the cell. These rings are grounded

and the current induced on them by the arrival of the avalanches is read out. The geometry of a SuperNEMO Geiger cell is sketched in Figure 10.2.

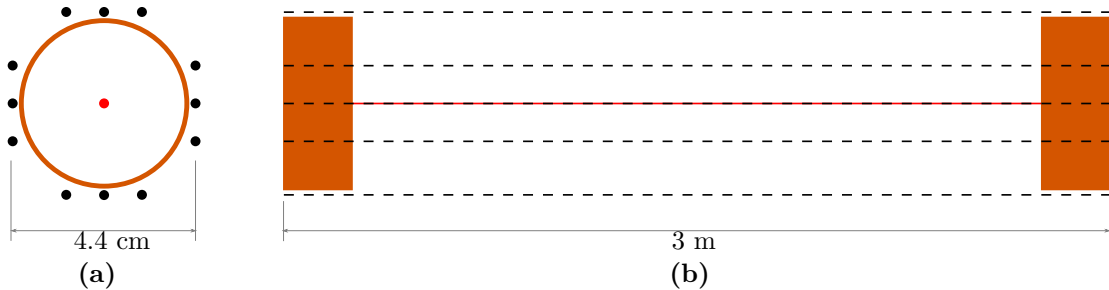


Figure 10.2.: Sketch of a SuperNEMO tracker cell. The geometry of a Geiger cell is shown in the view looking into the wires in (a) and looking across the wires in (b). The field shaping wires are shown as black dotted lines and the anode wire is drawn in red. The copper rings are shown at both ends of the cell in brown.

The tracker operates in the same atmosphere as NEMO-3, the main component of the gas being helium, with argon and ethanol added at 1% and 4% volume fractions. Argon has a lower ionisation energy than helium (15.8 eV and 24.6 eV, respectively [150]) and its addition to the tracking gas was found to enhance the propagation of the avalanches. Ethanol is used as a quenching agent. While in NEMO-3 a small quantity of water vapour (1500 ppm) was added to the tracking gas, no significant improvement was found in the tracker operation. The addition of water vapour to the SuperNEMO tracking gas is not envisaged at first.

In standard operation, a potential difference of around 1800 V is applied between the grounded field shaping wires and the anode wire. The optimal operating voltage is specific to each cell, depending on the position of the cell in the array (*i.e.*, the number of neighbouring cells) and on the intrinsic properties of the cell. The main properties which characterise a tracker cell are the Geiger plateau width, the avalanche propagation efficiency and the avalanche propagation time.

The Geiger plateau is defined as the range of anode voltages for which the cell is in the Geiger regime, with an approximately constant amount of charge being generated with each hit. For voltages below the plateau the efficiency of the cell decreases significantly as the size of the signal pulses becomes small and dependent on the number of gas atoms ionised by the traversing particle. At voltages above the plateau the cells become unstable and spuriously trigger at high rates (hundreds

of Hz) generating large currents. A robust operation of the cells is achieved when a voltage roughly in the middle of the Geiger plateau is used. A Geiger plateau spanning a wide range of voltage is thus a desirable characteristic of a cell. Typical plateaus for SuperNEMO tracker cells are 200 – 300 V wide, starting at around 1700 V. Examples of Geiger plateaus measured in SuperNEMO tracker cells can be seen in Figure 11.8.

The avalanche propagation efficiency is defined as the fraction of hits where the avalanches have propagated the whole length of the cell, reaching the pick-up rings. For voltages in the Geiger plateau this efficiency is very high being typically above 99%. However, it drops significantly for voltages outside the plateau.

An additional characteristic related to the propagation of avalanches which is a useful tool to assess the performance of tracker cells is the time it takes for the avalanches to propagate through the entire length of the wire. This property depends on the operating conditions, with times becoming shorter at higher voltages. In standard operating conditions (middle of the plateau) the avalanches spread through the 3 m long cells in around 50 μ s.

After a traversing particle triggers an avalanche in the cell which successfully propagates through the length of the wires, there is a period during which the cell is insensitive to additional passing particles, *i.e.*, no part of the wire is able to produce avalanches, or if avalanches start developing they will reach infertile regions of the wire where they will die down and will not propagate the entire length of the cell. This period of dead time or reduced propagation efficiency has been measured in SuperNEMO cells to be 3 ms, with measurable but harmless effects lasting up to 10 ms [151].

An example of a set of signals from a Geiger discharge in a SuperNEMO tracker cell is shown in Figure 10.3. Three signals are read-out from each cell: one anode pulse on the wire and two cathode pulses from the pick-up rings. The anode pulse is of negative polarity and it lasts for the duration of the avalanche propagation process, beginning with the earliest avalanche reaching the vicinity of the anode wire and ending when the avalanches reach both ends of the cell. Once one end of the cell is reached by the avalanches, the amplitude of the anode signal drops to roughly half of its initial value as with only one “propagation front” the amount of charge being generated is halved. As the avalanches reach the copper rings at the ends of the

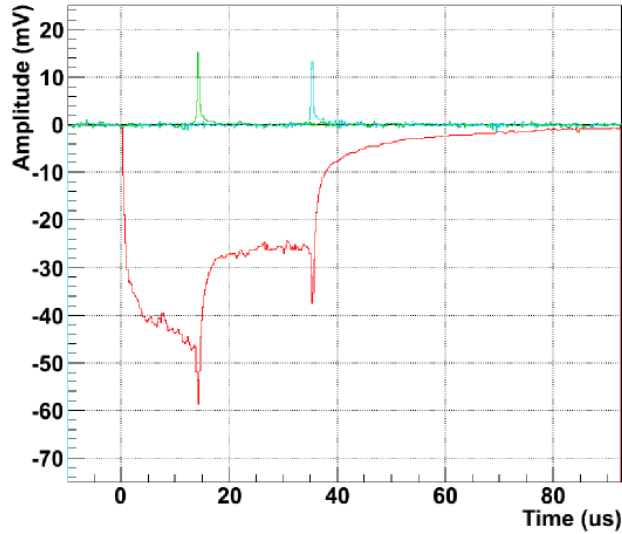


Figure 10.3.: Example set of signals from a Geiger discharge in a SuperNEMO tracker cell. The signal extracted from the anode wire is shown in red and the cathode signals extracted from the pick-rings are shown in green [152].

cell a current is induced on them. This generates a short pulse, positive in polarity. The amplitude of the signals is highly dependent on the impedance of the read-out circuit. Typical amplitudes for the anode pulse are 50 – 200 mV, while the cathode pulses are smaller at 10 – 20 mV.

From the arrival times of this set of signals (t_{Anode} , $t_{Cathode_1}$ and $t_{Cathode_2}$) two positional coordinates can be extracted: r , the radial distance of the closest ionisation point to the anode wire; and z , the position along the length of the cell.

The arrival time of the anode signal t_{Anode} is measured relative to the much faster signal of the calorimeter. An avalanche will take up to 7 μ s to reach the anode wire, depending on how far from it the initial point of ionisation is. This time can be converted back to a radial position with a drift model which is measured by fitting tracks to a series of hits in a cell array. In NEMO-3 the drift model took the form:

$$r = \frac{A \times t_{Anode}}{t_{Anode}^B + C} \quad (10.1)$$

where A , B and C are parameters measured in data. Alternative drift models are under investigation for SuperNEMO, some of which include the angle of incidence of the track as a parameter.

The propagation times of the avalanche to the ends of a tracker cell are given by the difference between the arrival times of the anode pulse and the relevant cathode ring pulse: $t_{Prop_i} = t_{Cathode_i} - t_{Anode}$. These times can be as long as 50 μs , depending on the voltage applied to the anode wire. The sum of the two cathode times ($t_{Prop_1} + t_{Prop_2}$) is the avalanche propagation time described above. In NEMO-3, the coordinate z was extracted via the expression:

$$z = \frac{L_{eff}}{2} \frac{t_{Prop_2} - t_{Prop_1}}{t_{Prop_1} + t_{Prop_2}} \left(1 + D \left| \frac{t_{Prop_2} - t_{Prop_1}}{t_{Prop_1} + t_{Prop_2}} \right| \right), \quad (10.2)$$

where L_{eff} is an effective length, roughly corresponding to the length of the cells with the copper rings subtracted, D is a tuned parameter and $Cathode_2$ is on the top of the detector (positive z). The last factor in the expression above corrects for the fact that the total propagation time is longer for hits very close to one end of the cell, where only one ‘‘propagation front’’ travels the entire length of the cell.

10.3. The tracker frame

In a SuperNEMO module the source foil is sandwiched between two tracker frames. A tracker frame accommodates 1017 cells in a 9×113 configuration. Each frame is further subdivided into two C-sections, named after their C-shaped structural frames. Each C-section contains 504 cells in a 9×56 configuration. The 9 additional cells required to complete the frame are positioned at the joining of two C-sections. These will be added at the time of detector integration at LSM.

In addition to the tracker cells, the tracker frame is populated with calorimeter modules, with a C-section having 32 modules on its vertical wall (X-wall blocks) and 16 larger blocks on the top and bottom (veto blocks). These modules are identical in construction to the NEMO-3 calorimeter blocks and hence of lower specification than those used on the main walls, with energy resolutions of around 10% and 16% at 1 MeV for X-wall and veto blocks, respectively. The modules are equipped with the best performing 5” PMTs recovered from NEMO-3 and the scintillator blocks are custom made to fit the dimensions of the new detector.

A sketch of a C-section is shown in Figure 10.4, where the cells and calorimeter modules are shown but the structural frame is omitted.

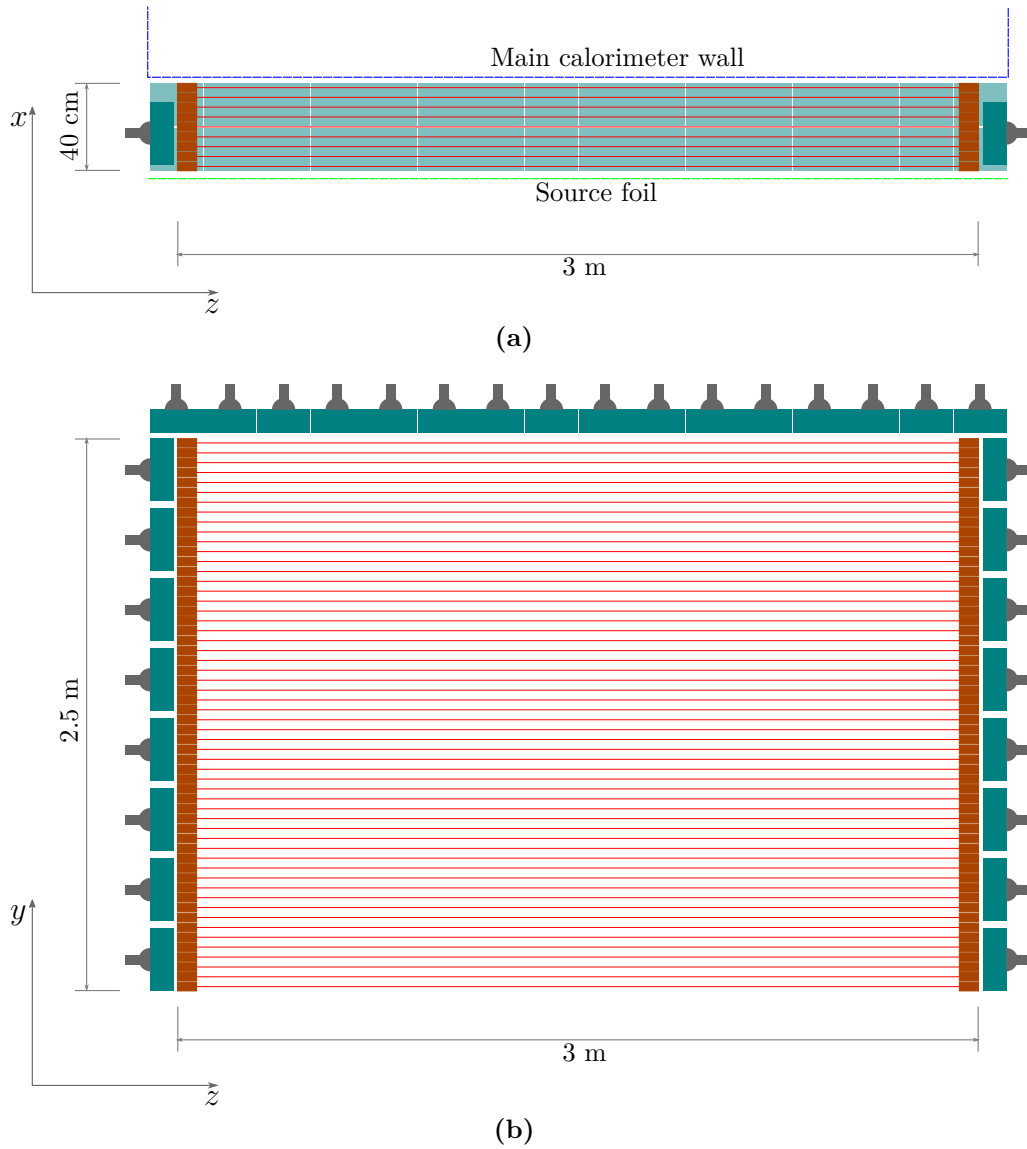


Figure 10.4.: Sketch of a SuperNEMO tracker C-section. Tracker cells are shown as in Figure 10.2 with the field shaping wires omitted for clarity. Scintillator blocks are shown in blue and PMTs in grey. In (a) the positions of the source foil and the main calorimeter wall are shown relative to the C-section. Dimensions are approximate and not to scale.

10.4. Construction of the tracker

The SuperNEMO tracker cells are produced at the University of Manchester in units of 2×8 referred to as cassettes. All the components that will be in contact with the tracker volume go through an intensive cleaning procedure adapted from a technique with proven results in other low-background experiments [153].

In addition to the cleaning, the stainless steel wire undergoes a testing procedure during which it is spooled through a test tank that mimics the operating conditions of a tracker cell. Data is acquired under cosmic rays as the wire is passed through the tank, allowing for the assessment of the wire performance. In particular, points that block the propagation of avalanches and points responsible for high rates of spurious discharges are identified. These can be caused by dust contamination or imperfections (dents or twists) on the wire. Sections of the wire that perform poorly are rejected [154].

The cassettes are strung by a purpose built robot and without human manipulation of the components (Figure 10.5). They are then transferred to a tank that is filled with the tracking gas mixture and a high voltage is applied to the anodes. A conditioning period of around two days is required for all the cells to stabilise and start showing normal operation characteristics. Cassettes that fail to stabilise during the conditioning period are rejected. Criteria for the acceptance of a cassette include: uniform hit rate, signal amplitude, avalanche propagation time and optimal operating voltage across all cells; avalanche propagation efficiency above 95% for all cells; and all plateaus being wider than 50 V. The conditioning of the cassettes dominates the total production time, with cassettes being built and tested at a rate of two per week.

The calorimeter modules are assembled and tested at UCL. They are then transported to the Mullard Space Science Laboratory (MSSL) where the structural frames of the C-sections are built. After being populated with the calorimeter modules, the C-sections are sealed and the ^{222}Rn activity inside them is measured. Upon satisfactory results the cassettes are inserted into the C-section frame (Figure 10.6). At the time of writing the first C-section (C0) has been fully populated with tracker cells.



Figure 10.5.: Photograph of the wiring robot in the University of Manchester clean-room. The end-caps of an assembled cassette are seen in the foreground and the wiring robot in the background.

Before the C-section is shipped to LSM, the ^{222}Rn activity in the fully populated frame is re-measured. At this point the tracker cells comprising an entire C-section are commissioned under cosmic rays. This is discussed in detail in Chapter 11.

10.5. Tracker electronics and DAQ

The SuperNEMO tracker HV supply and DAQ systems differ significantly from those used in NEMO-3.

The main improvement in the HV distribution system is the ability to regulate the supply to individual cells within a range 500 V from a common supply feeding several cells [155]. This will allow for each cell to be operated at its optimum voltage level.

Regarding the DAQ system, a novel technique to measure the longitudinal position (z) of tracker cell hits has been developed which, if successful will reduce the number of DAQ channels for future SuperNEMO modules. In parallel with recording the



Figure 10.6.: Photograph of the C0 frame at MSSL, partially populated with cells. The X-wall calorimeter modules PMTs are seen in the foreground.

arrival time of pulses on the pick-up rings, the Demonstrator electronics will pass the anode signal through a differentiating circuit and record the time of a series of three peaks. The first peak indicates the leading edge of the anode pulse, *i.e.*, the arrival of the avalanche to the anode wire, and the further two peaks signal the arrival of the avalanche to the ends of the cell (Figure 10.7). These three recorded times allow for the full reconstruction of a tracker cell hit, apart from an ambiguity regarding which $t_{Cathode_i}$ corresponds to the arrival of the avalanche to the top and bottom of the detector. This degeneracy can be resolved by either reading out a single pick-up ring, or by matching tracks to calorimeter hits at track reconstruction level.

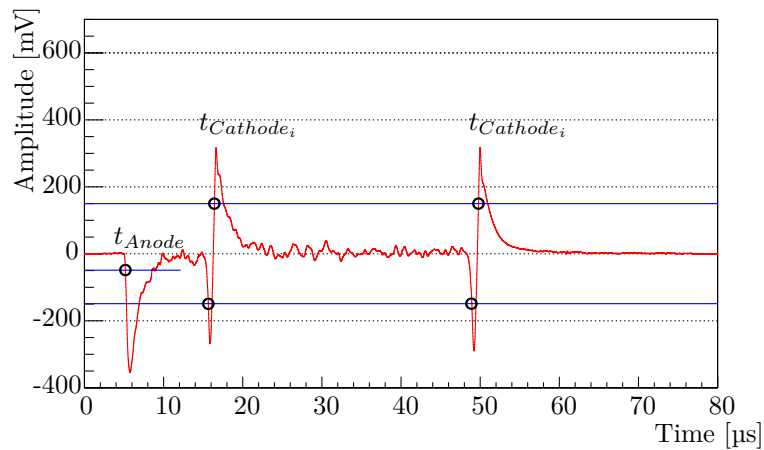


Figure 10.7.: Derivative of the anode signal. The leading edge of the anode pulse is labelled t_{Anode} and the peaks which signal the arrival of the avalanche to the ends of the cell are indicated as $t_{Cathode_i}$ [156]

Chapter 11.

Electronics for surface commissioning

As described in Section 10.4, the SuperNEMO tracker is built in C-section units ($\frac{1}{4}$ of the tracker). Before the C-sections are shipped to LSM, where they are integrated with each other and the other components of the detector, the C-sections undergo surface commissioning using cosmic rays at MSSL.

Given that in the final configuration the open faces of the tracker volume are sealed by the main calorimeter walls, temporary sealing plates were built such that the tracker can be filled with gas. This allows for leak testing of the permanent components of the frame, for the ^{222}Rn emanation measurements to take place and for the tracker to be operated independently of the other detector modules. The sealing plates are also part of the transportation structure which allows the tracker C-sections to be transported over to the French-Italian Alps without contamination of their internal volume.

The surface commissioning of the tracker will take place with the C-sections on their side, *i.e.*, with the x coordinate (as shown in Figure 10.4) along the vertical direction. The C-section calorimeter modules are tested independently of the tracker, prior to installation in the C-section, in a dedicated test stand at UCL.

This chapter describes the electronics for the surface commissioning of C-sections. The main components of the system are:

- the HV supply and distribution;

- the cosmic ray trigger;
- the VME DAQ cards;
- the DAQ computer and the VME controller.

The HV distribution system is recommissioned from NEMO-3, while the power supply itself has been newly acquired for the commissioning. The DAQ system has also been partially recovered from NEMO-3, namely the bespoke read-out VME cards, with the VME controller being a new off-the-shelf component. The cosmic ray trigger is comprised of two reused $1 \times 1 \text{ m}^2$ scintillator planes from the MINOS calibration detector [157], a custom made board hosting a field-programmable gate array chip (FPGA) and Nuclear Instrumentation Modules (NIM). The system is completed by a rack-mounted computer which communicates with the trigger board and the VME controller. A detailed diagram of the entire system is shown in Figure 11.1.

11.1. HV supply and distribution

The HV for the surface commissioning system is provided by a *CAEN SY1527* modular system, equipped with negative and positive polarity modules. The negative polarity modules provide HV to the cosmic ray trigger PMTs while the positive polarity channels are used to power the tracker cells.

The positive polarity module installed in the *CAEN* system provides 24 HV channels, each with a maximum voltage of 3.5 kV and with a power rating of 8 W. In normal operation, with a voltage under 2 kV, tracker cells draw up to 4 μA of current. When in an unstable, self-discharging mode the current drawn by each cell can increase by one order of magnitude. Each HV channel can therefore feed up to 50 cells. This allows for an entire C-section to be comfortably powered by a single *CAEN* module, including spare capacity for other purposes, if necessary.

The system can be controlled locally or remotely via an Ethernet connection. The latter allows for interactive control through a Telnet session or for automation with a C library provided by *CAEN*.

Safe high voltage (SHV) cables connect the *CAEN* module to the backplane of a NEMO-3 HV distribution crate (Figure 11.2), which is populated with up to

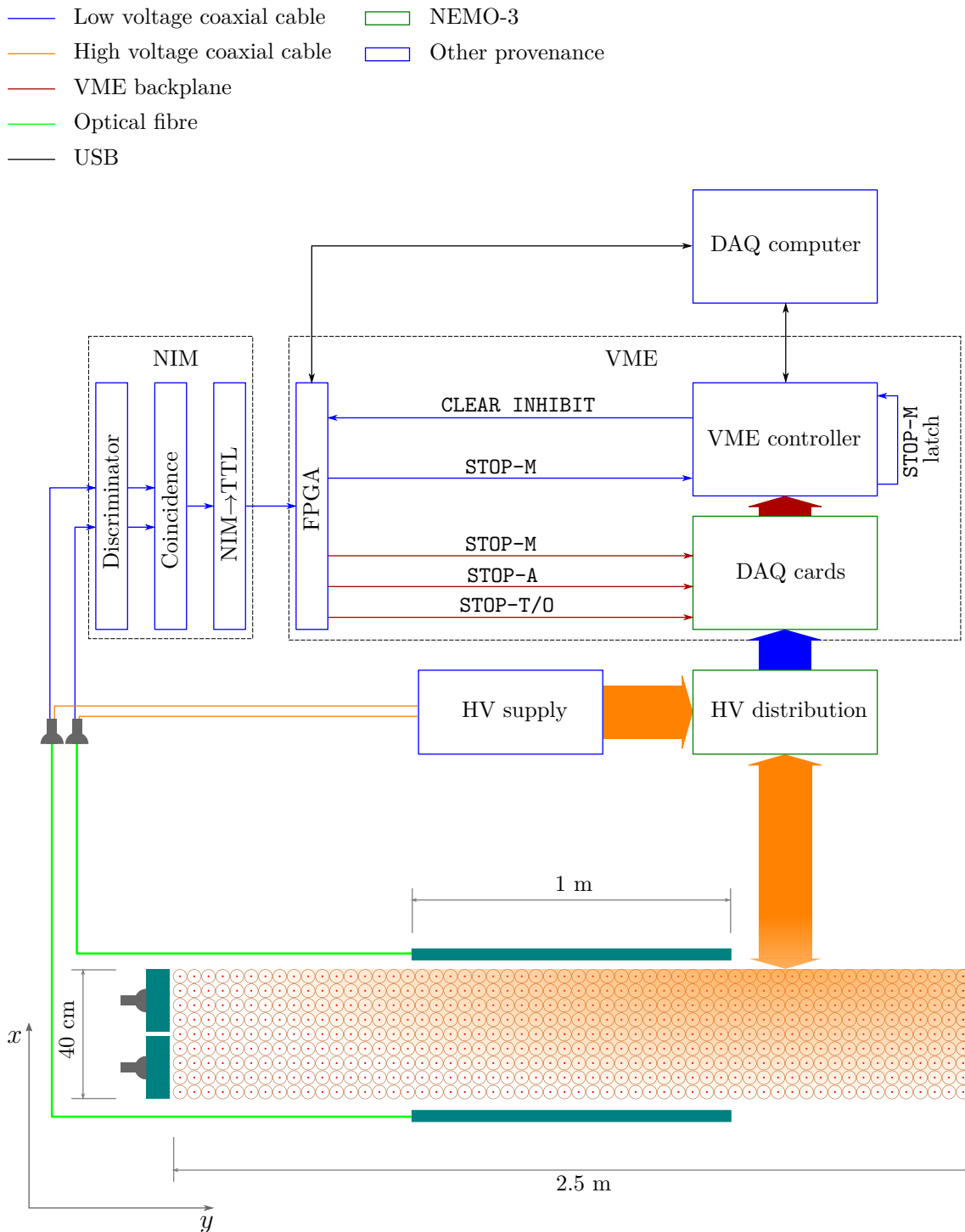


Figure 11.1.: Schematic diagram of the tracker commissioning electronics. The physical arrangement of the C-section and the cosmic trigger scintillator planes is shown on the bottom of the diagram, with the scintillator planes in blue, PMTs in grey and the tracker cells as drawn in Figure 10.2, with the field shaping wires omitted. On the top, the detailed interactions between the system’s components are described. The types of connections used are described in the legend, as is the provenance of the main components.

20 HV distribution cards, although only 16 are expected to be necessary for the commissioning of the C-sections. Each HV distribution card (HV motherboard) can be supplied by up to three different HV channels, with the mapping of the HV channels to motherboards being defined by the adjustable backplane of the HV distribution crate.

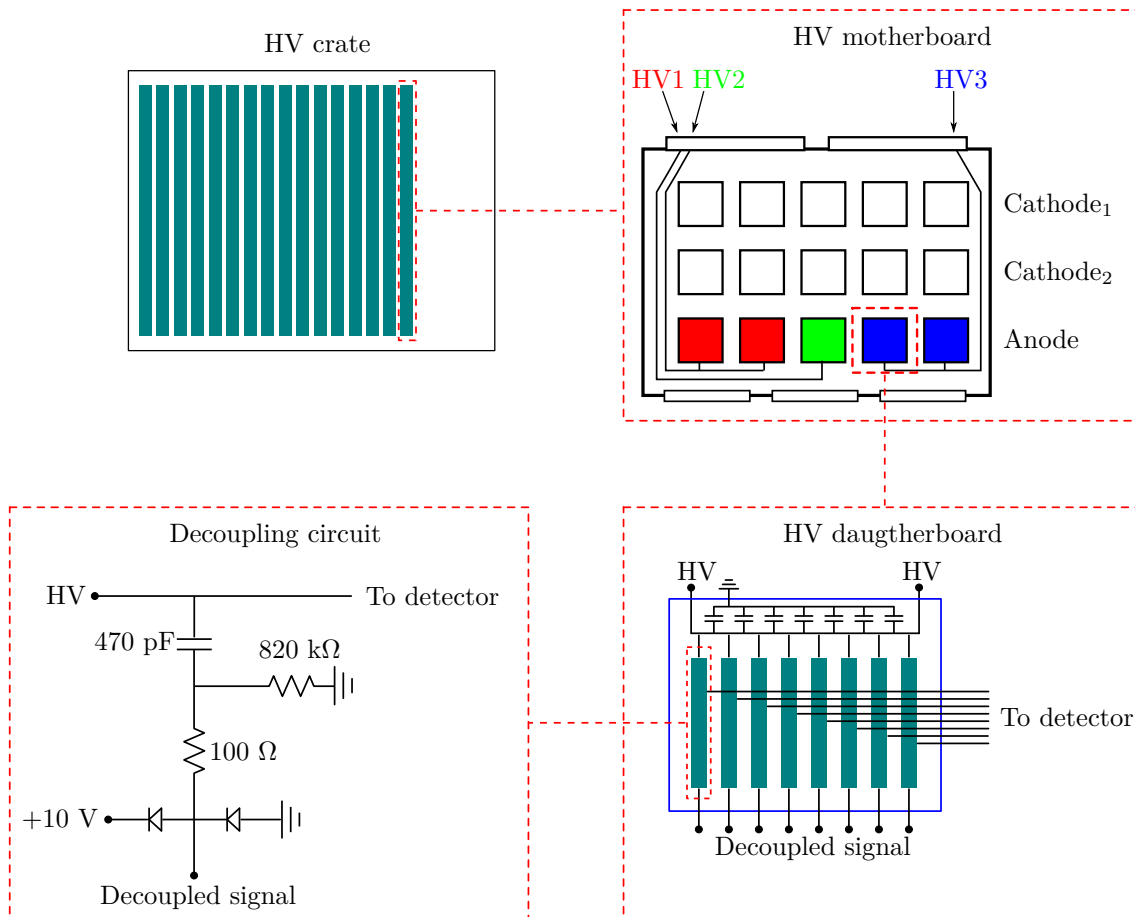


Figure 11.2.: The NEMO-3 HV distribution and decoupling system. Clockwise from the top left corner: sketch of a NEMO-3 HV crate populated with the number of cards required for the commissioning of C-sections; detailed diagram of an HV motherboard in one of the possible HV distribution configurations; sketch of a daughterboard showing a common HV being distributed across eight channels; diagram of the anode signal decoupling circuit.

The HV motherboards are populated with daughterboards which distribute the HV to individual cells and decouple the signal pulses from the HV lines. The daughterboards are arranged in sets of three: two for the pick-up cathode rings and

one for the anode wire¹. Each daughterboard contains eight decoupling circuits, each of them supplying one tracker cell with HV (or ground, in the case of the pick-up rings) and extracting the relevant signal. The decoupling circuits are high-pass RC filters with a cut-off frequency of around 400 Hz which allow the signal pulses through to the read-out electronics but block the HV. The decoupled signals from both the anode and cathode daughterboards are routed to connectors on the front face of the HV motherboards, which are in turn connected to the DAQ boards with coaxial signal cables (Figure 11.1).

The high voltage coaxial cables that carry the HV to the cells are directly soldered on to the decoupling circuits on the daughterboards. The detector ends of the cables were adapted to use in the SuperNEMO tracker feedthroughs fitted to the C-sections.

11.2. Cosmic ray trigger

The cosmic ray trigger prepared for the commissioning of the tracker consists of two MINOS calibration detector scintillator planes. These will be placed above and below the C-section, with a coincident signal on both scintillator planes indicating the traversal of the C-section by a charged particle. Even though each scintillator plane is segmented in thin strips, the light from all strips is collected in a single optical fibre bundle which is interfaced with one PMT. The PMT analogue signals are put through a NIM discriminator unit which in turn produces NIM logic pulses with a predefined width when the analogue signals exceed a preset threshold. The discriminated signals are then fed to a NIM coincidence unit which produces a single NIM pulse if the two signals overlap. Before being sent to the FPGA trigger board the coincidence trigger pulse is converted from a $50\ \Omega$ NIM standard signal to a high-impedance TTL pulse (Figure 11.1). The PMTs which instrument the scintillator planes operate at around 1800 V, with a coincidence rate of around 50 Hz.

A custom made trigger board hosting an FPGA receives the TTL trigger pulse and produces a set of signals required by the NEMO-3 DAQ cards [158]. The board is interfaced with the DAQ cards via the VME backplane, with the VME controller by coaxial cables and with the DAQ computer via USB (Figure 11.1). Through

¹Even though the pick-up rings were kept at ground in NEMO-3, the electronics were designed such that a voltage up to 300 V could be applied to them.

the VME backplane the FPGA sends a set of three pulses (`STOP-T/0`, `STOP-A` and `STOP-M`) with predefined delays to all the DAQ cards. The last of these signals, `STOP-M` is also sent to the VME controller where it is used to initiate the read-out of data to disk. Upon receiving a trigger signal the FPGA is set in an inhibited mode in which it does not react to further trigger pulses. The system is reverted back to its active mode only after the read-out is complete and a `CLEAR INHIBIT` pulse is sent from the VME controller. The FPGA is powered via the USB connection to the computer, which is also used to configure the delays of the `STOP-A` and `STOP-M` pulses relative to the trigger signal.

11.3. DAQ cards

The NEMO-3 tracker DAQ cards match one-to-one with the HV motherboards, with their front faces having the same connectors and compatible pin maps.

Each DAQ card contains ten pairs of bespoke application-specific integrated circuits (ASICs), each pair consisting of an analogue ASIC and a digital one. Each pair of ASICs reads out four tracker cells, giving a DAQ card the same capacity as the HV distribution boards: 40 cells.

The decoupled signals are routed from the front face of the cards to the analogue ASICs where they are amplified and fed to a comparator together with a reference threshold voltage. On each ASIC a parameter can be adjusted which scales the threshold voltages on all four channels for both the anode and cathode ring signals. If the signals exceed the threshold, a TTL pulse is sent to the corresponding digital ASIC's channel.

A digital ASIC consists of a total of 16 time-to-digital converters (TDCs): four for each tracker cell. Three of the TDCs are 12-bit and, given the 50 MHz clock of the DAQ cards, can record times up to 82 μs . The third TDC has a higher capacity of 17 bits or 2.6 ms. The first TDCs are used to record the arrival times of the prompt anode signals ($\text{TDC}_{\text{Anode}}$) and the propagation time for each cathode ring (TDC_{C1} and TDC_{C2}) while the latter (TDC_{α}) is used to record delayed tracker hits for tagging BiPo type events.

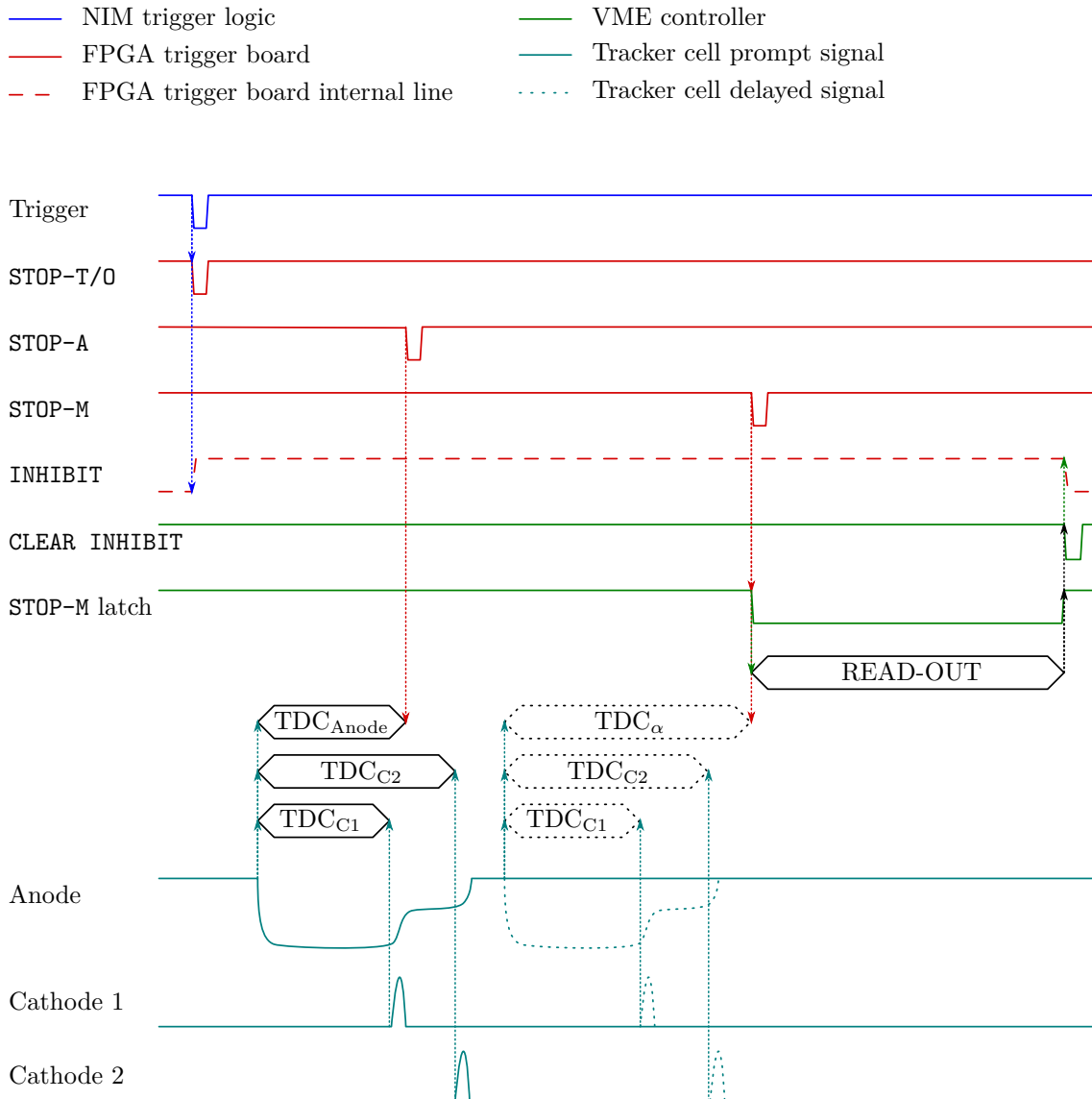


Figure 11.3.: Timing diagram for the tracker commissioning DAQ system. The signal lines of the DAQ components are shown colour coded, as defined in the legend. The causal relationship between the pulses is shown with dotted arrows. Two sample sets of pulses from a tracker cell are shown: one prompt and one delayed.

As a passing particle is detected by the trigger system a **STOP-T/0** pulse is sent to all DAQ cards in the crate. This signal interrupts the periodic time-out which resets all TDCs in the cards every 100 μs . This time-out minimises the chances of tracker hits unrelated to a triggered event (*e.g.*, a spurious discharge in a cell) being read out as part of the event. After this, two more signals are produced by the trigger system and fed to all cards: a **STOP-A** pulse, with a preset delay ($\Delta_{\text{STOP-A}}$) of around 7 μs ; and a **STOP-M** pulse, delayed by a much longer time ($\Delta_{\text{STOP-M}}$) of around 700 μs (Figure 11.3).

If an anode signal arrives before the **STOP-A** signal is received, all 12-bit TDCs are started: $\text{TDC}_{\text{Anode}}$; TDC_{C1} ; and TDC_{C2} . $\text{TDC}_{\text{Anode}}$ is stopped by the arrival of **STOP-A**, while $\text{TDC}_{\text{C}i}$ are stopped by the detection of the relevant signals from the cell's pick-up rings. Therefore, the arrival time of the anode pulse relative to the trigger signal, *i.e.*, the drift time of avalanches which allows for the radial position of the hit to be calculated, is given by $t_{\text{Anode}} = \Delta_{\text{STOP-A}} - t_{\text{TDC}_{\text{Anode}}}$, where $t_{\text{TDC}_{\text{Anode}}}$ is the time measured by $\text{TDC}_{\text{Anode}}$. The arrival times of the pick-up rings relative to the anode pulse, which allow for the calculation of the longitudinal coordinate of the tracker hit, are directly given by the time recorded by the relevant TDCs: $t_{\text{Prop}i} = t_{\text{TDC}_{\text{C}i}}$. If no cathode ring pulses are detected, the $\text{TDC}_{\text{C}i}$ are stopped by the arrival of **STOP-M**.

If, on the other hand, a hit on the anode wire occurs after **STOP-A**, the 17-bit TDC_{α} is started instead of $\text{TDC}_{\text{Anode}}$, being stopped by the arrival of **STOP-M**. In this case, no radial position information of the hit is obtained. Instead, the tracker hit is assumed not to be directly correlated to the external trigger with the delay of the hit relative to the trigger being given by: $t_{\alpha} = \Delta_{\text{STOP-M}} - t_{\text{TDC}_{\alpha}}$. This variable is used to identify delayed α emissions from BiPo events. The behaviour and positional information from the cathode ring TDCs is the same as in the prompt-hit case described above. It should be noted that a given channel cannot have both prompt and delayed hits in a single event. The physical dead time of a tracker cell is typically longer than the read-out window ($\Delta_{\text{STOP-M}}$) and the DAQ cards are not designed to keep to a second hit in the same event.

Each digital ASIC contains a status register consisting of a bit-mask which specifies which, if any, of the TDCs have been started in the group of four channels. Furthermore, each DAQ card has a status register indicating which, if any, of the

ASICs has been activated in the triggered event. This information is used in the software read-out loop to decide which data is written to disk.

11.4. VME controller and read-out cycle

The DAQ rack-mounted computer communicates with the rest of the DAQ system via a USB connection to the *CAEN* controller on the VME crate. Upon receiving the **STOP-M** signal from the FPGA trigger board, the VME controller changes the state of a line which is fed back to itself, latching the **STOP-M** signal (Figures 11.1 and 11.3). This is necessary due to the relatively slow software read-out loop, compared to the fast FPGA: producing a **STOP-M** pulse long enough that it is consistently detected in the software read-out loop is cumbersome at the level of the FPGA.

When the system is in operation, the read-out software remains in a loop, repeatedly querying the state of the **STOP-M** latch. If the latch has been activated, the read out of the cards is initiated.

The software instructs the VME controller to retrieve the statuses and TDC counts stored in all cards. While the NEMO-3 DAQ cards do not support the VME *block transfer* mode, which allows for fast data transmission, the *CAEN* VME controller provides a *Multiread* method which allows several registers to be probed in a single USB exchange. It was found that separately querying the status registers and then querying only the registers on which useful data was stored (the contents of activated TDCs) offered no significant advantage over querying all the registers at once (including those with meaningless data). This is thought to be due to both the operating system's process scheduling and the overhead required for USB communication.

Once all the data from the DAQ cards has been transferred to the computer, the status registers are inspected and data regarding channels on which an anode wire pulse has been detected are written to disk in a predefined textfile format.

After the data have been written to disk the read-out code instructs the VME controller to deactivate the **STOP-M** latch and to send out the **CLEAR INHIBIT** line which in turn deactivates the **INHIBIT** line on the trigger board FPGA, leaving the system in its initial, receptive, state (Figure 11.3).

11.4.1. Read-out cycle duration and dead time

Most of the time during a read-out cycle is spent retrieving the data from the DAQ cards. The dead time resulting from a long read-out cycle is not of particular concern for commissioning purposes as the physical dead time of a cell is itself long and the trigger rate from cosmic rays is relatively low. It is nevertheless important to understand the reduction of the system's efficiency resulting from the read-out dead time.

The duration of the read-out cycle was estimated by obtaining time-stamps at the beginning and end of each cycle. The read-out cycle duration was found to increase linearly with the number of DAQ cards in the system, with roughly 1 ms added to the read-out time per card (Figure 11.4a).

Initial tests, with a trigger rate of 53.4 Hz and using 13 DAQ cards, gave a read-out rate of 28.9 Hz, in good agreement with a simple toy MC simulation (Figure 11.4b). With the full set of 16 DAQ cards the expected read-out time is 19.5 ms, giving a predicted read-out rate of 26.2 Hz.

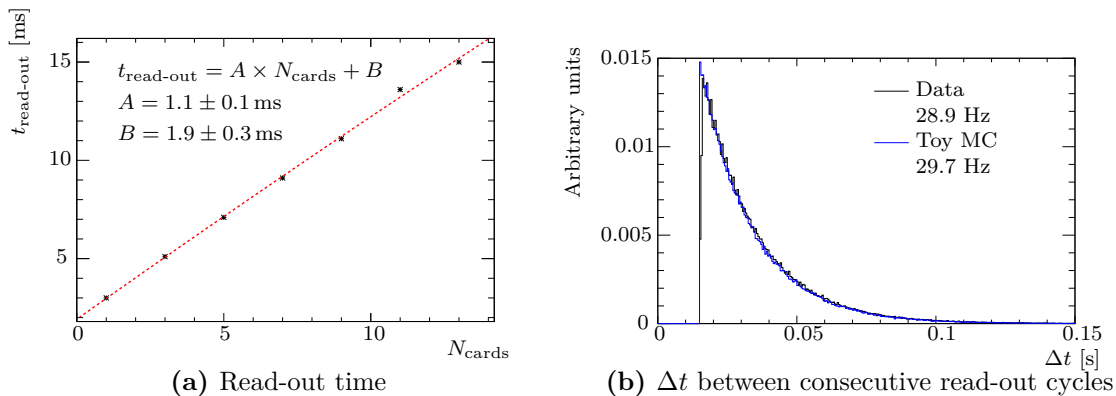


Figure 11.4.: Read-out dead time and rate of the tracker commissioning DAQ system. In (a) the read-out time is shown against the number of DAQ cards used and in (b) the time interval between consecutive events read out with 13 cards is compared to a toy MC prediction, showing good agreement.

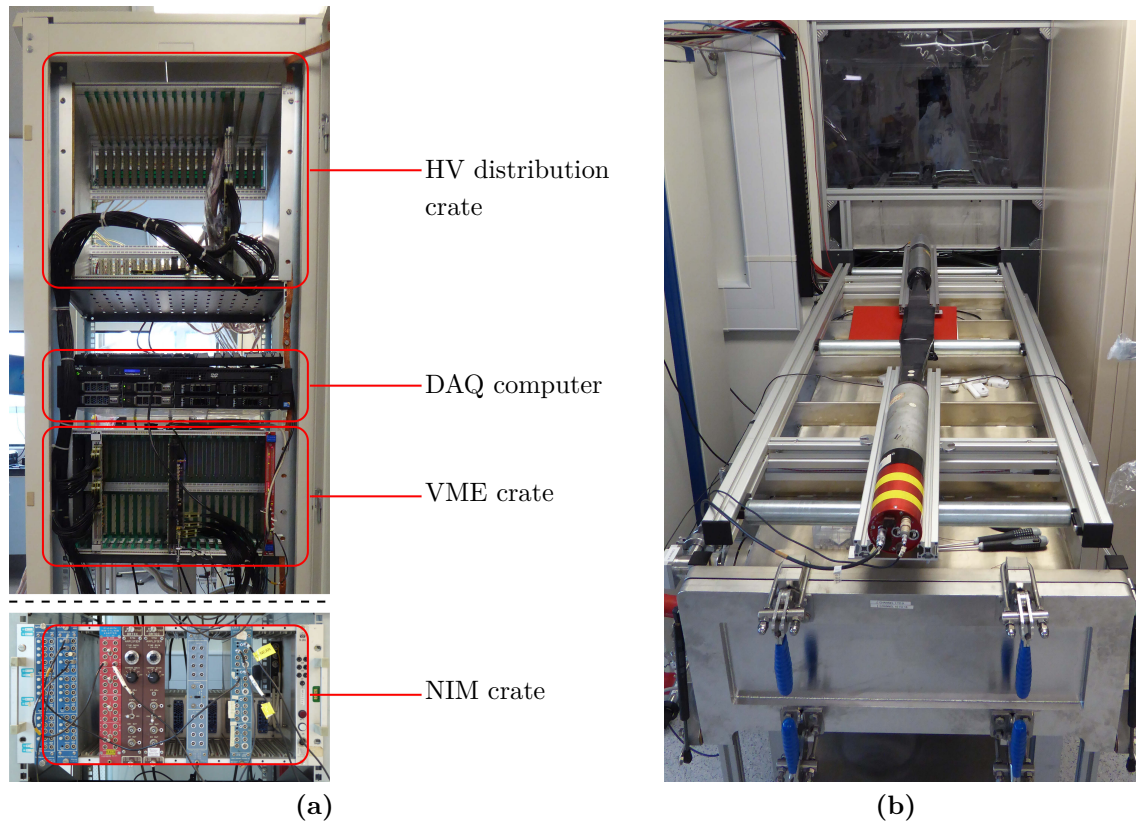


Figure 11.5.: Photograph of the UCL electronics and cosmic ray trigger at the University of Manchester. The electronics rack is shown in (a). On the top of the rack the NEMO-3 HV distribution crate is seen, populated with a single HV motherboard, with the DAQ computer below it. The VME crate can be seen below the computer. It is populated with one NEMO-3 DAQ card (left), the FPGA trigger board (middle) and the VME controller (right). The NIM crate where the trigger logic is implemented was housed in a separate rack. It is shown on the bottom of the figure. The arrangement of the small scintillator planes on top of the cassette test tank is shown in (b). The planes are in their *nominal* position, roughly in the middle of the tank on the transverse direction (x) and about $\frac{3}{4}$ of the cells' length away from the read out cathode ring in the longitudinal direction (z). Only half of the test tank is visible, with the other half being on the far side of the blackened window.

11.5. Testing the tracker commissioning DAQ system on the cassette test tank

The tracker commissioning DAQ system was tested on two tracker prototypes. Initial tests were performed on a single cell prototype at UCL [159]. This prototype was not built to the final SuperNEMO specifications, with arrangement of the field shaping wires and cell radius being those of NEMO-3 tracker cells. Given the different cell geometry and the limitation of a single read-out channel of the UCL prototype, the commissioning system developed at UCL was transported to the University of Manchester to be tested on SuperNEMO production cells in the cassette test tank.

The testing was carried out over three sessions, during which a significant amount of time was spent troubleshooting the system. The main issues encountered were related to the mapping of the pins on the test tank feedthrough and inappropriate grounding of the cells.

For each testing session, the commissioning electronics were connected to a cassette which had previously been conditioned and had passed the criteria for insertion into the Demonstrator tracker (Section 10.4).

The configuration of the system for the cassette tests differed significantly from the C-section commissioning setup in two aspects:

- the cassette test tank is equipped with a feedthrough which is only connected to the anode wire and one of the two pick-up rings, therefore the read-out of one of the cathode pulses is not possible;
- smaller scintillator planes were used for the cosmic ray trigger, with a coincidence rate of around 1 Hz and only illuminating a few cells at a time.

The two small scintillator planes were placed on top of the test tank, overlapping with each other as much as possible. The planes were nominally positioned in the middle of the test tank in the transverse direction (x) and about $\frac{3}{4}$ of the test tank's length away from the read out cathode ring in the longitudinal direction (z).

Photographs of the electronics rack and the arrangement of the cosmic trigger scintillators on the test tank are shown in Figure 11.5.

x -axis scan

To validate both the mapping of the physical position of the cells to the DAQ channels and the effectiveness of the cosmic ray trigger, a scan of the cells was performed by moving the scintillator planes along the x -axis and taking data in four positions (Figure 11.6).

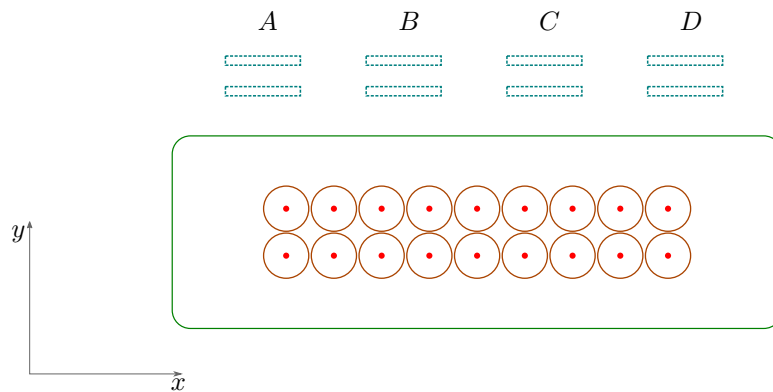


Figure 11.6.: Sketch of a cassette in the test tank. The four positions of the scintillator planes for the x -axis scan are shown.

The hit rates of the 18 tracker cells in the four configurations of the scintillator planes is shown in Figure 11.7. The area of highest incidence of hits can be seen shifting from left to right, according to the position of the scintillator planes. This correlation indicates that the trigger is selecting events with cosmic rays traversing the cassette, as expected. These results also validate the map between the DAQ channels and the position of the tracker cells in the cassette.

Geiger plateau scan

As described in Section 10.1, the Geiger plateau is an important characteristic of Geiger detectors. In particular for the SuperNEMO tracker, it is critical that the plateaus of the many tracker cells overlap sufficiently such that all cells can be operated near their optimal point with a limited range of voltages applied to the anode wires. It is thus important to measure the Geiger plateau of the tracker cells during the commissioning of the detector.

To test this ability of the system, a scan was performed on a cassette, with the same voltage applied to all wires, increasing in steps from 1600 to 2000 V. The hit

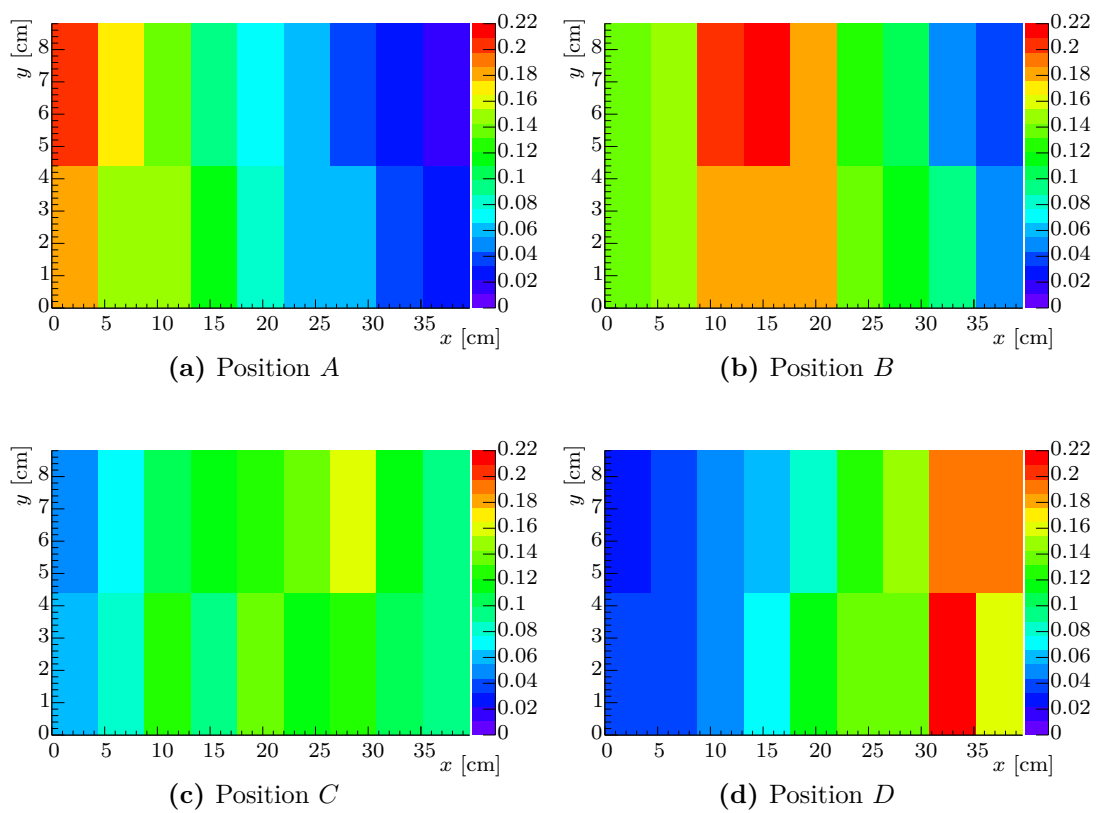


Figure 11.7.: Results of the x -axis scan of the cassette. The hit rate for each cell is given in Hz by the colour scale. The four positions A , B , C and D correspond to the ones shown in Figure 11.6.

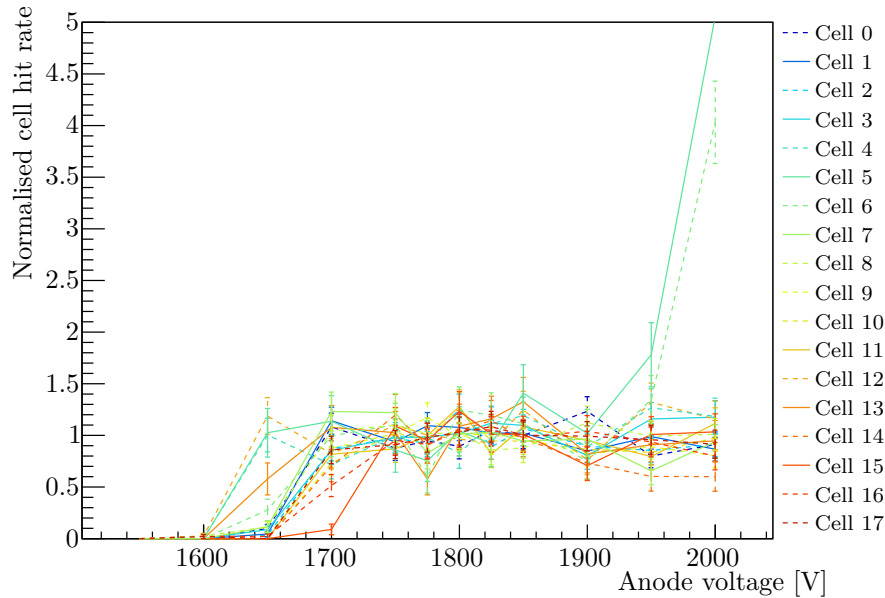
rate on each cell was measured for each step, with the results being shown in Figure 11.8a. Given the uneven illumination of the cells in the cassette (as shown in Figure 11.7) the plateau curve for each cell was normalised to its nominal hit rate, taken to be the average hit rate at voltages between 1750 and 1900 V. The resulting plateaus can be compared to a scan performed previously with the test tank DAQ system (Figure 11.8b). It should be noted that the latter system is triggered by individual hits on cells and not by an external cosmic ray trigger. As such, the measured hit rates can be directly compared between different cells with no normalisation required for the plateau to become apparent. Both scans give compatible results, with similar starting points and widths. The earlier scan shows a larger number of cells becoming unstable at the high end of the applied voltage compared to the scan performed later with the commissioning DAQ system. The more stable behaviour of the cassette is likely to be due to the longer conditioning time experienced by the cassette at the time of the tests with the commissioning DAQ system.

Cathode ring read-out

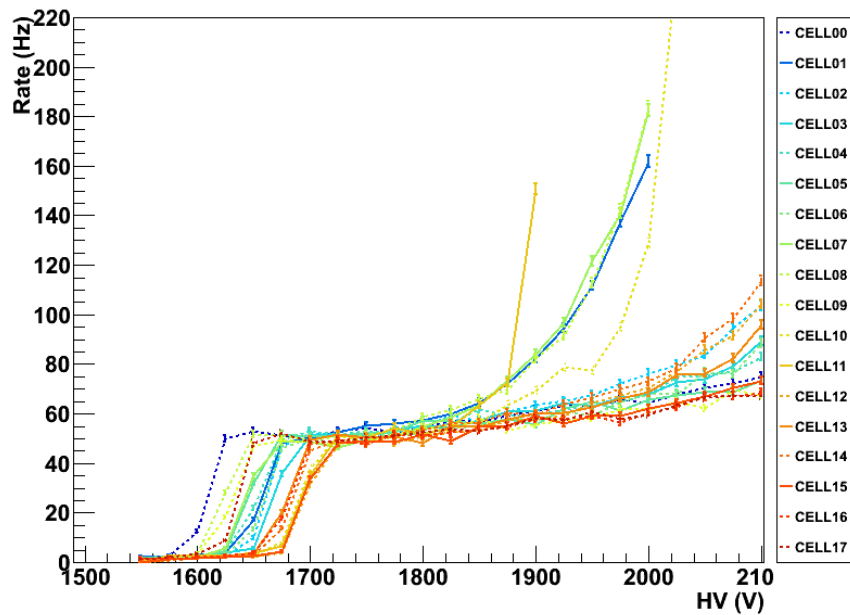
An important part of the tests of the commissioning DAQ system with the SuperNEMO cells was to demonstrate the ability of the system to adequately read out the signals on the cathode rings. These signals allow for the measurement of the efficiency and speed of the propagation of the avalanches along the cell, both being important characteristics of the tracker cells.

As mentioned above, the feedthrough on the cassette test tank allows for the read out of the cathode rings on one end of the cassette only, limiting the scope of these tests. Due to detector grounding issues which have been identified at the time of writing, but had not been resolved when the cassette data was obtained, only six of the 18 instrumented cathode rings in the cassette were correctly read out.

As no pulse shape analysis is possible with the commissioning DAQ system, the only indication of the successful propagation of the Geiger avalanche to both ends of the detector is given by the cathode ring pulses. The efficiency of the propagation is then given, for each cell, by the ratio of hits in which the cathode ring pulses have been detected to the total number of hits. The efficiency of the avalanche propagation to the available cathode for the six read out cells is shown in Figure 11.9. All cells show a good efficiency, expected to be above 90%.



(a) Commissioning DAQ



(b) Cassette testing DAQ [160]

Figure 11.8.: Scan of the Geiger plateau. Two scans of the Geiger plateau of the same cassette are shown: (a) was measured with the DAQ system described here and (b) was obtained with the system used for testing the cassettes during production. The hit rates of each cell in (a) have been normalised to the average hit rate between 1600 and 1900 V.

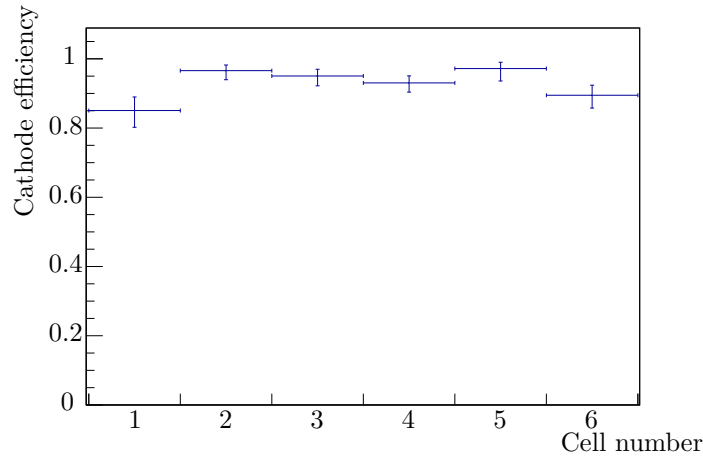


Figure 11.9.: Efficiency of the avalanche propagation of six cells in a cassette.

Another measurement of interest is the time of propagation of the avalanches to the cathode rings. To a good approximation, the ratio of this time to the total propagation time gives the longitudinal position of the hit in units of the effective length of the cells. With the scintillator planes in their *nominal* position the read-out hits are expected to be roughly $\frac{3}{4}$ of a cell's length away from the read out cathodes (Figure 11.5). The total propagation time cannot be directly measured with the setup described here, given that only one cathode pulse is read out. However, the cassette being used for the tests had previously been characterised with the test tank electronics which allow for measurement of the total propagation time by the analysis of the anode pulse shape. The average total propagation time for cells 1 – 6 on the cassette was $42.4 \mu\text{s}$ [160]. For tracker hits occurring in the range of z covered by the scintillator planes (a region a few cm wide at about $\frac{3}{4}$ of the cassette's length) it is expected that the propagation time to the read out cathode rings is $t_{Prop_1} \approx \frac{3}{4} \times 42.4 \mu\text{s} = 31.8 \mu\text{s}$.

The propagation times to the available cathode read out with the commissioning DAQ system are shown in Figure 11.10. The average propagation time for cells 1 – 6 is $33.1 \mu\text{s}$, consistent with the expectation given above.

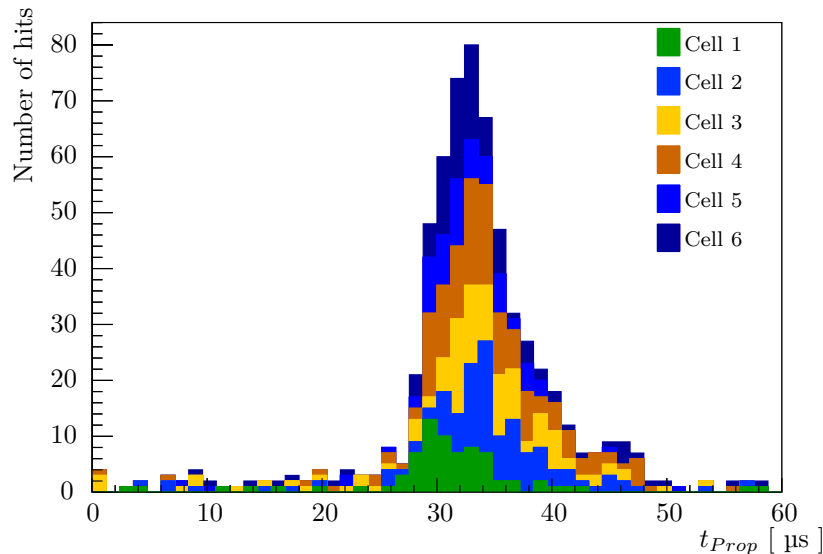


Figure 11.10.: Distribution of the propagation time to the read out cathode ring for six cells in a cassette.

Discussion of results

The tests of the commissioning DAQ system on the cassette test tank at the University of Manchester have demonstrated that the system can read out a multiple-cell detector. In particular, the following capabilities of the system were shown:

- the selection of cosmic ray tracker hits with the trigger system;
- the measurement of the cells' Geiger plateau;
- the measurement of the efficiency and time of the avalanche propagation (for one cathode ring only).

The system is now ready for large scale implementation, to instrument the 504 cells of a C-section for surface commissioning. In this setup, with a large number of cells, and the remaining cathode rings instrumented, the following characteristics of the tracker can be probed, in addition to the above:

- the drift model converting the arrival of the anode wire pulse into a radial coordinate, by fitting straight-line tracks to ~ 9 hit events;
- the total propagation time, by reading out the two cathode pulses, and subsequent calibration of the reconstruction of longitudinal hit positions.

Chapter 12.

Gas mixing system for the Demonstrator module

As described in Section 10.2 the SuperNEMO tracker cells operate in a gas mix of helium, ethanol and argon at 95%, 4% and 1% fractions by volume, respectively. The three components of the gas mix are obtained separately, with the gaseous components being supplied in cylinder manifolds and the ethanol in its liquid state. The system to mix the three components of the gas and supply it to the SuperNEMO Demonstrator was recovered from NEMO-3 and largely rebuilt for the SuperNEMO Demonstrator. The main purposes of the rebuild were to reduce the ^{222}Rn emanation level of the system and to make it more compact and transportable such that it can be used both for the commissioning of the tracker and for running the experiment in its final configuration at LSM.

12.1. Principle of operation

The purpose of the gas system is to supply the tracking detector with a well defined and adjustable gas mixture at a given flow rate, while maintaining a small but constant over-pressure inside the detector volume.

Helium and argon are supplied to the system from separate gas cylinder manifolds. The gases enter the system through separate lines, each going through a filter to remove any particulate contaminants that might have been introduced into the gas flow upstream of the system (Figure 12.1). The required ratio of helium to argon

is achieved by regulating the flow rate of the gases in the two lines with mass flow controllers (MFCs). The MFCs contain an electrically operated flow control valve and measure the flow rate of the gas through thermal dispersion: the gas is heated at one point and its temperature is measured at the same point and further downstream. The resulting temperature gradient depends on the flow rate and composition of the gas, with the flow meters being factory calibrated for the required gases, allowing for the measurement of the flow rate. A system supplied by the manufacturer is connected to the MFCs and regulates the flow control valve such that the desired flow rate is achieved.

The two MFCs in the system have a range up to 1.3 and 0.13 m³/hr for helium and argon, respectively. This allows for a range of argon to helium ratios to be used, depending on the required flow rate. At the nominal ratio of 1%, the system allows for precise control of the gas mixture from around 0.2 to 1.3 m³/hr, with the maximum flow rate corresponding to 2.6 replacements of the Demonstrator's internal volume per day. This volume change rate is two orders of magnitude faster than what was used in NEMO-3.

The system includes a line for faster flow rates which bypasses the MFCs, going instead through a less accurate variable area flow meter which provides readings up to 30 m³/hr. The flow rate on this line is manually adjustable with a flow control needle valve. This line is intended for initially flushing the detector with pure helium to remove air and moisture from the system.

The system contains several pressure relief valves to prevent a large over-pressure being transmitted to the internal volume of the detector, in the event of a failure of one of the gas system's components (*e.g.*, a pressure regulator or a flow controller). In normal operating conditions the over-pressure in the detector will be set by an output bubbler. While the design of this component is in progress, it is likely to consist of a mineral oil bubbler placed downstream of a sump. In the event of a large under-pressure being generated in the detector volume, the mineral oil is transferred to the sump without contaminating the internal volume of the detector. An over-pressure of 10 – 20 mbar is foreseen, corresponding to 13 – 26 cm of mineral oil (Figure 12.2). This level of over-pressure presents an engineering challenge as it generates forces equivalent to around 15 – 30 tonnes on the main calorimeter walls, which are themselves populated with fragile detector equipment. However, pressure measurements at LSM have revealed that the passage of heavy vehicles in the road

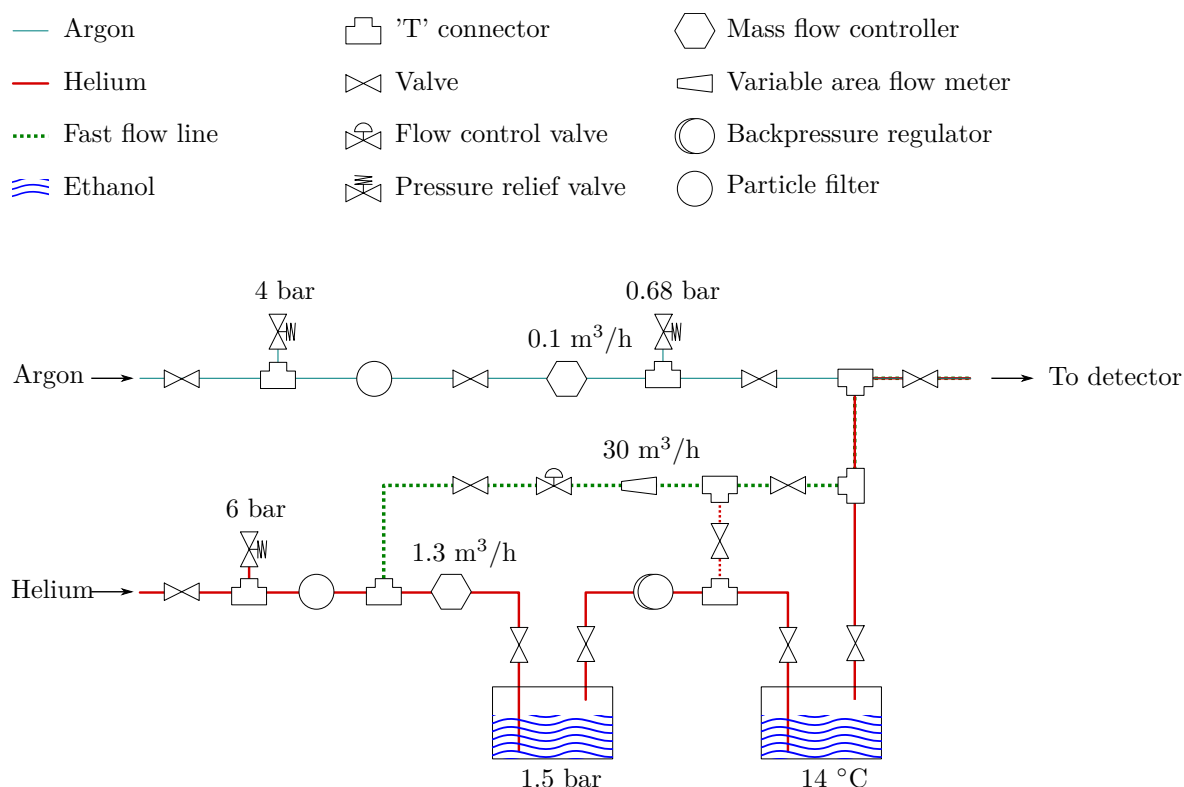


Figure 12.1.: Flow diagram for the Demonstrator's gas mixing system. The gas flow is from left to right with the argon line shown on the top and the helium line on the bottom. The diversion for fast flow rates is shown between the two lines. The vent pressures are indicated over the pressure relief valves and the maximum flow rates for each flow controller/meter are displayed above the relevant components. The two ethanol bubblers are shown on the bottom of the diagram, with typical values for the controlled conditions indicated below them.

tunnel to which the laboratory is attached can generate pressure fluctuations as large as 10 mbar over a few minutes [161].

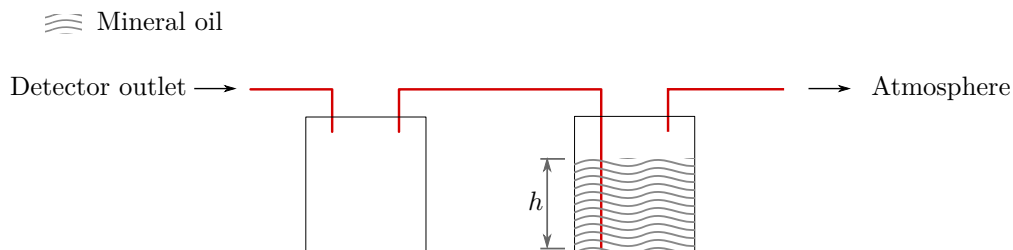


Figure 12.2.: Diagram of a tentative gas outlet system of the Demonstrator. The gas flow is from left to right with the gas coming out of a detector going through a sump followed by a mineral oil bubbler from which it is released to the atmosphere. The height of the mineral oil column (h) determines the over-pressure of the detector relative to the atmosphere. A height of 13 – 26 cm corresponds to an over-pressure of 10 – 20 mbar.

12.1.1. Two-stage ethanol vapour addition

The ethanol vapour component of the gas mixture is added to the helium before it is mixed with the argon. The gas is passed through two ethanol bubblers which are under controlled pressure and temperature conditions so that the required amount of ethanol evaporates into the gas flow.

For ideal gases at equilibrium, Dalton’s law states that the total pressure of a gas mix in a constant volume at constant temperature is equal to the sum of the partial pressures of the individual components, with the partial pressure of a gas component being defined as the hypothetical pressure that component would exert if it occupied the volume by itself. This can be combined with Amagat’s law, stating that at fixed temperature and pressure, the total volume of an ideal gas mix is equal to the sum of its constituents’ volumes, to give:

$$V_i = V_{\text{Total}} \times \frac{p_i}{p_{\text{Total}}}, \quad (12.1)$$

where V_i and V_{Total} are the volumes of gas component i and the total gas volume; p_i is the partial pressure of gas i ; and p_{Total} is the pressure of the combined gas mix.

It is clear from Equation 12.1 that the fractional volume taken up by a gas component is given by the ratio of its partial pressure to the total pressure of the gas mix.

Through evaporation, liquid surfaces exert a vapour pressure on their surroundings. This pressure is described, in terms of the temperature of the liquid surface, by the Antoine equation:

$$\log_{10} p_{\text{Vapour}} = A - \frac{B}{C + T}, \quad (12.2)$$

where p_{Vapour} is the vapour pressure at equilibrium, T is the temperature and A , B , C are parameters tuned for each particular substance, and valid over a range of temperatures.

The dependence of the fractional volume of a vapour on the total pressure of the vessel (Equation 12.1) and on the temperature of the liquid (Equation 12.2) is used to control the amount of ethanol added to the helium component of the tracker gas mixture.

At a first stage, the helium is bubbled through ethanol at room temperature in a large vessel under pressure. The pressure is controlled by a back-pressure regulator placed downstream of the vessel, and adjusted such that 4% of ethanol is added to the helium (Figure 12.3a). While this allows for the helium to be exposed to a large surface of ethanol, giving a high evaporation rate, the pressure control is not precise and the amount of ethanol added to the helium will change with fluctuations of the ambient temperature.

The helium mixed with roughly the required quantity of ethanol vapour is then put through a second ethanol bubbler, this one at atmospheric pressure but under precise temperature control. The volume fraction of ethanol is fine tuned as the mix passes through the bubbler: if a small excess of vapour was added in the first stage it will condense in the refrigerated bubbler; and conversely, if not enough ethanol was added in the first stage, ethanol evaporates to fill the deficit. The volume fraction of ethanol achieved at equilibrium over a range of temperatures is shown in Figure 12.3b, for atmospheric pressures at sea level (1 bar) and at the level of LSM (880 mbar).

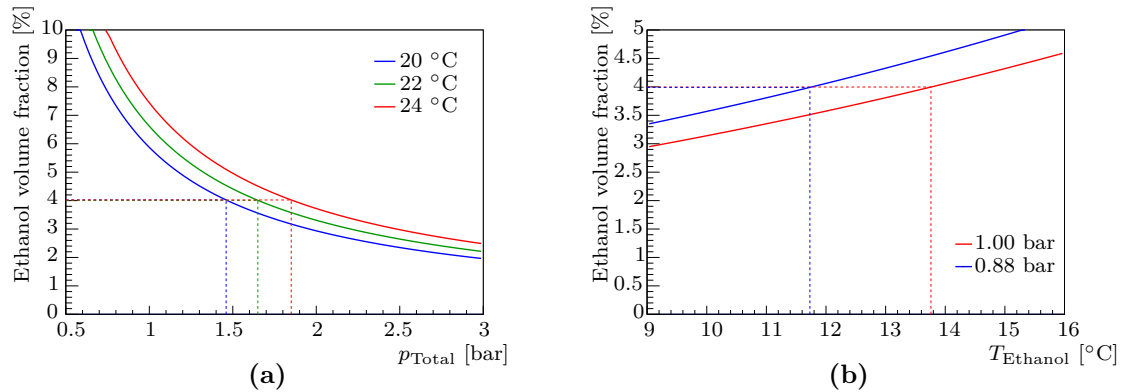


Figure 12.3.: Fractional volumes of ethanol obtained at equilibrium under controlled temperature and pressure conditions. The curves follow from Equations 12.1 and 12.2, where the Antoine equation parameters from [150] were used. In (a) the volume fraction is shown as a function of the total pressure of the gas, for three temperatures of the ethanol. The dependence of the fractional volume on the temperature of the ethanol is shown in (b) for two atmospheric pressures: at sea level in red; and at the level of the underground laboratory in blue. Dotted lines indicate the parameters required to achieve an ethanol volume fraction of 4%.

The addition of a small amount of water vapour to the gas mixture, if it is deemed necessary, can be achieved with the same method, with the vapour pressure of water at 22 °C and 1 bar giving a partial pressure of around 3%.

The pressure and temperature conditions on both bubblers are electronically monitored and accessible to a computer via an RS-485 network for logging or remote monitoring. The probes and monitoring system are reused from NEMO-3. The MFCs are also connected to the RS-485 network, allowing for remote operation and logging of the flow rate readings.

12.2. Materials

Any ^{222}Rn which emanates from the gas system's components or otherwise diffuses into the gas will be transferred to the detector's volume. As such, the ^{222}Rn activity originating from the gas system must be considered to be part of the total ^{222}Rn activity budget allowed in the tracker. While this criterion is the main constraint on the materials which can be used in the gas mixing system, compatibility with

ethanol and the out-gassing of substances which might drive the ageing of the tracker must also be taken into account for the selection of materials used. A photograph of the system is shown in Figure 12.4.

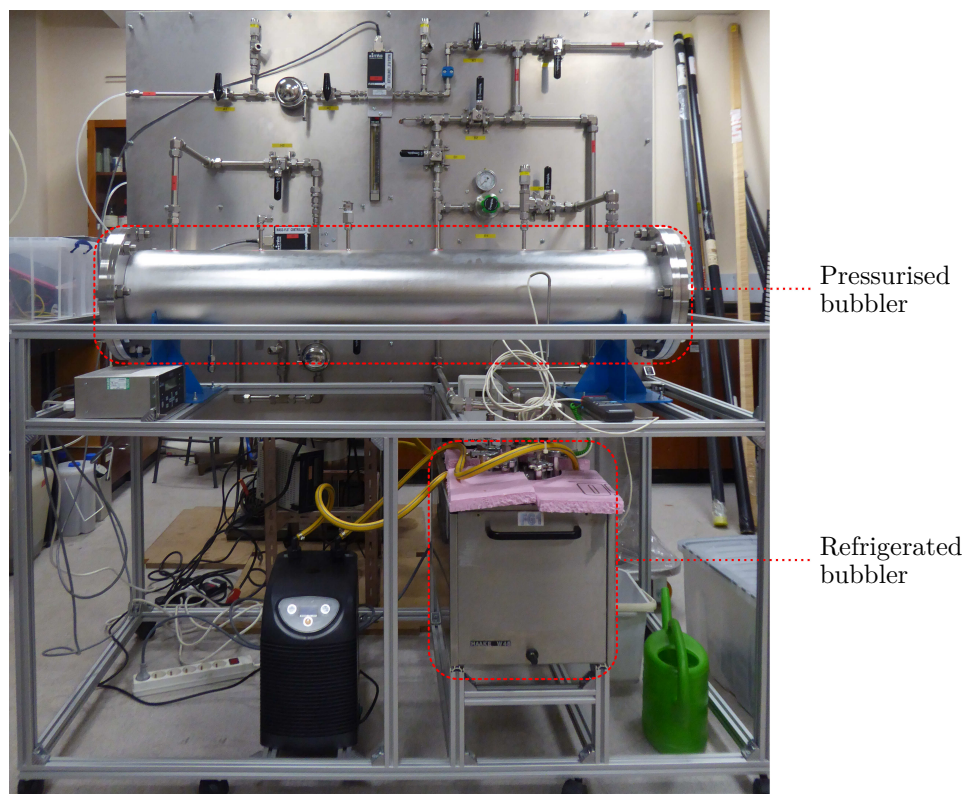


Figure 12.4.: Photograph of the Demonstrator's gas mixing system. The two ethanol bubblers are indicated by the dotted lines.

The NEMO-3 system was entirely rebuilt in stainless steel and mounted on an aluminium frame, designed for easy transportation. Stainless steel was chosen as the main material to be used in the gas routing (tube and gas connectors) as it had previously been used in the ^{222}Rn concentration line with good results [31]. Another consideration is that the wires in the tracker are made of the same material and present a larger area to the gas.

Both bubblers were initially reused from NEMO-3. However, it was found that the large pressurised bubbler emanated too much ^{222}Rn into the gas. After unsuccessful efforts to reduce this by sealing the bubbler with SBR and removing potentially contaminated parts (such as a glass window), it was decided to build a new vessel out of seamless tube, as the weld running the length of the NEMO-3 bubbler was suspected to be responsible for the high ^{222}Rn emanation. The new component was

electropolished and installed in the system and ^{222}Rn emanation measurements are ongoing.

Other material considerations included removing all glass (used for ethanol level sights) and replacing all sealing materials (O-rings) with PTFE, or other materials previously used in the ^{222}Rn concentration line.

12.3. Tests

Several tests were performed to verify that the gas mixing system was performing well and supplying an adequate gas mixture to the tracker.

The MFCs were tested by placing them in line with other available flow meters (both thermal and variable-area) and comparing the readings over a range of flow rates. It was also shown that the flow rates on the two lines of the gas system could be set at a ratio of 1%, with the flow rate readings reporting stable values over a range of flow rates.

The amount of ethanol being evaporated into the gas flow was verified using only the second-stage refrigerated bubbler. The system was operated at a flow rate of $0.12 \text{ m}^3/\text{hr}$ for two days, during which the level of ethanol in the bubbler was monitored. The readings agreed with an expected depletion rate of $1 \text{ cm}/\text{day}$, corresponding to a volume fraction of ethanol vapour in the gas mixture of 4% (Figure 12.5).

The final test of the gas mixing system was performed by using it to run the single-cell tracker prototype at UCL. This test did not include the pressurised bubbler, with the ethanol being added only in the second-stage and pre-mixed cylinders of the helium/argon mixture were used. Good performance of the cell was attained and the system was run for a long time during which studies on the ageing of the tracker cell and on the detector performance under high flow rates were carried out.

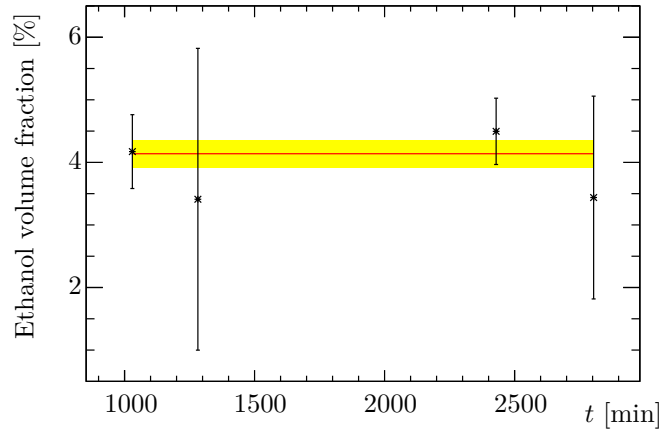


Figure 12.5.: Ethanol volume fraction in the gas measured by the depletion rate of liquid ethanol. Volume fractions corresponding to the difference in the ethanol level between each reading are shown as black markers. The measurement equivalent to the level drop over the course of the full two days is shown as a red line with a yellow band representing the estimated uncertainty.

12.4. Flow rate and ^{222}Rn activity in the tracker

The replacement rate of the gas inside the detector volume can be used as a tool to further reduce the backgrounds due to ^{222}Rn in the detector. As an inert gas ^{222}Rn will tend to simply follow the gas flow in and out of the detector. However, ^{222}Rn will α decay to ^{218}Po with a half-life of 3.8 days, leaving it in an ionised state, with a tendency to drift towards the wires and surfaces of the detector and stick to them. The backgrounds resulting from the progeny of ^{222}Rn can therefore be reduced by increasing the flow rate of the gas through the detector, flushing away ^{222}Rn before it decays. The suppression factor from the gas flow is given by:

$$F = \frac{1}{(\phi\tau/V) + 1}, \quad (12.3)$$

where ϕ is the gas flow rate, V is the detector internal volume (15.2 m^3) and τ the life-time of ^{222}Rn . At the nominal flow rate envisaged for the SuperNEMO Demonstrator, of $0.5 \text{ m}^3/\text{hr}$, the ^{222}Rn activity inside the detector would be reduced by a factor of $1/F = 5$ compared to the static case [31]. At the maximum flow rate supported by the gas system ($1.3 \text{ m}^3/\text{hr}$), a larger reduction factor of 12 would be

obtained. An increase in the flow rate by a factor of two has been shown to produce no negative effects on the operation of a SuperNEMO tracker cassette [162].

If very high gas flow rates are required, to reduce the ^{222}Rn activity in the detector, it is likely that the cost of helium, which in the baseline design is vented to the atmosphere after being used in the detector, will become the limiting factor. In this case, a gas re-circulation system might be necessary. This would require the removal of ^{222}Rn out of the used gas before injecting it back into the detector. The removal of ^{222}Rn by passing the gas through a charcoal trap would require the gas to be largely free of ethanol, as it would otherwise saturate the charcoal, preventing the adsorption of ^{222}Rn . Cooling the gas down to $-40\text{ }^\circ\text{C}$ and 5 bar would condense most of the ethanol out, leaving, at equilibrium, around 0.01% of vapour in the gas mixture. Studies are ongoing to investigate the performance of charcoal traps for gas mixtures with this amount of ethanol vapour [163].

Chapter 13.

Conclusion

Neutrinoless double- β decay is a lepton number violating process forbidden in the SM. The observation of this process would establish the Majorana nature of the neutrino. In the standard scenario, the decay proceeds through the exchange of light neutrinos. Other decay modes are predicted by theories beyond the SM, namely \mathcal{R} supersymmetry, models with left-right symmetry and those which predict the existence of Majorons.

The double- β decay of ^{48}Ca was investigated in data taken with the NEMO-3 detector over a period of eight years, from 2003 to 2011, with an accumulated live time of 5.2 years.

The $2\nu\beta\beta$ half-life of ^{48}Ca was measured to be:

$$t_{2\nu}^{1/2} = 6.4_{-0.7}^{+0.6} (\text{stat.})_{-0.9}^{+1.2} (\text{syst.}) \times 10^{19} \text{ yr}, \quad (13.1)$$

being the most precise measurement to date. This measurement is in agreement with previous measurements by the Hoover Dam and TGV experiments, although the uncertainties on these results are significantly larger.

From this result, the nuclear matrix element for the decay can be extracted:

$$|M^{2\nu}| = 0.020 \pm 0.002. \quad (13.2)$$

The value measured here is smaller than the nuclear theory predictions. It should be noted, however, that different models assumed in these calculations result in a

spread of predictions which is wider than the discrepancy with the value reported here.

No evidence was found in the data for the neutrinoless modes of double- β decay. A limit on the half-life of the mass mechanism $0\nu\beta\beta$ was set:

$$t_{0\nu}^{1/2} > 2.0 \times 10^{22} \text{ yr (90\% CL)}, \quad (13.3)$$

which does not improve the limit previously set by the ELEGANT IV experiment. From this result, a limit on the effective Majorana mass of the neutrino can be extracted:

$$\langle m_{\beta\beta} \rangle < 6.1 - 38 \text{ eV (90\% CL)}, \quad (13.4)$$

where the range reflects the disparity in nuclear matrix element calculations. While this limit is not competitive with the current best limits obtained by the KamLAND-Zen and EXO-200 ^{136}Xe experiments, it should be noted that due to the small mass (6.99 g) of ^{48}Ca present in the NEMO-3 detector, the exposure with which the result presented here was obtained is three orders of magnitude smaller than the combined exposure of the ^{136}Xe experiments. Given the very low level of background expected in the region of interest of ^{48}Ca in the NEMO-3 experiment, a simple extrapolation indicates that, in principle, a large exposure ^{48}Ca experiment would provide results competitive with current state-of-the-art experiments. The main challenge to this would be due to the very small natural abundance of ^{48}Ca and difficulties associated with its enrichment.

The half-life limit of Equation 13.3 also allows for the extraction of a limit on the \not{R} supersymmetry trilinear coupling λ'_{111} :

$$\lambda'_{111} < 0.11 - 0.14 \times f \text{ (90\% CL)}, \quad (13.5)$$

where f is given by

$$f = \left(\frac{m_{\tilde{q}}}{1 \text{ TeV}} \right)^2 \left(\frac{m_{\tilde{g}}}{1 \text{ TeV}} \right)^{1/2}. \quad (13.6)$$

Left-right symmetric models predict $0\nu\beta\beta$, either through a small admixture of a right-handed component in the SM W or via the existence of an as yet undiscovered

heavy, right-handed W' , with such decays being governed by the couplings $\langle\lambda\rangle$ and $\langle\eta\rangle$, respectively. The limits on these decay modes of ^{48}Ca were found to be:

$$t_{0\nu\lambda}^{1/2} > 1.2 \times 10^{22} \text{ yr (90\% CL)}, \quad (13.7)$$

$$t_{0\nu\eta}^{1/2} > 1.9 \times 10^{22} \text{ yr (90\% CL)}. \quad (13.8)$$

The constraints on the couplings derived from the limits above are:

$$\langle\lambda\rangle < 7.7 - 48 \times 10^{-6} \text{ (90\% CL)}, \quad (13.9)$$

$$\langle\eta\rangle < 0.76 - 55 \times 10^{-7} \text{ (90\% CL)}. \quad (13.10)$$

Lastly, the neutrinoless decay mode with the emission of a single Majoron with spectral index $n = 1$ was investigated. The broader summed electron energy spectrum of this decay results in a weaker limit compared to the ones given above:

$$t_{0\nu\chi^0}^{1/2} > 4.6 \times 10^{20} \text{ yr (90\% CL)}, \quad (13.11)$$

with the coupling of the Majoron to electrons being constrained to be:

$$\langle g_{\chi^0} \rangle < 0.44 - 3.1 \times 10^{-3} \text{ (90\% CL)}. \quad (13.12)$$

SuperNEMO is a next-generation double- β decay experiment. It is based on the same detection technique as NEMO-3, with both a tracking detector and a calorimeter being used to uniquely identify electrons and measure their individual energies. The first stage of this experiment, the Demonstrator module, is currently in an advanced stage of construction. Its tracker is being assembled and will be commissioned at surface with cosmic rays.

The data acquisition and high voltage supply systems of the NEMO-3 detector were recovered at the end of running to be used in the surface commissioning of the Demonstrator's tracker. The tracker will be commissioned in parts, with each quarter of the chamber being commissioned in turn. The NEMO-3 electronics were adapted to instrument 504 SuperNEMO cells at a time, with parts of the system,

including the high-voltage supply, VME controller and data acquisition computer being newly acquired. A bespoke board hosting an FPGA was developed to provide the set of trigger signals required by the NEMO-3 data acquisition cards. A cosmic ray trigger was developed, based on the coincident signals on two 1 m² scintillator planes, to be placed above and below the tracker C-sections.

The system was shown to perform well in tests with a 2 × 9 array of SuperNEMO production tracker cells.

A gas mixing system to supply the SuperNEMO gas mix of He:Ar:ethanol at 95:1:4 % fractions by volume to the Demonstrator's tracker was designed and built. The system is based on the one used in NEMO-3, with a number of parts being reused. The helium and argon are supplied separately and their flow rates are individually controlled to achieve the required mix. Ethanol vapour is added by passing the helium through two bubblers: one under controlled pressure and the other under controlled temperature. The conditions set in the bubblers dictate the partial pressure of the evaporated ethanol, which is tuned to achieve the required fraction in the final gas mix.

One important concern in the construction of the gas system was to reduce as much as possible the amount of ²²²Rn emanating or diffusing into the tracking gas. To this end, the system was entirely built in stainless steel (known for its low ²²²Rn emanation) and all sealing materials were selected based on previous evidence for low ²²²Rn emanation and permeation. The system is capable of sustaining flow rates much higher than what was used in NEMO-3, as high flow rates are a powerful tool for reducing the ²²²Rn activity inside the detector volume.

The system was successfully tested with a single-cell tracker prototype and the amount of ethanol being introduced into the gas was verified by measuring the ethanol depletion rate under a fast flow of gas over a few days.

Bibliography

- [1] J. Chadwick, *The intensity distribution in the magnetic spectrum of beta particles from radium (B + C)*, Verh. Phys. Gesell. **16** (1914) 383.
- [2] H. Kragh, *Niels Bohr and the quantum atom: the Bohr model of atomic structure 1913-1925*. Oxford Univ. Press, Oxford, 2012.
- [3] L. M. Brown, *The idea of the neutrino*, *Phys. Today* **31N9** (1978) 23.
- [4] F. L. Wilson, *Fermi's Theory of Beta Decay*, *American Journal of Physics* **36** (1968) no. 12, 1150.
- [5] C. Cowan, F. Reines, F. Harrison, H. Kruse, and A. McGuire, *Detection of the free neutrino: A Confirmation*, *Science* **124** (1956) 103.
- [6] C. S. Wu, E. Ambler, R. W. Hayward, D. D. Hoppes, and R. P. Hudson, *Experimental Test of Parity Conservation in Beta Decay*, *Phys. Rev.* **105** (Feb, 1957) 1413.
- [7] T. D. Lee and C. N. Yang, *Question of Parity Conservation in Weak Interactions*, *Phys. Rev.* **104** (Oct, 1956) 254.
- [8] M. Goldhaber, L. Grodzins, and A. Sunyar, *Helicity of Neutrinos*, *Phys.Rev.* **109** (1958) 1015.
- [9] J. Street and E. Stevenson, *New Evidence for the Existence of a Particle of Mass Intermediate Between the Proton and Electron*, *Phys. Rev.* **52** (1937) 1003.
- [10] M. L. Perl, G. S. Abrams, A. M. Boyarski, M. Breidenbach, Briggs, et al., *Evidence for Anomalous Lepton Production in e^+e^- Annihilation*, *Phys. Rev. Lett.* **35** (Dec, 1975) 1489.

- [11] G. Danby, J. Gaillard, K. A. Goulianos, L. Lederman, N. B. Mistry, et al., *Observation of High-Energy Neutrino Reactions and the Existence of Two Kinds of Neutrinos*, *Phys. Rev. Lett.* **9** (1962) 36.
- [12] DONUT Collaboration Collaboration, K. Kodama et al., *Observation of tau neutrino interactions*, *Phys. Lett. B* **504** (2001) 218, [arXiv:hep-ex/0012035 \[hep-ex\]](#).
- [13] ALEPH Collaboration, DELPHI Collaboration, L3 Collaboration, OPAL Collaboration, SLD Collaboration, LEP Electroweak Working Group, SLD Electroweak Group, SLD Heavy Flavour Group Collaboration, S. Schael et al., *Precision electroweak measurements on the Z resonance*, *Physics Reports* **427** (2006) no. 5 - 6, 257.
- [14] C. Giunti and C. W. Kim, *Fundamentals of Neutrino Physics and Astrophysics*. Oxford University Press, Oxford, UK, 2007. ISBN 978-0-19-850871-7.
- [15] B. Pontecorvo, *Mesonium and anti-mesonium*, *Sov. Phys. JETP* **6** (1957) 429.
- [16] J. Davis, Raymond, D. S. Harmer, and K. C. Hoffman, *Search for neutrinos from the sun*, *Phys. Rev. Lett.* **20** (1968) 1205.
- [17] P. Anselmann, W. Hampel, G. Heusser, J. Kiko, T. Kirsten, E. Pernicka, et al., *Solar neutrinos observed by GALLEX at Gran Sasso*, *Phys. Lett. B* **285** (1992) no. 4, 376.
- [18] J. Abdurashitov, E. Faizov, V. Gavrin, A. Gusev, A. Kalikhov, T. Knodel, et al., *Results from SAGE (The Russian-American gallium solar neutrino experiment)*, *Phys. Lett. B* **328** (1994) no. 1 - 2, 234.
- [19] Z. Maki, M. Nakagawa, and S. Sakata, *Remarks on the unified model of elementary particles*, *Prog. Theor. Phys.* **28** (1962) 870.
- [20] B. Pontecorvo, *Neutrino Experiments and the Problem of Conservation of Leptonic Charge*, *Sov. Phys. JETP* **26** (1968) 984.
- [21] SNO Collaboration Collaboration, Q. Ahmad et al., *Measurement of the rate of $\nu_e + d \rightarrow p + p + e^-$ interactions produced by 8B solar neutrinos at the Sudbury Neutrino Observatory*, *Phys. Rev. Lett.* **87** (2001) 071301, [arXiv:nucl-ex/0106015 \[nucl-ex\]](#).

- [22] Super-Kamiokande Collaboration Collaboration, Y. Fukuda et al., *Evidence for oscillation of atmospheric neutrinos*, *Phys. Rev. Lett.* **81** (1998) 1562, [arXiv:hep-ex/9807003 \[hep-ex\]](#).
- [23] B. Kayser, *Neutrino physics*, eConf **C040802** (2004) L004, [arXiv:hep-ph/0506165 \[hep-ph\]](#).
- [24] L. Wolfenstein, *Neutrino oscillations in matter*, *Phys. Rev. D* **17** (May, 1978) 2369.
- [25] S. Mikheev and A. Y. Smirnov, *Resonant amplification of neutrino oscillations in matter and solar neutrino spectroscopy*, *Nuovo Cim.* **C9** (1986) 17.
- [26] LSND Collaboration Collaboration, A. Aguilar-Arevalo et al., *Evidence for neutrino oscillations from the observation of anti-neutrino(electron) appearance in a anti-neutrino(muon) beam*, *Phys. Rev. D* **64** (2001) 112007, [arXiv:hep-ex/0104049 \[hep-ex\]](#).
- [27] MiniBooNE Collaboration Collaboration, A. Aguilar-Arevalo et al., *A Search for electron neutrino appearance at the $\Delta m^2 \sim 1\text{eV}^2$ scale*, *Phys. Rev. Lett.* **98** (2007) 231801, [arXiv:0704.1500 \[hep-ex\]](#).
- [28] Particle Data Group Collaboration, J. Beringer et al., *Review of Particle Physics (RPP)*, *Phys. Rev. D* **86** (2012) 010001.
- [29] LBNE Collaboration Collaboration, C. Adams et al., *The Long-Baseline Neutrino Experiment: Exploring Fundamental Symmetries of the Universe*, [arXiv:1307.7335 \[hep-ex\]](#).
- [30] NOvA Collaboration Collaboration, D. Ayres et al., *NOvA: Proposal to build a 30 kiloton off-axis detector to study $\nu_\mu \rightarrow \nu_e$ oscillations in the NuMI beamline*, [arXiv:hep-ex/0503053 \[hep-ex\]](#).
- [31] J. Mott, *Search for double beta decay of ^{82}Se with the NEMO-3 detector and development of apparatus for low-level radon measurements for the SuperNEMO experiment*. PhD thesis, University College London, 2013.
- [32] E. Majorana, *Teoria simmetrica dell'elettrone e del positrone*, *Il Nuovo Cimento* **14** (1937) no. 4, 171.
- [33] J. Schechter and J. W. F. Valle, *Neutrino masses in $SU(2) \otimes U(1)$ theories*,

- Phys. Rev. D **22** (Nov, 1980) 2227.
- [34] T. Bowles and R. Robertson, *Tritium beta decay and the search for neutrino mass*, Los Alamos Sci. **25** (1997) 86.
- [35] G. Drexlin, V. Hannen, S. Mertens, and C. Weinheimer, *Current direct neutrino mass experiments*, *Adv.High Energy Phys.* **2013** (2013) 293986, [arXiv:1307.0101 \[physics.ins-det\]](#).
- [36] J. Wieslander, J. Suhonen, T. Eronen, M. Hult, V.-V. Elomaa, et al., *Smallest Known Q Value of Any Nuclear Decay: The Rare beta- Decay of In-115 ($9/2+$) \rightarrow Sn-115 ($3/2+$)*, *Phys. Rev. Lett.* **103** (2009) 122501.
- [37] A. Belesev, A. Bleule, E. Geraskin, A. Golubev, N. Golubev, et al., *Results of the Troitsk experiment on the search for the electron anti-neutrino rest mass in tritium beta decay*, *Phys. Lett. B* **350** (1995) 263.
- [38] C. Kraus, B. Bornschein, L. Bornschein, J. Bonn, B. Flatt, et al., *Final results from phase II of the Mainz neutrino mass search in tritium beta decay*, *Eur. Phys. J. C* **40** (2005) 447, [arXiv:hep-ex/0412056 \[hep-ex\]](#).
- [39] KATRIN Collaboration Collaboration, A. Osipowicz et al., *KATRIN: A Next generation tritium beta decay experiment with sub-eV sensitivity for the electron neutrino mass. Letter of intent*, [arXiv:hep-ex/0109033 \[hep-ex\]](#).
- [40] MARE Collaboration Collaboration, A. Nucciotti, *Neutrino mass calorimetric searches in the MARE experiment*, *Nucl. Phys. Proc. Suppl.* **229-232** (2012) 155, [arXiv:1012.2290 \[hep-ex\]](#).
- [41] B. Monreal and J. A. Formaggio, *Relativistic cyclotron radiation detection of tritium decay electrons as a new technique for measuring the neutrino mass*, *Phys. Rev. D* **80** (Sep, 2009) 051301.
- [42] WMAP Collaboration, G. Hinshaw et al., *Nine-Year Wilkinson Microwave Anisotropy Probe (WMAP) Observations: Cosmological Parameter Results*, *Astrophys. J. Suppl.* **208** (2013) 19, [arXiv:1212.5226 \[astro-ph.CO\]](#).
- [43] S. A. Thomas, F. B. Abdalla, and O. Lahav, *Upper Bound of 0.28 eV on the Neutrino Masses from the Largest Photometric Redshift Survey*, *Phys. Rev. Lett.* **105** (2010) 031301, [arXiv:0911.5291 \[astro-ph.CO\]](#).

- [44] KamLAND-Zen Collaboration Collaboration, A. Gando et al., *Limit on Neutrinoless $\beta\beta$ Decay of Xe-136 from the First Phase of KamLAND-Zen and Comparison with the Positive Claim in Ge-76*, *Phys. Rev. Lett.* **110** (2013) no. 6, 062502, [arXiv:1211.3863 \[hep-ex\]](#).
- [45] W. Rodejohann, *Neutrinoless double beta decay and neutrino physics*, *J. Phys. G* **39** (2012) 124008, [arXiv:1206.2560 \[hep-ph\]](#).
- [46] S. D. Biller, *Probing Majorana neutrinos in the regime of the normal mass hierarchy*, *Phys. Rev. D* **87** (2013) no. 7, 071301, [arXiv:1306.5654 \[physics.ins-det\]](#).
- [47] C. Weizsacker, *Zur Theorie der Kernmassen*, *Z. Phys.* **96** (1935) 431.
- [48] M. Goeppert-Mayer, *Double beta-disintegration*, *Phys. Rev.* **48** (1935) 512.
- [49] R. Saakyan, *Two-Neutrino Double-Beta Decay*, *Annual Review of Nuclear and Particle Science* **63** (2013) no. 1, 503.
- [50] E. Caurier, A. P. Zuker, A. Poves, and G. Martínez-Pinedo, *Full pf shell model study of $A=48$ nuclei*, *Phys. Rev. C* **50** (Jul, 1994) 225.
- [51] R. Arnold et al., *Probing new physics models of neutrinoless double beta decay with SuperNEMO*, *The European Physical Journal C* **70** (2010) no. 4, 927.
- [52] P. Bamert et al., *Multi-majoron modes for neutrinoless double-beta decay*, *Nucl. Phys. B* **449** (1995) no. 1-2, 25.
- [53] J. D. Vergados et al., *Theory of neutrinoless double-beta decay*, *Rep. Prog. Phys.* **75** (2012) no. 10, 106301.
- [54] F. T. Avignone, S. R. Elliott, and J. Engel, *Double beta decay, Majorana neutrinos, and neutrino mass*, *Rev. Mod. Phys.* **80** (Apr, 2008) 481–516.
- [55] Super-Kamiokande Collaboration, H. Nishino et al., *Search for Nucleon Decay into Charged Anti-lepton plus Meson in Super-Kamiokande I and II*, *Phys. Rev. D* **85** (2012) 112001, [arXiv:1203.4030 \[hep-ex\]](#).
- [56] R. Barbier et al., *R-parity violating supersymmetry*, *Phys. Rept.* **420** (2005) 1, [arXiv:hep-ph/0406039 \[hep-ph\]](#).
- [57] J. Dechargé and D. Gogny, *Hartree-Fock-Bogolyubov calculations with the D1*

- effective interaction on spherical nuclei*, *Phys. Rev. C* **21** (Apr, 1980) 1568.
- [58] H. Klapdor-Kleingrothaus et al., *Search for neutrinoless double beta decay with enriched ^{76}Ge in Gran Sasso 1990-2003*, *Phys. Lett. B* **586** (2004) 198, [arXiv:hep-ph/0404088](#) [hep-ph].
- [59] C. Aalseth et al., *Comment on ‘Evidence for neutrinoless double beta decay’*, *Mod. Phys. Lett. A* **17** (2002) 1475, [arXiv:hep-ex/0202018](#) [hep-ex].
- [60] EXO Collaboration Collaboration, M. Auger et al., *Search for Neutrinoless Double-Beta Decay in ^{136}Xe with EXO-200*, *Phys. Rev. Lett.* **109** (Jul, 2012) 032505.
- [61] GERDA Collaboration Collaboration, M. Agostini et al., *Results on Neutrinoless Double- β Decay of ^{76}Ge from Phase I of the GERDA Experiment*, *Phys. Rev. Lett.* **111** (2013) no. 12, 122503, [arXiv:1307.4720](#) [nucl-ex].
- [62] M. B. Heider, *Semiconductor-based experiments for neutrinoless double beta decay search*, *Nucl. Phys. Proc. Suppl. B* **229-232** (2012) no. 0, 141. Neutrino 2010.
- [63] J. Shirai, *KamLAND-Zen: Status and Future*, *Nucl. Phys. Proc. Suppl. B* **237-238** (2013) no. 0, 28. Proceedings of the Neutrino Oscillation Workshop Proceedings of the Neutrino Oscillation Workshop.
- [64] NEXT Collaboration Collaboration, J. Gomez-Cadenas et al., *Present status and future perspectives of the NEXT experiment*, [arXiv:1307.3914](#) [physics.ins-det].
- [65] H. Klapdor-Kleingrothaus et al., *Latest results from the Heidelberg-Moscow double beta decay experiment*, *Eur. Phys. J. A* **12** (2001) 147, [arXiv:hep-ph/0103062](#) [hep-ph].
- [66] C. Aalseth et al., *Recent results of the IGEX ^{76}Ge double-beta decay experiment*, *Physics of Atomic Nuclei* **63** (2000) no. 7, 1225.
- [67] GERDA Collaboration Collaboration, M. Agostini et al., *Measurement of the half-life of the two-neutrino double beta decay of Ge-76 with the Gerda experiment*, *J. Phys. G* **40** (2013) 035110, [arXiv:1212.3210](#) [nucl-ex].
- [68] K. Knöpfle, *GERDA – Status and Perspectives*, *Nucl. Phys. B - Proc. Suppl.*

- 237-238** (2013) no. 0, 31. Proceedings of the Neutrino Oscillation Workshop
Proceedings of the Neutrino Oscillation Workshop.
- [69] Majorana Collaboration Collaboration, N. Abgrall et al., *The Majorana Demonstrator Neutrinoless Double-Beta Decay Experiment*, **Adv. High Energy Phys.** **2014** (2014) 365432, [arXiv:1308.1633 \[physics.ins-det\]](#).
- [70] J. R. Wilson, *Double Beta Decay Measurement with COBRA*, **Nuclear Physics B - Proceedings Supplements** **221** (2011) no. 0, 313. The Proceedings of the 22nd International Conference on Neutrino Physics and Astrophysics The Proceedings of the 22nd International Conference on Neutrino Physics and Astrophysics.
- [71] E. Andreotti et al., *^{130}Te Neutrinoless Double-Beta Decay with CUORICINO*, **Astropart. Phys.** **34** (2011) 822, [arXiv:1012.3266 \[nucl-ex\]](#).
- [72] L. Pattavina and the Cuore collaboration, *Status of the CUORE experiment*, **Journal of Physics: Conference Series** **447** (2013) no. 1, 012066.
- [73] J. R. Wilson, *Non-accelerator Neutrino Physics*, IoP HEPP & APP Group Meeting, 2013.
- [74] EXO-200 Collaboration Collaboration, J. Albert et al., *An improved measurement of the $2\nu\beta\beta$ half-life of ^{136}Xe with EXO-200*, **Phys. Rev. C** **89** (2014) 015502, [arXiv:1306.6106 \[nucl-ex\]](#).
- [75] L. Yang, *The Enriched Xenon Observatory (EXO)*, PANIC conference, 2011.
- [76] NEMO-3 Collaboration Collaboration, R. Arnold et al., *Search for Neutrinoless Double-Beta Decay of ^{100}Mo with the NEMO-3 Detector*, **Phys. Rev. D** **89** (2014) 111101, [arXiv:1311.5695 \[hep-ex\]](#).
- [77] E. d. Mateosian and M. Goldhaber, *Limits for Lepton-Conserving and Lepton-Nonconserving Double Beta Decay in ^{48}Ca* , **Phys. Rev.** **146** (Jun, 1966) 810.
- [78] K. You et al., *A search for neutrinoless double β decay of ^{48}Ca* , **Phys. Lett. B** **265** (1991) no. 1, 53.
- [79] A. Balysh et al., *Double Beta Decay of ^{48}Ca* , **Phys. Rev. Lett.** **77** (Dec, 1996) 5186.

- [80] V. Brudanin et al., *Search for double beta decay of ^{48}Ca in the TGV experiment*, *Phys. Lett. B* **495** (2000) 63.
- [81] S. Umehara et al., *Neutrino-less double- β decay of ^{48}Ca studied by CaF_2 (Eu) scintillators*, *Phys. Rev. C* **78** (Nov, 2008) 058501.
- [82] NEMO-3 Collaboration Collaboration, J. Argyriades et al., *Measurement of the two neutrino double beta decay half-life of ^{96}Zr with the NEMO-3 detector*, *Nucl. Phys. A* **847** (2010) 168, [arXiv:0906.2694 \[nucl-ex\]](#).
- [83] NEMO Collaboration Collaboration, R. Arnold et al., *First results of the search of neutrinoless double beta decay with the NEMO 3 detector*, *Phys. Rev. Lett.* **95** (2005) 182302, [arXiv:hep-ex/0507083 \[hep-ex\]](#).
- [84] NEMO Collaboration Collaboration, L. Simard et al., *The NEMO-3 results after completion of data taking*, *Journal of Physics: Conference Series* **375** (2012) no. 4, 042011.
- [85] NEMO-3 Collaboration Collaboration, R. Arnold et al., *Measurement of the Double Beta Decay Half-life of ^{130}Te with the NEMO-3 Detector*, *Phys. Rev. Lett.* **107** (2011) 062504, [arXiv:1104.3716 \[nucl-ex\]](#).
- [86] NEMO Collaboration Collaboration, J. Argyriades et al., *Measurement of the Double Beta Decay Half-life of ^{150}Nd and Search for Neutrinoless Decay Modes with the NEMO-3 Detector*, *Phys. Rev. C* **80** (2009) 032501, [arXiv:0810.0248 \[hep-ex\]](#).
- [87] F. A. Danevich et al., *Search for 2β decay of cadmium and tungsten isotopes: Final results of the Solotvina experiment*, *Phys. Rev. C* **68** (Sep, 2003) 035501.
- [88] R. Arnold, C. Augier, A. Bakalyarov, J. Baker, A. Barabash, et al., *Technical design and performance of the NEMO-3 detector*, *Nucl. Instrum. Meth. A* **536** (2005) 79, [arXiv:physics/0402115 \[physics\]](#).
- [89] V. Tretyak, *^{48}Ca troubleshooting*, Internal Note **DocDB:2080** (2011) .
- [90] V. Tretyak, *^{48}Ca data analysis*, Internal Note **DocDB:2081** (2012) .
- [91] V. Tretyak, *Measurement of the ^{48}Ca strip rotation angle*, Internal Note **DocDB:2255** (2012) .

- [92] EDELWEISS Collaboration Collaboration, B. Schmidt et al., *Muon-induced background in the EDELWEISS dark matter search*, *Astropart. Phys.* **44** (2013) 28, [arXiv:1302.7112 \[astro-ph.CO\]](#).
- [93] NEMO-3 Collaboration Collaboration, J. Argyriades et al., *Measurement of the background in the NEMO-3 double beta decay experiment*, *Nucl. Instrum. Meth. A* **606** (2009) 449, [arXiv:0903.2277 \[nucl-ex\]](#).
- [94] O. Ponkratenko, V. Tretyak, and Y. Zdesenko, *The Event generator DECAY4 for simulation of double beta processes and decay of radioactive nuclei*, *Phys. Atom. Nucl.* **63** (2000) 1282, [arXiv:nucl-ex/0104018 \[nucl-ex\]](#).
- [95] R. Brun, F. Bruyant, M. Maire, A. McPherson, and P. Zancarini, *GEANT3*, CERN-DD-EE-84-1 (1987) .
- [96] S. Blot and J. Mott, *New model for the electron-gamma time-of-flight hypothesis in NEMO-3*, Internal Note **DocDB:3343** (2014) .
- [97] F. James and M. Roos, *Minuit: A System for Function Minimization and Analysis of the Parameter Errors and Correlations*, *Comput. Phys. Commun.* **10** (1975) 343.
- [98] R. Brun and F. Rademakers, *ROOT – An object oriented data analysis framework*, *Nucl.Instrum.Meth.* **A389** (1997) 81 – 86.
<http://root.cern.ch/>. New Computing Techniques in Physics Research V.
- [99] G. Cowan, *Statistical Data Analysis*. Oxford University Press, 1998.
- [100] G. Zech, *Upper limits in experiments with background or measurement errors*, *Nucl. Instr. Meth. A* **277** (1989) no. 2–3, 608.
- [101] A. L. Read, *Presentation of search results: the CL_s technique*, *Journal of Physics G: Nuclear and Particle Physics* **28** (2002) no. 10, 2693.
- [102] S. S. Wilks, *The Large-Sample Distribution of the Likelihood Ratio for Testing Composite Hypotheses*, *Ann. Math. Statist.* **9** (03, 1938) 60.
- [103] G. Cowan, *Statistics for Searches at the LHC*, [arXiv:1307.2487 \[hep-ex\]](#) .
- [104] W. Fisher, *Collie: A Confidence Level Limit Evaluator*, DØ note **5595** (2009) .

- [105] Brookhaven National Laboratory, *NNDC On-Line Data Service from the ENSDF database, file revised as of July 2014*, .
<http://www.nndc.bnl.gov/ensdf/>.
- [106] S. Blondel, *^{150}Nd Analysis*, Internal Note **DocDB:2398** (2012) .
- [107] P. Loaiza, *^{48}Ca radiopurity measurements*, Internal Note **DocDB:2076** (2012) .
- [108] R. Arnold, *Comments on the angular distribution between electrons from $\beta\beta$ events*, Internal Note **DocDB:927** (2009) .
- [109] V. Tretyak, *Same-side/Opposite-side $2e$ events in ^{100}Mo* , Internal Note **DocDB:3346** (2014) .
- [110] S. Torre, *^{100}Mo Analysis Systematics*, Internal Note **DocDB:3238** (2014) .
- [111] J. Kotila and F. Iachello, *Phase-space factors for double- β decay*, *Phys. Rev. C* **85** (Mar, 2012) 034316.
- [112] J. Suhonen and O. Civitarese, *Weak-interaction and nuclear-structure aspects of nuclear double beta decay*, *Physics Reports* **300** (1998) no. 3, 123.
- [113] L. Zhao, B. A. Brown, and W. A. Richter, *Shell-model calculation for two-neutrino double beta decay of ^{48}Ca* , *Phys. Rev. C* **42** (Sep, 1990) 1120.
- [114] E. Caurier, G. Martínez-Pinedo, F. Nowacki, A. Poves, and A. P. Zuker, *The shell model as a unified view of nuclear structure*, *Rev. Mod. Phys.* **77** (Jun, 2005) 427.
- [115] E. Caurier, A. Poves, and A. Zuker, *A full $0\hbar\omega$ description of the $2\nu\beta\beta$ decay of ^{48}Ca* , *Physics Letters B* **252** (1990) no. 1, 13.
- [116] M. Horoi, S. Stoica, and B. A. Brown, *Shell-model calculations of two-neutrino double- β decay rates of ^{48}Ca with the *GXPFI1A* interaction*, *Phys. Rev. C* **75** (Mar, 2007) 034303.
- [117] E. Caurier, F. Nowacki, and A. Poves, *Shell Model description of the $\beta\beta$ decay of ^{136}Xe* , *Physics Letters B* **711** (2012) no. 1, 62.
- [118] T. Tsuboi, K. Muto, and H. Horie, *Double beta decay nuclear matrix element of ^{48}Ca* , *Phys. Lett. B* **143** (1984) no. 4-6, 293.

- [119] K. Ogawa and H. Horie, *A new method of calculating the nuclear matrix element of the double beta decay*, in *Nuclear Weak Processes and Nuclear Structure*, pp. 308–313. World Scientific, 1989.
- [120] D.-C. Zheng, L. Zamick, and N. Auerbach, *Nuclear structure studies of double Gamow-Teller and double beta decay strength*, *Annals of Physics* **197** (1990) no. 2, 343.
- [121] K. Muto and H. Horie, *Shell-model study on $M1$ strength distributions in $N = 28$ isotones*, *Phys. Lett. B* **138** (1984) no. 1-3, 9.
- [122] W. Richter, M. V. D. Merwe, R. Julies, and B. Brown, *New effective interactions for the $0f1p$ shell*, *Nucl. Phys. A* **523** (1991) no. 2, 325.
- [123] T. Kuo and G. Brown, *Reaction matrix elements for the $0f-1p$ shell nuclei*, *Nucl. Phys. A* **114** (1968) no. 2, 241.
- [124] A. Yokoyama and H. Horie, *Intruder states of the odd-mass $N=27$ isotones*, *Phys. Rev. C* **31** (Mar, 1985) 1012.
- [125] M. Honma, T. Otsuka, B. A. Brown, and T. Mizusaki, *Effective interaction for pf -shell nuclei*, *Phys. Rev. C* **65** (May, 2002) 061301.
- [126] O. Helene, *Upper Limit of Peak Area*, *Nucl. Instrum. Meth.* **212** (1983) 319.
- [127] M. Horoi, *Shell model analysis of competing contributions to the double- β decay of ^{48}Ca* , *Phys. Rev. C* **87** (Jan, 2013) 014320.
- [128] E. Caurier et al., *Influence of Pairing on the Nuclear Matrix Elements of the Neutrinoless $\beta\beta$ Decays*, *Phys. Rev. Lett.* **100** (Feb, 2008) 052503.
- [129] J. Suhonen, *Calculation of the beta and beta beta decay observables of ^{48}Ca using QRPA with and without particle-number projection*, *J. Phys. G* **19** (Jan., 1993) 139.
- [130] G. Pantis et al., *Neutrinoless double beta decay within the quasiparticle random-phase approximation with proton-neutron pairing*, *Phys. Rev. C* **53** (Feb, 1996) 695.
- [131] J. Barea et al., *Nuclear matrix elements for double- β decay*, *Phys. Rev. C* **87** (Jan, 2013) 014315.

- [132] T. R. Rodríguez and G. Martínez-Pinedo, *Energy Density Functional Study of Nuclear Matrix Elements for Neutrinoless $\beta\beta$ Decay*, Phys. Rev. Lett. **105** (Dec, 2010) 252503.
- [133] A. Wodecki et al., *Grand unified theory constrained supersymmetry and neutrinoless double β decay*, Phys. Rev. D **60** (Nov, 1999) 115007.
- [134] M. Hirsch et al., *Double beta decay, supersymmetry and lepton number violation*, Nucl. Phys. B - Proc. Suppl. **62** (1998) no. 1-3, 224. Proceedings of the Fifth International Conference on Supersymmetries in Physics.
- [135] B. Allanach et al., *Explaining the CMS $eejj$ Excess With \mathcal{R} -parity Violating Supersymmetry and Implications for Neutrinoless Double Beta Decay*, arXiv:1408.5439 [hep-ph].
- [136] M. Günther et al., *Heidelberg-Moscow $\beta\beta$ experiment ^{76}Ge : Full setup with five detectors*, Phys. Rev. D **55** (Jan, 1997) 54.
- [137] S. P. Das et al., *Heavy neutrinos and lepton flavor violation in left-right symmetric models at the LHC*, Phys. Rev. D **86** (Sep, 2012) 055006.
- [138] P. S. B. Dev et al., *TeV Scale Left-Right Symmetry and Large Mixing Effects in Neutrinoless Double Beta Decay*, arXiv:1405.1399 [hep-ph].
- [139] KamLAND-Zen Collaboration Collaboration, A. Gando et al., *Limits on Majoron-emitting double- β decays of ^{136}Xe in the KamLAND-Zen experiment*, Phys. Rev. C **86** (Aug, 2012) 021601.
- [140] R. Tomàs et al., *Generalized bounds on Majoron-neutrino couplings*, Phys. Rev. D **64** (Oct, 2001) 095005.
- [141] H. Gómez and SuperNEMO Collaboration, *BiPo: A dedicated radiopurity detector for the SuperNEMO experiment*, AIP Conference Proceedings **1549** (2013) no. 1, 94.
- [142] F. Mamedov et al., *High sensitivity detectors for measurement of diffusion, emanation and low activity of radon*, AIP Conference Proceedings **1549** (2013) no. 1, 120.
- [143] D. Wilkinson, *The Geiger discharge revisited Part I. The charge generated*, Nucl. Instr. Meth. A **321** (1992) no. 1–2, 195.

- [144] D. Wilkinson, *The Geiger discharge revisited Part II. Propagation*, *Nucl. Instr. Meth. A* **383** (1996) no. 2–3, 516.
- [145] S. H. Liebson, *The Discharge Mechanism of Self-Quenching Geiger-Mueller Counters*, *Phys. Rev.* **72** (Oct, 1947) 602.
- [146] E. Chauveaux, *Développement de compteurs à scintillation hautes performances et de très basse radioactivité pour le calorimètre du projet SuperNEMO*. PhD thesis, Université Bordeaux 1, 2010.
- [147] S. S. Friedland and H. S. Katzenstein, *Factors Influencing the Life of Self-Quenching Counters*, *Rev. Sci. Instrum.* **24** (1953) no. 2, .
- [148] L. Malter, *Thin Film Field Emission*, *Phys. Rev.* **50** (Jul, 1936) 48.
- [149] J. Va'vra, *Physics and chemistry of aging – early developments*, *Nucl. Instr. Meth. A* **515** (2003) no. 1 – 2, 14. Proceedings of the International Workshop on Aging Phenomena in Gaseous Detectors.
- [150] National Institute of Standards and Technology, *NIST Chemistry WebBook, NIST Standard Reference Database Number 69, retrieved September 2014, . <http://webbook.nist.gov/>*.
- [151] E. Chauveaux, *SuperNEMO cell at Manchester: efficiency and dead time*, Internal Note **DocDB:1768** (2011) .
- [152] E. Chauveaux, *Differentiator circuit for anode signal analysis*, Internal Note **DocDB:1714** (2011) .
- [153] W. Maneschg et al., *Measurements of extremely low radioactivity levels in stainless steel for GERDA*, *Nucl. Instr. Meth. A* **593** (2008) no. 3, 448.
- [154] E. Chauveaux, *Status of the wire rig test for massive wire control*, Internal Note **DocDB:1842** (2011) .
- [155] M. Perry, *Tracker HV Update*, Internal Note **DocDB:2627** (2013) .
- [156] E. Chauveaux et al., *FEAST testing in Manchester with 18-cell prototype*, Internal Note **DocDB:2500** (2012) .
- [157] P. Adamson et al., *The MINOS calibration detector*, *Nucl. Instr. Meth. A* **556** (2006) no. 1, 119.

- [158] S. Kilani, *Private communication*, .
- [159] C. Vilela et al., *Commissioning electronics and DAQ update*, Internal Note **DocDB:1957** (2011) .
- [160] S. de Capua and P. Guzowski, *Private communication*, .
- [161] C. Vilela, *Pressure fluctuations at LSM*, Internal Note **DocDB:2161** (2012) .
- [162] S. de Capua, *Flow rate study*, Internal Note **DocDB:3146** (2014) .
- [163] J. Busto, *Private communication*, .